UNIVERSITY OF BIRMINGHAM

CHARACTERISATION OF CRYSTALLISATION AND MELTING IN THERMOPLASTIC POLYMERS USING CHIP CALORIMETRY

BY

JOSEPH JACK MARSH

A THESIS SUBMITTED TO THE UNIVERSITY OF BIRMINGHAM FOR THE DEGREE OF DOCTOR OF PHILOSOPHY

SCHOOL OF METALLURGY AND MATERIALS
COLLEGE OF ENGINEERING AND PHYSICAL SCIENCES
UNIVERSITY OF BIRMINGHAM
DECEMBER 2016

ACKNOWLEDGEMENTS

I would like to express my sincere appreciation to all who have supported me during my PhD. I would like to thank my supervisors, Dr. Mike Jenkins and Dr. Stephen Kukureka for their guidance and continued support and Mr. Frank Biddlestone for his invaluable technical assistance and friendship.

I would also like to thank the support of my family and friends, without whom I would not have come so far.

ABSTRACT

Fast scanning chip-calorimetry was used to explore the crystallisation and melting of three semi-crystalline polymers: poly(ε-caprolactone) (PCL), poly(lactic acid) (PLA) and poly(ether-ether-ketone) (PEEK). In each case, the heating and cooling rates required to prevent crystallisation on cooling (from above the melting point) and on re-heating (from below the glass to liquid transition temperature) were determined as: 3,000 and 8,000˚C/s respectively in PCL, 75 and 250˚C/s respectively in PEEK and 10 and 100˚C/s respectively in PLA. The effect of the thermal lag was considered using indium as a standard and corrections were subsequently made to all melting and crystallisation points. Corrections of >5˚C were required at rates in excess of 5,000˚C/s with a sample mass ≥~66 ng. When nuclei are present in PCL, the heating rates accessible in the chip-calorimeter are insufficient to prevent recrystallisation, which was a surprising observation.

As readily observed in conventional differential scanning calorimetry (CDSC), PEEK exhibited a double melting endotherm and this was attributed to a melting-recrystallisation-melting process. The absence of recrystallisation above 250˚C allowed a Hoffman-Weeks analysis to be carried out over a broader temperature range than is general possible in CDSC. The interplay between thermal lag and re-crystallisation was analysed using heating rates covering 5 orders of magnitude. At an optimum heating rate of 1,500˚C/s, an equilibrium melting temperature of 359˚C was determined.

The consideration of thermal lag led to the measurement of diffusivity using the technique of laser flash apparatus (LFA). The high measurement speed in the LFA

allowed a time and temperature resolved study of diffusivity in PLA. On heating through T_g, PLA showed a reduction in thermal diffusivity, comparable to the change in specific heat (ΔC_p). This is explained in terms of the concepts of free volume, molecular mobility and phonon transport.

LFA, chip-calorimetry and CDSC were used in parallel to explore the cold-crystallisation kinetics of PLA and the development of the relatively unstable α' crystals. A good correlation between chip-calorimetry and LFA was found, showing an Avrami exponent of 2 and nucleation constant of 6.58 $x10^5$ and 6.87 $x10^5$ respectively, corresponding to regime III.

TABLE OF CONTENTS

LIST OF ILLUSTRATIONS

LIST OF TABLES

CHAPTER 1 INTRODUCTION

1.1 Polymer Morphology

Polymers are long chain molecules formed through chemical reactions, bonding monomers together by a process known as polymerization. These monomer units are covalently bonded to create longer chains. In the liquid state, polymer chains are coiled, entangled and in a constant state of long-range motion. Quench cooling a polymer (thereby preventing crystallisation) 'freezes-in' the disordered structure, resulting in the transition of a mobile liquid into a glassy solid. This transition is known as the glass transition temperature (T_g). The resulting glass is in a non-equilibrium state, as illustrated in Figure 1-1.

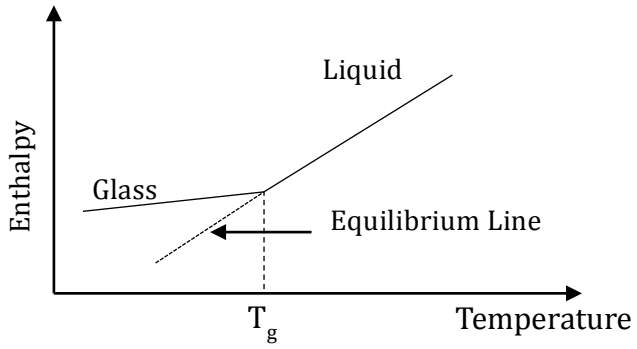

Figure 1-1 - Change in enthalpy with temperature

The cooling rate dependence of T_g results in a glass formation that is not in thermal equilibrium increasing with elevated cooling rates. Polymer chains require time to relax and accommodate changes in thermodynamic properties with temperature. Raised cooling rates reduce the time for chain motion, resulting in an excess free volume and

enthalpy within the system. The cooling rate dependence of T_g may be described by the Arrhenius equation:

$$k = Ae^{-E_a/RT}$$

Equation 1-1

where k is equal to cooling rate (˚C/s), A is the pre-exponential factor, E_a is activation energy (J/mol), R is the universal gas constant (8.31447 J/mol.K) (Moldover *et al.*, 1988) and T is temperature (K).

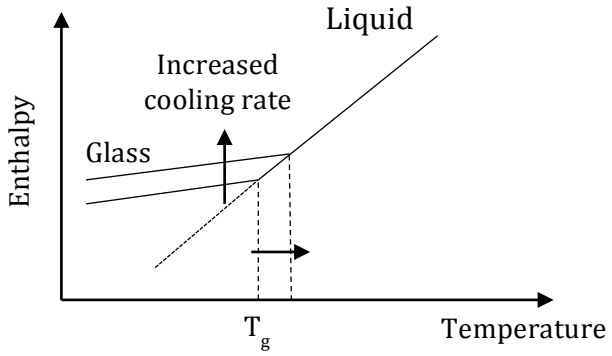

Figure 1-2 - The effect of cooling rate on the enthalpy of the system with temperature

Above T_g, the cooperative nature of conformational transitions occurs around the carbon-carbon bonds, permitting long range order. The absence of long range order below T_g does not stop chain motion due to short range order at the atomic scale from the nature of the chemical bonds, localising movement of chain segments, i.e. crankshaft and 3- or 4- bond motions (Bahar *et al.*, 1992).

Unless the system is cooled infinitely slowly, below T_g, the chains have excess enthalpy providing a driving force for chain relaxation towards the equilibrium value. A change in the thermodynamic quantities occurs with storage time at a constant temperature below T_g. Short range order allows molecular motions to occur below T_g, gradually

allowing equilibrium to be achieved with time. This reduction in enthalpy and volume is described as physical ageing, illustrated in Figure 1-3. The ageing process is visible as an endothermic peak at T_g on heating traces in differential scanning calorimetry (DSC). The size of the endotherm can be attributed to the time period of ageing showing an increase in size with ageing time (Cowie and Ferguson, 1993).

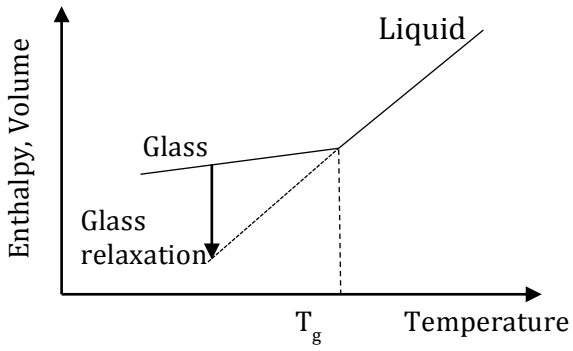

Figure 1-3 - Change in enthalpy through relaxation of polymer chains below T_g

1.2 Crystallinity and the Crystallisation Process

Crystallisation is the process through which a disordered phase becomes an ordered structure. Crystallisation can occur in a polymeric liquid below the melting temperature (T_m) where there is chain motion. Crystallisation cannot occur at temperatures below T_g as the chains are not mobile enough. The crystallisation process can be split into two stages: nucleation and growth.

1.2.1 The Nucleation Process

Nucleation occurs when a polymer passes below its T_m where there is a tendency for alignment of chains forming small ordered regions, known as nuclei (or embryo). The formation of nuclei was shown through early experimentation by Barnes (1906), Young (1911), Berkeley (1912) and Young and Van Sicklen (1913) to be induced through agitation, mechanical shock, friction and extreme pressures within solutions and melts.

These nuclei can disappear and reform dependant on the degree of free energy present (Adam and Gibbs, 1965). Nucleation can occur through two different processes as described by Wunderlich (1976): homogeneous and heterogeneous nucleation. Homogeneous nucleation requires a high degree of free energy for the chains to spontaneously create a nucleus; however, is not the primary nucleation mechanism due to the small possibility of random chain arrangement. Heterogeneous nucleation is artificially induced by foreign bodies or impurities such as dust particles and is the most common nucleation mechanism seen in polymer crystallisation (Long *et al.*, 1995). It is more thermodynamically favoured, occurring at lower degrees of super-cooling ($\Delta T=T_m^0-T_c$), where T_m^0 is the equilibrium melting temperature and T_c is the crystallisation temperature) as the free energy barrier to nucleation is reduced where nucleation on pre existing surface occurs.

An important driving force for crystallisation is the Gibbs free energy difference between the solid and the liquid (ΔG). ΔG is a temperature dependent parameter, which can be related to the change in enthalpy (ΔH) and the entropy difference (ΔS) between the solid and the liquid.

$$\Delta G = \Delta H - T\Delta S$$

Equation 1-2

At T_m, ΔG =0 where

$$T_m = \frac{\Delta H}{\Delta S}$$

Equation 1-3

Crystallisation cannot occur above T_m where $\Delta G>0$; however, crystallisation can occur below T_m where $\Delta G<0$. As supercooling increases, ΔG becomes more negative, increasing the driving force for crystallisation.

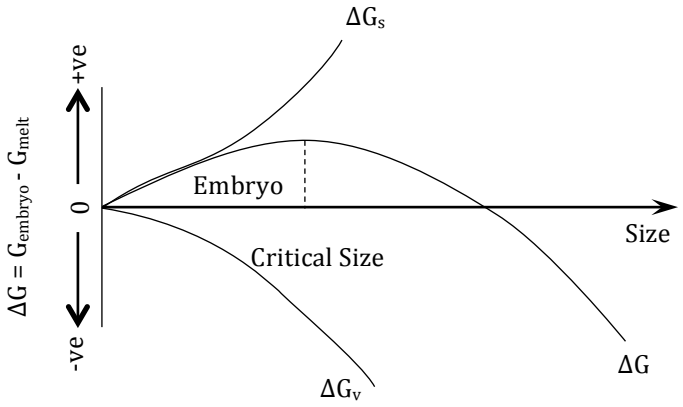

Figure 1-4 - Schematic diagram of the change in free energy during nucleation

The overall excess free energy (ΔG) is the sum of the surface free energy (ΔG_s), the excess free energy between the surface and the bulk of the nucleus, and volume free energy ΔG_v, the excess free energy between in infinitely large nucleus and the nucleus in the liquid. ΔG_s is a positive quantity, proportional to r^2 (where r is nuclei radius); ΔG_v is a negative quantity, proportional to r^3. The dependence of ΔG on the nuclei radius causes ΔG to pass through a maximum corresponding to the critical nuclei (Figure 1-4). For a spherical nucleus the critical free energy, ΔG^*, can be described through Equation 1-4, where σ is the surface tension and r_c is the critical radius (Schultz, 2001).

$$\Delta G^* = \frac{4}{3}\pi\sigma r_c^2$$

Equation 1-4

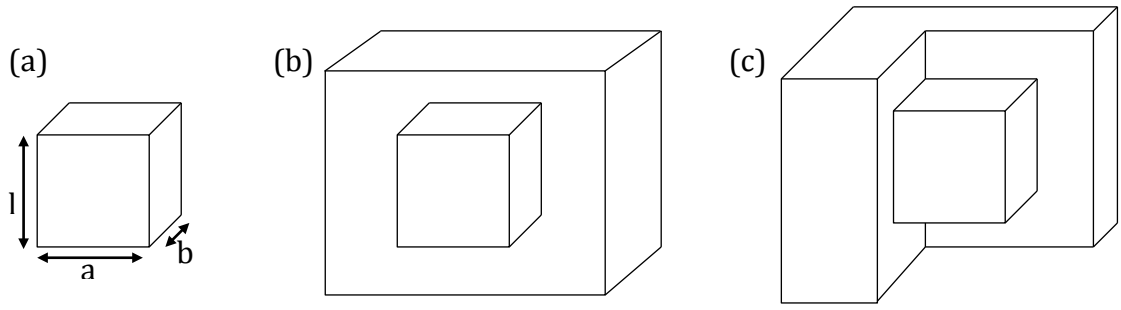

Figure 1-5 - (a) Regime I, (b) Regime II and (c) Regime III

According to Hoffman and Lauritzen (1961), nucleation development can be separated into three different stages (Figure 1-5) where a, b and l are dimensions of the nuclei. The first, primary nucleation, describes the initial formation of a nuclei (or embryo). Secondary nucleation is the building of a new layer of material on the growth face of a pre-existing crystal. Secondary nucleation determines the crystal growth rate and requires a lower free energy in comparison to primary nucleation since nucleation occurs on a pre-existing surface and the surface-to-volume ratio is lower. The free energy barrier is lower since less new surface area is added compared to a new nucleus. Tertiary nucleation occurs along an existing crystal edge, resulting in the lower free energy in comparison to secondary due to a smaller surface to volume ratio (Hoffman *et al.*, 1969).

1.2.2 Crystal Growth

It is described in crystallisation theories that the growth process occurs through secondary nucleation, whereby the growth occurs from the pre-existing crystal surface. Depending on the geometric shape of the crystals, growth can develop in 1-, 2-, or 3-dimensions as rods, discs and spheres respectively. Molecules are added to a molecularly smooth crystal surface, requiring the creation of less new surface per unit

volume of the crystal compared to primary nucleation. This is followed by the addition of more segments through a chain folding process (Figure 1-6).

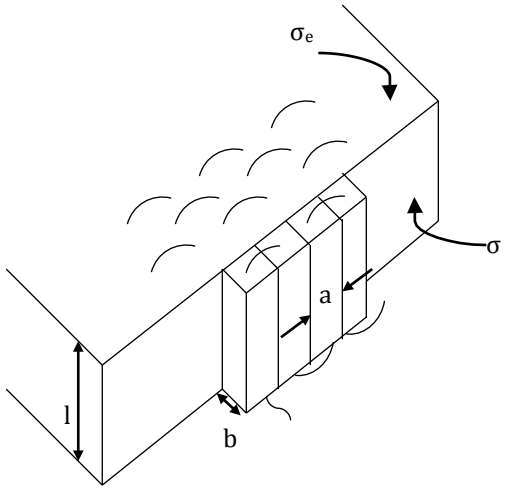

Figure 1-6 - The growth of lamellae on a polymer crystal through consecutive layers of adjacent molecular strands

Chain folding occurs through the rotation of motion about the polymer backbone. The secondary nucleation process represents chain folding to create a lamella structure. The increase in ΔG_n involved in the laying down of n adjacent strands of length, l, can be shown by:

$$\Delta G_{n(surface)} = 2bl\sigma + 2nab\sigma_e$$

Equation 1-5

Each new strand has a cross-section of ab (Figure 1-6) and surface and fold free energy, σ and σ_e, respectively. The incorporation of the molecular strands yields a reduction in the free energy of the crystal. This free energy is given by:

$$\Delta G_{n(crystal)} = -nabl\Delta G_v$$

Equation 1-6

The overall free energy change when n strands are formed is given by:

$$\Delta G_n = 2bl\sigma + 2nab\sigma_e - nabl\Delta G_v$$

Equation 1-7

where ΔG_v can be estimated from the simplified calculation shown in Equation 1-2.

1.2.2.1 Temperature Dependence of the Crystal Growth Rate

Optimum growth rates occur due to the combination of the thermodynamic driving force for crystallisation and melt viscosity. As crystallisation temperature (T_c) decreases the thermodynamic driving force increases, opposed by an increase in melt viscosity resulting in the more difficult transport of material to the growth face. As a result, at temperatures close to T_m, the growth rate reduces with increasing temperature and half-life of crystallisation increases. In contrast, at low crystallisation temperature close to T_g, growth rate decreases with decreasing temperature. An optimum growth rate is commonly found midway between T_g and T_m.

The growth rate of crystals was proposed by Turnbull and Fisher (1949) to have the following dependence on temperature :

$$G = G_0 exp\left(-\frac{\Delta E_a}{RT}\right) exp\left(\frac{\Delta G_n^*}{RT}\right)$$

Equation 1-8

where G is the steady-state growth of a crystal, G_0 is a temperature-independent constant (dependant on molecular parameters and crystals geometry), ΔE_a is the activation energy for viscous flow, ΔG_n^* is the free energy of formation of a critical size secondary nucleus and R is the gas constant. At temperatures close to T_g, $\left(-\frac{\Delta E}{RT}\right)$ is the

dominant term as growth of the crystal is diffusion controlled. Close to T_m, $\left(\frac{\Delta G_n^*}{RT}\right)$ is dominant as growth is nucleation controlled.

The Turnbull and Fisher equation was modified by Lauritzen and Hoffman (1973) to describe the temperature dependence of crystallisation over a wide range of temperatures:

$$G = G_0 exp\left(\frac{-U^*}{R(T - T_\infty)}\right) exp\left(-\frac{K_g}{T\Delta Tf}\right)$$

Equation 1-9

where G is the linear growth rate, G_0 is the pre-exponential factor, U^* is the activation energy for viscous flow (6300 J/mol), K_g is the nucleation constant, ΔT is the supercooling ($\Delta T=T_m-T_c$), f is the correction factor ($f=2T_c/(T_m+T_c)$) and T_∞ is a hypothetical value where motion associated with viscous flow concludes. T_∞ is usually taken 30 ˚C below the glass transition temperature.

According to the nucleation theory of Hoffman and Lauritzen, the nucleation mechanism can be determined from the gradient of the dependence: $\ln(g) + \left(\frac{U^*}{R(T-T_\infty)}\right)$ against $\frac{1}{T\Delta Tf}$, where a change in slope is diagnostic of a change in regime (Figure 1-7). The slope of the line corresponds to the nucleation constant, K_g.

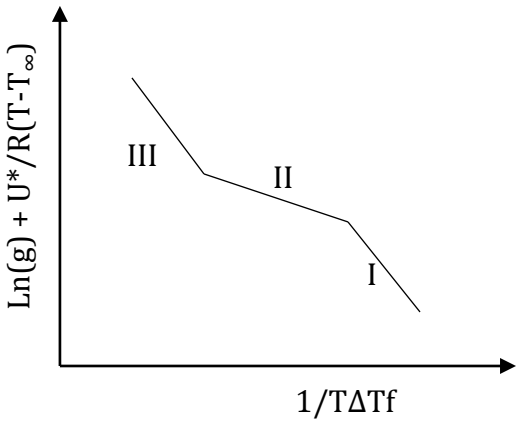

Figure 1-7 - Schematic representation of three nucleation regimes

1.3 Crystallisation Kinetics by Avrami Analysis

Crystallisation kinetics are commonly analysed using the Avrami model. It is an isothermal model, originally derived from the crystallisation in metals but was later extended to crystallisation in polymers. The model is used to predict the dimensional formation of the crystal structure. The Avrami model is a kinetics model of crystallisation phase change (Avrami, 1940). The model was simplified by Evans (1945) relating the fraction of crystallinity with time as:

$$1 - X_c = \exp(-kt^n)$$

Equation 1-10

where X_c is the relative crystallinity formed over the time period t. k is the Avrami constant, a rate constant incorporating both nucleation and growth characteristics and n is the Avrami exponent, describing the crystal geometry. The growth of a crystal can occur in 1-, 2- or 3- dimensions represented by crystals in the form of rods, discs and spheres respectively. Crystals of rod-like structure produce a value for n of 1, disc-like crystals, a value of 2, and spherulitic growth is shown by a n value of 3.

1.3.1 Spherulites

Polymers usually crystallise in a spherical super structure, whereby the chain segments in branching lamellae align perpendicular to the direction of growth. Spherulites grow radially from the nucleus until impingement with neighbouring spherulites stops growth producing linear boundaries. The spherulite is size dependent with temperature, increasing with an elevation in temperature to the melting point.

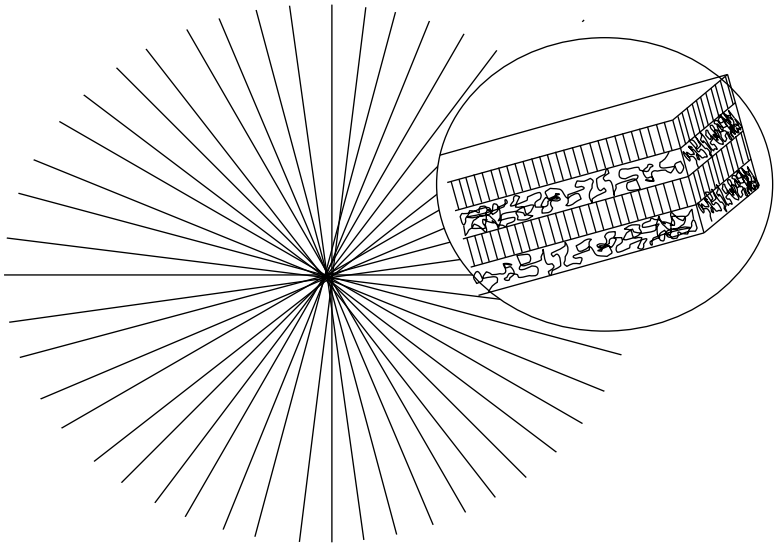

Figure 1-8 - Schematic structure of a polymer spherulite

A spherulite contains numerous chain folded lamella structures approximately 10 to 20 nm in thickness (Muthukumar, 2004), layered with amorphous regions of comparable thickness (Figure 1-8). The amorphous regions exhibit a T_g combined with a T_m of the crystalline regions at a higher temperature, causing chain disorder in an amorphous liquid.

1.4 Polymer Melting and the Equilibrium Melting Temperature

The T_m can be altered according to two mechanisms: the temperature of primary crystallisation, at which the crystals structure forms, and the progressive thickening of the lamella through secondary crystallisation. Crystal thickness increases with T_c and is thus inversely proportional to super-cooling. A positive linear relationship is observed between T_c and T_m, where the intersection to $T_c = T_m$ describes the equilibrium melting temperature (T_m^0). This relationship was derived by Hoffman and Weeks (1961) expressed in the equation:

$$T_m = T_m^0\left(1 - \frac{1}{2}\beta\right) + \frac{T_c}{2\beta}$$

Equation 1-11

where the slope of the line is equal to ½ β, where β is the thickening factor, equal to 1 if recrystallisation does not occur during melting. Thin crystals grown at low temperature are thermodynamically unstable and, after melting, will recrystallise to form more thermodynamically stable crystals at higher temperatures before remelting at an elevated T_m (Hoffman and Weeks, 1961). These crystals can be described as metastable and if time permits, result in double melting (Bassett *et al.*, 1988). Increased heating rates reduce the effect of recrystallisation as a consequence of a reduction in time between T_g and T_m.

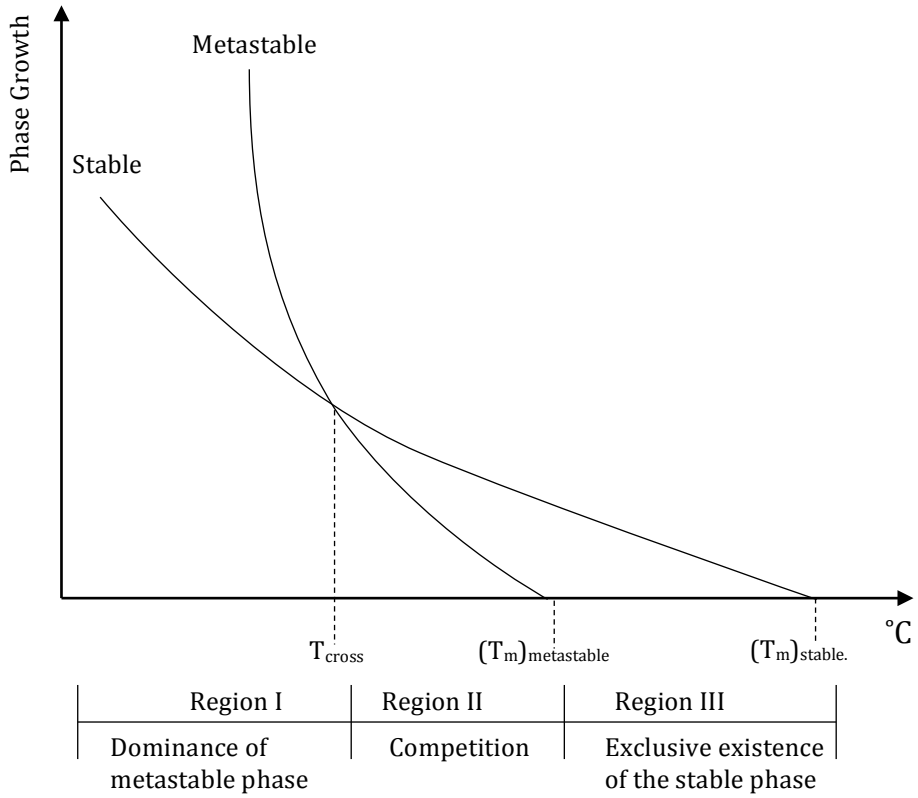

Figure 1-9 - Schematic of the stable and metastable phase transformation kinetics.

The competition between stable and metastable phase growth with temperature is illustrated in Figure 1-9. The possibility of metastable crystal growth increases as temperature falls (supercooling increases) below the stable growth region (Region III).

CHAPTER 2 LITERATURE REVIEW

2.1 Thermal Analysis

2.1.1 Thermal Calorimetry Scanning Techniques

Differential scanning calorimetry (DSC) has developed over the last 50 years from when they were first commercially released by Perkin-Elmer in 1963 (O'Neill and Watson, 1966). The conventional DSC (CDSC) is the most common calorimeter used since 1963 to explore thermal changes in polymers during heating and cooling. Commonly, CDSC has the capacity to heat and cool up to 100˚C/min and accommodate a sample mass between 5 and 20 mg. Perkin-Elmer further developed the CDSC technique in 2002 releasing the HyperDSC™ (Pijpers *et al.*, 2002). Sample mass for HyperDSC™ was reduced to ~1 mg to compensate for thermal lag effects that are incurred from faster scanning rates, (100-500˚C/s). The HyperDSC™ has a greater temperature range from -176 to 585˚C compared to CDSC, -90 to 450˚C.

Mettler-Toledo have since commercialised a different form of thermal analyser: in 2010, the Flash DSC chip-calorimeter was released. It is the most recent development in differential thermal analysis available to purchase. FDSC has scanning capabilities of up to 20,000˚C/s in heating and up to 4,000˚C/s in cooling (Mathot *et al.*, 2011) with a temperature range equivalent to CDSC, -95˚C to 450˚C.

2.1.2 The Importance of Increased Scanning Rate

Faster heating and cooling rates have been achieved in recent years through development of chip calorimetry. Some manufacturing techniques subject polymer liquids to fast cooling where the morphology may be unknown (e.g. injection molding). These cooling profiles can be simulated using FDSC where comparable cooling provides information into the material final properties e.g. melting temperature, crystallinity and modulus (Adamovsky *et al.*, 2003).

Advances in scanning rates also provide an insight into systems not in thermal equilibrium, i.e. those that are said to be metastable. Systems that are metastable are susceptible to variations in their morphology made possible through slower heating. FDSC enables regions of some materials to be investigated that have previously not been possible using CDSC and HyperDSC™. Applying fast heating rates can prevent a metastable phase from reorganising and further analysis of the material is possible.

2.2 Flash DSC (FDSC)

2.2.1 Flash DSC Chip Sensor

The FDSC makes use of a MultiSTAR UFS 1 twin chip sensor based on Micro-Electro-Mechanical Systems (MEMS) technology. The FDSC is controlled through power compensation where micro sensors monitor temperature change. The chip consists of a sample and reference membrane, 1.6 mm square. Two separate identical membranes permit a sample to be loaded on the upper membrane and the lower left empty as a reference (Figure 2-1). The chip is developed from a thin silicon-nitride/oxide membrane with an approximate thickness of 2 μm (Figure 2-3) (Mathot *et al.*, 2011).

The sample area on the chip sensor has an 8-thermocouple polysilicon thermopile measuring temperature elevation with respect to the silicon frame. The silicon frame acts as heat sink, maintaining a constant temperature through all experiments, -90˚C (Figure 2-2). Each sample area has 2 heaters: one maintains temperature according to the programmed method and the other equalises the sample temperature to the programmed temperature (see Section 3.1). Outside the 0.5 mm sample area only 0.15 mm area is effectively involved in heating and cooling; further away temperature changes are insignificant (Poel *et al.*, 2012).

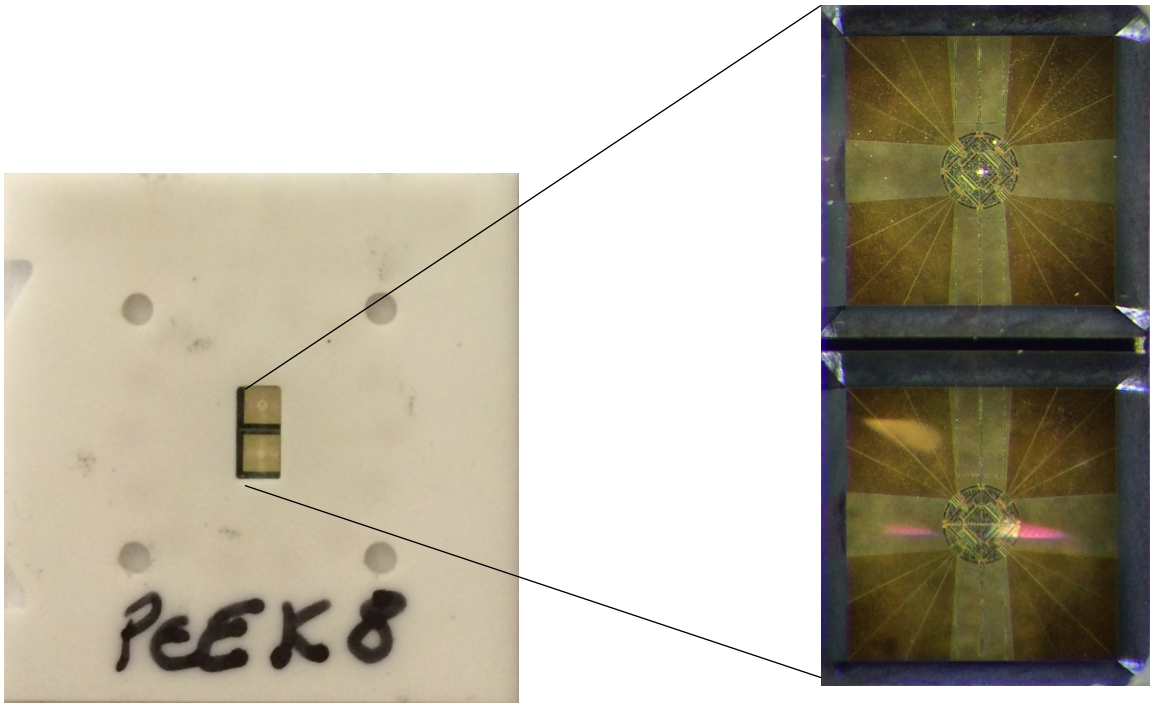

Figure 2-1 – FDSC chip with magnified central area showing the sample area with sample, top membrane, and reference, bottom membrane

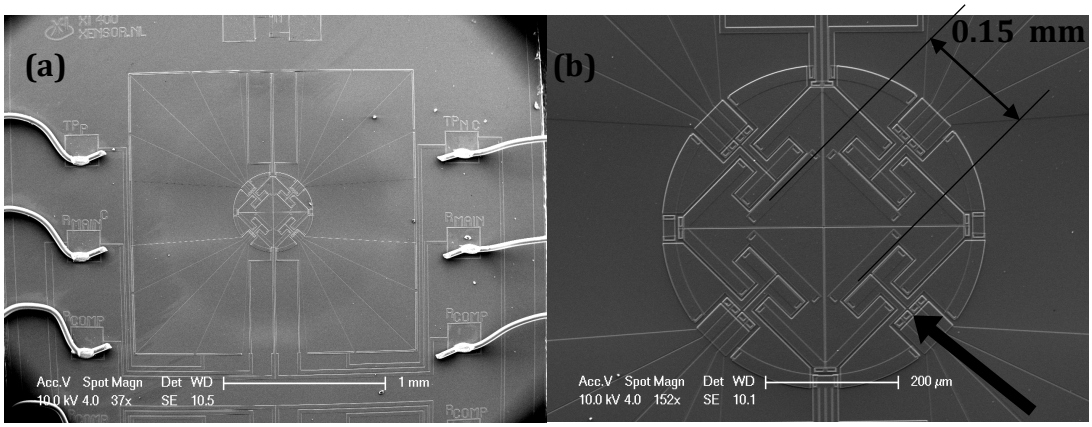

Figure 2-2 - (a) SEM image of the reverse side of the chip sensor showing six of eight bonding wires. (b) The circular 0.5 mm diameter sample area with a central square representing the 0.15 mm heating region. The arrow points to two hot junctions

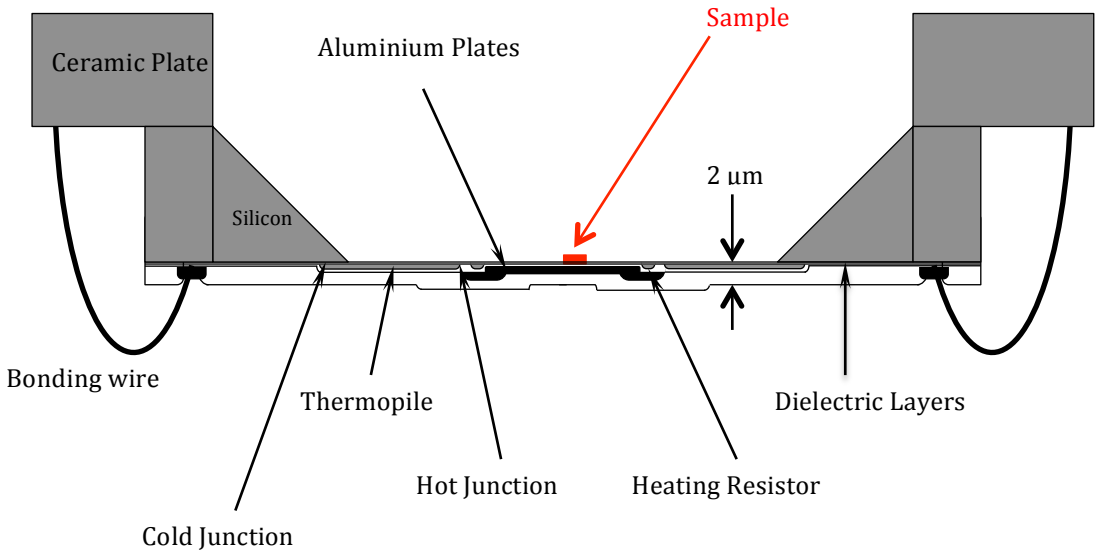

Figure 2-3 - Schematic representation (not to scale) of the chip sensor cross-section

A temperature calibration and electrical characterisation of the chip sensors, provided with the Mettler Toledo FDSC, was carried out by Iervolino *et al.* (2011). The temperature range of the chip was explored with a maximum operating temperature for reliable and repeatable results found to be 450˚C and failure of the chip sensor occurred at 577˚C. An electrical calibration of the chip sensor was carried out using a series of primary standards to determine the accuracy of the temperature calibration. An error in results of ±2˚C enables the chip sensor to be used with an uncalibrated heater resistance in a temperature range of -56 to 450˚C.

The chip sensor is pre-calibrated in batches before release from the factory using the electrical methodology described by Iervolino *et al.* (2011). This calibration gives an overall calibration for the produced batch from randomly selected chips. The typical maximum error for temperature is ± 5˚C (Iervolino *et al.*, 2011). Each chip is conditioned and corrected prior to loading a sample to check its condition (Chapter 4). Sample location further influences this temperature error and increases thermal lag. Poel *et al.* (2012) carried out work revealing discrepancies in sample melting temperature (T_m) when located in different positions across the sensor.

2.2.2 Thermal Lag Effects

Fast heating rates create thermal gradients with an FDSC sample. These gradients result in a temperature lag in the sample shifting the thermal transition to higher temperatures (discussed in Chapter 5). Sample mass is reduced to minimise this thermal lag, desirably to a value between 0.01 and 20 μg, with a preferred polymer sample mass ~ 0.02 μg.

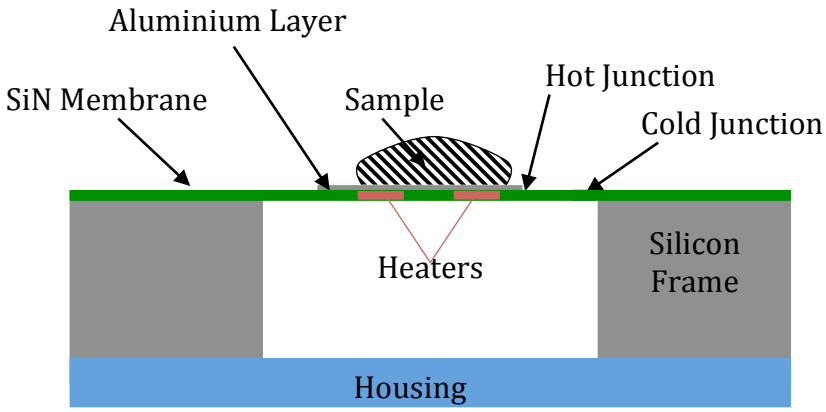

Figure 2-4 - Schematic cross section of a sample on the Flash DSC sensor

The heaters within the chip sensor and the temperature of the surrounding inert gas control FDSC sample temperature. Therefore, heat is input into the sample from the base of the sample, causing a temperature gradient from the bottom of the sample to the top. Cooling the sample introduces a temperature gradient in the opposing direction from the cooled gas (-90˚C). Thermal lag effects arise from a temperature gradient within a sample. These thermal gradients have been explored by Zhuravlev and Schick (2010) using indium and PCL. The location of indium beneath and on top of the PCL sample allows the melting temperature (T_m) of indium to be recorded. When indium is placed underneath PCL, the melting onset temperature is equal the onset of an individual indium sample. With indium placed on top of a PCL sample, the onset of melting is delayed as a result of the thermal gradients within the polymer sample. Therefore it is important to reduce sample size; if possible by reducing sample height.

2.2.3 Flash DSC Performance

Mathot *et al.* (2011) and Poel *et al.* (2012) have studied the calibration, repeatability, scan rate control and window of operation of FDSC. A six step calibration process has

been considered by Poel *et al.* (2012) where repeatability, thermal lag and symmetry are examined in detail. The six steps that are used are:

- Performance
- Primary Temperature Calibration
- Check of Primary Calibration
- Calibration with respect to mass and scanning rates
- Check of mass and scan rate calibration
- Symmetry

In their approach, all the experiments for the calibration were carried out using indium or a blank chip sensor. Indium is a well-known calibration material used in thermal analysis, due to its an exact melting onset temperature of 156.59˚C, providing accurate temperature calibration of thermal equipment.

The FDSC cooling and heating performance was tested in an inert atmosphere of nitrogen and helium as separate purge gases with flow rates between 1-20 mL/min. A faster cooling rate was maintained with an atmosphere of helium in comparison to nitrogen due to a higher thermal conductivity. The flow rate of nitrogen did not have an effect upon results, consequently, helium maintained greater cooling rates for extended periods of time when the flow rate was reduced from 20 mL/min to 1 mL/min. Nitrogen however, showed constant heating rates up to 20,000˚C/s through the entire temperature range of the FDSC. In heating and cooling an initial acceleration period was observed before the programmed scanning rate was reached. Scanning rate deceleration was also observed as the final temperature was approached. Cooling reveals the same

acceleration, as on heating, to the programmed scanning rate; however, a temperature range >400˚C is only maintained for rates at and below 5,000˚C/s. The most appropriate gas should therefore be selected in accordance to experimental parameters.

Indium was used to measure the temperature accuracy of the instrument; a linear regression of the melting point, as a function of time, was recorded and subsequent measurements were adjusted to allow calibration to be accurate. Repeatability of the FDSC results show very small standard deviation between measurements of the same and other samples of a similar mass (207 and 285 ng). The largest standard deviation value recorded for the same sample was 0.03˚C, a change in 0.1˚C. This accuracy ensures that subsequent experimentation on the same sample is acceptable and comparable, unless degradation occurs (Poel *et al.*, 2012).

An increase in sample mass subsequently increases sample height. Sample height results in increases in thermal gradients in the sample and thus thermal lag. Thermal lag, with respect to sample mass, was determined using a series of indium samples of varied mass (unknown height). A sample mass range from 0.016 µg to 2.508 µg resulted in a 1.6˚C difference in melting onset during heating at 1,000˚C/s. A thermal lag correction with mass and heating rate was expressed by Poel *et al.* (2012) as:

$$T_{m_{Onset}} = a_0 + a_1\beta^{a_2} + a_3\beta m$$

Equation 2-1

where a_0, a_1, a_2 and a_3 are constants and β and m are heating rate (˚C/s) and mass (µg), respectively.

The last step of the calibration ensures symmetry of the FDSC. If symmetry is present, thermal lag calculations can be applied to both cooling and heating. Symmetry of the FDSC allows the correction factors obtained from thermal lag data in heating to be used for cooling data. Heating rates were mirrored for cooling and the experimental data collected was compared to this mirrored data. The difference that was found between the heating and cooling was 0.3˚C, which was acknowledged to be acceptable (Poel *et al.*, 2012).

2.3 Applications of Chip Calorimetry

2.3.1 Preventing Crystallisation of Polymers from the Melt

2.3.1.1 Key Studies using Conventional Non-Chip-Based Calorimetry Techniques

Crystallisation within a polymer can be desirable. Polymers in a crystalline state tend to be stiffer, harder and denser than polymers in an amorphous state (Lohse and Gaylord, 1978). To study the effects of polymer morphology through processing, and low crystallisation temperatures, it is important to obtain an amorphous solid, unachievable for a number of polymers through CDSC and HyperDSC™. Prevention of crystallisation to form an amorphous solid can occur when a polymer system is cooled rapidly (Mathot *et al.*, 2011). Poly(ε-caprolactone) (PCL) has fast crystallisation kinetics, preventing the formation of a fully amorphous solid from the liquid state using calorimetry (Wurm *et al.*, 2012). These fast kinetics cannot be prevented using CDSC or HyperDSC™ and has resulted in a substantial amount of literature on isothermal melt-crystallisation above 39˚C (Jenkins and Harrison, 2006, Mucha *et al.*, 2015). Amorphous PCL can be created through an alternative polymerization process, resulting in increased chain branching, preventing crystallisation (Agarwal and Speyerer, 2010). Temperatures lower than 39˚C

cannot produce reliable isothermal crystallisation data due to the onset of crystallisation at ~35˚C (Mdletshe *et al.*, 2015). A number of studies have explored molecular weight dependence on crystallisation kinetics and the addition of additives to increase crystallisation rate at higher temperatures (Jenkins and Harrison, 2006, Mucha *et al.*, 2015).

Huang *et al.* (2002) applied a cooling rate of 160˚C/min to quench PCL to a selected isothermal crystallisation temperature. The lowest crystallisation temperature achievable before non-isothermal crystallisation occurred was 30˚C. However, cooling at 160˚C/min was not fast enough to prevent non-isothermal crystallisation of PCL below 30˚C. Crystallisation cannot be prevented with the use of non-chip base calorimeters. Quenching in liquid nitrogen would provide a faster cool in comparison to CDSC and Hyper™ DSC, but, due to the low glass transition temperature (T_g) of PCL, crystallisation would not be preventable before further thermal analysis.

Poly(ether-ether-ketone) (PEEK) is an aerospace, high performance polymer with excellent mechanical, thermal and chemical stability. PEEK has been quenched, by a number of authors, with liquid nitrogen to prevent crystallisation, forming an acceptable amorphous sample (Papkov *et al.*, 1997, Chun *et al.*, 1999). The temperature difference from PEEK in the melt (400˚C) to liquid nitrogen (-197˚C) is approximately 600˚C. A quenched cooling rate achieved using liquid nitrogen is estimated to be 150˚C/s if cooling has resulted in temperature equilibrium after 4 seconds and was maintained at 400˚C prior to cooling. The thickness of the PEEK sheet determines the rate of cooling required due to thermal lag experienced within the material. Formation of an

amorphous PEEK below T_g allows crystallisation to occur on subsequent heating, known as cold crystallisation.

Work has been carried out, whereby amorphous PEEK has been created through different mechanisms. PEEK was described to be 'fully amorphous' through the quenching of liquid nitrogen, followed by a rolling process at room temperature (Papkov *et al.*, 1997). It was explained that a percentage of paracrystallinity (short to medium range order, no crystal like long range order) remained within the sample after the rolling process. This results in PEEK having a small degree of crystallinity, not a completely amorphous structure.

Dandy (2015) quenched PEEK in liquid nitrogen to create an amorphous structure. CDSC and Fourier transform infrared spectroscopy (FTIR) analysis were applied to the quenched sample, where a 2.28% remaining crystallinity was detected through FTIR. CDSC analysis revealed a 10% crystallinity difference in the exothermic and endothermic peak areas suggesting a fully amorphous structure was not formed. A low crystallinity percentage was observed by Toft (2011) when quenched in liquid nitrogen. A very limited crystallinity was still present within the sample, implying fully amorphous PEEK was therefore not achieved during a quench cool using liquid nitrogen. The reduction in crystallinity may have been sufficient for the literature, but in the calculation of crystallisation kinetics a fully amorphous sample is required.

Vitrification of poly(lactic acid) (PLA) and polyethylene terephthalate (PET) does not require quenching in liquid nitrogen. PLA and PET have slower crystallisation rates in

comparison to PEEK and thus, maximum cooling rates available on CDSC and HyperDSC™ are sufficient in preventing visible crystallisation in PLA and PET. The maximum cooling rate on HyperDSC™ was shown to prevent visible crystallinity in PLA, but not the formation of nuclei (Salmerón Sánchez *et al.*, 2007, Pan *et al.*, 2007). Cooling at 500˚C/min revealed a reduced number of nuclei present in comparison to cooling at a slower rate. Therefore, PLA must be subjected to faster cooling to prevent the both stages of crystallisation: nucleation and growth.

Cold crystallisation has been clearly observed during heating of PLA at 10˚C/min from an amorphous solid below T_g (Pan *et al.*, 2007, Salmerón Sánchez *et al.*, 2007). The molecular weight (M_w) of PLA impacts the temperature of the cold crystallisation exotherm. An increase in the cold crystallisation exotherm temperature was observed with a higher M_w PLA (Pan *et al.*, 2007). Cold crystallisation of PLA can be prevented using HyperDSC™ with a heating rate above 100˚C/min (Salmerón Sánchez *et al.*, 2007). Therefore it is possible to maintain an amorphous morphology in PLA from the glass to the liquid state.

2.3.1.2 Key studies using Chip-Based Fast Scanning Calorimeters

PTFE has crystallisation kinetics so fast that a specially designed ultra fast differential scanning chip calorimeter (UFDSC) cannot provide a cooling rate fast enough to prevent crystallisation. A cooling rate of 800,000˚C/s was applied to a PTFE sample from the melt, where a crystallisation exotherm was visible during cooling. Increasing cooling rate reduces time for crystallisation, crystallisation temperature (T_c) falls and the observed exotherm is broadened, occurring over a 100˚C temperature range. The

UFDSC operates using a similar chip to the FDSC, with a smaller sample area and mass to compensate for increased scanning rates. Thermal lag corrections were not applied to the data in this study (Bosq *et al.*, 2013).

Wurm *et al.* (2012) exploited fast scanning with FDSC to determine the rate required to prevent crystallisation during cooling of PCL. The exothermic crystallisation peak illustrated a reduction in the onset of T_c as cooling rate is increased. Cooling rates in excess of 1,000˚C/s resulted in complete vitrification of PCL below T_g (-56˚C) for PCL with a molecular weight (M_w) of 6,100 Da. A rate of 2,000˚C/s was required to prevent crystallisation of PCL with a M_w of 1,400 Da. Higher molecular weight samples posses a higher crystallisation temperature onset due to increased chain length and activity of heterogeneous nuclei; thus, faster cooling is required for vitrification.

Heating amorphous PCL at 400 to 10,000˚C/s causes cold crystallisation and subsequent melting. A critical heating rate of 18,000˚C/s was found to prevent crystallisation once an amorphous structure had been formed on prior cooling. Applying this critical heating rate after isothermal crystallisation allows different annealing temperatures and times to be studied without the formation of additional nuclei (Wurm *et al.*, 2012).

Zhuravlev *et al.* (2011) found that 20,000˚C/s was not fast enough to prevent crystallisation of PCL on heating, contradicting the work of Wurm *et al.* (2012). Heating amorphous PCL displayed equal cold crystallisation and melting transitions. The equal enthalpy change was attributed to growth of crystals on pre-existing nuclei. A cooling rate of 300˚C/s is enough to prevent growth of crystal structures during cooling of PCL;

according to Zhuravlev et al. (2011) preventing the formation of nuclei requires a faster cooling rate unattainable on FDSC. Specially designed chip calorimeters were employed with the capacity to cool at rates of 50,000˚C/s. After cooling at 50,000˚C/s, the formation of nuclei remained, shown by cold crystallisation and melting peaks during subsequent heating. The reduction in peak area was caused by the prevention of homogenous nuclei formation. Heterogeneous nuclei form at such excessive rates, from dust and other impurities, that specially designed chip calorimeters do not have the capacity to prevent their development.

According to Wurm *et al.* (2012), the critical heating rate to stop nucleation during heating of an amorphous sample was 18,000˚C/s. The heating rate applied to the experiments by Zhuravlev *et al.* (2011) was just 1,000˚C/s. This slow heating rate causes nucleation in amorphous PCL to occur during heating. Therefore, a cooling rate of 50,000˚C/s may have prevented nucleation, but an acceptable heating rate was not applied, allowing non-isothermal crystallisation on heating.

FDSC has been applied to heating and cooling to cyclic PCL to prevent crystallisation. A continual heating rate of 10,000˚C/s post cooling, between 500 and 4,000˚C/s, illustrated a reduction in the cold crystallisation peak and corresponding melting endotherm. Heating at 4,000˚C/s prevented nucleation during heating from an amorphous solid (Wang *et al.*, 2015).

FDSC was used to explore PEEK for the first time by Tardif *et al.* (2014) and later by Jin *et al.* (2014). Neither author explicitly describes the rates required to prevent

crystallisation as shown in the work on PCL. However, 2,000˚C/s was applied to subsequent isothermal experimentation in both heating and cooling, providing an acceptable rate to prevent crystallisation. Therefore, according to the critical rates acquired by Wurm *et al.* (2012) and Zhuravlev *et al.* (2011) in PCL , both heating and cooling rates required to prevent nucleation in PEEK must be slower than 2,000˚C/s.

Kolesov *et al.* (2011) exploited the overlapping CDSC and FDSC cooling rates to explore the rate required to vitrify PA6. CDSC reveals a reduction in the change in enthalpy (ΔH) with cooling rate; corresponding to the increased cooling capacity of FDSC an amorphous solid was obtained after cooling in excess of 150˚C/s. A reduction in the peak melting temperature (T_m) was accompanied by a reduction in ΔH at all cooling rates. A quench cool of 1,000˚C/s provided an insight into the rate necessary to prevent crystallisation during heating. Slow heating results in the development of cold crystallisation at ~77˚C, increasing to ~130˚C with heating rate elevation. The critical heating rate was obtained from the removal of the cold crystallisation and melting heating in excess of 500˚C/s.

2.3.2 Accessible Isothermal Crystallisation Temperatures

2.3.2.1 Key Studies using Conventional Non-Chip-Based Calorimetry Techniques

Polymer crystallisation can occur in between T_g and T_m. Crystallisation regions explored are commonly close to T_g or T_m where crystallisation rate is slowest. Maximum crystallisation rate occurs at approximately $(T_g+T_m)/2$.

The high T_c range has been explored using PCL by a number of authors employing kinetic analysis to data. A high temperature range of 42-47˚C was used for isothermal crystallisation of PCL by Jenkins and Harrison (2006) where an Avrami 'n' value ~2 was calculated and an increase in t½ with elevated T_c, opposed by the Avrami constant, K. A lower isothermal temperature range, 38.5-41.5˚C, was tested by Mucha *et al.* (2015) with the addition the nucleating agents: nanosilver and talc, where a reduction in half-life (t½) was observed with addition of nucleation agents. Huang *et al.* (2002) measured isothermal crystallisation of PCL across a 15˚C temperature range achieved with a cooling rate of 160˚C/min. A low T_c of 30˚C was achieved by preventing non-isothermal crystallisation with fast cooling (160˚C/min). A large temperature range measured an equilibrium melting temperature (T_m^0) of 45˚C which increased with an increase in molecular weight (M_w) to a value of 67˚C.

Double melting endotherms in PEEK were first reported by Blundell and Osborn (1983). The appearance of a double melting endotherm was shown in the temperature range 200-230 and 270-320˚C. The origin of the double peak was evaluated as a continual recrystallisation and melting behaviour. Subsequent work by Lee and Porter (1987) agreed with Blundell and Osborn on the formation of the double peak. Cold crystallisation and melt crystallisation were employed to explore a low and high T_c with a limited scanning rate capacity. Melt crystallisation temperatures above 314˚C were used in the determination of T_m^0 to a value of 389 ± 4˚C. A T_m^0 value close to 400˚C has been calculated by other authors; however, a lower value has been calculated more recently with elevated cooling rates of 200˚C/min, reducing non-isothermal crystallisation, by Yang *et al.* (2006) as 359˚C.

Faster heating and cooling rates, up to 320˚C/min, have been exploited by Ko and Woo (1996) to prevent crystallisation during scanning. A continual T_c range was achieved from 230-310˚C where double melting was observed. A continual stepwise programme was exploited with fast scanning rates to grow several different sized crystal colonies before heating. A number of melting endotherms were visible due to a variety of crystal stabilities grown at different crystallisation temperatures. However, a variety of cooling rates were used, presenting inconsistent experimental methodology and the estimation of T_m^0 was obtained from limited data.

In contrast to PEEK, scanning rates using CDSC has provided sufficient suppression of crystallisation in PLA to explore a large T_c range, from 80 to 140˚C. Slow crystallisation rates limit crystallisation close to T_g, ~60˚C and T_m ~155˚C. Wide-angle x-ray scattering (WAXS) has shown a regular scattering angle for crystals growth above 120˚C, but irregular and absent scattering below 120˚C. The lack of diffraction patterns below 120˚C was suggested to represent a different crystal structure. The crystal structure formed below 120˚C is called the α' form crystal and the structure formed above 120˚C, the α form crystal (Kawai *et al.*, 2007). Calorimetry heating traces show a double melting behaviour below 120˚C and a single melting endotherm above 120˚C, corresponding to the crystal formation shown in the WAXS study. The α' crystal formed below 120˚C shows thermal instability and recrystallisation during heating; the α crystal grown above 120˚C shows thermal stability in a single melting temperature endotherm. Lower M_w PLA results in double melting up to 135˚C where crystallisation is faster in comparison to high M_w PLA (Pan *et al.*, 2007, Zhang *et al.*, 2015).

2.3.2.2 Key studies using Chip-Based Fast Scanning Calorimeters expanding the accessible isothermal crystallisation temperatures

Zhuravlev *et al.* (2011) and Wurm *et al.* (2012) have used FDSC and specially designed chip calorimeters to crystallise PCL between T_g and T_m. The insight into a low T_c has shown the formation of a significant metastable phase. During subsequent heating, this metastable phase is shown to recrystallise with the presence of an exothermic peak separating the endotherms. Intermediate and high crystallisation temperatures result in the appearance of a single melting endotherm as thicker lamellae forms more stable crystals. A limited range of temperatures were studied by Wurm *et al.* (2012) despite the capability of the FDSC. A change in T_g step was visible with crystallisation time across all three isothermal temperatures. A larger temperature range from below T_g to T_m was tested by Zhuravlev *et al.* (2011).

FDSC, in conjunction with fast scanning rates, has the capacity to employ very short isothermal hold times. This has proved vital to exploiting the T_c range of polymers with rapid crystallisation kinetics. The short isothermal hold time has provided additional data for PA6 and PCL analysis. PA6 shows a shortest half-life of $\sim 10^{-1}$ s at the maximum crystallisation temperature, ~147˚C (Kolesov *et al.*, 2011). The half-life in PCL is similar to PA6 (Zhuravlev *et al.*, 2011). Androsch *et al.* (2014b) utilised FDSC to explore the crystallisation half-life in PLA finding a similar value in comparison to literature using CDSC. Slow crystallisation kinetics and fast heating result in a single endotherm for crystallisation rate calculation.

As a rule, nucleation is not visible on existing techniques due to its small size and thus heat flow. According to (Tammann, 1898), analysis of nucleation is possible with fast cooling from the melt to a temperature of interest followed by annealing to allow nuclei to form with time. Heating from the annealing temperature allows crystal growth from the pre-formed nuclei. Short isothermal hold times available on FDSC provide possible determination of nucleation. A simple data-treatment method was proposed for PCL to isolate nucleation data for analysis (Zhuravlev *et al.*, 2011). Heating after short isothermal crystallisation of PCL results in cold crystallisation, followed by melting. When the cold crystallisation enthalpy (ΔH_{cc}) and melting enthalpy (ΔH_{melt}) are equal, time spent at T_c can be attributed to formation of nuclei and not growth. Crystal growth at T_c results in a larger enthalpy value for melting in comparison to cold crystallisation; therefore, at time points before total enthalpy ($\Delta H_{cc}+\Delta H_{melt}$) increases, only nucleation occurs. This method was used to calculate nucleation half time in PCL for all isothermal crystallisation temperatures. Nucleation half-life was calculated in the order of 10^{-1} at -20˚C (Zhuravlev *et al.*, 2011).

Further work on PCL by Zhuravlev *et al.* (2015) explored nucleation effects on crystallisation with a specially designed chip calorimeter capable of heating and cooling at 500,000 and 100,000˚C/s respectively. This specially designed calorimeter was used to acquire very short isothermal hold times at different temperatures to develop a nucleated amorphous solid. Subsequent heating at 50,000˚C/s presented a shorter half-life for nucleated systems in comparison to non-nucleated systems.

The full crystallisation region of PEEK has been possible with the use of CDSC with fast heating and cooling rates (<up to 320˚C/min). FDSC was employed by Tardif *et al.* (2014) to study isothermal crystallisation of PEEK, between 170 and 310˚C, with heating and cooling rates of 2,000˚C/s to ensure crystallisation is prevented. This large temperature range enabled a detailed understanding into the temperature shift of double melting. PEEK is well known to exhibit a double melting endotherm and the reasoning behind the origin of double melting has been debated since the synthesis of PEEK in 1983 (Lee and Porter, 1987, Lattimer *et al.*, 1992).

The use of Avrami analysis by Tardif *et al.* (2014) across the large crystallisation temperature range allowed the Avrami exponent and the Avrami kinetics coefficient to be calculated; however, the presence a double endotherm, resulting from recrystallisation, introduces error into Avrami calculations. Results obtained matched those found previously by Cebe and Hong (1986), in a limited temperature range, with a value of ~3 for the Avrami coefficient, indicating instantaneous growth of spherical crystals. Crystallisation kinetics of PCL using the Avrami equation have not currently been applied in current FDSC literature.

2.3.3 Preventing Recrystallisation of an Amorphous System on Heating

2.3.3.1 Key Studies using Conventional Non-Chip-Based Calorimetry Techniques

Recrystallisation can occur during heating of isothermally grown metastable crystals, if a thermodynamically more stable crystal has time to form at a higher temperature. An increase in temperature promotes a more stable temperature for crystals to grow if unstable crystals have melted. The phenomenon can be visible as an endotherm-

exotherm-endotherm with temperature rise, but in some cases, a continual recrystallisation process omits a visible exotherm. The reduction in enthalpy of recrystallisation and in some cases, removal of the endotherm completely, can be achieved with increased heating rate.

Recrystallisation is time and temperature dependant; however, with elevated heating rates, time for recrystallisation to develop is shortened. Recrystallisation of isotatic poly(4-methylpentene-1) was examined on heating using CDSC. Increased heating rate from 5-80˚C/min showed a reduction in the upper endotherm peak temperature. An increase in the lower endotherm was observed as a result of thermal lag. The removal of the upper endotherm was achieved at 80˚C/min (Bassett and Patel, 1994).

Chao *et al.* (1998) applied increasing heating rates to PEEK after isothermal crystallisation at 314˚C. Increasing heating up to 80˚C/min revealed a shift in the lower endotherm into the upper endotherm, finally resolved as a shoulder. The lower endotherm shift to higher temperature is expected to be a result of a thermal lag shift as no lag correction was applied. Work by Lee *et al.* (1989), at a higher isothermal crystallisation temperature of 320˚C, resolved a single endotherm at elevated heating rates. The peak location was central to the two endotherms observed at slow heating rates. Heating rates up to 200˚C/min were employed with the use of a Perkin-Elmer DSC-2. The coalescence of the endotherms was considered to represent the melting temperature of the as-grown crystals. Thermal lag calculations were not taken into account despite fast heating rates; therefore, the shift in the lower endotherm to a higher temperature may represent an elevated T_m due to thermal lag.

A thermal lag correction was applied successfully to data presented by Salmerón Sánchez *et al.* (2007) as heating rate was increased to remove the double peak seen in PLA. The thermal lag correction was applied in line with guidance detailed by Vanden Poel and Mathot (2006). The correction displayed a reduction in the upper endotherm representing recrystallisation and minimal change in the lower endotherm, indicating the as-grown crystals. The reorganisation of α' to α crystals in PLA precedes melting through recrystallisation. Different endotherms described by Shen *et al.* (2011) originate from crystals of differing lamella thicknesses. Recrystallisation of PLA was prevented after high temperature crystallisation on heating using CDSC. A single endotherm was formed on heating at 50˚C/min after crystallisation at 110˚C; after crystallisation at 100˚C, a heating rate of 300˚C/min was required to prevent recrystallisation and display a single endotherm. Lamella thickness and thus crystals stability was influenced by T_c and faster heating was required to stop recrystallisation of less stable crystals (Salmerón Sánchez *et al.*, 2007).

2.3.3.2 Key studies using Chip-Based Fast Scanning Calorimeters

The removal of recrystallisation using CDSC can be achieved after high temperature crystallisation. Reducing T_c increases the thermodynamic driving force for the recrystallisation of unstable crystals. To prevent recrystallisation after crystallisation at lower temperatures faster scanning rates are required. FDSC literature has exploited the rates available to prevent recrystallisation and observe as-grown crystals temperature lower than previously possible in calorimetry.

Slow heating (with respect to the capacity of FDSC) was used by Androsch *et al.* (2014a) to prevent recrystallisation of isothermally formed α' crystals after low temperature crystallisation of PLA. Crystallisation at 90˚C displayed two endotherms after slow heating, 5˚C/s. A reduction in upper melting endotherm area was reported with increased heating rate from 5-40˚C/s. This reduction agreed with work carried out on HyperDSC™ where 300˚C/min (5˚C/s) on heating resulted in a single endotherm after crystallisation at 100˚C. A reduction in T_c requires faster heating to prevent recrystallisation as the thermodynamic driving force increases. A larger range of cold crystallisation temperatures in PLA would provide an increased knowledge of results with a single isothermally dependent endotherm.

FDSC was employed by Tardif *et al.* (2014) to expand the heating rate required to prevent recrystallisation of PEEK. Heating at 2,000˚C/s resolves a single endotherm after crystallisation at 250˚C. This single endotherm is broad for temperatures below 300˚C. A clear, sharp single endotherm is present at 300 and 310˚C only. It is expressed that the presence of a single endotherm represents single crystal formation of stable crystals that do not force reorganisation of as-grown crystals. The observed melting after an isothermal hold at 250˚C results in a broad melting endotherm. The broad temperature peak could be considered to represent a continual recrystallisation. The presence of a single crystal may not fulfil the experimental results obtained.

Another study on PEEK was conducted with FDSC by Jin *et al.* (2014). Melting endotherm movement was shown after isothermal crystallisation at 240˚C on heating between 50 and 2,000˚C/s. A reduction in the upper endotherm was observed in

conjunction with a temperatures shift in the lower endotherm. This shift is comparable to the shift seen in CDSC by (Lee *et al.*, 1989). Complete removal of the recrystallisation endotherm after crystallisation >190˚C was completed very recently with the use of FDSC (Furushima *et al.*, 2016). FDSC has provided an increased temperature range of a single endotherm at high temperature in comparison to CDSC data. No further analysis of the single endotherm was carried out in the literature.

2.4 Thermal Diffusivity

A limiting factor in the FDSC work, that prevents a definite thermal lag adjustment of the data, is a different rate of heat transfer during thermal transitions. A small sample mass is employed to minimise the effects of thermal lag at fast scanning rates; however, thermal lag is still present within the sample. Thermal diffusivity is a measure of the rate of heat transfer through a body of material. Heat transfer in a metallic solid occurs through electron transport; the absence of free electrons in polymers results in heat transfer through vibrations in the lattice from thermal energy (Srivastava, 1990). These lattice vibrations can be described in a polymer system as vibrations of the chemically bonded atoms. Polymers typically involve more than one type of chemical bonding: e.g. strong covalent intramolecular forces and weaker intermolecular forces, of which impact the capability for heat transfer.

Phonons are acoustic/elastic waves and are described through the Planck-Einstein energy-frequency relationship: $\Sigma=h\nu$ where Σ is energy, h is the Planck constant and ν is the wave frequency. This relationship describes the quantized energy of light, a photon, and can be used to describe the quantized energy of heat, a phonon.

Phonon movement can be modeled as vectors describing their momentum through a body of material. Phonons in a polymer chain can interact and exchange energy causing a reduction in the energy transfer described as a scattering event of phonons. Two different phonon-phonon interaction processes can be described: normal and Umklapp.

In a normal phonon-phonon interaction (N process) two interacting phonons combine to create a larger phonon, with a wave vector equal to the sum of the two interacting phonons. Alternatively, the initial wave vector can decompose into two smaller phonons, through defect or boundary scattering. In both cases momentum is continuous in the direction of the initial phonon wave (Figure 2-5(a)).

Umklapp scattering (U process), occurs where two larger interacting wave vectors combine to produce a resultant vector greater than the Brillouin zone. The large wave vector impedes the momentum of the phonon, emitting a wave vector opposing the initial phonon momentum (Figure 2-5(b)). Umklapp scattering does not show conservation of momentum of phonons and thus shows a significant effect on thermal diffusivity. The Brillouin zone is described as a primitive cell in a reciprocal lattice.

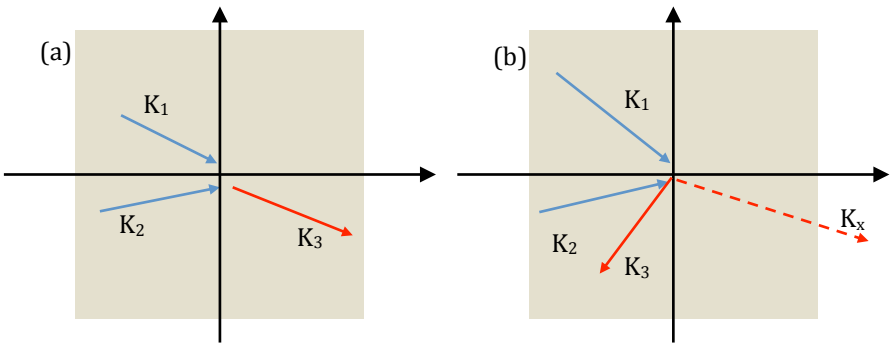

Figure 2-5 - Phonon-phonon scattering processes (a) Normal (N process), momentum is conserved (b) Umklapp (U process), momentum is not conserved

The total scattering can be defined as:

$$\frac{1}{\tau_{total}} = \frac{1}{\tau_{defect}} + \frac{1}{\tau_{boundary}} + \frac{1}{\tau_{Umklapp}}$$

Equation 2-2

where τ_x is the phonon scattering by different mechanisms, x.

In an ideal crystal lattice the mean free path is infinite, various imperfections in a real crystal cause scattering of the phonons through the recently mentioned mechanisms. These imperfections decease symmetry and order in a sample and thus reduce thermal conductivity. Since amorphous polymers have more unordered structure compared to a semi-crystalline polymer, they are expected to cause more phonon scattering and thus less thermally conductive.

Chen *et al.* (1977), using laser flash apparatus (LFA) (detailed further in Chapter 4), measured the thermal diffusivity in amorphous and semi-crystalline poly(ethylene terephthalate) (PET). Thermal diffusivity was greater for all temperatures in semi-crystalline PET in comparison to amorphous PET. A discontinuous change in diffusivity ($\Delta\alpha$) was measured as PET changed from a glassy to a rubber at T_g. A positive relationship of $\Delta\alpha/\alpha$ (at T_g) and T_g shows that a polymer with a higher T_g has a more drastic change in thermal diffusivity ($\Delta\alpha$) (Morikawa *et al.*, 1995). The change can be attributed to the increased mobility of the polymer chains resulting from an increase in free volume at T_g. According to this process, the thermal diffusivity is lowered.

According to the reduction in conductivity with an increase in disorder of a system, it is acceptable to suggest that the increase in chain length would result in a reduction in thermal conductivity. However, this is not true and the increase in chain length presents and increase in the thermal conductivity. This increase in conductivity is resolved from the increased conductivity of the main backbone of a polymer molecule (Hattori, 1962). The thermal conductivity of a short chain is smaller than that of a longer chain, amounting from larger amount of energy transactions between chains. The finite length of the polymer chain causes defect and boundary scattering, or interchain processes, in polymers (Brédas and Silbey, 2012).

The molecular weight (M_w) dependence of polystyrene (PS) was studied above and below T_g. The results show an increase in thermal conductivity with M_w, where the increase in conductivity with M_w is determined by an increased efficiency of propagation of vibrations (phonons) along the chain through intramolecular bonds. However, an increase in M_w above 100,000 g/mol saturated the thermal conductivity.

The transfer of phonons through intra- and intermolecular bonds was further defined through strain-induced crystallisation, where an amorphous but crystallisable polymer is orientated through drawing Choy *et al.* (1980). Drawing creates chain alignment that is comparable to the alignment found in a lamella. Phonon transport is favoured parallel to the oriented chains, occurring along the intramolecular bonds, covalent bonds. However, where chain alignment is perpendicular to the direction heat transfer, phonon transport is restricted through weaker intermolecular (Van der Waals) forces. If complete orientation is achieved, the only mechanism for heat transfer perpendicular to

chain alignment is the intermolecular forces between the aligned chains (Choy, 1977). These results also produce a significant finding that crystallinity percentage does not increase the thermal conductivity, in fact it is the direction of heat transfer in relation to the chain orientation.

More recently the study of the thermal conductivity and diffusivity, using non-contact experimental techniques (laser flash apparatus (LFA) and laser radiography), has provided rapid data collection. A good comparison of the non-contact LFA and the contact hot wire method, was shown in various semi-crystalline and amorphous polymers. The small sample size (12mm diameter, 1mm thick) in LFA compared to a 1.5kg sample in hot wire significantly reduces measurement time. The results provided a reasonable comparison of the techniques and previous literature where a continual reduction in diffusivity with temperature was reported in both amorphous and semi-crystalline structures with temperature. Limited data prevented further analysis of the data (dos Santos *et al.*, 2005).

The use of a specialised liquid cell provided a larger temperature range for diffusivity measurement from below T_g to above T_m in semi-crystalline poly(vinylidene fluoride) (PVDF) (dos Santos *et al.*, 2008). The calculation of specific heat and density provided an indirect measure of thermal conductivity using the relationship $K = \alpha\rho C_p$, where K is thermal conductivity, α is thermal diffusivity, ρ is density and C_p is specific heat (Parker *et al.*, 1961). A reduction in thermal diffusivity was observed with temperature below T_m. Once in the liquid state, a constant thermal diffusivity was observed (slight fluctuations in diffusivity in the liquid state were described as irregularity in the chain

orientations). Similar results were obtained in a study of four other semi-crystalline polymers: high and low density polyethylene, polypropylene and nylon 6 (dos Santos *et al.*, 2013). The results in this study are restricted by the temperature intervals (up to 38˚C) between thermal diffusivity measurements, preventing a detailed analysis of the results.

Thermal diffusivity of polyethylene terephthalate (PET) was recorded with crystallisation time using flash radiometry, a non-contact heat pulse technique, similar to LFA. Thermal diffusivity measurements showed an increase in diffusivity with crystallisation time representing primary crystallisation. A second, slower increase in diffusivity was recorded after the initial rise in diffusivity representing secondary crystallisation of PET. The change in diffusivity with crystallisation time was modified to allow an Avrami analysis of the data where values between 1.5 and 3.2 were shown at low temperature, the change in crystal growth mechanism was described; however, the growth of different crystal structures was not explored in PET. PET samples were also crystallised for one hour at different crystallisation temperatures. After one hour, the thermal diffusivity was measured showing an increase in diffusivity with degree of crystallisation. Following crystallisation at 220 and 240˚C, a step in the thermal diffusivity was observed representing the change in the thermodynamic stability of the crystal formation (Tsutsumi *et al.*, 1990).

Various different instruments have been designed and used to measure diffusivity change in polymers. The non-contact LFA and laser radiometry provide rapid data

acquisition with good accuracy of results. The recent work carried out by dos Santos using the LFA shows a limited amount of data in comparison to older techniques.

2.5 Project Aims

The newly developed FDSC provides further insight into polymer systems that has previously not been possible with other calorimetry techniques. The application of FDSC allows further analysis of the crystallisation regions and the scanning rates required to prevent crystallisation and double melting. Current literature has explored the benefits of FDSC and this thesis aims to further current knowledge and establish classical kinetic analysis through FDSC data of PCL, PEEK and PLA. The use of an LFA will be employed for the first time to measure diffusivity change in PLA with time and temperature. LFA will be used independently and as a comparative method for crystallisation kinetic analysis to FDSC data.

Chapter 5 demonstrates the novel method of chip sensor and sample preparation on Flash DSC (FDSC) and sample mass approximation. It covers an analysis of the FDSC instrument capabilities, including scanning rates, thermal accuracy, sample repeatability and thermal lag effects. Thermal lag equations have been calculated to provide a correction factor for data correction of the polymer system explored.

Chapter 6 and 7 will explore the heating and cooling rates required to prevent non-isothermal crystallisation of PCL and PEEK respectively, using FDSC. A wider range of isothermal crystallisation temperatures provides an insight into the crystallisation rate

of PCL at temperatures that have not been achievable with CDSC. Avrami analysis will be carried out for the first time over a larger temperature range in PCL and the equilibrium melting temperature of PEEK will be calculated with FDSC for the first time using a range of heating rates in FDSC and CDSC. The origin of the double melting phenomenon in PEEK will also be resolved after a long-standing uncertainty.

Chapter 8 will compare the cold crystallisation region (85-105˚C) of PLA using CDSC and FDSC. The removal of the recrystallisation endotherm using FDSC provides an opportunity to compare the two techniques and the increased accuracy of analysis of the independent as-grown endotherm will be displayed.

Chapter 9 will look at the change in diffusivity with temperature in PLA samples with different thermal histories. LFA will be employed to examine the development of metastable crystals with time and the change in diffusivity applied to classic crystallisation theories.

CHAPTER 3 MATERIALS

3.1 Poly(ε-caprolactone)

Poly(ε-caprolactone) (PCL) is a partially crystalline aliphatic polymer (Elzein *et al.*, 2004), derived from by-products of crude oil distillation. It is produced through ring opening polymerization of ε-caprolactone using stannous octoate ($Sn(Oct)_2$) as a catalyst (Figure 3-1). Ring opening polymerisation (ROP) causes the terminal end of a polymer chain to become a reactive centre, this allows for further cyclic monomers to react through opening of the ring, forming longer chains. The driving force for ROP is the relief of steric repulsion or bond-angle strain between atoms in the centre of the ring (Young and Lovell, 1991).

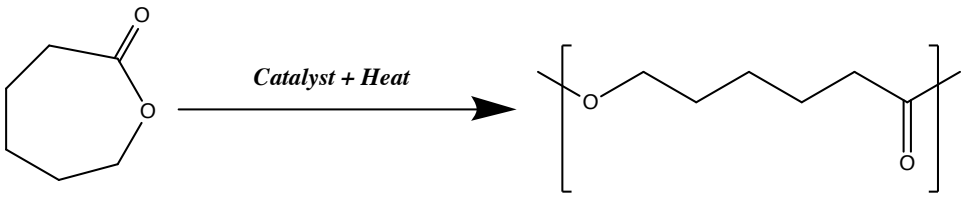

Figure 3-1 - The polymerisation of PCL through ring opening polymerisation (ROP). The process uses stannous octoate (Sn(oct)2) as a catalyst

In this study the grade of PCL used was CAPA 6800, supplied in pellet form by Perstorp UK Ltd (Warrington, UK). The glass transition temperature (T_g) and melting temperature (T_m) were typically around -60˚C and 60˚C respectively. The molecular weight (M_w) of CAPA 6800 is 80,000 g/mol and generally crystallisation commences on cooling from the melt at 30˚C (Acierno, 2006).

3.2 Poly(ether-ether-ketone)

Poly(ether-ether-ketone) (PEEK) is a thermally stable polymer; however, degradation occurs through pyrolysis at temperatures of 550 ˚C and above. Synthesis of PEEK is achieved through step-growth polymerization by the dialkylation of bisphenolate salts (Shukla *et al.*, 2012). The reaction is conducted close to T_m to maintain solubility in a polar aprotic solvent, diphenyl sulfone. The mechanical properties, chemical resistance and thermal stability of PEEK make it a suitable material for the automotive and aerospace industry. The chemical structure of PEEK is shown in Figure 3-2.

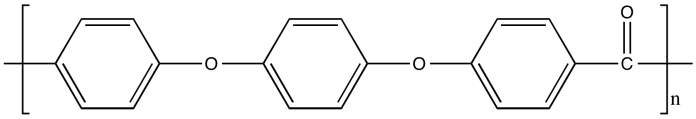

Figure 3-2 - Chemical structure of PEEK

PEEK 150PF was supplied by Victrex (Lancashire, UK) in a fine power form for use in this study. PEEK has a T_g and T_m of 143 and 343 ˚C respectively with an equilibrium melting temperature (T_m^0) of around 390 ˚C (Lee and Porter, 1987). PEEK has a M_w of 68,000 g/mol, introducing a relative crystallinity of ~40% (Tardif *et al.*, 2014).

3.3 Poly(lactic acid)

Poly(lactic acid) (PLA) is often referred to as a bio-renewable linear polyester, the precursor is lactic acid which can be produced via fermentation of cornstarch. PLA is synthesized in a number of stages beginning with a condensation reaction of lactic acid and a depolymerisation reaction to form a lactide. The lactide is produced through ROP to produce a high M_w (>100,000 Da) polymer, PLA. Different lactides can be formed due to the presence of an asymmetrical carbon atom (MacDonald, 1996) and the

stereoisomerism of the hydrogen and methyl group (–CH3) (Södergård and Stolt, 2002). D- and L-lactides in their purest form (highest optical purity) crystallise; however, when L- and D- lactides combine in a co-polymer, the polymer can become amorphous (R. Auras *et al.*, 2010). PLA containing less than 6% D-lactide is considered semi-crystalline; in contrast, greater than 6% D-lactide prevents crystallisation, creating an amorphous morphology (Kolstad *et al.*, 2012). The chemical structure of D-, L- and meso- lactides is shown in Figure 3-3.

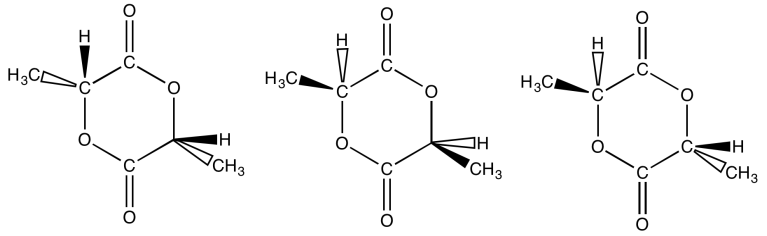

Figure 3-3 - PLA repeat unit and stereoisomer chemical structures D-, L- and Meso lactides

The PLA grade used in this study was 2002D, a semi-crystalline copolymer PDLLA with a 4.25% D-lactide content (Rathi *et al.*, 2011). It was supplied in pellet form by NatureWorks LLC (Minnetonka, MN, USA) has a reported M_w average of 200,000 g/mol (Mihai *et al.*, 2009).

CHAPTER 4 EXPERIMENTAL

4.1 Differential Scanning Calorimetry (DSC)

Differential scanning calorimetry is a well-known thermal analysis technique used to characterise thermal transitions in materials, detected from heat flow in and out of the sample. Some instrumentation presents exothermic heat flow as a negative change, however others present a positive change. The Flash DSC (FDSC) uses a positive change to represent exothermic heat flow; therefore, the results presented in this work show exothermic heat flow as a positive change through all figures. In a polymer, three transitions can be detected and are illustrated in Figure 4-1. All three transitions can be observed in partially crystalline polymers; however, amorphous polymers only show a T_g. DSC will be used to characterise thermal transitions, calculate degree of crystallinity and measure crystallisation kinetics.

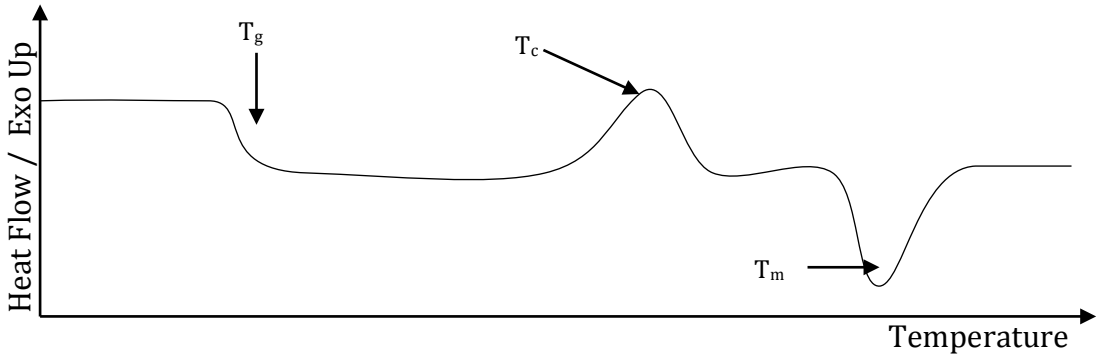

Figure 4-1 - Schematic of a DSC trace with three transitions, glass transition, melting and crystallisation

One feature common to all DSC equipment is a separate reference and sample cell. In this research a Mettler-Toledo (Greifensee, Switzerland) DSC1 (CDSC) and a Mettler Toledo Flash DSC1 (FDSC) were used to record experimental data. The CDSC used

aluminium crucibles, consisting of a pan and lid crimped together to secure the sample inside; in contrast a Xensor chip sensor housing both sample and reference sections in FDSC (see Section 2.2.1).

Two types of DSC are available: heat flux and power compensation. They operate in different ways producing heat flow traces with time. In a heat flux DSC a single heater controls the temperature of the sample and reference pans, compared to individual heaters in power compensation DSC maintaining a constant programmed temperature through thermal transitions. In heat flux DSC, the difference in temperature of the sample and reference pan resolves any thermal transitions and records changes in heat flow. In power compensation, the two individual heaters ensure programmed temperature is maintained as thermal transitions alter sample temperature. The energy required to maintain sample and programmed temperature is the measure of the heat flow within the sample. Heat flux and power compensation DSC schematics are illustrated in Figure 4-2.

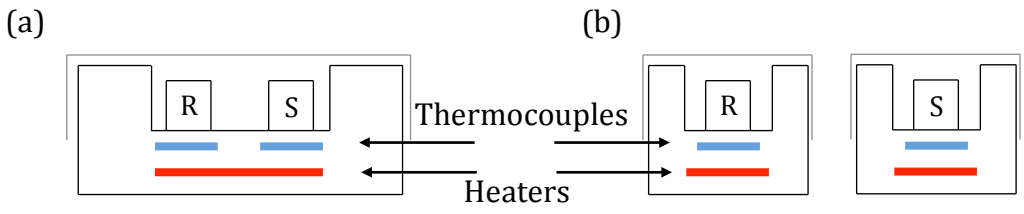

Figure 4-2 - Schematic representation of (a) heat flux and (b) power compensation DSC. and S and R denote sample and reference pans respectively

4.2 The Mettler Toledo Flash DSC-1 (FDSC)

4.2.1 Experimental Technique

The Flash DSC (FDSC) was interfaced with a personal computer running proprietary control software (Mettler Toledo StarE V10). Scan rates are achievable up to 20,000˚C/s on heating and 4,000˚C/s on cooling in a temperature range, -90˚C to 450˚C. Sample preparation and mass estimation is explained in Chapter 5.

$$\text{Scan Rate} = \frac{dT}{dt}$$

Equation 4-1

where *T* is temperature and *t* is time.

4.3 Mettler Toledo DSC 1 (CDSC)

4.3.1 Experimental Technique

A Mettler Toledo conventional DSC (CDSC) was interfaced with a personal computer. A known mass of indium (99.999%) and tin (99.999%) was used to calibrate the instrument from the onset of melting and heat of fusion.

4.3.1.1 Intracooler

Separate Huber TC100 intercoolers were used for both CDSC and FDSC calorimeters. This intracooler is a two-step gas compression cooling device, enabling a purge gas to be cooled to a temperature of -90°C. Low temperature cooling is important when investigating materials that have transition temperatures below room temperature and to assist in rapid cooling.

4.3.1.2 Purge Gas

An inert purge gas (argon or nitrogen) was used to prevent any water condensation on the cell from the environment. The flushing of volatiles by a purge gas helps to prevent oxidation and degradation. The gas between the surroundings and sensor aids heat transfer from the gas to the sample. A flow rate of 20-30±2 mL/min and 50±2 mL/min were used for FDSC and CDSC respectively. The thermal conductivity of the inert purge gas impacts the operating window on cooling and heating (Poel *et al.*, 2012).

4.3.2 Methodology

Samples of mass 5±2 mg were cut from polymer pellets (as received) or hot pressed sheets (see section 4.4). Samples were heated between 10 and 80˚C/min in the temperature range -90 to 400˚C; specific temperature ranges were selected for each polymer according to the thermal transition temperature to prevent degradation. The analysis was recorded on the second run to ensure removal of stresses remaining from prior processing.

4.3.2.1 Glass Transition Temperature (T_g)

The change in specific heat capacity *(ΔC_p)* (where $\Delta C_p = C_{p(liquid)}$-$C_{p(glass)}$) represents the change of state from a liquid to a glass. The midpoint of the glass to liquid transition is recorded as the glass transition temperature (T_g) (Figure 4-3); however, when an endothermic peak is present on T_g, an alternative definition of T_g must be used. Thermodynamic (or fictive) T_g is defined by the Richardson method (Aras and Richardson, 1989) where taking the temperature intersection of ½ΔC_p, in these cases, does not provide an accurate value for T_g. Figure 4-4 illustrates the Richardson method

for calculating a thermodynamic T_g. The T_g is calculated at the AB junction when areas A + C = B.

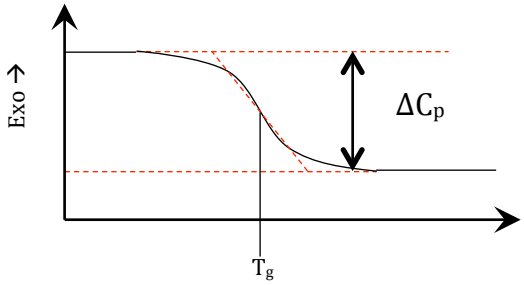

Figure 4-3 - Schematic of a glass transition temperature measurement

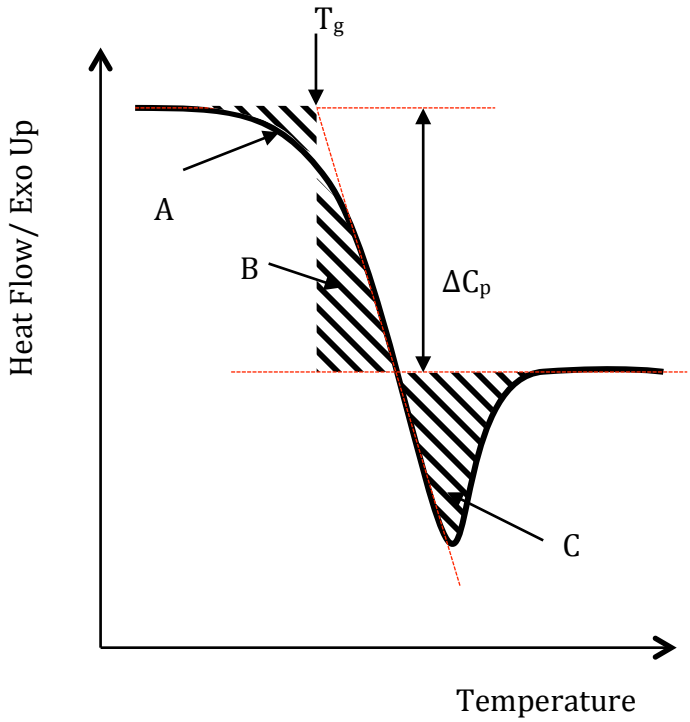

Figure 4-4 - Schematic of the measurement of the Tg using the Richardson method

4.3.2.2 Heat of Fusion

The heat of fusion (H_f) is the amount of heat required to melt a crystalline solid and is of equal magnitude to the heat of crystallisation (H_c). ΔH_f was measured from the area of the peak using a linear baseline from the first to the last trace of melting (shown in Figure 4-5). ΔH_f was calculated from the integration of this curve (Equation 4-2). The

weight fraction degree of crystallinity (X_c) was defined using Equation 4-3, where ΔH_f^0 is the heat of fusion of a 100% crystalline sample. The literature value of ΔH_f^0 for PCL is 139 J/g (López-Rodríguez *et al.*, 2006), PEEK 130 J/g (Cebe and Hong, 1986) and PLA 93 J/g (Ahmed, 2009).

$$\int \left(\frac{dH}{dt}\right)_{sample} dt = \Delta H_{sample}$$

Equation 4-2

$$Xc = \frac{\Delta H_f}{\Delta H_f^0} \times 100$$

Equation 4-3

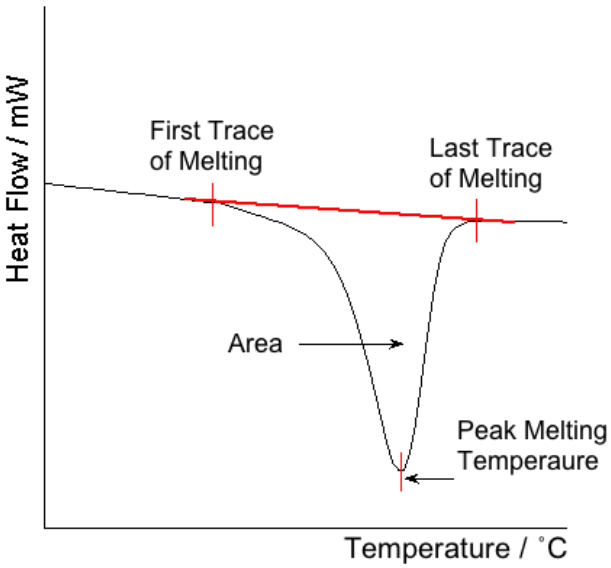

Figure 4-5 - Schematic representation of T_m data and the baseline on a DSC trace

4.3.2.3 Isothermal Crystallisation

Crystallisation was carried out isothermally using both CDSC and FDSC. Crystallisation temperature and time were changed to calculate crystallisation kinetics over a crystallisation temperature range between T_g and T_m. Prior to crystallisation, melting was carried out above the polymers equilibrium melting temperature (T_m^0) to remove

residual order within the system. CDSC samples were heated to T_m^0 and held for 2 minutes before cooling at 10˚C/min to the crystallisation temperature (T_c) where the sample was held for a specified time. After the isothermal hold, the sample was heated at 10˚C/min from T_c to T_m^0 (blue lines - Figure 4-6).

FDSC samples were heated to T_m^0 at a specified rate (˚C/s) and held for 0.1 seconds before rapid cooling to the crystallisation temperature (T_c) where the sample was held for a specified time. After the isothermal hold, the sample was rapidly cooled at a specified rate to a temperature below T_g. A 0.1 second isothermal hold was carried out before heating at a specific rate to T_m^0 (red lines - Figure 4-6). Heating from below T_g on FDSC produces a longer baseline for further analysis compared to heating from T_c. This is demonstrated in Figure 4-7.

As stated previously (in Section 4.3.2.2), a linear baseline is required for analysis of ΔH_f. The benefit of a full temperature scan from below T_g to T_m^0 provides a more accurate baseline; therefore, more repeatable data analysis.

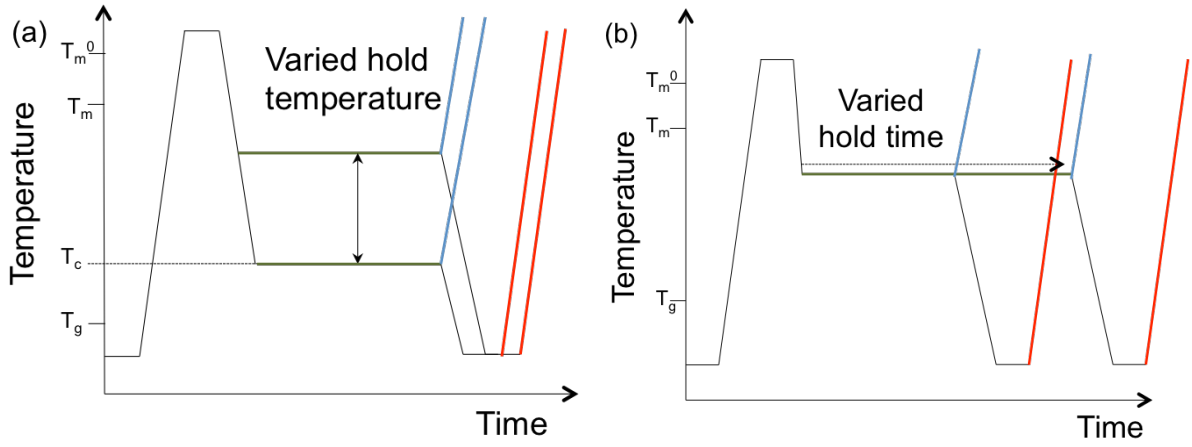

Figure 4-6 - Methods for isothermal crystallisation with varied (a) temperature and (b) time (blue line heat from T_c; red line heat from below T_g after quench cool from T_c)

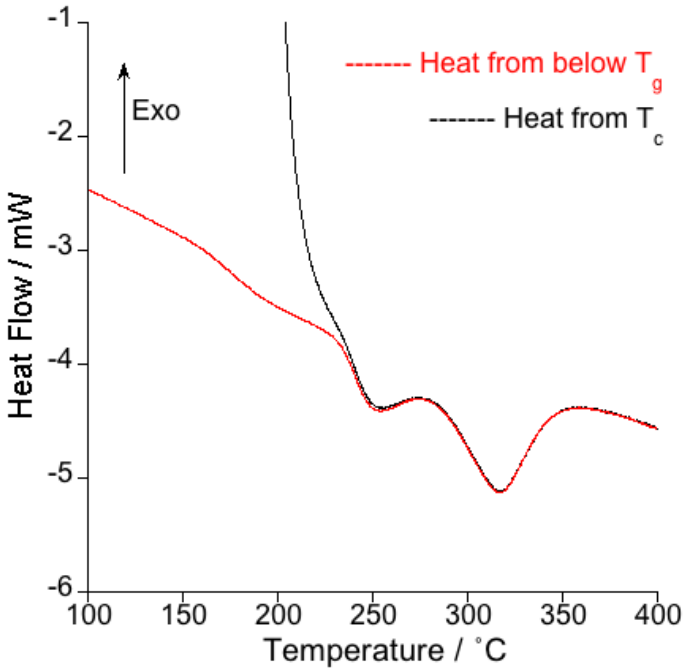

Figure 4-7 - Comparison of heating traces from below T_g (red trace) and from T_c (black trace) after isothermal crystallisation

4.3.2.4 Normalisation of DSC Traces

FDSC has a large range of scanning rates, up to 7 orders of magnitude. This results in many different scanning rates, ranging from 0.01 – 20,000˚C/s presenting a different sensitivity of thermal transitions. This sensitivity increases perception of features within the trace making it difficult to compare results. Therefore, it is important that when comparing results for a visual analysis, heating rates must be equal, or, normalised data to heating rate. To normalise data according to heating rate, the sample heat flow is divided by the respective heating rate. The resulting trace shows normalised heat flow (mJ/˚C) over temperature (˚C).

4.4 Hydraulic Press

4.4.1 Experimental Technique

PLA sheets were formed using a Moore hot press with variable temperature and pressure, integrated with a water-cooling system. Samples were subjected to a pressure of 10 tons at 200˚C. Before processing, polymer pellets were dried in an oven at 70˚C for 4 hours according to manufacturers data.

4.4.2 Methodology

PLA sheets were created using PLA pellets placed into the press within 1 mm thick mold. The pellets were held for 3 minutes at 200˚C, before 10 tons of pressure was applied for 2 minutes. The sample was cooled through water irrigation of the platens for 20 minutes before removal (~10˚C/min). A pressure of 10 tons was maintained through cooling.

4.5 Scanning Electron Microscope (SEM)

4.5.1 Experimental Technique

Scanning electron microscopy is a characterization technique used to study surface topography of materials to a resolution of a few nanometers. Operating within a vacuum, an incident electron causes ionized electrons (secondary electron) to leave the surface of a conductive sample with a small amount of kinetic energy (≤ 50eV).

4.5.2 Methodology

A Philips ESEM XL 30 FEG (using only SEM) was used to observe the surface of an FDSC chip and sample located on the membrane. All analyzed chips were coated with a thin platinum layer approximately 10 to 12 nm thick using a sputter coater to provide sufficient conductivity. A conductive silver dag solution was applied to the edge of each

sample to improve conductivity to the stub. An electron beam acceleration voltage of 10 kV was used to observe samples with a spot size 4 nm.

4.6 Hot Stage Microscopy

4.6.1 Experimental Technique

A Linkam TR600 hot-stage was used on a Leitz polarised light microscope to observe crystal growth in PLA samples. The temperature of the hot-stage was controlled using a Linkam LK600 controller with ±0.1˚C accuracy. A white light source was used to illuminate the sample and a polarised lens was used to examine the birefringent regions in thin films of the polymer.

4.6.2 Methodology

Thin layers of PLA (~15μm) were taken from a single PLA pellet produced using a hot-press and placed between two glass slides. The sample was melted for one minute at 200˚C and rapidly cooled to room temperature, resulting in an amorphous morphology. The sample was heated at 30˚C/min from room temperature and isothermally crystallised at 70˚C for 12 hours. Optical images were captured using a digital camera mounted on the microscope.

4.7 Laser Flash Apparatus (LFA)

4.7.1 Experimental Technique

A Netzsch LFA 427 was interfaced with a personal computer running proprietary control software (Proteus®) to investigate the temperature dependence of the thermal diffusivity. A class 4 laser pulse (power <25 Joules/pulse; wavelength, 1064 nm) quickly heats the bottom of the sample as the temperature on the opposing side (top) is

measured as a function of time using an Indium antimonide (InSb) photovoltaic infra-red (IR) detector cooled with liquid nitrogen.

4.7.1.1 Purge Gas

An inert purge gas was used to remove moisture in the furnace. The flushing of volatiles helps prevent oxidation and degradation of the sample at elevated temperatures. The furnace was purged with nitrogen gas at a flow rate of 100±5 mL/min.

4.7.1.2 Sample Preparation

Cylindrical PLA samples were cut from a hot pressed sheet (see Section 4.4), the diameter and thickness was 12.6 ± 0.1 mm and 1.0 ± 0.1 mm respectively. To eliminate light penetration through the thickness of the sample and improve emissivity, a graphite spray (Kontakt Chemie Graphit 33) was used to cover the sample surfaces. The graphite was applied from a pressurised spray at a height of approximately 0.3 m to a thickness of 3.5 ± 0.5µm. The sample before and after the application of graphite is shown in Figure 4-8. A new sample was cut and coated for each experiment.

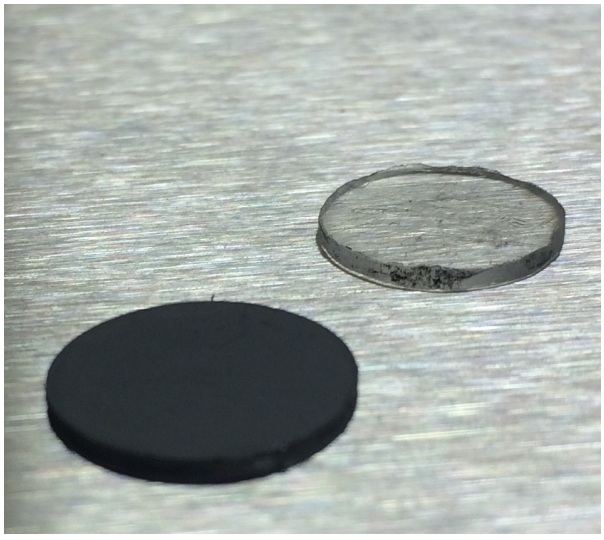

Figure 4-8 - PLA sample uncoated (transparent) and graphite-coated (black)

4.7.2 Methodology

A graphite-coated sample was loaded into the sample holder, placed into the apparatus tube and covered with a sample cover (Figure 4-9). A high intensity laser pulse (shot) quickly heats the sample homogeneously (laser voltage, 400V; pulse width duration, 0.4 ms). An accurate time-temperature rise and fall, on the opposite side (top) of the sample to the laser pulse[1], was resolved through an IR detector. A thermocouple connected to the apparatus tube measured the sample temperature and a thermocouple in the body of the furnace measured the furnace temperature (Figure 4-10). An external thermocouple was placed next to the thermocouple on the apparatus tube and on the top surface of the sample (Figure 4-9) in calibration experiments.

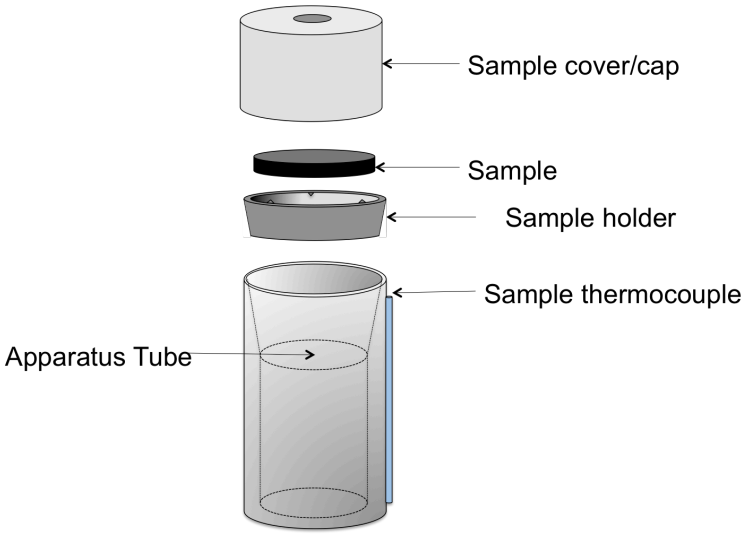

Figure 4-9 - LFA sample holder apparatus and sample location

The laser was shot at the sample three times (with 3 minute intervals) at pre-determined temperatures during non-isothermal heating experiments at temperature intervals between 2 and 5˚C. The average thermal diffusivity was recorded with a

[1] The phrase 'laser pulse', used to heat the sample surface is often referred to as a 'shot'; this term will be used in this study.

standard error to indicate variability of the data. The laser was shot at various time intervals between 220 and 1,300 seconds during isothermal experiments. Samples were heated from ambient conditions to the selected isothermal crystallisation temperature at 5˚C/min. In order to minimise the temperature overshoot, a 0.5˚C/min heating rate was applied 5 ˚C below the programmed isothermal temperature.

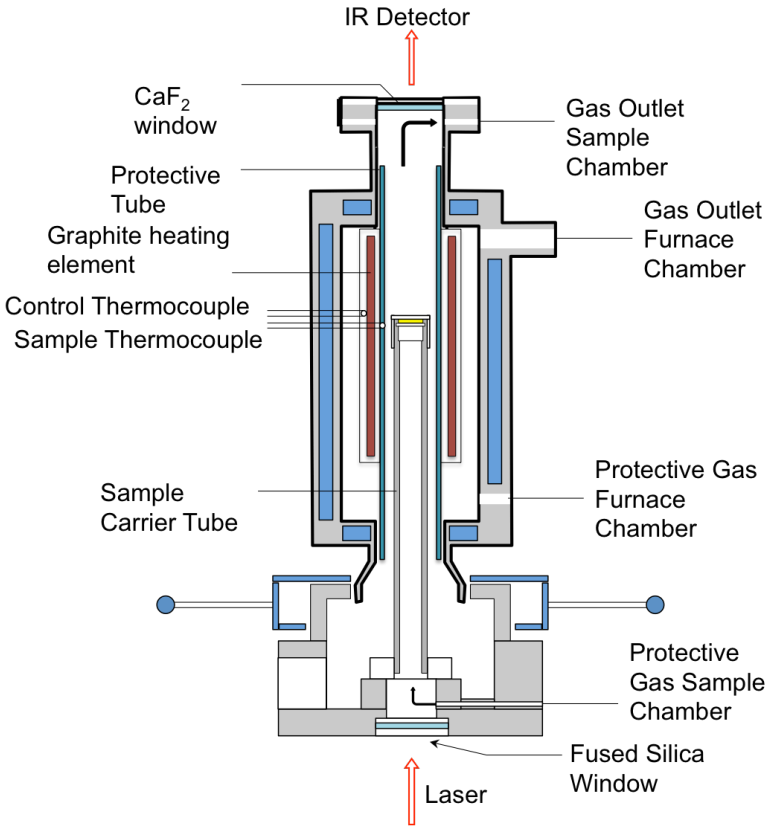

Figure 4-10 - A schematic diagram of the laser flash apparatus (LFA)

4.7.2.1 Calculation of Thermal Diffusivity

Thermal diffusivity was calculated from the time-dependant temperature increase and decrease on the top surface of the sample after each shot. Various models can be used to correlate this time-dependence directly to thermal diffusivity. An adiabatic model was proposed by Parker *et al.* (1961) where sample thickness (L) and time required for the

top surface of the sample to reach half the maximum temperature rise ($t_{½}$) (Figure 4-11) were used to determine thermal diffusivity (α) where:

$$\alpha = \frac{1.38L^2}{\pi^2 t_{\frac{1}{2}}}$$

Equation 4-4

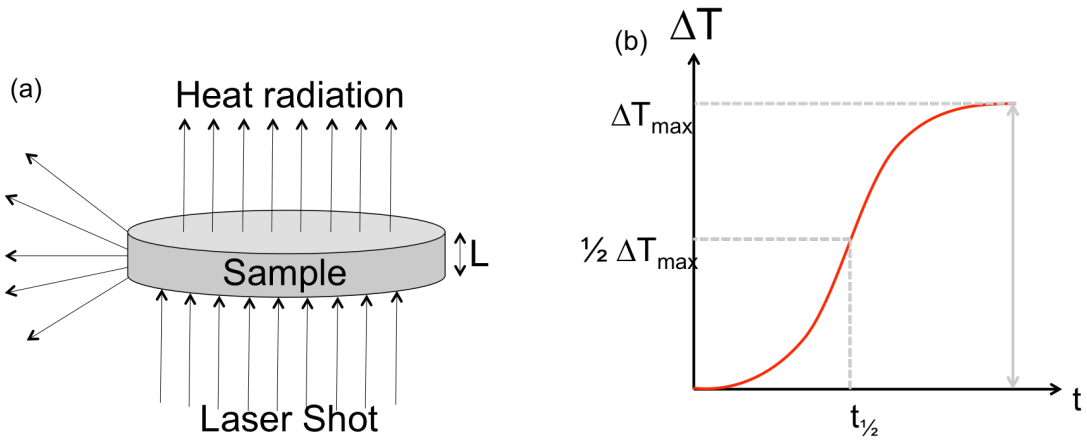

Figure 4-11 - An illustration of (a) the laser pulse interaction with the sample and (b) half time calculation

Under experimental conditions, the adiabatic curve fit does not provide an accurate thermal diffusivity value due to the assumed ideal boundary conditions, a closed system with no heat loss. Cape and Lehman (1963) formulated a curve fit to account for two heat loss parameters: facial and radial. The Cape-Lehman model is given as

$$T(r,t) = T_\infty \sum_{m=0}^{\infty} C_m X_m \sum_{i=0}^{\infty} D_i(r, Y_r) \int_0^t d\tau W(\tau) \exp\left[\frac{\omega_{im}(t-\tau)}{t_c}\right]$$

Equation 4-5

where *T(r,t)* is the temperature rise on the top surface of the sample as a function of time, *t*, and radial location, *r*. T_∞ is the signal rise under isothermal conditions and C_m and X_m are facial heat loss parameters. *W(τ)* is the laser pulse shape, τ is the pulse length

and t_c is the characteristic time for the heat pulse to propagate through a sample of thickness, L; $t_c = (L/\pi)^2(1/\alpha)$.

$$C_m X_m = (-1)^m \frac{2\alpha}{L} \frac{X_x^2}{X_m^2 + 2Y_x + Y_x^2}$$

Equation 4-6

The quantity Y_r is the radial Biot number and describes the amount of radial radiative heat loss. The quantity Y_x is the facial Biot number and described the facial radiative heat loss. The equations for the radial and facial Biot numbers are:

$$Y_r = 4\sigma\varepsilon_r T_0^3 \lambda^{-1} r_0$$

$$Y_x = 4\sigma\varepsilon_r T_0^3 \lambda^{-1} L$$

Equation 4-7

where σ is the Stefan-Boltzmann constant and ε is the total emissivity of the sample. T_0 is the sample temperature, λ its thermal conductivity and r_0 is the sample radius.

The work in this study will be analysed using the Cape-Lehman model due to the accuracy of the fit to the experimental data. A comparison of the two models: adiabatic and Cape-Lehman, and their fit to the data is displayed in Figure 4-12. The Cape-Lehman model shows a good fit to the data in comparison to the adiabatic fit where no heat loss is considered.

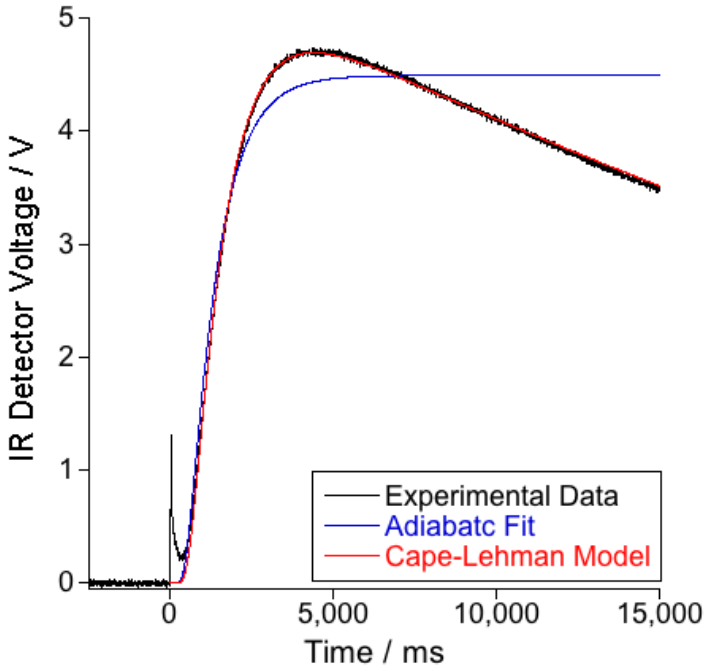

Figure 4-12 - A comparison of the data fit models; adiabatic and Cape-Lehmann to the experimental

CHAPTER 5 FLASH DSC PERFORMANCE AND THERMAL LAG VALIDATION

5.1 Introduction

This chapter aims to provide a performance validation of Flash DSC (FDSC) and demonstrate the novel method of chip sensor preparation, sample preparation and mass estimation. This chapter investigates the achievable heating and cooling rates available on the FDSC, comparing two different inert purge gases with varied flow rates. The most suitable gas and flow rate will be selected to study the repeatability of sensor calibration, using a series of different samples and sensors, calculating a correction factor, permitting thermal lag effects experienced within a system to be removed for data analysis.

5.2 Methodology

5.2.1 Sensor Preparation

The 'as supplied' FDSC chip sensors were subjected to two preparation methods (designed by Mettler Toledo) before sample application or experimentation: conditioning and correction. These methods were carried out with a blank chip, each with a unique identification number (Figure 5-1). The first preparation stage, 'conditioning', heats the chip over the hot temperature range from 25-450˚C (method shown in Figure 5-2). This is carried out two to three times to relieve stresses in the sensor wires within the sensor membrane. This stress relief is important when samples

are loaded onto the membrane, preventing movement of the sample from the ideal location.

Conditioning of the chip is performed in order to reduce noise during measurements and ensure that the sensor baseline is acceptable. An example of a conditioning run that is acceptable is presented in Figure 5-3 (a). A chip sensor exhibiting an unacceptable conditioning trace is presented in Figure 5-3 (b), where large spikes in the trace during heating and cooling are visible. The presence of large, unwanted deviations in the trace during conditioning may obscure sample results within that temperature range. Thus, it is important that the conditioning trace is as smooth as possible.

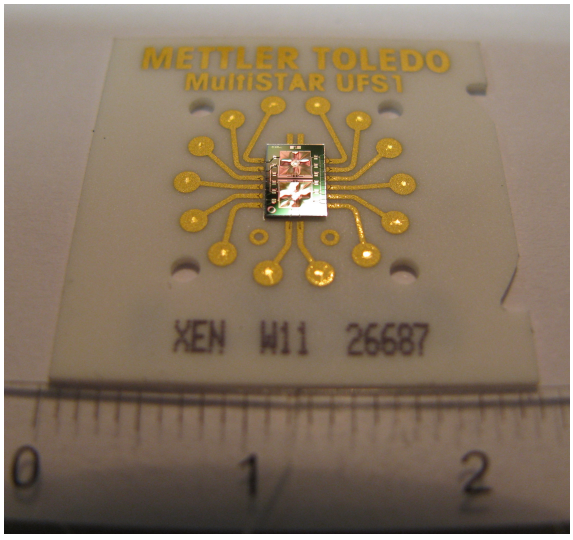

Figure 5-1 - The reverse side of a MEMS chip sensor, supplied by Mettler Toledo with a unique identification number

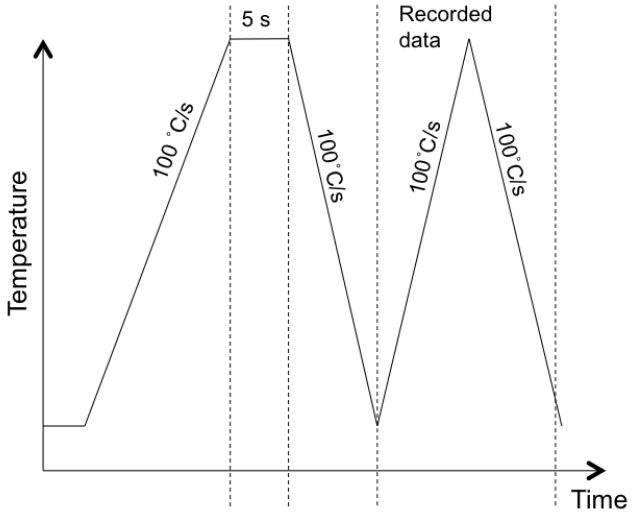

Figure 5-2 - Conditioning method pre-determined by Mettler Toledo

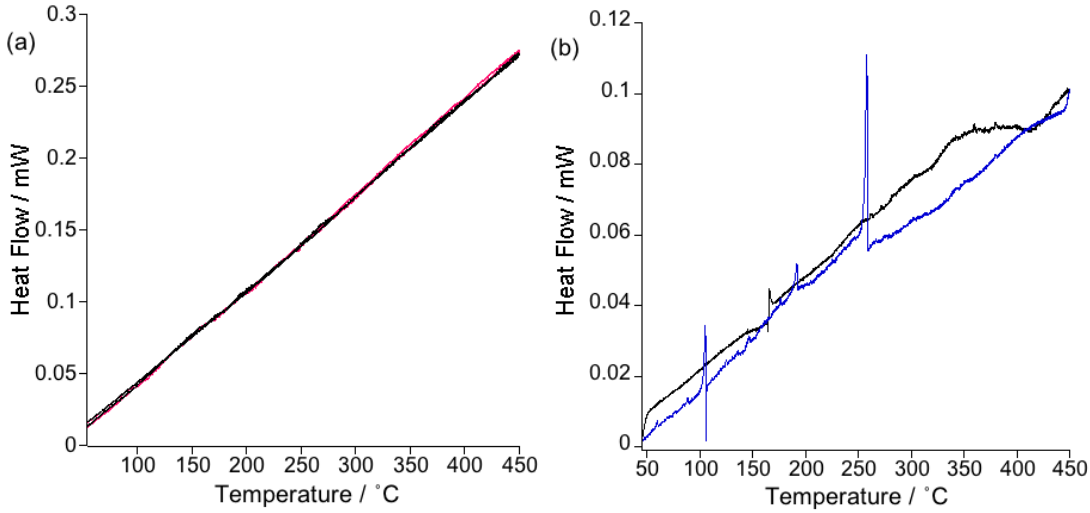

Figure 5-3 - Conditioning traces obtained during sensor preparation (a) acceptable and (b) unacceptable

The second stage in the preparation of the chip sensor is a 'correction' run. The correction records the thermocouple measurement between the hot and cold junction on the chip sensor. This is important as the cold junction temperature can be altered for different chip sensors and thus ensures accurate temperature calibration of the hot junction. The correction was recorded with a sample support temperature (T_{ss}) of -90°C. The T_{ss} is the temperature of the cold junction and is constant throughout experiments.

All subsequent experiments carried out using that chip sensor must use the corresponding T_{ss} applied during the correction experiment.

5.2.2 Sample Preparation

Conventional DSC (CDSC) samples are placed in an aluminium pan and sealed shut. A typical sample (mass, ~5-10 mg) is taken from an 'as received' polymer pellet or a processed sheet. Due to the increased sensitivity of the FDSC, a twin MEMS (Micro-Electro-Mechanical-System) sensor chip is used. As a result of using a small sample in FDSC, small heat flow readings are obtained. An aluminium pan has been shown to cause unpredictability in the results recorded (van Herwaarden *et al.*, 2011); therefore, samples are placed directly onto the sensor (Figure 5-4).

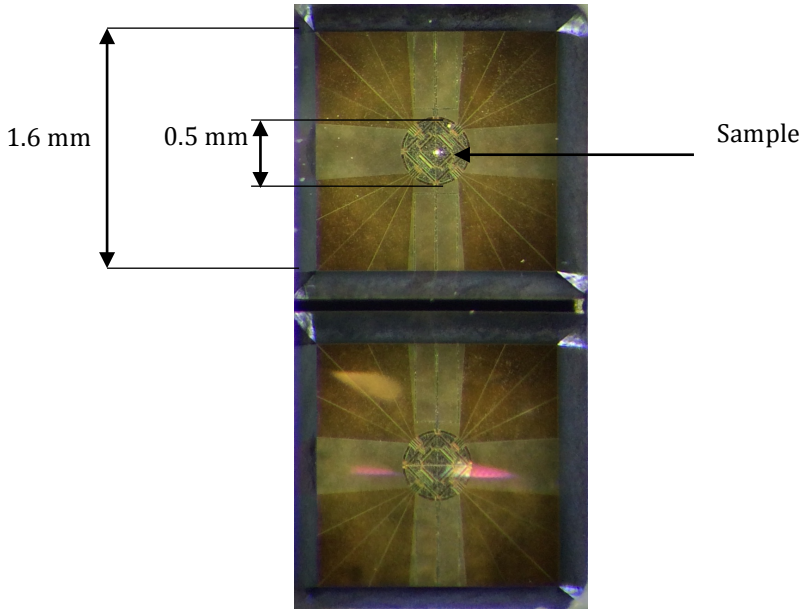

Figure 5-4 - The sample and reference membranes on an FDSC chip sensor

Sample preparation for the FDSC varies from all other DSC preparation procedures. The sample preparation technique is intricate and can be extremely time consuming. The small sample size requires the use of a microtome, an optical microscope and a scalpel

to create samples of an appropriate mass, 10-300 ng. The sample (pellet as-received) was prepared using a microtome. This creates a thin slice (~100 nm) of polymer film. A scalpel is then used to reduce the size of the microtome section under an optical microscope. Figure 5-5 and Figure 5-6 show an indium sample located on the blade of the scalpel and a hair, respectively. The sample must be as thin as possible to reduce thermal lag (Figure 2-4) because polymers are poor conductors of heat (dos Santos *et al.*, 2005, Zhuravlev and Schick, 2010). Therefore, it is important that the influence of thermal lag, upon measured results, is determined (see section 4.4).

Once the sample has been cut, it is held on a synthetic hair by static forces present, enabling placement of the sample onto the sensor. The membrane of the sensor is brittle with a thickness of 2 μm. Therefore, it is important that the sample loading method does not damage the membrane. After the sample is loaded, a series of slow heating experiments at <10˚C/s are applied to the sensor to ensure that good contact is achieved between sample and sensor. Fast heating rates may cause 'jumping' of the sample from the sensor as a result of fast relaxation of the polymer chains. The sample is heated to a temperature above the T_m (or T_g depending on the polymer morphology) to adhere it to the membrane and remove and stresses in the sample from prior processing. The chip can only be used once as, after the sample has adhered to the membrane, due to the membrane fragility, cleaning is not a feasible option (Mathot *et al.*, 2011).

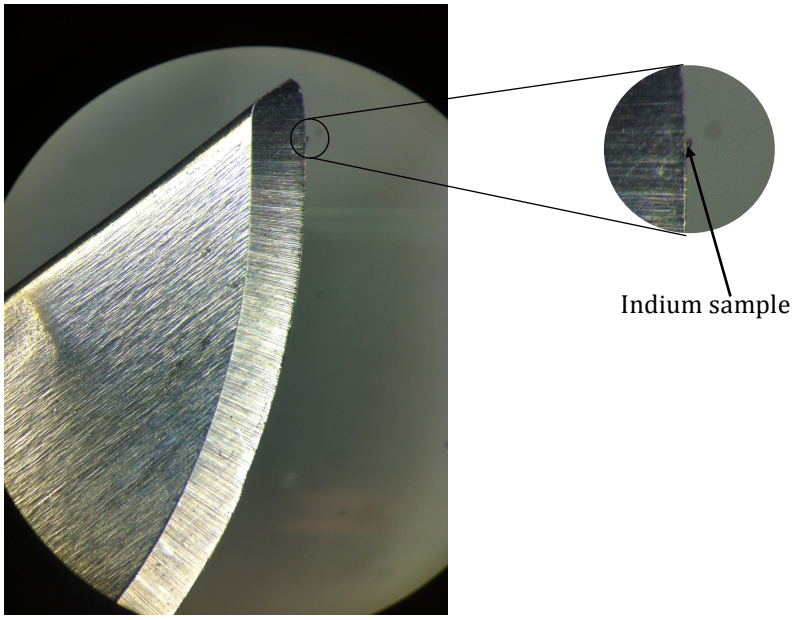

Figure 5-5 - Indium sample located on a scalpel after being cut to an appropriate size for FDSC

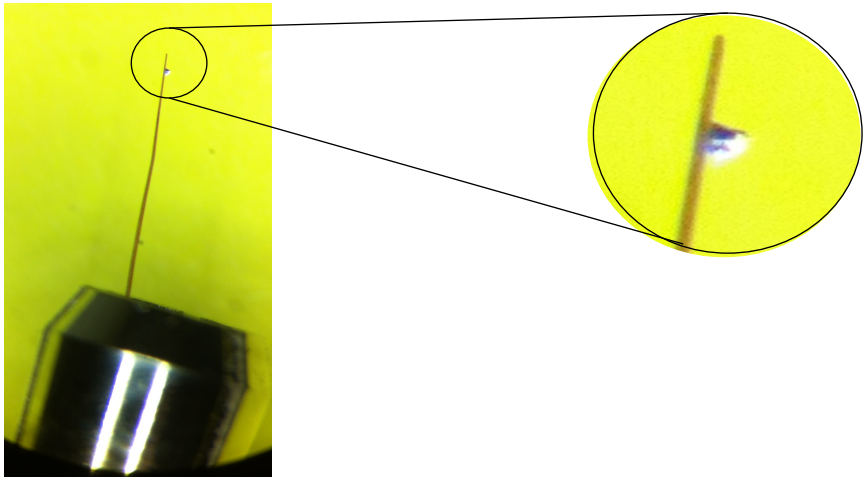

Figure 5-6 - A sample of indium located on a synthetic hair before being loaded onto a FDSC chip

5.2.3 Sample Mass Estimation

FDSC sample mass is in the order of 10-300 ng and not detectable on a standard laboratory balance. A comparison between the enthalpy on melting (heat of fusion) on FDSC and a CDSC, for identical sample materials, was used for an approximation of the mass. The overlap in scanning rates between the calorimeters was essential to generate the same crystallinity on cooling before measuring the enthalpy on heating during melting.

The FDSC has a wide scanning rate range from 0.05˚C/s (3˚C/min) up to 20,000˚C/s (1,200,000˚C/min) in comparison to CDSC, which achieves 0.01 to 80˚C/min. It is essential to subject the FDSC and CDSC samples to an identical cooling rate. The degree of crystallinity is assumed identical in both samples if cooled at the same rate from a temperature above the equilibrium melting temperature (T_m^0). By definition, the change in heat of fusion (ΔH_f) should therefore be identical:

$$\Delta H_{f\,CDSC} = \Delta H_{f\,FDSC}$$

Equation 5-1

$$\frac{\Delta h_{CDSC}}{m_{CDSC}} = \frac{\Delta h_{FDSC}}{m_{FDSC}}$$

Equation 5-2

where $\Delta H_{f\,CDSC}$ and $\Delta H_{f\,FDSC}$, measured in Joules per unit mass (J/g), represent the specific enthalpy of melting for the CDSC and FDSC, respectively. $\Delta H = \Delta h/m$, where Δh_{CDSC} and Δh_{FDSC} represent the integral of the melting endotherm in the CDSC and FDSC, respectively and m_{CDSC} and m_{FDSC} represent the mass of the samples in CDSC and FDSC, respectively.

In order to calculate the sample mass in the FDSC, a quantified mass of material was first cooled at a rate of 10˚C/min using CDSC. If cooling rate is sufficiently slow to allow complete crystallisation to occur, cold crystallisation is prevented during heating. The same material, of unknown mass, was subjected to an identical cooling rate of 10˚C/min in the FDSC.

Using Equation 5-3, a mass approximation was calculated from the enthalpy of melting of the CDSC sample and integral of the melting endotherm from the FDSC sample.

$$m_{FDSC} = \frac{\Delta h_{FDSC}}{\Delta H_{CDSC}}$$

Equation 5-3

Indium (mass, 6.33 mg) was subjected to a cool at 10˚C/min, followed by a heat at 10˚C/min using CDSC. Integrating the resultant melting curve from the heating trace allows a value of ΔH_f to be calculated: 25.34 J/g. The same cooling rate was used for a sample of indium with unknown mass using FDSC, which was subjected to a heating rate of 100˚C/s. The applied heating rate used to measure ΔH_f is respective of the calorimetry technique: 10˚C/min and 100˚C/s on CDSC and FDSC respectively. The area of melting endotherm for the FDSC sample was calculated by integrating the melting endotherm: 0.02403 mJ.

$$\frac{\Delta h_{FDSC}}{\Delta H_{CDSC}} = m_{FDSC}$$

$$\frac{0.02403 \times 10^{-3}}{25.34} = m_{FDSC}$$

$$9.483\times10^{-11}g = m_{FDSC}$$

$$948.3\,ng = m_{FDSC}$$

Equation 5-4

Some polymers may possess slow crystallisation kinetics or do not crystallise at all, resulting in an amorphous solid. If an amorphous morphology is formed after cooling at a rate of 10˚C/min, the mass estimation can be calculated using the change in the specific heat capacity (ΔC_p) obtained from T_g. Assuming that the heat capacity of the reference pan or membrane is constant throughout the temperature range, the ΔC_p can be determined from a shift in baseline, recorded at T_g (Figure 5-7).

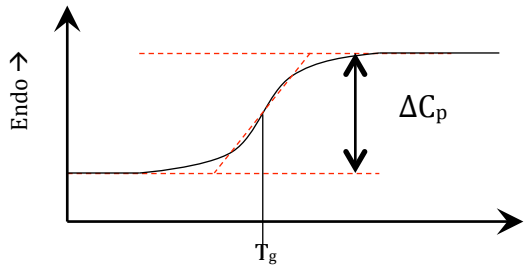

Figure 5-7 - Glass transition temperature (T_g) specific heat calculation

The same theory was used to estimate the mass of amorphous samples as previously shown in the semi-crystalline samples. The ratio of the ΔC_p between the two techniques is used to estimate the FDSC sample mass where an apparent specific heat capacity ($\Delta C_{p.a}$) can be obtained from the T_g of the FDSC sample. The sample mass is defined using Equation 5-5.

$$m_{FDSC} = \frac{C_{p.a}}{C_p} 1ng$$

Equation 5-5

Poly(lactic acid) (PLA) 2002D is an example of a semi-crystalline polymer with slow crystallisation kinetics. A PLA 2002D sample (mass 3.79 mg) was heated through T_g at

10˚C/min on CDSC with a ΔC_p equal to 0.478 J/g/˚C. The apparent specific heat capacity of the FDSC PLA 2002D sample (of unknown mass) was 105.634 J/˚C. Equation 5-5 allows the approximate mass of the FDSC sample to be calculated as:

$$m_{FDSC} = \frac{105.634}{0.478} 1ng$$

$$m_{FDSC} = 220.99\, ng$$

Equation 5-6

5.3 Performance Analysis of Flash DSC

5.3.1 Performance Validation

The performance of the FDSC was measured using an empty chip sensor. The empty chip ensures a constant heat flow measurement across both sample and reference sides. The 'real' scanning rates were determined by applying a range of heating and cooling rates to an empty chip. The temperature range covered by these experiments spans 540˚C, from -90 to 450˚C, the maximum for the instrument. The empty chip was tested across a range of scanning rates from 1,000–20,000˚C/s in both heating and cooling. Three steps were applied to the raw data (heat flow as a function of temperature) from the heating and cooling traces:

1) The extraction of sample temperature as a function of time from the recorded heat flow-temperature graph.
2) The temperature-time curve was differentiated as a function of dT/dt. The derivative produces scanning rate as a function of time.

3) The x-axis representing time was changed to represent sample temperature, creating a common axis between all rates to allow an accurate comparison of the scanning rate from -90˚C – 450˚C.

This performance was completed using two separate purge gases, argon and nitrogen. Two different purge rates were applied for each gas: 20 and 30 mL/min. The thermal conductivity of these gases are different (Johns *et al.*, 1986), and for heating and cooling rates, shows different results. Argon can be used for thermal experiments, specifically CDSC; however, as yet, has not been utilised in FDSC.

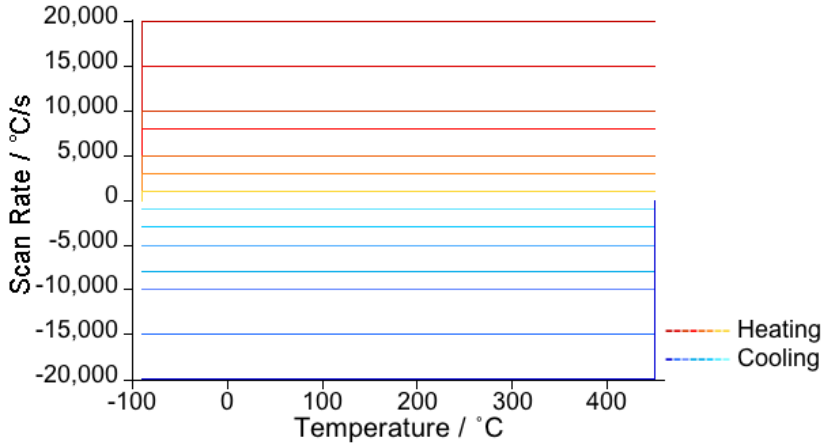

Figure 5-8 - The desired heating and cooling rates on FDSC up to 20,000˚C/s

The desired scanning rate with temperature shown in Figure 5-8 provides a continuous rate across the entire temperature range. However, the instrument requires time to achieve the programmed rate, and due to the retardation before reaching the final temperature (to prevent a temperature overshoot), a 540˚C operating window is not attainable.

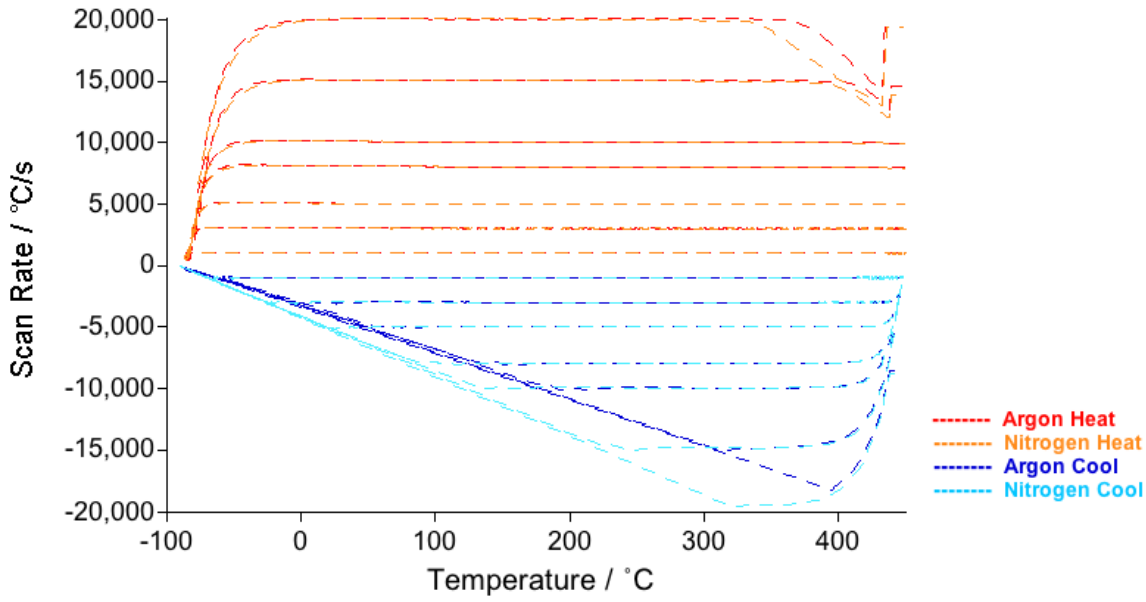

Figure 5-9 - Chip performance comparison between nitrogen and argon as a purge gas at 20 mL/min between -90 and 450°C

The comparison of the two gases at a flow rate of 20 mL/min is shown in Figure 5-9. In comparison to nitrogen, at 15,000 and 20,000°C/s on heating, a longer sustained plateau can be observed in argon. A shorter sustained plateau is visible on cooling at all rates with argon in comparison to nitrogen (Figure 5-10 (b)), due to a greater thermal conductivity in nitrogen. The operating window demonstrates a greater dependence upon cooling rates in comparison to heating (Table 5-1). This is due to the method by which the sample is heated and cooled (see Section 5.4). Comparing a different gas flow rate (10 and 20 mL/min) revealed no deviation in the achieved scanning rate for either inert gas (see Appendix).

The extremes of the entire temperature range reveal acceleration and deceleration on heating and cooling. Heat transfer takes time to occur; therefore, as scanning rate increases, time at each unit temperature decreases. The acceleration to the programmed rate is the same across all the heating and cooling rates, shown in Figure 5-10(a) and (b)

respectively. The acceleration during heating was calculated at ~500,000°C/s², five times faster than the retardation after the programmed rate, ~100,000°C/s².

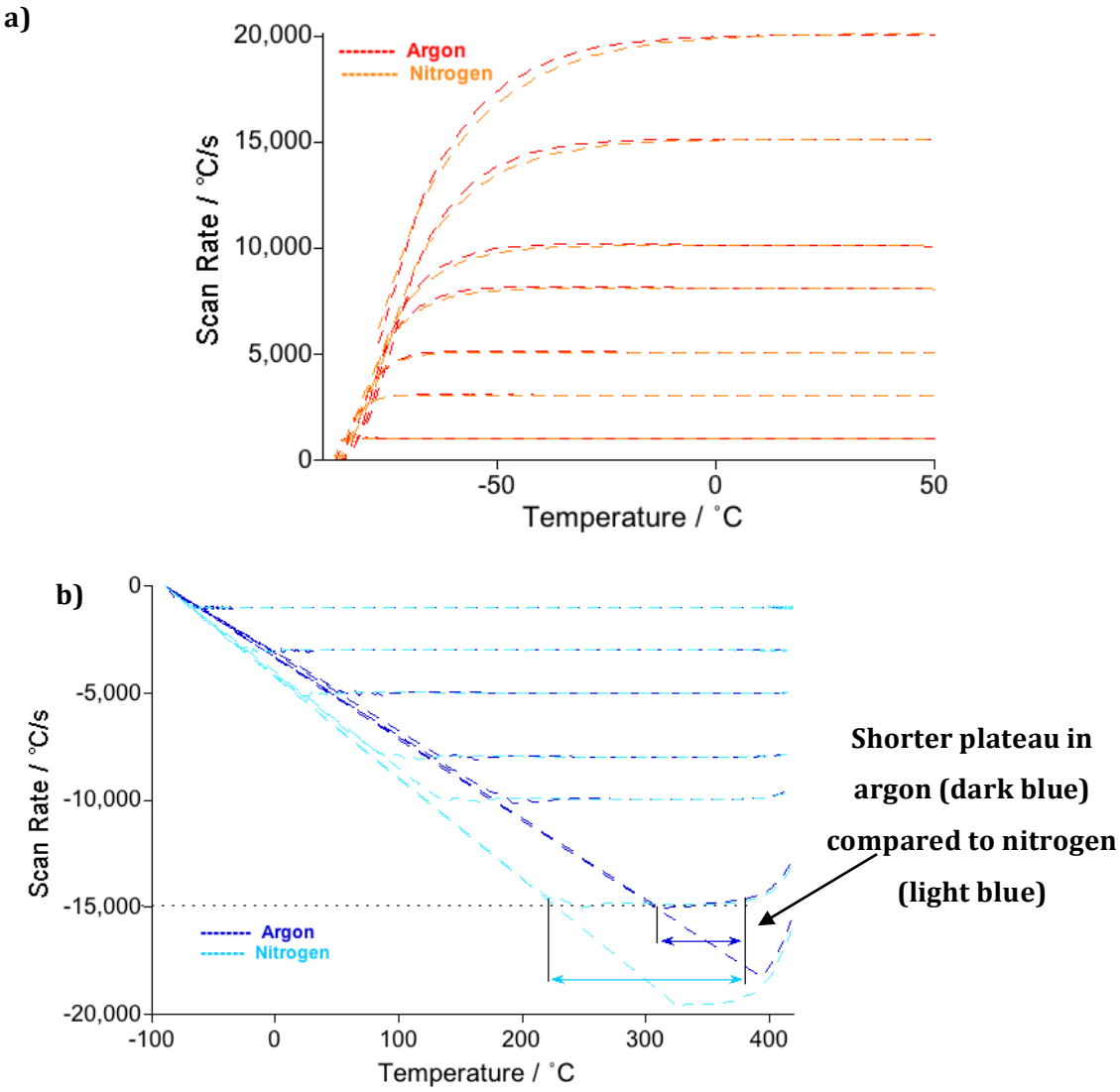

Figure 5-10 - And illustration of the acceleration in heating (a) and cooling (b) at a purge flow rate of 20 ml/min using argon and nitrogen

Table 5-1 - Operating windows for scanning rates during heating and cooling using nitrogen and argon

	Nitrogen		Argon	
Scanning Rate (˚C/s)	**Heating (˚C)**	**Cooling (˚C)**	**Heating (˚C)**	**Cooling (˚C)**
1,000	**-85 → 450**	**450 → -70**	**-85 → 450**	**445 → -65**
3,000	**-80 → 450**	**440 → -25**	**-75 → 450**	**435 → 0**
5,000	**-70 → 450**	**435 → 25**	**-70 → 450**	**425 → 50**
8,000	**-50 → 450**	**425 → 85**	**-60 → 450**	**410 → 130**
10,000	**-40 → 450**	**410 → 130**	**-45 → 450**	**400 → 180**
15,000	**-20 → 450**	**375 → 240**	**-25 → 450**	**335 → 310**
20,000	**10 → 450**	**N/A**	**-5 → 450**	**N/A**

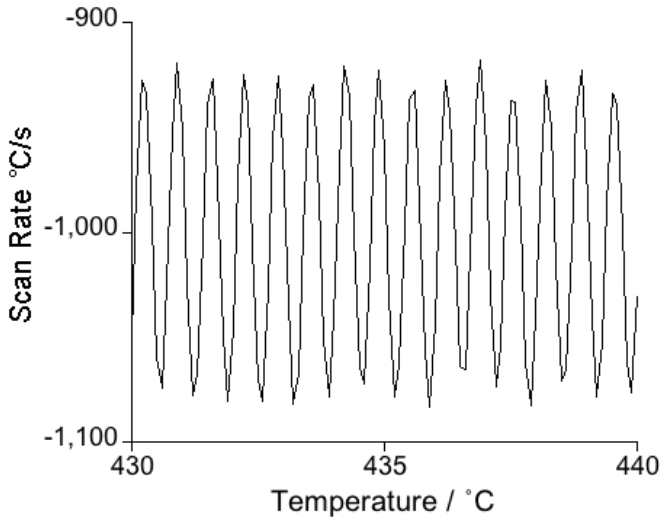

Figure 5-11 - Scanning rate fluctuations during cooling at 1,000˚C/s, with a nitrogen flow rate of 20 ml/min

Figure 5-11 shows scanning rate fluctuations of over 100˚C/s during cooling at 1,000˚C/s between 440-430˚C. This is a result of the instrument's inability to maintain low scanning rate at high temperature. The FDSC uses power compensation to maintain

a constant temperature change; thus, continual power inputs are made to attempt to maintain a constant temperature. The large temperature difference between the programmed temperature and the cold junction may be liable for these fluctuations.

5.3.2 Primary Temperature Calibration

FDSC was calibrated using a primary temperature standard, indium. Indium was selected based on its phase transition located in the centre of the temperature range of the instrument; 156.6˚C. A sample of indium with a mass between 200 and 300 ng was prepared.

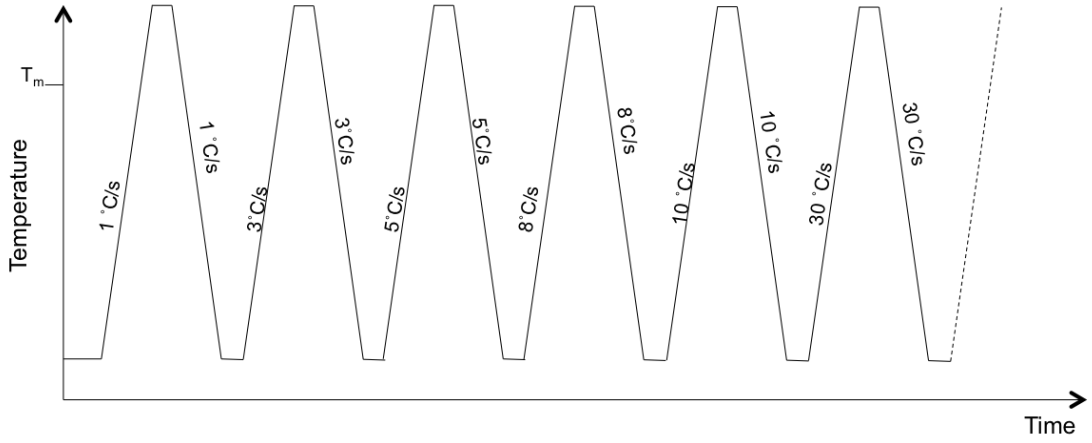

Figure 5-12 - A schematic of the performance method with heating and cooling rates between 1 and 1,000˚C/s

The indium sample was subjected to a variety of heating and cooling rates between 1 and 1,000˚C/s to obtain a melting onset temperature at a zero heating rate (Figure 5-12). The onset measurements of indium were extrapolated to the intersection of the temperature axis to obtain the zero heating rate. Using the difference between the zero heating rate literature value and the measured value, a temperature shift was calculated. The extrapolated onset of melting at zero heating rate for indium (mass, ~300 ng) prior to calibration was 153.0˚C, which is within the maximum error of the sensor, ±5˚C.

Measurements on the same sample of indium were repeated five times to ensure reliability of the results. The melting onset temperatures were calculated with the standard deviation for all of the measurements. The standard deviation for these measurements is negligible at ≤0.03˚C, showing exceptional repeatability of the FDSC (Table 5-2 & Figure 5-13). These results demonstrate a positive comparison to the results obtained by Poel *et al.* (2012).

Table 5-2 - The melting onset temperature of indium with heating rate using FDSC

	Melting Onset Temperature / ˚C					
Heating rate / ˚C/s	Test 1 (˚C)	Test 2 (˚C)	Test 3 (˚C)	Test 4 (˚C)	Test 5 (˚C)	STDEV (˚C)
0	156.6	156.6	156.6	156.6	156.6	0.00
1	156.7	156.7	156.7	156.7	156.7	0.01
3	156.9	156.9	156.9	156.9	156.9	0.01
5	156.9	156.9	156.9	156.9	156.9	0.01
8	156.9	156.9	156.9	156.9	156.9	0.01
10	156.8	156.8	156.8	156.9	156.8	0.01
30	157.0	157.0	157.0	157.0	157.0	0.01
50	157.0	157.0	157.0	157.0	157.0	0.01
80	157.0	157.0	157.0	157.0	157.0	0.01
100	157.1	157.0	157.0	157.1	157.0	0.01
300	157.4	157.3	157.3	157.3	157.3	0.01
500	157.5	157.4	157.4	157.5	157.4	0.02
800	157.6	157.6	157.6	157.6	157.6	0.03
1,000	157.7	157.6	157.6	157.6	157.6	0.03

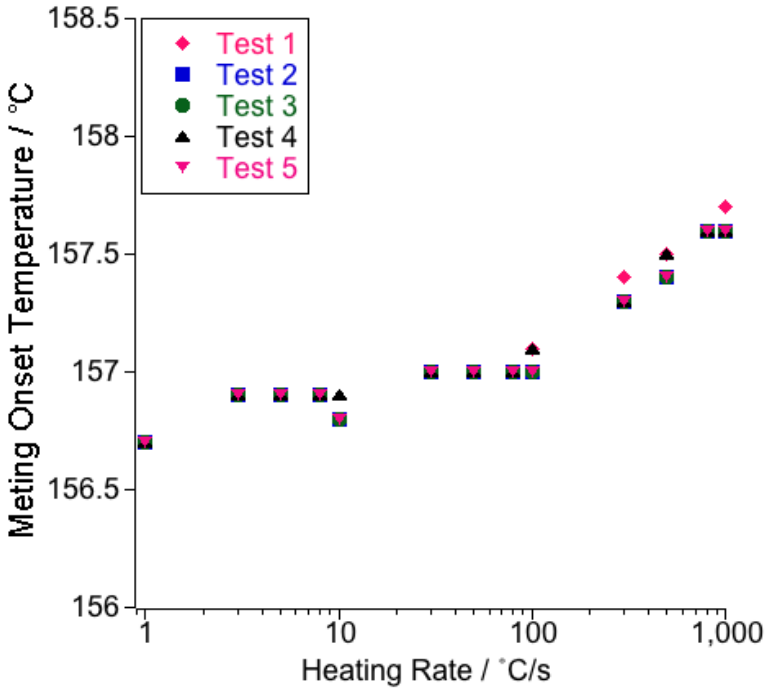

Figure 5-13 - The influence of heating rate on indium melting onset

5.3.3 Validation of the Primary Temperature Calibration

Validation accuracy of the primary calibration is conducted by comparing results from a different chip sensor and indium sample of similar mass. The same procedure described in section 5.3.2 was used with a new sample of indium (mass, ~370 ng) prepared and loaded onto a new chip sensor membrane. This was tested and compared with the ~300 ng indium sample. The variation in the standard deviation on heating rates from 1 to 1,000°C/s differed by a maximum of 0.2°C. Thus, it was concluded that the primary calibration was correct and results are within acceptable limits (Table 5-3). Assessing the validity of the calibration is important to ensure that the correction was accurate on more than one chip sensor.

Table 5-3 - A comparison of melting onset temperature between ~300 and ~370 ng samples on indium with heating rate

	Indium ~300 ng		Indium ~370 ng	
	Melting Onset Temperature / ˚C			
Heating Rate (˚C/s)	Before Calibration	After Calibration	Primary Calibration Check	STDEV (˚C)
1	153.1	156.58	156.59	0.0
3	153.3	156.81	156.82	0.0
5	153.3	156.79	156.73	0.0
8	153.3	156.77	156.63	0.1
10	153.2	156.77	156.64	0.1
30	153.4	156.81	156.72	0.1
50	153.4	156.83	156.76	0.0
80	153.4	156.86	156.81	0.0
100	153.5	156.89	156.83	0.0
300	153.8	157.15	157.04	0.1
500	153.9	157.31	157.18	0.1
800	154.0	157.5	157.32	0.1
1,000	154.1	157.6	157.38	0.2

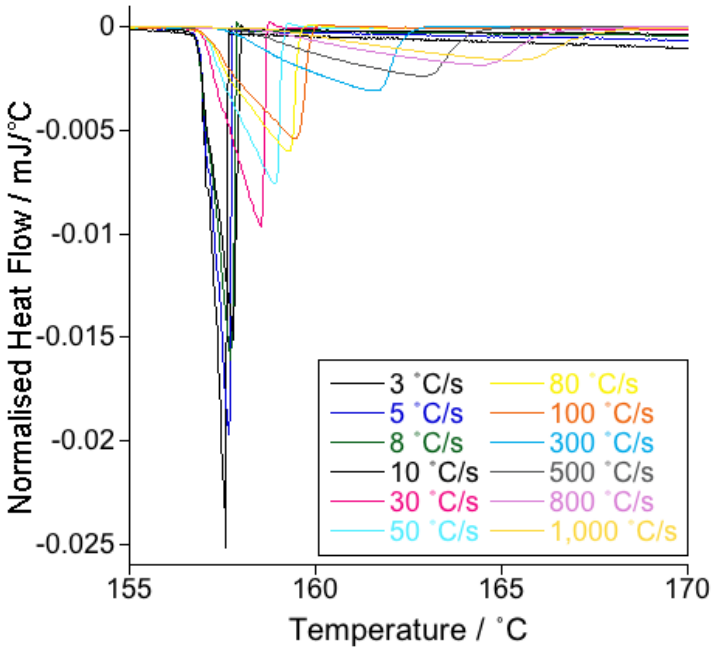

Figure 5-14 - The melting endotherm of indium (mass ~370 ng) heat flow normalised to heating rate with varied heating rates

Figure 5-14 shows melting of the indium sample as the heating rate increases using the method described in Figure 5-12. The result illustrates that faster heating rates broaden the melting endotherm. This is a direct result of the time in which the crystals have to melt.

5.3.4 Calibration with Respect to Sample Mass and Scan Rates

Fast heating rates create thermal lag effects within the sample according to the sample mass. The samples used in FDSC are very small to assist with reducing effects of thermal lag. It is essential to know the thermal lag experienced at all scanning rates and must be accounted for when analysing results.

Previous literature demonstrates that faster scanning rates result in greater thermal gradients within a sample (Scheirs, 2000). These thermal gradients cause the sample

temperature to lag behind the experimental temperature, impacting the results. The sample is heated from the base via the sensor and cooling is achieved using a cooled inert purge gas surrounding the sensor (Figure 5-15). Temperature gradients occur through the height of a sample and consequently possess greater thermal lag. Larger samples may have a greater height, increasing the temperature gradients and thus thermal lag.

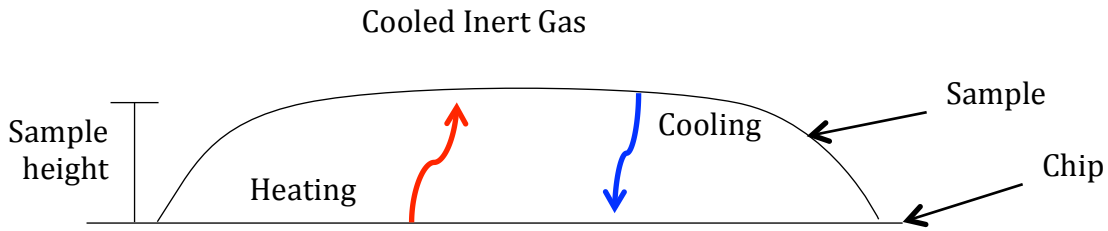

Figure 5-15 - The mechanism of sample heating (via chip sensor) and cooling (via purge gas)

Four samples with mass between 300 and 3,000 ng were used to provide results over a range of masses. The active heating area on the chip sensor limits the sample mass to a maximum of ~3,000 ng. If a sample is outside the active heating area, lateral thermal gradients in addition to vertical gradients will be present, increasing thermal lag effects.

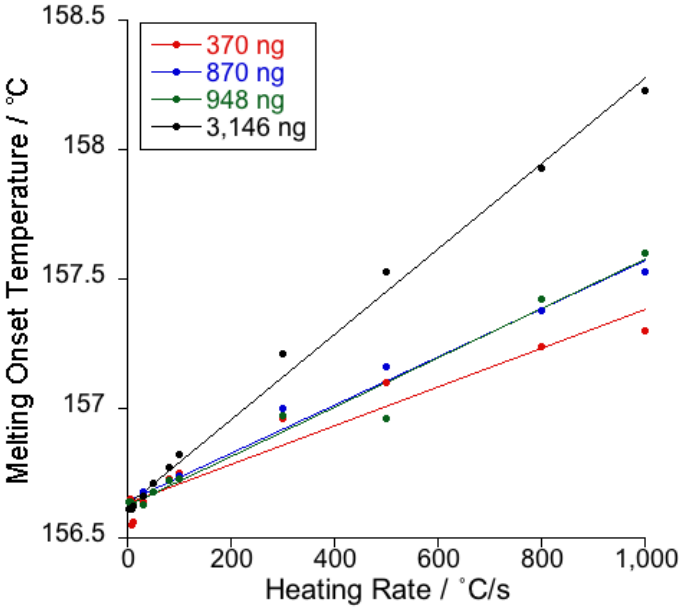

Figure 5-16 - The influence of heating rate and sample mass on the melting onset temperature of indium

The results in Figure 5-16 and Table 5-4 show an increase in the onset of melting with all sample masses as a function of heating rate. As sample mass increases, the amount of thermal lag experienced by the sample increases due to thermal gradients in the sample. The sample mass for FDSC is in the order of 10^5 times smaller than CDSC. This results in an appreciable presence of thermal lag with the increase in scanning rates. The onset of melting can be calculated according to sample mass and heating rate using Equation 5-7.

$$T_{m\,corr} = T_{m\,OBSV} - \left(6.7402\times10^{-4} + (3.1583\times10^{-7}\times m)\right)\beta$$

Equation 5-7

where T_{mOBSV} and $T_{m\ corr}$ are the observed and corrected melting temperatures, respectively, β is the heating rate (°C/s) and m is the mass of the FDSC sample (ng).

Table 5-4 - The melting onset temperature with heating rate and sample mass

Mass (ng) / Heating Rate / ˚C/s	~370	~870	~950	~3150
1	156.59	158.56	156.45	157.05
3	156.82	158.7	156.67	157.1
5	156.73	158.72	156.67	157.1
8	156.63	158.72	156.65	157.1
10	156.64	158.71	156.66	157.11
30	156.72	158.77	156.66	157.15
50	156.76	158.77	156.71	157.2
80	156.81	158.81	156.75	157.26
100	156.83	158.83	156.76	157.31
300	157.04	159.09	157	157.7
500	157.18	159.25	156.99	158.02
800	157.32	159.47	157.45	158.42
1,000	157.38	159.62	157.63	158.72
Thermal Lag (˚C) at 1,000˚C/s.	0.8	1.1	1.2	1.7

5.3.5 Validating the Melting Temperature Onset Correction

To assess the calibration from the previous samples, a new sample of indium (mass, ~66 ng) was prepared. Heating rates between 1 and 1,000˚C/s were applied to check the thermal lag correction (Equation 5-7). Table 5-4 shows the experimental onset T_m of the sample. The maximum variation of the onset T_m using Equation 5-7 was 0.2˚C. The small differences observed can be attributed to sample position and geometry. The findings of Poel *et al.* (2012) show the thermal lag at 1,000˚C/s with a sample mass of 50-500 ng varies by 0.2˚C. Thus, these results reveal that the thermal lag in a ~66 ng sample exhibits a similar degree of error to the previously tested ~300 ng indium samples.

Table 5-5 - Check of mass and scanning rate calibration

Heating Rate / ˚C/s	66 ng sample Melt Onset / ˚C	Adjusted Melt Onset / ˚C	Corrected Onset T_m from Equation 5-7 / ˚C (± 0.03)
0	156.64	156.60	156.60
1	156.68	156.64	156.60
3	156.74	156.7	156.60
5	156.72	156.68	156.60
8	156.71	156.67	156.61
10	156.73	156.69	156.61
30	156.79	156.75	156.62
50	156.81	156.77	156.63
80	156.86	156.82	156.66
100	156.87	156.87	156.67
300	157.03	156.03	156.81
500	157.15	157.11	156.94
800	157.34	157.30	157.16
1,000	157.50	157.46	157.39

5.4 Thermal Lag Adjustment

The thermal lag determined by measurements with an indium sample was used to shift all the data in this study. This enabled the analysis of data at a zero heating rate. The shifting of recorded data can be adjusted following the extraction of the raw results.

These methods have been employed previously by Salmerón Sánchez *et al.* (2007) using a HyperDSC™ when looking at a variety of heating rates. Thermal lag adjustments have not previously been applied to other differential scanning calorimetry (DSC) techniques because thermal lag is minimal across the available scanning rates in comparison to the FDSC.

Thermal lag correction enables more accurate data analysis and visual normalisation of the data (see Section 3.4.2.4). The phase transition that is taken into account during calibration was the melting onset temperature. It is considered acceptable, when analysing polymers, to record the T_m from the peak of the endotherm; peak melting temperature (see Section 4.3.2.2).

The thermal lag adjustment for the peak T_m was calculated using three different mass samples of indium. Heating rates from 1 to 1,000˚C/s were applied using the method described in Figure 5-12. The peak T_m for all indium samples is shown in Figure 5-17. Two distinct linear regions are observed, splitting the thermal lag shift factor. Heating rates at 100˚C/s and slower are represented by the thermal lag correction shown in Equation 5-8. The thermal lag correction for heating rates at 300˚C/s and above is shown in Equation 5-9.

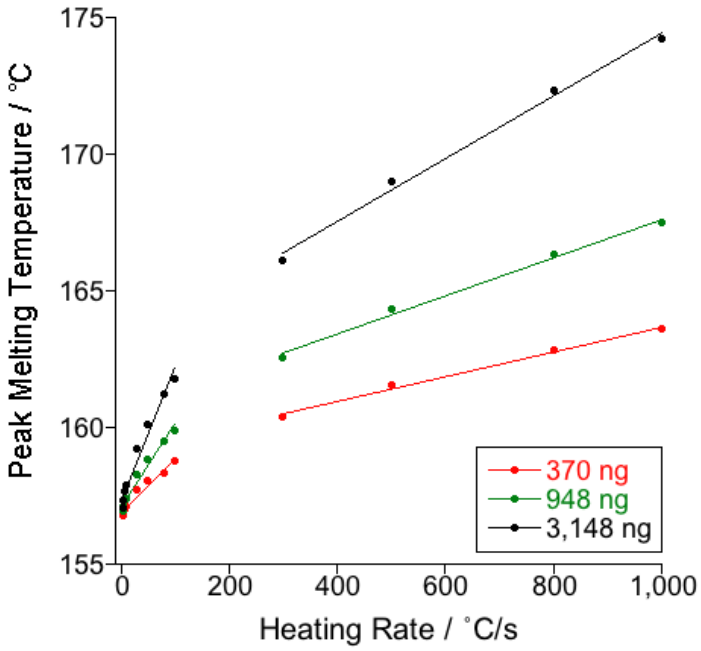

Figure 5-17 - The influence of heating rate and sample mass on the peak melting temperature of indium

$$T_{m\,Corr} = T_{m\,OBSV} - (0.66 + (1.47\times10^{-4}\times m) + (1.977\times10^{-2} + (9.3496\times10^{-6}\times m)))\beta$$

Equation 5-8

$$T_{m\,Corr} = T_{m\,OBSV} - (3.44 + (1.2613\times10^{-3}\times m) + (4.0896\times10^{-3} + (2.4\times10^{-6}\times m)))\beta$$

Equation 5-9

where T_{mOBSV} and $T_{m\ corr}$ are the observed and corrected melting temperatures, respectively, β is the heating rate (°C/s) and m is the mass of the FDSC sample (ng).

Thermal lag corrections have previously been measured using the linear regression suggested by Poel *et al.* (2012), however, it is not known (without further experimental data) if a linear change is valid at scanning rates in excess of 1,000°C/s. The FDSC has the capacity heat up to 20,000°C/s and thus a correction factor should incorporate scanning rates within this range. Figure 5-18 shows the peak melting temperature of indium

measured during heating between 1,000 and 15,000˚C/s. A non-linear regression in the peak T_m can be observed and thus a more appropriate correction should be carried out. It was not possible to construct a thermal lag correction equation including sample mass and heating rate, thus, indium samples of similar mass to polymer samples used in this study were recorded to enable thermal lag correction.

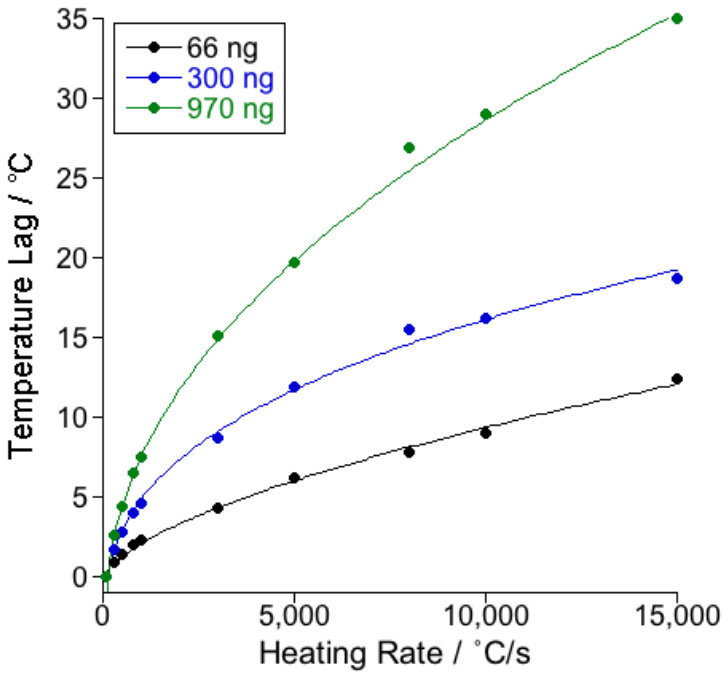

Figure 5-18 - The influence of heating rate up to 15,000˚C/s and sample mass on the peak melting temperature of indium

Equation 5-10, Equation 5-11 and Equation 5-12 show thermal lag correction factors (calculated from the data fit in Figure 5-18) for samples with approximate mass 66, 300 and 970 ng respectively.

$$T_{m\,Corr} = T_{m\,OBSV} - (0.032654 \times \beta^{0.61687} - 0.21134)$$

Equation 5-10

$$T_{m\,Corr} = T_{m\,OBSV} - (0.84443 \times \beta^{0.34668} - 4.4282)$$

Equation 5-11

$$T_{m\,Corr} = T_{m\,OBSV} - (0.46511 \times \beta^{0.46081} - 3.7613)$$

Equation 5-12

The T_g is not taken into account when evaluating thermal lag, unless a fully amorphous sample is tested. The adjustment of the entire trace to lower temperatures as a result of the thermal lag of $T_{m\ PEAK}$ could cause an incorrect evaluation of T_g. Further work exploring the thermal conductivity of polymers across the T_g is shown in Chapter 9. The use of a correction factor is currently the best solution to adjust for thermal lag and has been used by Salmerón Sánchez *et al.* (2007) and Poel *et al.* (2012).

5.4.1 Symmetry

The correction factors have been calculated with respect to melting peak temperatures and it is important to determine the symmetry of measurements during cooling. A sample of indium (~mass, 948 ng) was loaded onto a new chip sensor membrane and subjected to the method shown in Figure 5-12 from 300 to 1,000˚C/s. Figure 5-19 shows the peak melting temperature shift is equal to peak crystallisation temperature shift. This symmetry in the data allows for Equation 5-9 to be applied to both heating and

cooling on FDSC. A more detailed symmetry analysis was not required as crystallisation during cooling can be difficult to observe using FDSC, thus predominantly a correction is required during heating.

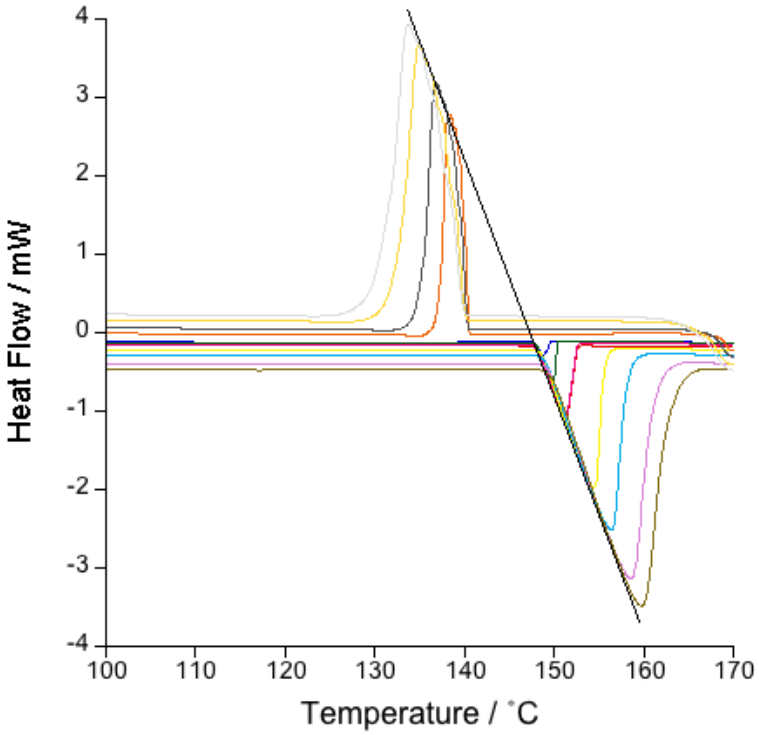

Figure 5-19 - The peak melting and crystallisation temperature symmetry during heating and cooling of indium

5.5 Half-life Variation with Flash DSC Sample Mass

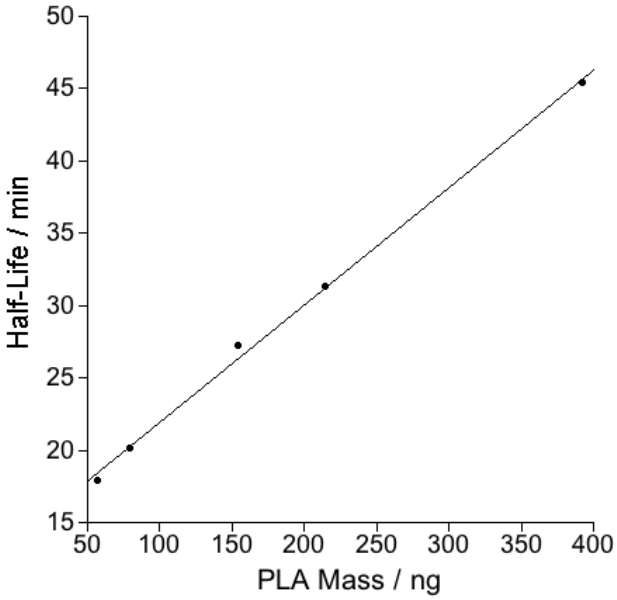

Figure 5-20 - The crystallisation half-life of PLA as a function of sample mass

Figure 5-20 shows a linear relationship of mass with crystallisation half-life ($t_{½}$). Half-life was calculated from isothermal crystallisation of PLA at 95˚C over a time interval range from 5 to 360 min. To maintain accuracy of data, the same chip sensor was used for all samples; additional material was melted into the initial sample to increase the total mass. Five sample masses were tested ranging from ~56.5 to ~400 ng. The half-life was acquired from half relative crystallinity (shown in Figure 5-21).

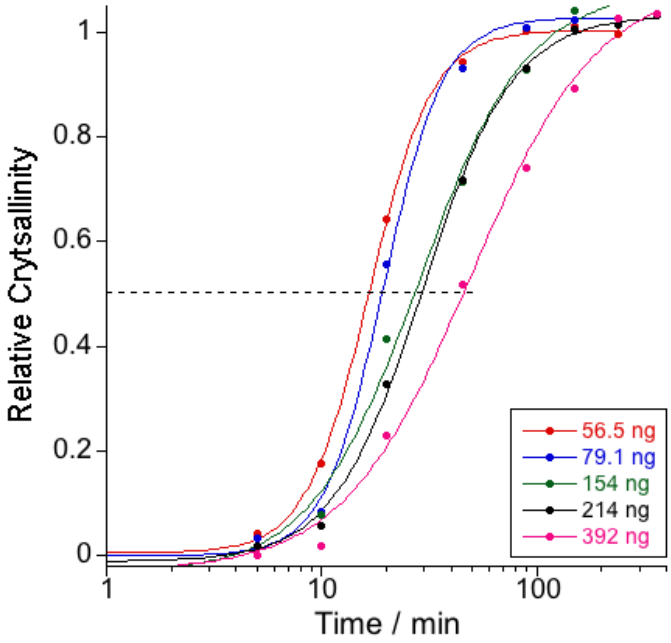

Figure 5-21 - The relative crystallinity of PLA against time with varied sample mass

Larger samples show greater thermal lag compared to smaller samples. Thus, smaller samples are equalised to the isothermal crystallisation temperature after a shorter period of time. However, thermal lag would cause a delay less than a second, not minutes; thus thermal lag can be excluded from the variation in half-life.

FDSC sample mass is so small that the sample surface causes an increased effect upon crystal nucleation. Surface nucleation requires lower activation energy to form stable nuclei in comparison to homogeneous nucleation. It has been described by Zhuravlev *et al.* (2011) that heterogeneous nucleation occurs on the sample surface prior to homogeneous nucleation developing within the sample volume. PLA crystals are large, ~20 µm in radius; therefore, it can be important to know the sample radius in accordance to sample mass.

Table 5-6 - PLA half-life, radii and surface area to volume ratio with sample mass variation

Sample Mass / ng	Half-Life / min	Sample radius / µm	Volume / µm³	Surface Area / µm²	Surface Area to Volume Ratio
56.5	17.9	27.9	45,565	7,345	0.16120
79.1	20.2	31.2	63,790	9,192	0.14409
154.0	27.3	38.9	124,190	14,332	0.11540
214.0	31.3	43.5	172,580	17,847	0.10341
392.0	45.4	53.2	316,129	26,718	0.084516

Table 5-6 shows approximate sample radii, assuming that the sample, when located on the surface of the chip, is a hemi-sphere. The ~56.5 ng sample has a radius of 27.9 µm. This would allow approximately one crystal to grow before impingement. Heterogeneous nucleation occurs on the surface before homogenous nucleation occurs within the volume of the sample; therefore, it is possible that this sample may contain <5 crystals. In a very small sample it is possible that at high temperature, a single spherulite would fill the volume. At low temperature it would be expected that heterogeneous nucleation would occur at multiple points on the sample surface and impingement would occur after a limited degree of crystal growth. Impingement occurs shortly after growth in a smaller sample where crystal size and sample size are almost equal (Figure 5-22).

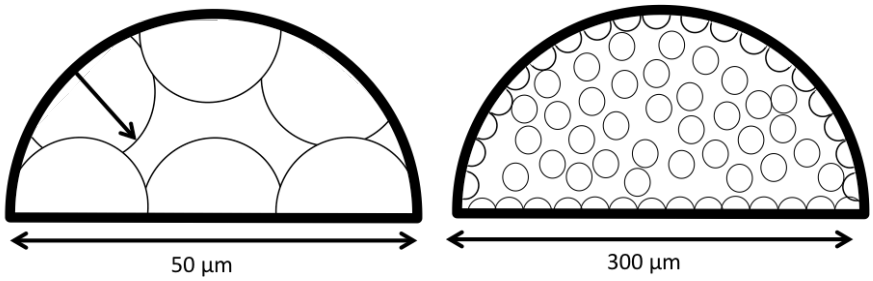

Figure 5-22 - An illustration of the sample size effects on crystal growth, impacting half-life

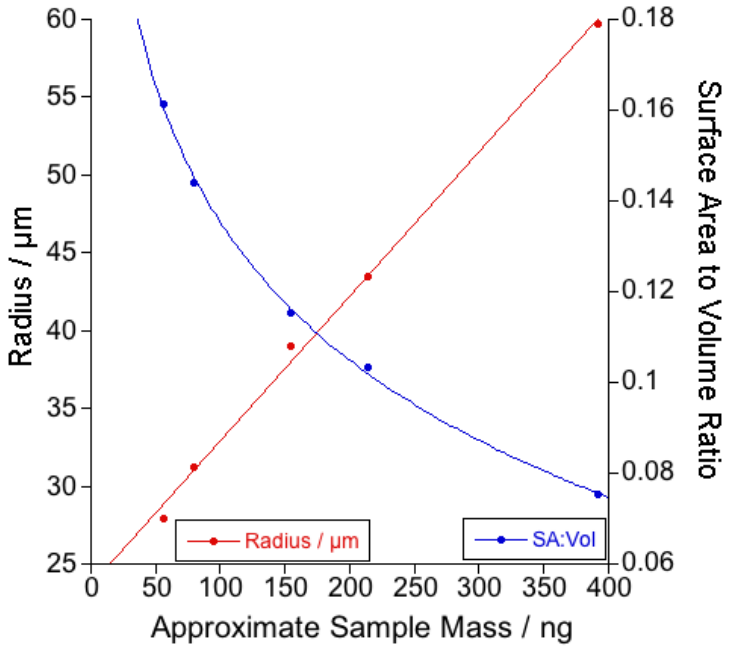

Figure 5-23 - The surface area to volume ratio and radius against PLA sample mass

Figure 5-23 shows a reduction in surface area to volume ratio with increased sample masses. Therefore, small samples on FDSC are expected to produce faster half-life values in comparison to CDSC half-life.

5.6 Conclusions

- FDSC chip sensors are subjected to two thermal calibration methods: conditioning and correction. Sample preparation and application can be carried out after sensor correction using a scalpel and synthetic hair
- FDSC sample mass estimation utilises the overlapping scanning rates on CDSC and FDSC ensuring percentage crystallinity is equal if cooling rate is identical
- Heating and cooling rate windows of operation are limited by purge gas but not purge gas rate. The window of operation is greater in cooling with nitrogen but smaller in heating compared to argon
- Indium sample onset of melting showed very good repeatability on the same sample and comparable results for a similar sample mass on a new chip. The repeatability was equal according to thermal lag effects on the onset of melting with heating rate from 1 to 1,000˚C/s
- Thermal lag correction equations were formulated for both melting onset and peak temperature from 1 to 1,000˚C and 1 to 15,000 respectively, to allow thermal lag effects to be eliminated
- Thermal lag effects are symmetrical in heating as well as cooling allowing the thermal lag correction equation to used in cooling
- Sample size influences the crystallisation half-life of PLA due to heterogeneous nucleation effects on the sample surface. Smaller samples therefore induce a faster crystallisation half-life in comparison to larger samples, where homogeneous nucleation within the sample volume is slow

CHAPTER 6 HIGH TEMPERATURE CRYSTALLISATION OF POLY(ε-CAPROLACTONE)

6.1 Introduction

This chapter aims to develop the work reported in the literature on poly(ε-caprolactone) (PCL) using Flash DSC (FDSC) (Zhuravlev *et al.*, 2011, Wurm *et al.*, 2012, Zhuravlev *et al.*, 2014). The beginning of the chapter investigates the heating and cooling rates required to prevent non-isothermal crystallisation of a different grade of PCL, CAPA 6800. These scanning rates will be used to explore isothermal crystallisation kinetics of PCL between 5 and 40˚C. The heat of fusion recorded from the single melting endotherm in this temperature range will be used to measure crystallisation kinetic analysis of PCL for the first time on FDSC with an Avrami and a Hoffman and Lauritzen analysis.

6.2 Non-Isothermal Crystallisation using Conventional DSC

Figure 6-1 shows that PCL exhibits a crystallisation exotherm during cooling (10˚C/min) from the melt, and subsequently followed on heating by a melting endotherm (10˚C/min). Faster cooling at 80˚C/min shifts the peak crystallisation temperature (T_c) from 22˚C to 5˚C. The crystallisation kinetics of PCL allows crystallisation of the sample during cooling at both 10˚C/min and at 80˚C/min. Heating at 10˚C/min after non-isothermal crystallisation during cooling at two different rates revealed near identical peak melting temperatures (T_m) at 56˚C. This indicates that the polymer is not

crystallising at a different temperature; the shift in T_c is related to thermal lag. Faster cooling results in increased thermal lag.

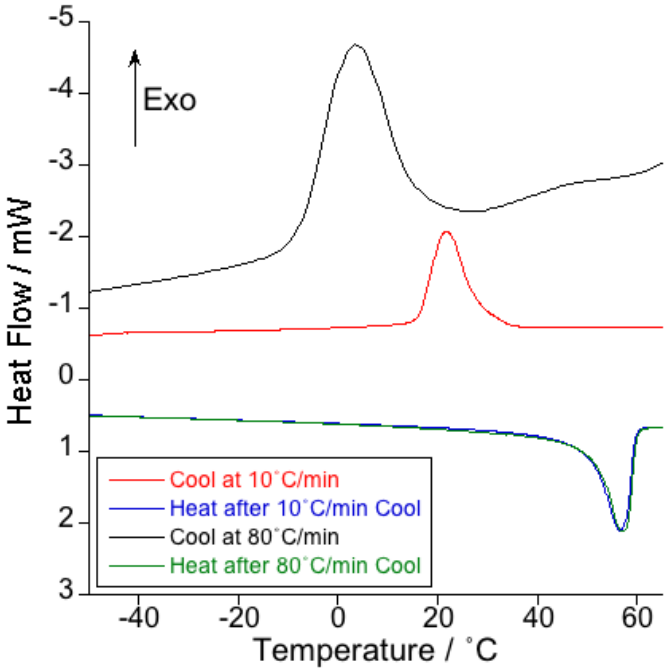

Figure 6-1 - The melting endotherms and crystallisation exotherms of PCL recorded using CDSC. Method: Heating at 10°C/min from -90 to 90°C before cooling from 90 to -90°C at 10 or 80°C/min followed by heating at 10 or 80°C/min fro -90 to 90°C

6.3 Non-Isothermal Crystallisation using Flash DSC

6.3.1 Preventing Crystallisation with Fast Scanning Calorimetry

Crystallisation occurs via a two-stage process; there is a nucleation event and growth of the resulting crystals. Nucleation occurs naturally (albeit slowly) during cooling from the melt if the adopted cooling rate is slow enough to allow chain entanglement and organisation. This nucleation process is termed 'homogeneous nucleation'. Nucleation will also occur during heating if the sample is amorphous below T_g. Overcoming the activation energy (E_a) barrier allows the development of nuclei, which in turn provides a

stable platform for crystal growth. Growth involves chain organisation and folding to form lamella, which are organised into spherulitic superstructures. Faster heating and cooling rates are capable of restricting crystallisation and if the rate is sufficiently rapid, preventing crystallisation.

6.3.1.1 Preventing Crystallisation during Heating

Unless the heating rate is sufficiently fast, cold crystallisation occurs during heating from amorphous PCL. It is clear from Figure 6-2 that crystallisation of amorphous PCL is prevented by adopting a heating rate of 7,500˚C/s. A flat trace demonstrates the prevention of crystallisation during heating. This has also been observed in PCL by Wurm *et al.* (2012) and Wang *et al.* (2015), however, rates of 18,000 and 10,000˚C/s respectively, were required to prevent crystallisation on heating. A higher molecular weight PCL grade was used in this study compared to the literature and thus did not require a cooling rate as fast to prevent crystallisation as longer chain length increases entanglement, preventing chain folding for lamella formation.

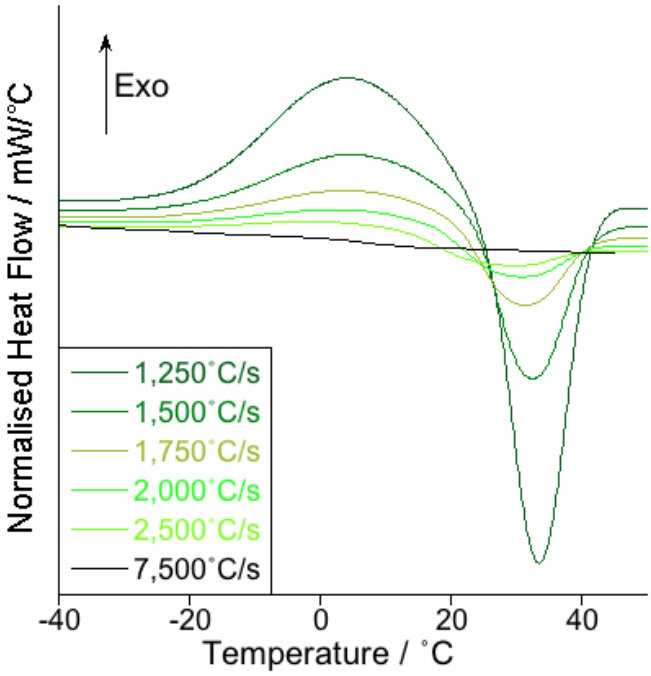

Figure 6-2 - Heating amorphous PCL ≥1,250°C/s after quench cooling at 5,000°C/s. Traces are normalised to heating rate[2] and corrected for thermal lag[3]. Method: Heating at 8,000°C/s from -90 to 100°C/s before cooling at 5,000°C/s and final heating (traces shown) between 1,250 and 7,500°C/s from -90 to 100°C

The area enclosed by the cold crystallisation exotherm (ΔH_{cc}) in Figure 6-2 increases in size with reduced heating rates. Consequently, there is also an increase in the area enclosed by the melting endotherm (ΔH_f). It is also apparent that the melting and crystallisation peak temperature is independent of heating rate.

Contradicting this, at heating rates less than 1,250°C/s a reduction in T_c is accompanied with an increase in T_m (Figure 6-3). As expected, at relatively slow heating rates (500-1,000°C/s), the crystallisation and melting processes become prominent. Closer inspection of the heating traces obtained for measurements less than 1,250°C/s revealed

[2] Heating rate normalisation provides comparison of the heating traces at a 0°C/s heating rate
[3] Thermal lag correction is applied when varied rates are used. Thermal lag adjustment has been made according to Equation 5-8.

two observations; the peak temperature for the cold-crystallisation increases with increasing heating rate and the corresponding T_m decreases with increasing heating rate. Elevated heating rates delay the onset of cold crystallisation, however, according to the Gibbs-Thomson equation (Equation 6-1), T_m is related to crystal stability and therefore, crystallisation at higher temperature increases lamella thickness and melting of corresponding lamella occurs at increased temperatures. The results are therefore, counter-intuitive as crystallisation at an elevated temperature usually results in an elevated melting point.

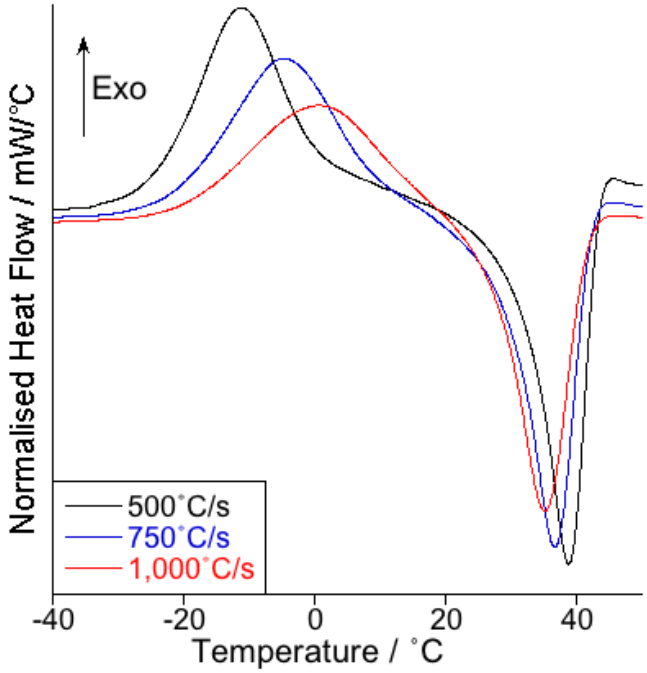

Figure 6-3 - Heating amorphous PCL <1,250°C/s after a quench cool at 5,000°C/s. Traces are normalised to heating rate[2] and corrected for thermal lag[3]. Method: Heating at 8,000°C/s from -90 to 100°C/s before cooling at 5,000°C/s from 100 to -90°C and heating (traces shown) between 500 and 1,000°C/s from -90 to 100°C

This behaviour is expected to occur from a series of undistinguishable multiple melting and crystallisation processes, occurring between the main cold crystallisation exotherm and the main melting endotherm, to increase the stability of the crystal as polymer

chains gain thermal energy permits with temperature. The resolution of simultaneous endothermic and exothermic reactions is not possible through calorimetry but a schematic in Figure 6-4 shows the continual cold crystallisation and melting that is predicted to be the cause of the elevated melting temperature.

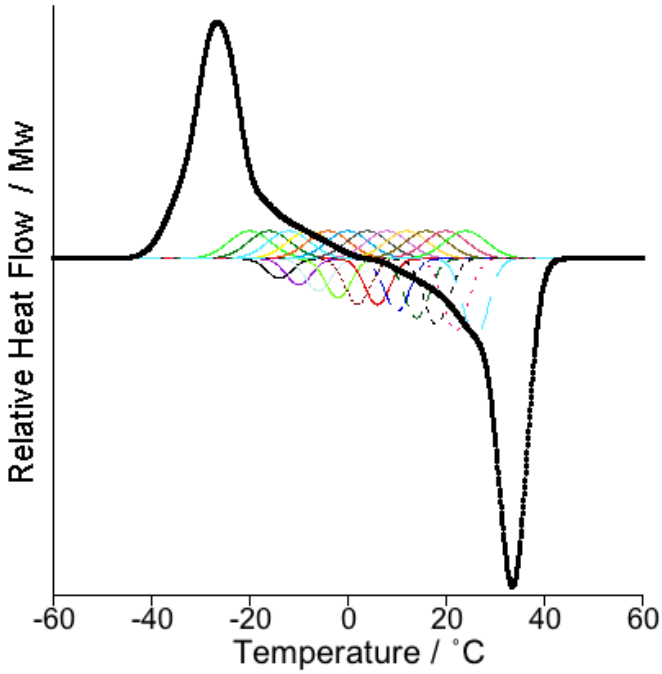

Figure 6-4 - Schematic of multiple melting and crystallisation during heating causing an elevated melting

$$T_m = T_m^0\left(1 - \frac{2\sigma_e}{\Delta H_f l}\right)$$

Equation 6-1

$$l = \frac{2\sigma_e}{\Delta H_f\left(1 - \frac{T_m}{T_m^0}\right)}$$

Equation 6-2

In addition to the reduction in peak T_c with slower heating rates, the crystallisation onset temperature also falls. Note, that a thermal lag correction has been made and can

therefore be eliminated from the interpretation. Nucleation rate is greatest at temperatures close to T_g and subsequent slow heating rates increase the time available for nuclei to form and therefore, growth can begin at lower temperatures. The reduction in peak crystallisation and onset temperature was also found by Wurm *et al.* (2012).

6.3.1.2 Cooling to Prevent Crystallisation

Figure 6-5 shows that as the cooling rate approaches 1,000˚C/s, the crystallisation exotherm reduces to a flat trace at 850˚C/s. This reduction is consistent with the assumption that crystallisation on cooling is being prevented. Additionally, the peak T_c falls with increased cooling rate due to the delayed onset of crystallisation. Faster heating rates reduce the time for nucleation; therefore, growth occurs at lower temperatures. Another relevant observation is the increased prominence of T_g with cooling rate. The increased step in T_g is consistent with the prevention of crystallisation; as the degree of crystallinity decreases, the amorphous fraction increases, accompanied with an increased change in specific heat capacity (ΔC_p)[4].

[4] The measurement of ΔC_p could not be obtained due to the unavoidable acceleration period of the FDSC to the programmed rate preventing a flat baseline at T_g.

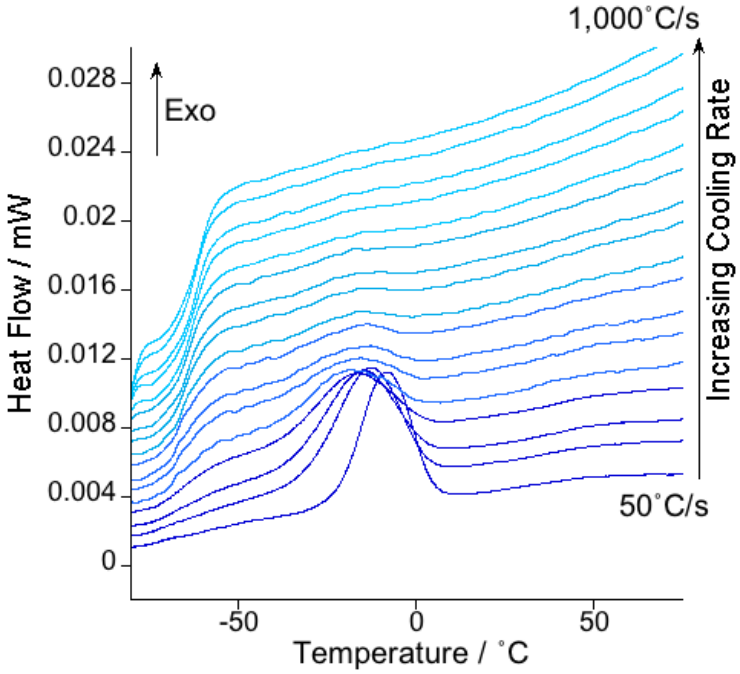

Figure 6-5 - The reduction in the exothermic crystallisation peak during cooling as cooling rate is increased from 50 to 1,000˚C/s. Method: Heating at 8,000˚C/s from -90 to 100˚C before cooling (traces shown) between 50 and 1,000˚C/s from 100 to -90˚C

The reduction in the crystallisation exotherm as cooling rate increases (Figure 6-5) corresponds to a reduction in the melting endotherm on subsequent heating (Figure 6-6). The endotherm was prevented on heating after being subjected to a cooling rate of 800˚C/s, agreeing with the inhibition of the exotherm in Figure 6-5. Cooling rates of 50 and 100˚C/s show a small step in T_g on heating. A large step in T_g is present following cooling rates in excess of 100˚C/s due to a significant increase in amorphous fraction. A small melting endotherm is detected on heating, in conjunction with a large step in T_g, after cooling at 300 and 500 ˚C/s. Work carried out by Wurm *et al.* (2012) found similar results with fast cooling on PCL where small molecules are suggested to be present, influencing a large step in T_g with a detectable endotherm.

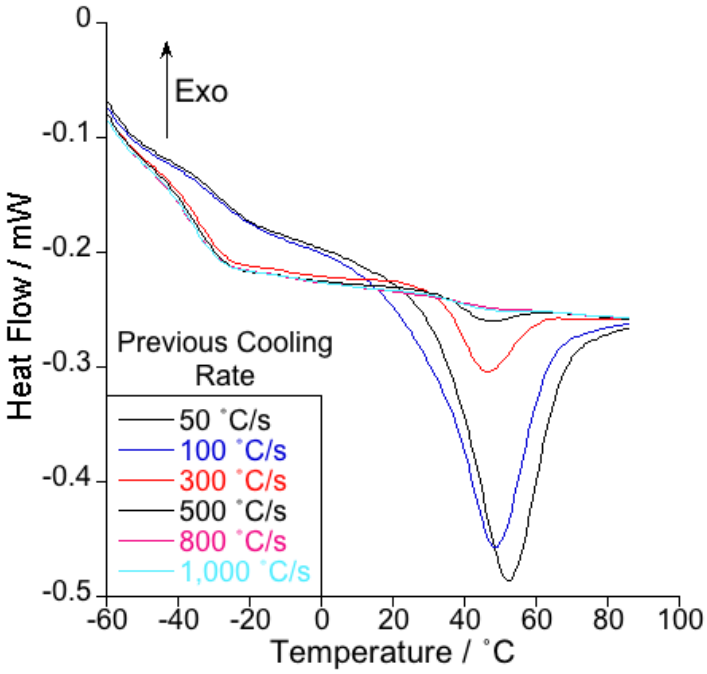

Figure 6-6 - The reduction in the melting endotherm during heating as cooling rate preceding heating is increased. Method: Heating at 8,000˚C/s from -90 to 100˚C before cooling between 50 and 1,000˚C/s from 100 to -90˚C and final heating (traces shown) at 8,000˚C/s from -90 to 90˚C

The key finding in the FDSC scanning rate experiments show that the rate required to prevent crystallisation on heating is 7,500˚C/s and the rate required to prevent crystallisation on cooling, 800˚C/s. Therefore, to ensure the crystallisation process is prevented, on heating a rate of 8,000˚C/s and a rate of 3,000˚C/s on cooling will be employed in the work following on PCL.

6.4 High Temperature Crystallisation of Poly(ε-caprolactone)

In Figure 6-7, the melting region demonstrates an increased T_m compared to PCL on CDSC due to thermal lag. The size of the melting endotherm increased with isothermal crystallisation time at T_c presenting evidence of the development of crystal structures. The peak T_m increases with increased time at T_c suggesting the development of lamella thickening through secondary crystallisation. The measure of an isothermal

crystallisation exotherm (ΔH_c) during isothermal crystallisation was not possible due to the small sample size minimising the visible heat flow. Heat flow during isothermal crystallisation with time has not been observed in other FDSC studies on PCL due to the small sample size required (Zhuravlev *et al.*, 2011, Wurm *et al.*, 2012). To measure isothermal crystallisation, the sample was exposed to a series of isothermal crystallisation times and the heat flow resulting from the melting endotherm (ΔH_f) was recorded.

The baseline of the FDSC trace in Figure 6-7 shows a step at -40°C. This is assumed to be T_g and appears at an elevated temperature in comparison to CDSC due to thermal lag. The step at T_g decreases with increased crystallisation time at T_c, consistent with an increase in crystallinity.

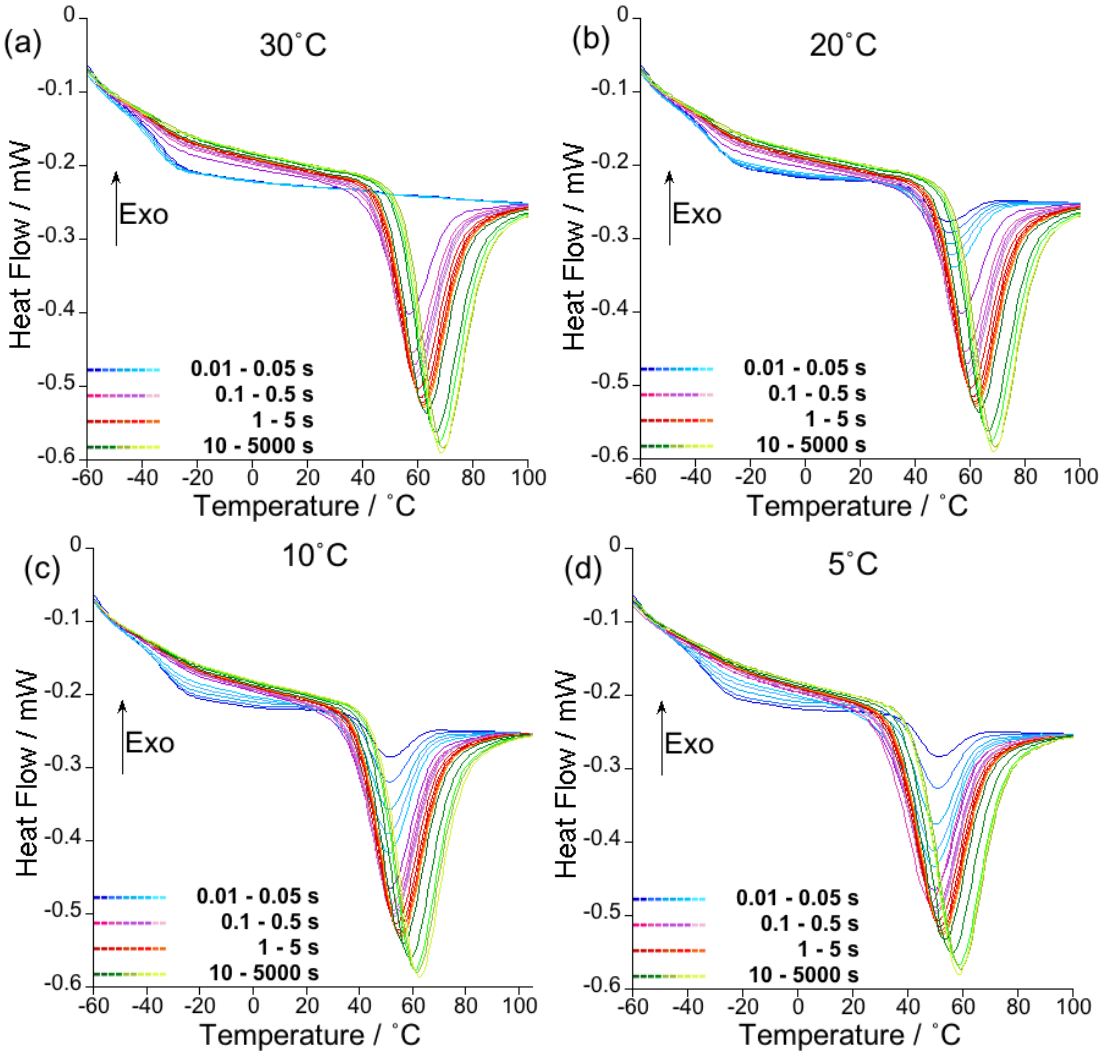

Figure 6-7 - Isothermal crystallisation of PCL at (a) 30˚C (b) 20˚C (c) 10˚C (d) 5˚C. Method: Heating at 8,000˚C/s from -90˚C to 100˚C before cooling at 3,000˚C/s from 100˚C to T_c and held for 0.01-5,000 seconds. Cooling at 3,000˚C/s from T_c to -90˚C before a final heating (traces shown) at 8,000˚C/s from -90 to 100˚C

In contrast to measuring crystallisation with time, ΔH_f increases continually with time demonstrating secondary crystallisation (Figure 6-8). It is important for further kinetic analysis that that the primary and secondary stages can be decoupled. A value of H_∞ was proposed by Sharples (1966) after secondary crystallisation was observed in polyethylene (PE) using a dilatometer. Sharples quoted that '*choosing an appropriate value of H_∞ in cases where secondary crystallisation constitutes a significant fraction of the total, is an arbitrary procedure which is likely to reduce the accuracy of the analysis,*

especially in the final stages of primary crystallisation'. It is therefore important to apply a more consistent method of determining a value of H_∞.

Figure 6-8 shows the increase in ΔH_f with time at T_c. Two distinct regions are apparent: the first is linear up to the time point of 0.07 seconds (log -1.15 seconds) reflecting primary crystallisation. A second linear region then dominates over this primary stage of crystallisation, showing a linear dependence with log time. The linear section can be explained in terms of secondary crystallisation, which is also consistent with the increase in T_m shown in Figure 6-7. Previous work has claimed that the secondary crystallisation process has a logarithmic dependence on time (Bassett and Carder, 1973). The linear region in Figure 6-8 is consistent with this dependence, indicating primary and secondary crystallisation regions can be defined by the intersection of the tangents in Figure 6-8. This intersection is recorded as H_∞ providing consistent data analysis of the primary crystallisation region.

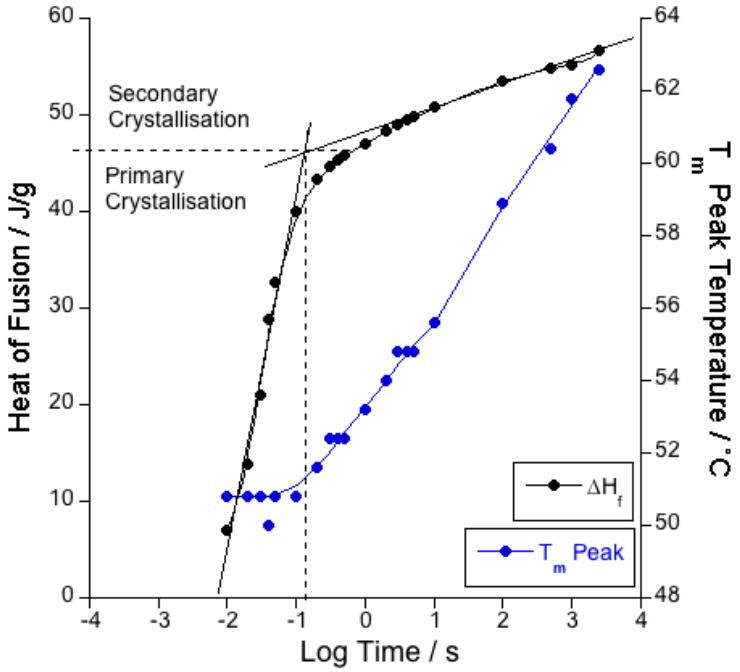

Figure 6-8 - The heat of fusion and peak T_m of PCL with log time after isothermal crystallisation at 5˚C for varied times between 0.01 and 5,000 s

The variation of T_m with crystallisation time shows two regions, supporting the idea that secondary crystallisation is occurring in the latter stages of the process. The increase in the peak T_m corresponds to the intersection of the tangents to the primary and secondary crystallisation regions (Figure 6-8). The secondary crystallisation region, where lamella thickening occurs, originates at a similar time to increased peak T_m during isothermal crystallisation at 10˚C. At higher isothermal crystallisation temperatures it is predicted that the secondary crystallisation process contributes to an increase in T_m during the primary crystallisation stage presenting a continual increase of T_m with log time. The overlap of the primary and secondary crystallisation processes has been recently seen in PCL and PEEK (Phillipson *et al.*, 2016, Al Lafi and Hay, 2017).

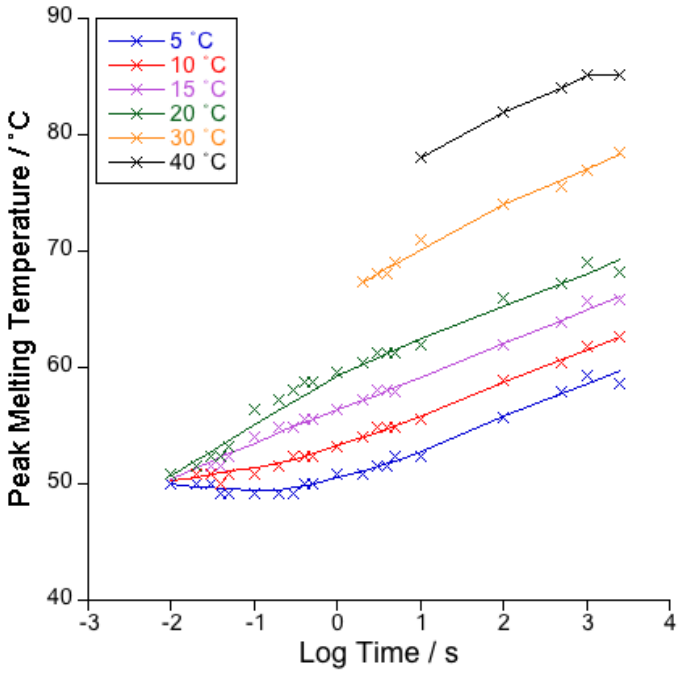

Figure 6-9 - The peak melting temperature of PCL as a function of log time with isothermal hold temperature between 5 and 40°C[5]

In this section, the presence of a single endotherm, increasing with crystallisation time and temperature demonstrates, the formation of stable crystal growth in the temperature range: 5-40°C. The end of the primary crystallisation process and the start of the secondary crystallisation process is indicated by the intersection of the tangents to the sigmoidal curve of heat of fusion with time (see Figure 6-8).

6.4.1 Avrami Analysis of PCL Hot Crystallisation

Given that the primary crystallisation process is commonly analysed using an Avrami approach, to enable the analysis, the secondary stage of the process was decoupled from the primary stage to yield a primary limited data set. The primary stage was decoupled using the intersection of the tangents to the primary and secondary crystallisation region. The ΔH_f at the intersection, H_∞, indicates the end of the primary crystallisation

[5] Heating traces after crystallisation at 15 and 40°C are shown in the appendix

region and a relative crystallinity of 1. Figure 6-10 shows the primary limited crystallisation decoupled from the secondary data.

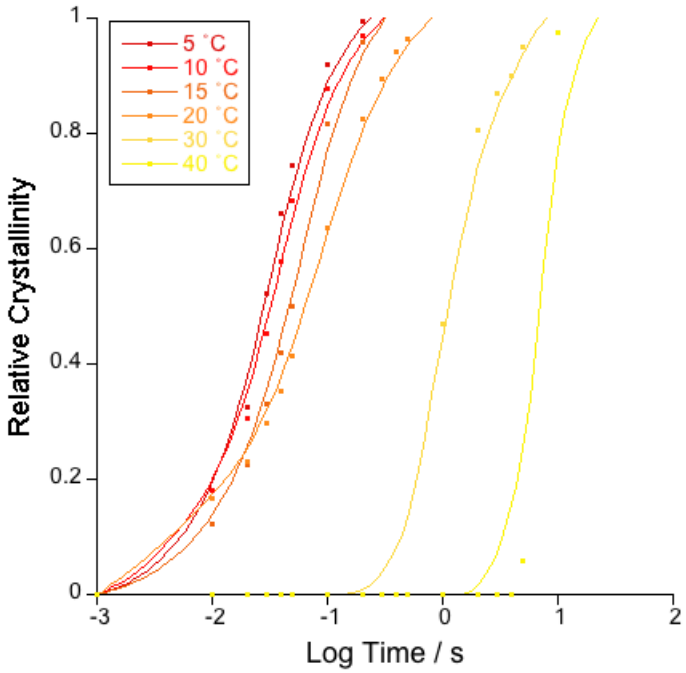

Figure 6-10 - Relative crystallinity of PCL showing the primary limited crystallisation region

Subjecting the data in Figure 6-10 to an Avrami analysis yields the Avrami plot shown in Figure 6-11. Linear regression of this data produced kinetic parameters shown in Table 6-1.

Table 6-1 - Avrami Parameters for PCL using FDSC

T_c / ˚C	n	Log K / min^{-n}	$t_{½}$ / s
5	1.1	1.3	0.048
10	1.0	1.1	0.055
15	1.1	1.0	0.078
20	0.8	0.6	0.10
30	1.4	-0.6	1.92
40	1.8	-3.0	39.3

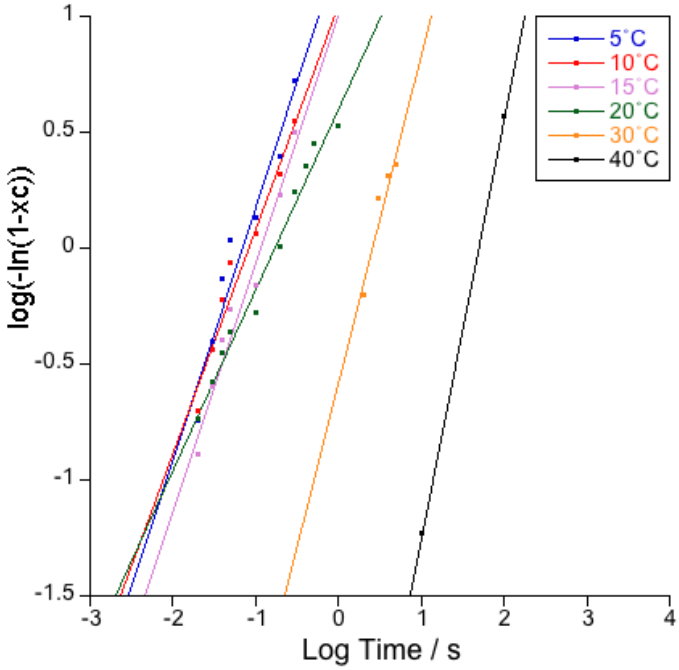

Figure 6-11 - PCL Avrami plot of log(-ln(1-Xc)) against log time

The Avrami exponent 'n' for temperatures up to 30˚C suggests spontaneous growth of rod like crystals. This growth is suggested to occur due to rapid heterogeneous nucleation on the surface of the chip and fast growth kinetics within a small sample (Sharples, 1966). An 'n' value of 1.8 at a T_c of 40˚C suggests a two-dimensional disc-like

crystal structure due to the reduction in the rate of crystal growth, a disc-like crystal structure can form. However, caution should be exercised since the Avrami equation assumes integer values for 'n' (Avrami, 1940).

The calculation of Avrami parameters has not been previously determined using FDSC and it must be mentioned that sample size and shape are expected to introduce variability in the crystallisation process. One of the main sources of variability is the sample geometry. The small sample mass is influenced by the surface area to volume ratio due to significant heterogeneous surface nucleation effects described by Zhuravlev *et al.* (2011) in PCL. An approximate sample mass of 16 ng results in a large surface area to volume ratio. Rapid surface nucleation reduces the time for crystal propagation and growth before impingement onto another crystal structure.

Half-life values were calculated using Equation 6-3 and the Avrami parameters shown in Table 6-1. Elevated T_c results in an increased crystallisation half-life. Rapid half-life is attributed to the sample geometry used on FDSC. A half-life of 3.48 minutes was determined by Jenkins and Harrison (2006) with an identical grade of PCL using CDSC during high temperature isothermal crystallisation at 42˚C. The crystallisation half-life shows good agreement with other work carried out on PCL using FDSC. Exact half-time values were not provided by Zhuravlev *et al.* (2015), however, graphical data provides evidence of a half-time of the same magnitude.

$$\boldsymbol{t_{\frac{1}{2}} = \left(\frac{ln2}{k}\right)^{1/n}}$$

Equation 6-3

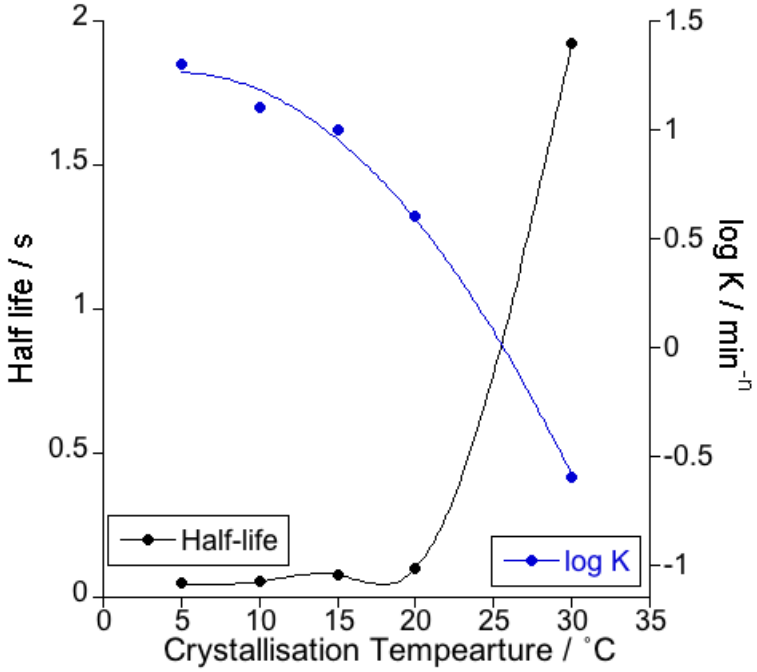

Figure 6-12 - The variation of half-life and log K as a function of crystallisation temperature in PCL

Figure 6-12 illustrates the variation of half-life ($t_{½}$) and rate constant (log k) as a function of T_c. T_c was used as a function of the $t_{½}$ and log *K* plot to provide a comparison of the data at the same thermodynamic driving force (Wunderlich, 1976). The plot shows an increase in $t_{½}$ opposed by a decrease in log *K* with increasing T_c as reported in other semi-crystalline polymer literature (Cebe and Hong, 1986, Jenkins, 2001).

6.4.2 Nucleation Constant and Surface Free Energy

Modifying the Hoffman-Lauritzen equation (Equation 1-8), by replacing the growth rate with the reciprocal of the half-life of crystallisation, the nucleation constant (K_g) can be determined from the gradient of the linear plot: $(In(1/t½)+(U^*/R(T_c - T_\infty))$ against $1/(T_c\Delta Tf)$.

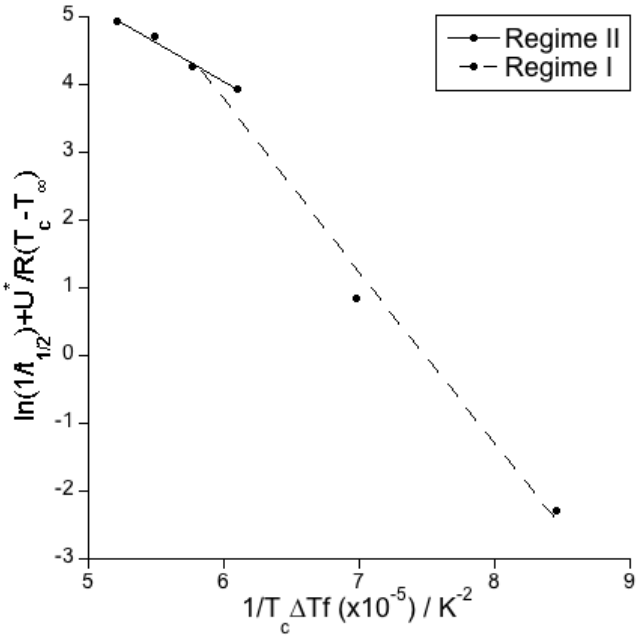

Figure 6-13 - A Hoffman-Lauritzen plot for PCL

Figure 6-13 shows two linear regions where a change in slope defines a change in nucleation regime as described by Hoffman and Lauritzen (1961). An increase in $1/(T_c\Delta Tf)$ shows a decrease in the slope, suggesting a shift from Regime II to Regime I with temperature rise. Accessible crystallisation temperatures (45-50˚C) have been used to calculate K_g in previous literature where Regime II has been suggested (Chen and Woo, 2008, Trujillo *et al.*, 2012). However, the T_c range shown in this work has not previously been attainable without the use of FDSC. Consequently, the gradient shift in this work specifies a K_g value of 1.1508×10^{-5} and 2.5331×10^{-5} K^2, representing Regime II to Regime I respectively.

6.5 Cold Crystallisation

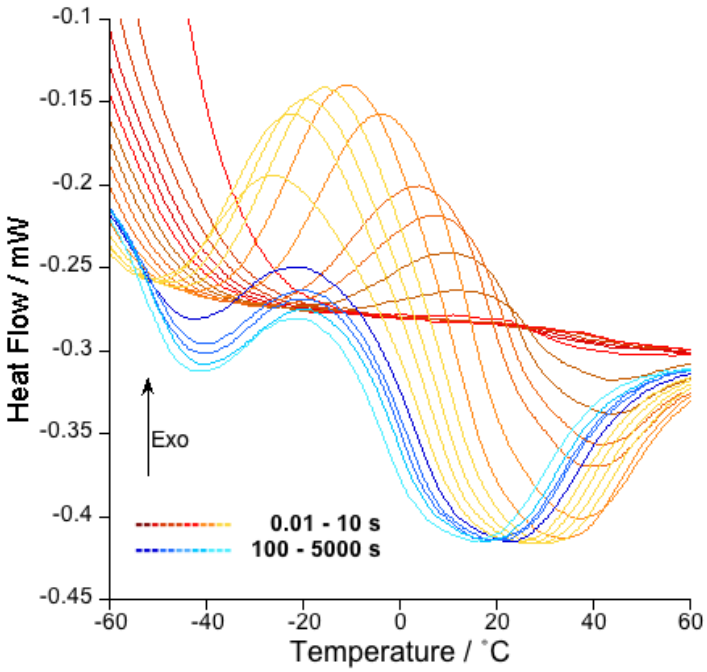

Figure 6-14 - The heating traces following isothermal crystallisation of PCL at -56˚C with varied crystallisation time. Method: Heat at 8,000˚C/s from -90 to 100˚C, cooling at 3,000˚C/s to -56˚C before an isothermal hold between 0.01 to 5,000 seconds; cooling at 3,000˚C from -56˚C to -90˚C before heating (traces shown) from -90 to 100˚C at 8,000˚C/s

Figure 6-14 shows double melting on heating following isothermal crystallisation at a temperature close to T_g, -56˚C. A crystallisation time of 100 to 5,000 seconds shows the development, and increase in area, of a low temperature endotherm. No change in peak temperature represents the growth of crystals at the isothermal crystallisation temperature, according to the results obtained in Figure 6-8. After a crystallisation time of 100 seconds, an exotherm is visible at a temperature between the two melting endotherms (dark blue trace). The exotherm displays the heat produced due to recrystallisation of PCL from remaining order from crystals melted at -40˚C. Heating at a rate of 8,000˚C/s (shown in Figure 6-2) inhibits crystallisation on heating from an amorphous material. However, this rate was not fast enough to prevent the

crystallisation during heating after melting unstable crystals grown close to Tg, seen as a double endotherm enclosing an exothermic peak in Figure 6-14. This rapid crystal growth from remaining nucleation sites was reported many years ago by Wood and Bekkedahl (1946).

6.5.1 Preventing Recrystallisation on Heating using Fast Heating Rates

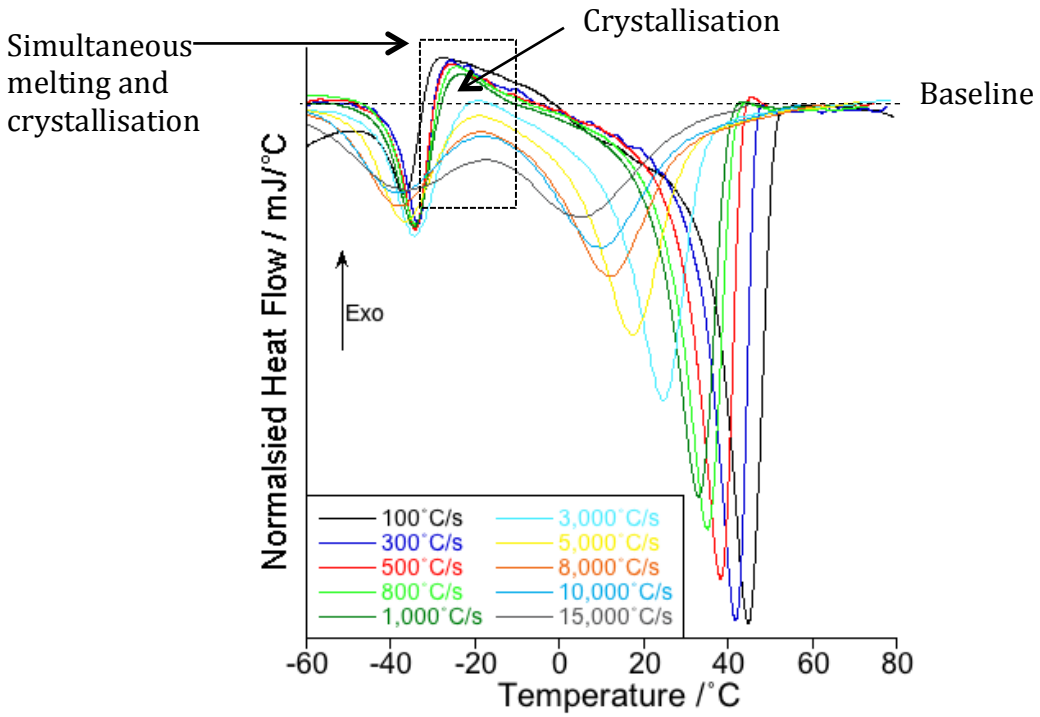

Figure 6-15 - The reduction in the upper melting endotherm after isothermal crystallisation at -56˚C using elevated heating rates up to 15,000 ˚C/s. Method: Heating at 8,000˚C/s from -90˚C to 100˚C before cooling at 3,000˚C/s from 100˚C to T_c and held for 5,000 seconds. Cooling at 3,000˚C/s from T_c to -90˚C before a final heating (traces shown) at 8,000˚C/s from -90 to 100˚C[6,7]

Figure 6-15 shows double melting on heating at rates up to 15,000˚C/s. The low temperature endotherm does not change position as heating rate is increased. The

[6] Heating rate normalisation provides comparison of the heating traces at a 0˚C/s heating rate
[7] A thermal lag adjustment has been made according to Equation 5-8.

isolation of the low temperature endotherm occurs due to heating rate having no effect on isothermally formed crystals. Fast heating decreases the time per unit temperature for non-isothermal crystallisation to occur on heating. A reduction in the size and location of the upper endotherm was observed with increased heating rate.

It can therefore be expressed that, during heating, at rates up to 15,000˚C/s the recrystallisation process on previously formed isothermal crystals of PCL was not supressed. The presence of a single endotherm is required for kinetic analysis of isothermally grown crystals. The removal of the double melting behaviour inhibits further kinetic analysis of the low isothermal crystallisation temperatures (Tardif *et al.*, 2014). Specially designed chip calorimeters, used in other fast scanning calorimetry studies (Zhuravlev and Schick, 2010, Bosq *et al.*, 2013), could provide the heating rates necessary to remove the recrystallisation of PCL following low temperature isothermal crystallisation.

6.6 Conclusions

- The crystallisation of PCL was prevented from an amorphous glass, below T_g, to and amorphous liquid, above T_m, with a heating rate of >7,500˚C/s. Vitrification of PCL was achieved from the melt at a cooling rate >850˚C/s
- High temperature crystallisation, ≥5˚C, revealed a single melting endotherm increasing in temperature with crystallisation time providing an extension of the current calorimetry literature on PCL
- Both primary and secondary stages of crystallisation can be observed from both the change in heat of fusion and the peak melting temperature where a deviation in the linearity, of the change in heat of fusion and peak temperature with crystallisation time, indicates the start of secondary crystallisation
- The Avrami analysis of PCL using FDSC further extends the current literature on PCL using FDSC. An Avrami exponent, 'n', of 1 or 2 was calculated, dependent on the crystallisation temperature between 5 and 40˚C. A spontaneous rod-like crystal structure is suggested to develop due to nucleation from the sample surface and rapid crystallisation. At elevated temperatures, slower crystallisation kinetics allows time for disc-like crystals to develop
- The short half-life values calculated from the Avrami parameters, between 0.05 and 40 seconds from 5 to 40˚C respectively, are representative of the small sample size in FDSC
- Although crystallisation can be prevented from an amorphous glass and vitrification from a liquid, the prevention of recrystallisation cannot be achieved on FDSC after low temperature crystallisation close to the glass transition temperature

CHAPTER 7 THERMAL ANALYSIS STUDIES ON POLY(ETHER-ETHER-KETONE)

7.1 Introduction

This chapter aims to determine non-isothermal crystallisation kinetics of poly-ether-ether-ketone (PEEK) 150PF for the first time using Flash DSC (FDSC) and propose the origin of double melting in PEEK. Current literature on PEEK focuses on isothermal crystallisation over a wide temperature range and the resulting double melting endotherms (Tardif *et al.*, 2014, Jin *et al.*, 2014). The beginning of the chapter investigates double melting in PEEK with fast heating at high isothermal crystallisation temperatures. FDSC will be used to determine the equilibrium melting temperature using a Hoffman-Weeks plot, from 260˚C to 330˚C, through different heating rates over 5 orders of magnitude, which has previously not been possible using non-chip-based calorimetry techniques.

7.2 Non-Isothermal Crystallisation using Conventional DSC

PEEK exhibits a crystallisation exotherm during cooling from the melt (10˚C/min), and consequently, is followed by a melting endotherm during the re-heat (10˚C/min). Faster cooling at 80˚C/min shifts the crystallisation process to a lower temperature. The crystallisation kinetics of PEEK allow crystallisation of the sample during cooling at both 10˚C/min and at 80˚C/min. Heating at 10˚C/min after both cooling rates presents almost identical peak melting temperatures (T_m), 344˚C. This indicates that the polymer is not crystallising at a different temperature on cooling and the shift in peak crystallisation

temperature (T_c) is related to thermal lag. A reduction in the endotherm area occurs after cooling at faster rates, due to a reduction in the degree of crystallinity; fast cooling reduces the time for crystallinity to develop. Fast heating (80˚C/min) creates a broadened endotherm and an elevated melting peak due to thermal lag. The crystallisation process cannot be prevented from the melt using scanning rates available on CDSC; a faster scanning calorimetry device is required to completely prevent the crystallisation process, vitrifying PEEK.

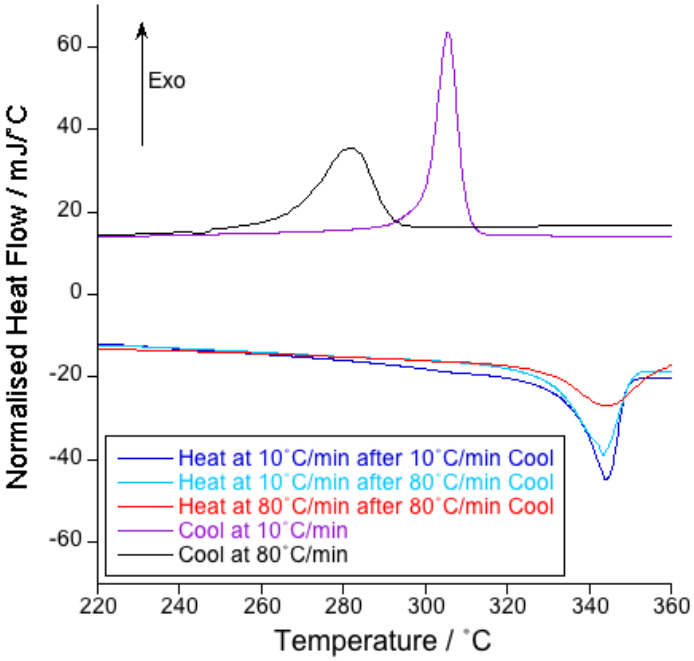

Figure 7-1 - The melting endotherms and crystallisation exotherms of PEEK recorded using CDSC. Method: Heating at 10˚C/min from 25 to 400˚C cooling at 10 or 80˚C/min from 400 to 25˚C and final heating at 10 or 80˚C/min from 25 to 400˚C[8]

[8] Heating rate normalisation has been made; no thermal lag correction has been made.

7.3 Non-Isothermal Crystallisation using Flash DSC

7.3.1 Preventing Crystallisation using Flash DSC

7.3.1.1 Heating to Prevent Crystallisation

It is clear from Figure 7-2 that the melting peak area reduces with increasing heating rate. Heating glassy PEEK slowly from below the glass transition temperature (T_g), after a quench cool at 2,500˚C/s, provides time for ordering to occur upon heating. An observable melting endotherm at 315˚C provides evidence that an unobservable crystallisation exotherm is present on heating. A combination of slower crystallisation rate, in comparison to other polymers (i.e. PCL shown in Chapter 6), and small sample mass is expected to be the cause of the undetectable crystallisation exotherm on heating. The increase in heating rate shows no impact on peak melting temperature (T_m), as thermal lag is minimal at 300˚C/s. The melting endotherm is no longer detectable on heating in excess of 250˚C/s. The heating rate required to prevent crystallisation on heating has not previously been shown; however, in previous work a rate of 2,000˚C/s was applied to prevent crystallisation (Jin *et al.*, 2014, Tardif *et al.*, 2014). The results obtained here show agreement with this literature as an elevated rate is commonly used to ensure crystallisation is prevented.

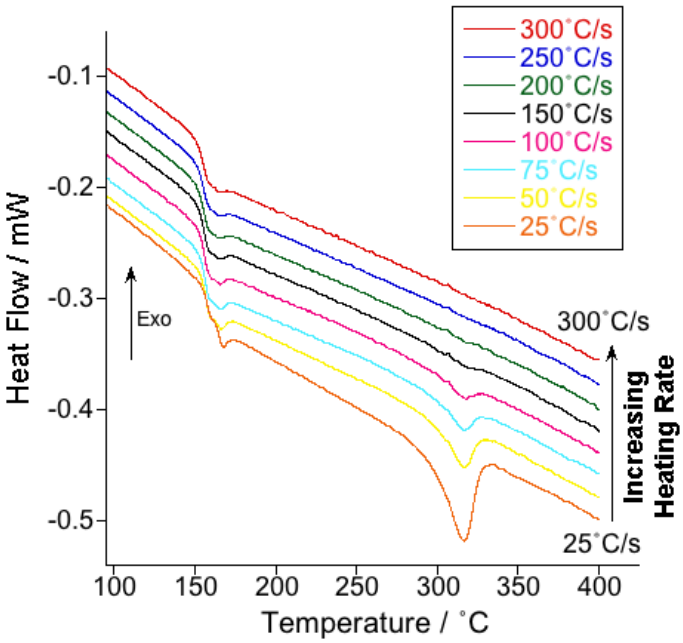

Figure 7-2 - The reduction in the melting endotherm with elevated heating rate in amorphous PEEK (cooled at 2,500˚C/s to vitrify). Method: Heating at 2,500˚C/s from 25 to 400˚C before quench cooling at 2,500˚C and final heating (traces shown) between 25 and 300˚C/s

The T_g reveals an ageing peak at relatively slow heating rates (25˚C/s). The T_g increases slightly due to thermal lag effects and an increased heating rate decreases the size of the ageing peak located on the T_g. The latent time below T_g is decreased with heating rate, decreasing the time for ageing to occur.

7.3.1.2 Cooling to Prevent Crystallisation

Figure 7-3 shows the subsequent heating traces at 2,500˚C/s after cooling between 25 and 100˚C/s. The crystallisation exotherm was not detectable during cooling of PEEK; consequently, the subsequent melting endotherm on heating is used to determine the occurrence of crystallinity. Elevated cooling rates reduce the endothermic melting peak area as crystallinity reduces. After a cooling rate of 75˚C/s no visible melting endotherm is visible; this reduction is consistent with the assumption that crystallisation on cooling

is prevented. The thermal transition appearance is smaller at slower heating rates, thus a heating rate of 2,500˚C/s was employed to increase the transition heat flow (Mathot *et al.*, 2011). The elevated T_g is a consequence of elevated heating rates used in FDSC in comparison to CDSC due to thermal lag at a heating rate of 2,500˚C/s.

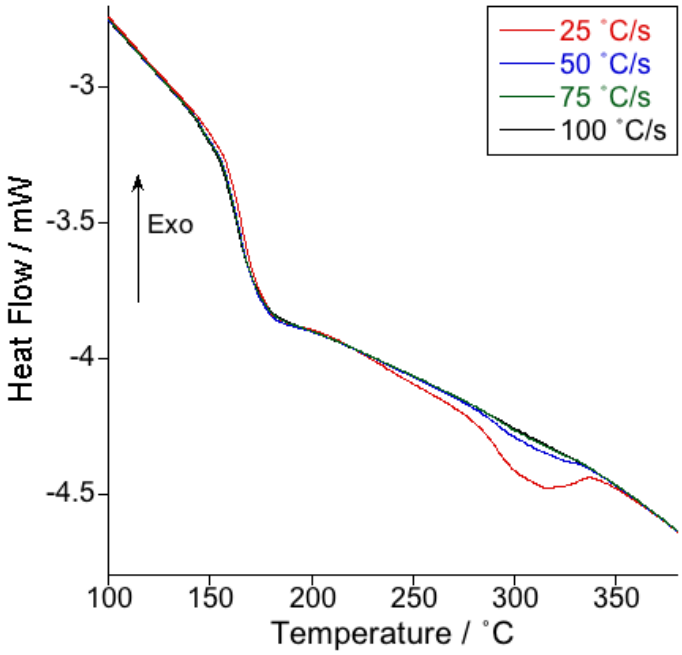

Figure 7-3 - PEEK heating traces using FDSC at 2,500˚C/s following cooling at rates between 25 to 100˚C/s. Method: Heating at 2,500˚C/s from 25 to 400˚C before cooling between 25 and 100˚C/s from 400 to 25˚C and final heating (traces shown) at 2,500˚C/s from 25 to 400˚C

The key finding in the FDSC scanning rate experiments show that the rate required to prevent crystallisation on heating was 250˚C/s and the rate required to prevent crystallisation on cooling was 75˚C/s. Therefore, to ensure the crystallisation process is prevented on both heating and cooling, a rate of 2,500˚C/s was selected for the continued work on PEEK.

7.4 Isothermal Crystallisation of PEEK between 180 and 320˚C

Figure 7-4 shows the melting region of PEEK on re-heating after isothermal crystallisation from the melt in the range 180-240˚C. From Section 7.3.1.1, a heating rate of 2,500˚C/s is fast enough to prevent non-isothermal crystallisation of an amorphous sample, but not fast enough to prevent further crystallisation of previously formed crystals, shown by a double melting endotherm behaviour. Both melting peak areas increase with isothermal crystallisation time, presenting evidence of the development of crystal structures. As T_c increases, the separation between endotherm peaks decreases. The growth of isothermally grown crystals is represented by the lower endotherm. This is determined from the combination of increased lower endotherm peak temperature and the unchanged upper endotherm peak temperature with dwell time.

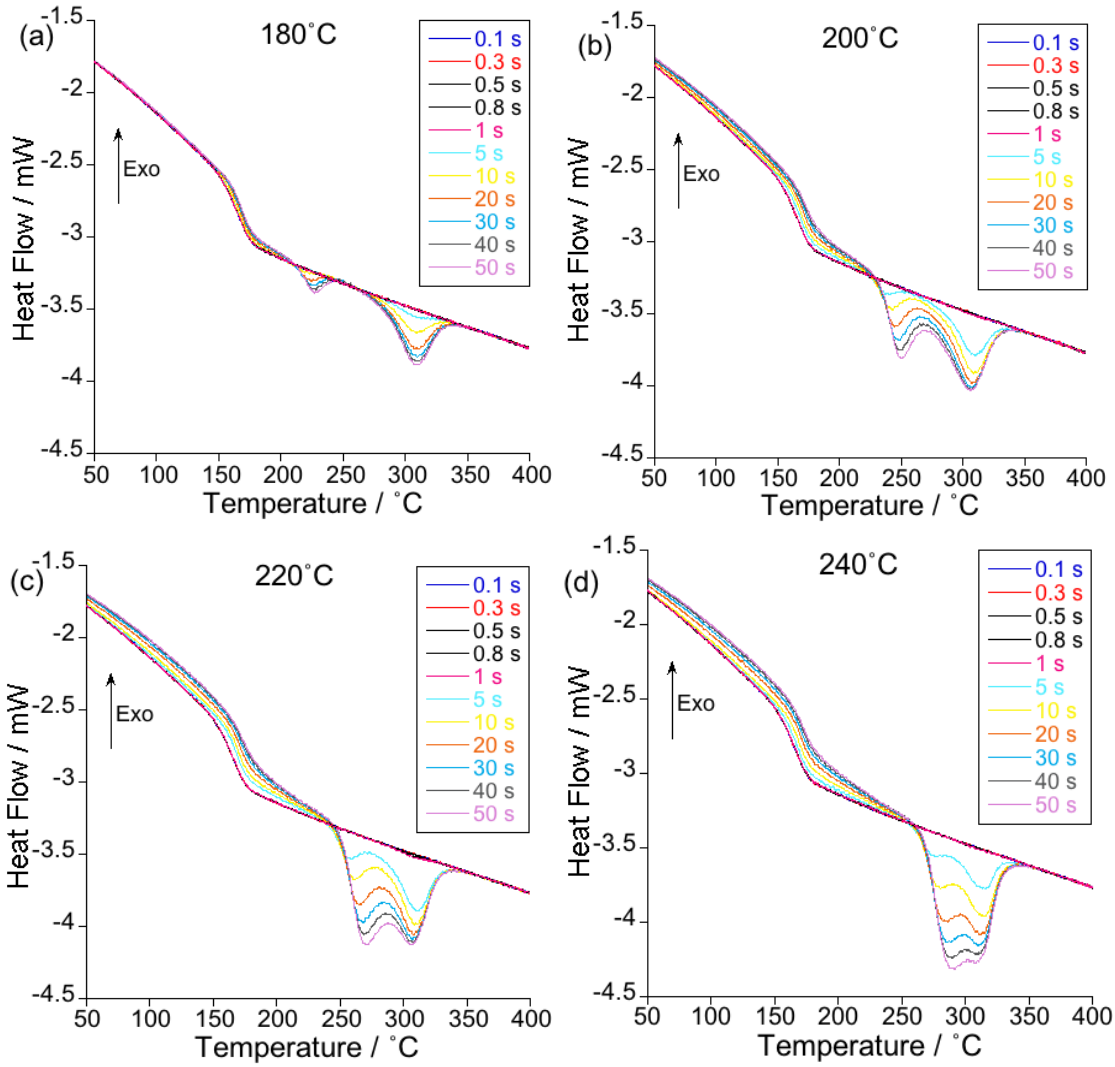

Figure 7-4 - Isothermal crystallisation of PEEK at (a) 180, (b) 200, (c) 220 and (d) 240˚C. Method: Heating at 2,500˚C/s from 25˚C to 400˚C before quench cooling at 2,500˚C/s from 400˚C to T_c and held for 0.1-50 seconds. Cooling at 2,500˚C/s from T_c to 25˚C before a final heating (traces shown) at 2,500˚C/s from 25 to 400˚C[9]

A maximum degree of recrystallisation can be observed as the upper endotherm area becomes saturated with dwell time. In Figure 7-4 (b) and (c), following a 30 seconds dwell time, further increases in the lower endotherm area does not impact the upper

[9] FDSC heating traces following isothermal crystallisation at 190, 210 and 230˚C are shown in the appendix

endotherm area. Further recrystallisation cannot occur from the previously melted thin lamella.

Figure 7-5 shows single endotherms during heating following high T_c, described by Tardif *et al.* (2014) to represent the development of a single crystal population. The area of the endotherm increases with time at T_c, indicating the development of a stable crystal structure. An increased T_c results in an elevated T_m due to an increase in lamella thickness in accordance with Thomson-Gibbs (Fakirov and Avramova, 1982). No endotherms are visible after dwell times up to 50 seconds at 320˚C due to the reduction in nucleation rate with temperature (Cowie, 1991). As T_c increases, the peak area at an equivalent dwell time falls as crystallisation rate slows. A decrease in the step at T_g with dwell time is in accordance with an increase in degree of crystallinity. The step in T_g does not change at an isothermal temperature of 300 and 320˚C where minimal or no crystallinity has developed (Wurm *et al.*, 2012).

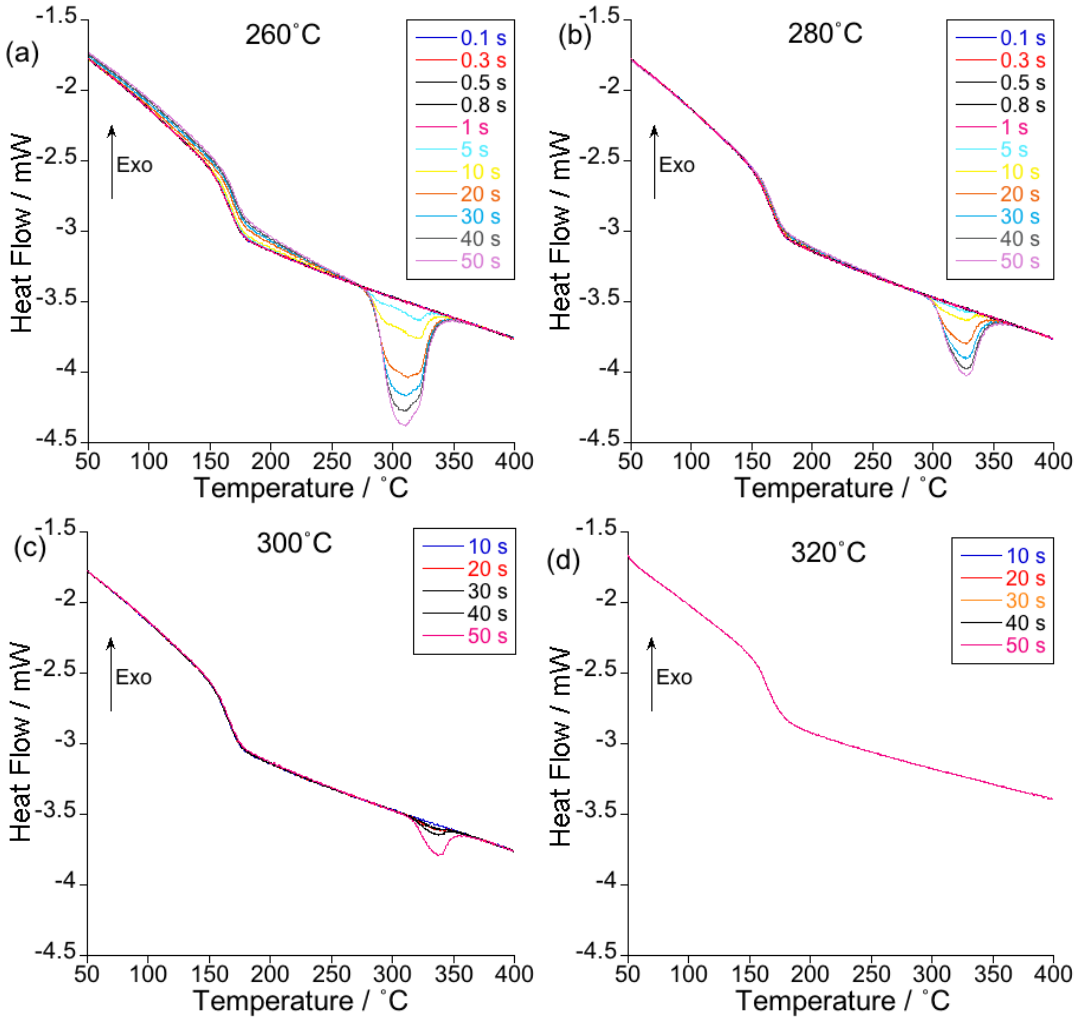

Figure 7-5 - Isothermal crystallisation of PEEK at (a) 260, (b) 280, (c) 300 and (d) 320˚C. Method: Heating at 2,500˚C/s from 25˚C to 400˚C before cooling at 2,500˚C/s from 400˚C to T_c and held for 0.1-50 seconds. Cooling at 2,500˚C/s from T_c to 25˚C before final heating (traces shown) at 2,500˚C/s from 25 to 400˚C[10]

Figure 7-6 (a) shows an increase in heat of fusion (ΔH_f) with dwell time at varied T_c. The rate of crystallisation increases with an elevated T_c and a maximum crystallisation rate at an isothermal temperature of 230˚C, showing good agreement with previous work (Blundell and Osborn, 1983, Tardif *et al.*, 2014). Crystallisation at temperatures greater

[10] FDSC heating traces following isothermal crystallisation at 250, 270 and 290˚C are shown in the appendix

than 230˚C reduces crystallisation rate (increasing half-life) as nucleation rate falls and chain mobility increases forming larger spherulites with thicker lamella structures (Figure 7-6 (b)). The primary crystallisation process was decoupled from the secondary crystallisation stage (as shown in section 5.3) to enable the half-life calculation from ½ H_∞ (the calculation of H_∞ is explained in section 6.4).

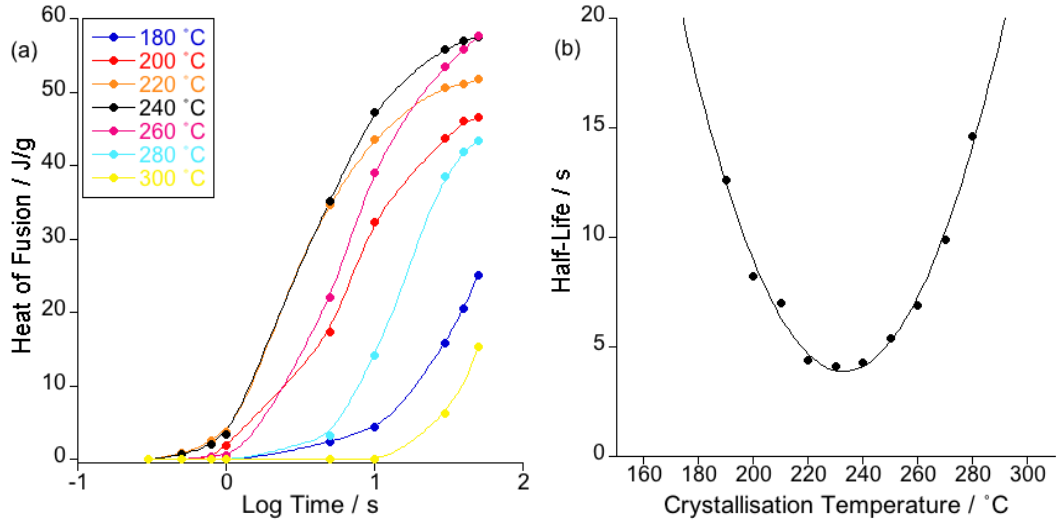

Figure 7-6 - (a) The heat of fusion (ΔH_f) measured from the endothermic melting peaks against log crystallisation time (b) Crystallisation half-life as against T_c, calculated from ½ ΔH_∞

On heating following a low temperature crystallisation, the ΔH_f calculated was elevated by the addition of both melting endotherms. The ΔH_f of the isothermal crystal cannot be separated from the double endotherm and thus the total ΔH_f is analysed. The half-life for low T_c where double melting was observed, resulting in a shorter value than if the endothermic peak of the as-grown crystals was measured separately. The separation of the two endotherms is not possible through calorimetry techniques as the presence of an exothermic reaction, indicating recrystallisation, is unknown. The absence of the recrystallisation exotherm and as T_c increases, the double endotherms become

connected, the exothermic reaction may potentially reduce the size of the measured endotherm, calculating an inaccurate heat of fusion. The importance of the separation of a double endotherm in unstable spherulites is explored further in Chapter 8 in poly(lactic acid).

A crystallisation half-life of 1 to 30 minutes was found in work by Blundell and Osborn (1983) using CDSC, approximately an order of magnitude larger than FDSC values. The crystallisation rate is shown to be a factor of sample size in FDSC (Chapter 4) with a half-life less than 30 s.

Table 7-1 - PEEK crystallisation half-Life

Crystallisation Temperature / ˚C	Half-Life / s	Crystallisation Temperature / ˚C	Half-Life / s
180	**-----**	**240**	**4.30**
190	**12.60**	**250**	**5.40**
200	**7.0**	**260**	**6.90**
210	**8.20**	**270**	**9.90**
220	**4.40**	**280**	**14.60**
230	**4.10**	**290**	**22.50**

Isothermal crystallisation shows double melting close to T_g (180-240˚C) and at isothermal hold temperatures close to T_m (260-320˚C), a single endotherm. The calculation of PEEK half-life presents a 'U' shaped curve of half-life with T_c. An optimum crystallisation rate occurs following an isothermal T_c of 230˚C.

7.4.1 The Effect of Heating Rate on Double Melting

7.4.1.1 One Minute Isothermal Crystallisation at 200, 250 and 300˚C

Figure 7-7 shows a reduction in the upper endotherm T_m with heating rate, due to the reduction in time per unit temperature for recrystallisation on heating. An upper endotherm peak temperature reduction has also been observed by Tardif *et al.* (2014), suggesting the double peak is a consequence of a melting-recrystallisation-melting mechanism and not a dual crystal population as reported by other authors (Lattimer *et al.*, 1992, Hsiao *et al.*, 1995). Heating at 100˚C/s presents a significant upper endotherm ΔH_f as a result of recrystallisation on heating. Following isothermal crystallisation at 200˚C, elevated heating rates up to 2,500˚C/s do not prevent recrystallisation of the isothermally grown crystals. Unstable crystal growth is enhanced at low temperature (explained further in Chapter 1), resulting in elevated thermodynamic driving forces for recrystallisation. Crystal stability is greater at a T_c of 250˚C where a single peak is visible on heating at ≥1,500˚C/s. At 300˚C heating rates ≥750˚C/s present a single endotherm due to the reduction of metastable crystal growth. Higher T_c increases the crystal stability, as stated by Lauritzen and Hoffman (1973), reducing the degree of recrystallisation and consequently requiring a slower heating rate to remove the presence of double melting as T_c increases. The removal of the recrystallisation endotherm at isothermal temperatures close to T_g has recently been shown by Furushima *et al.* (2016) at elevated heating rates >20,000˚C/s using specially designed chip calorimeters. In this study however, heating rates greater than 2,500˚C/s in PEEK were not investigated.

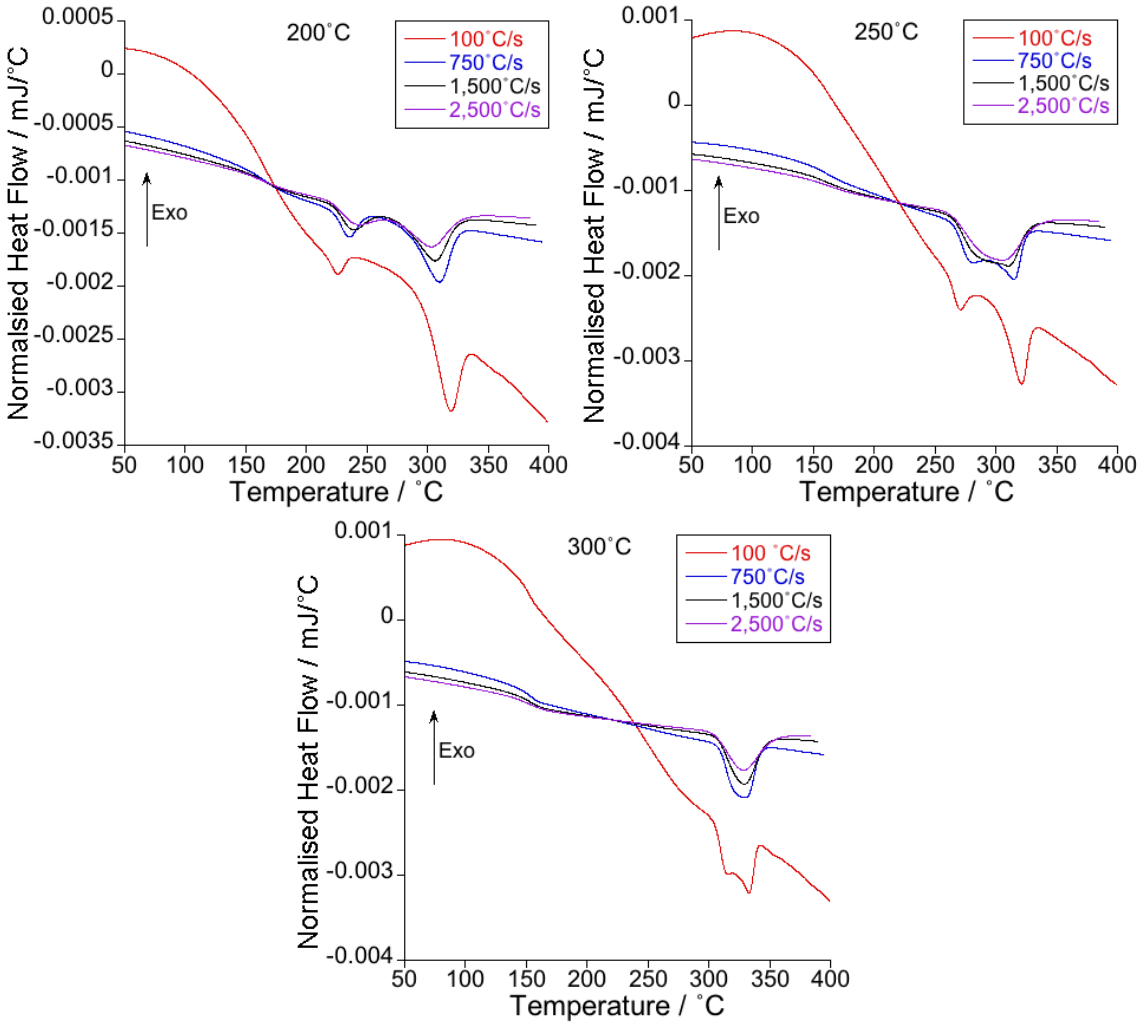

Figure 7-7 - Isothermal crystallisation of PEEK at (a) 200, (b) 250 and (c) 300. Method: Heating at 2,500˚C/s from 25˚C to 400˚C before cooling at 2,500˚C/s from 400˚C to T_c and held for one-minute. Cooling at 2,500˚C/s from T_c to 25˚C before final heating (traces shown) between 100 and 2,500˚C/s from 25 to 400˚C [11]

7.4.1.2 One Hour Isothermal Crystallisation at 200, 250 and 300˚C

Figure 7-8 shows the effect of heating rate on thicker, more stable crystals after an isothermal dwell time of one hour. A greater degree of crystallinity is obtained after a longer isothermal dwell time from an increase in lamella thickness, and peak T_m (Lee and Porter, 1987). However, heating rates required to prevent recrystallisation were the

[11] Thermal lag adjustment has been made to all data according to Equation 5-9.

same as the rates studied in the one-minute isothermal experiments. The single endotherm observed at 300˚C at a heating rate of 750˚C/s in Figure 7-8 shows a more symmetrical appearance in comparison to the endotherm at 300˚C in Figure 7-7. The broader, less symmetrical peak is formed due to the presence of a broader array of crystal sizes present. A degree of unobservable recrystallisation may occur at this lower heating rate resulting in this broader range of crystal sizes and thus endotherm.

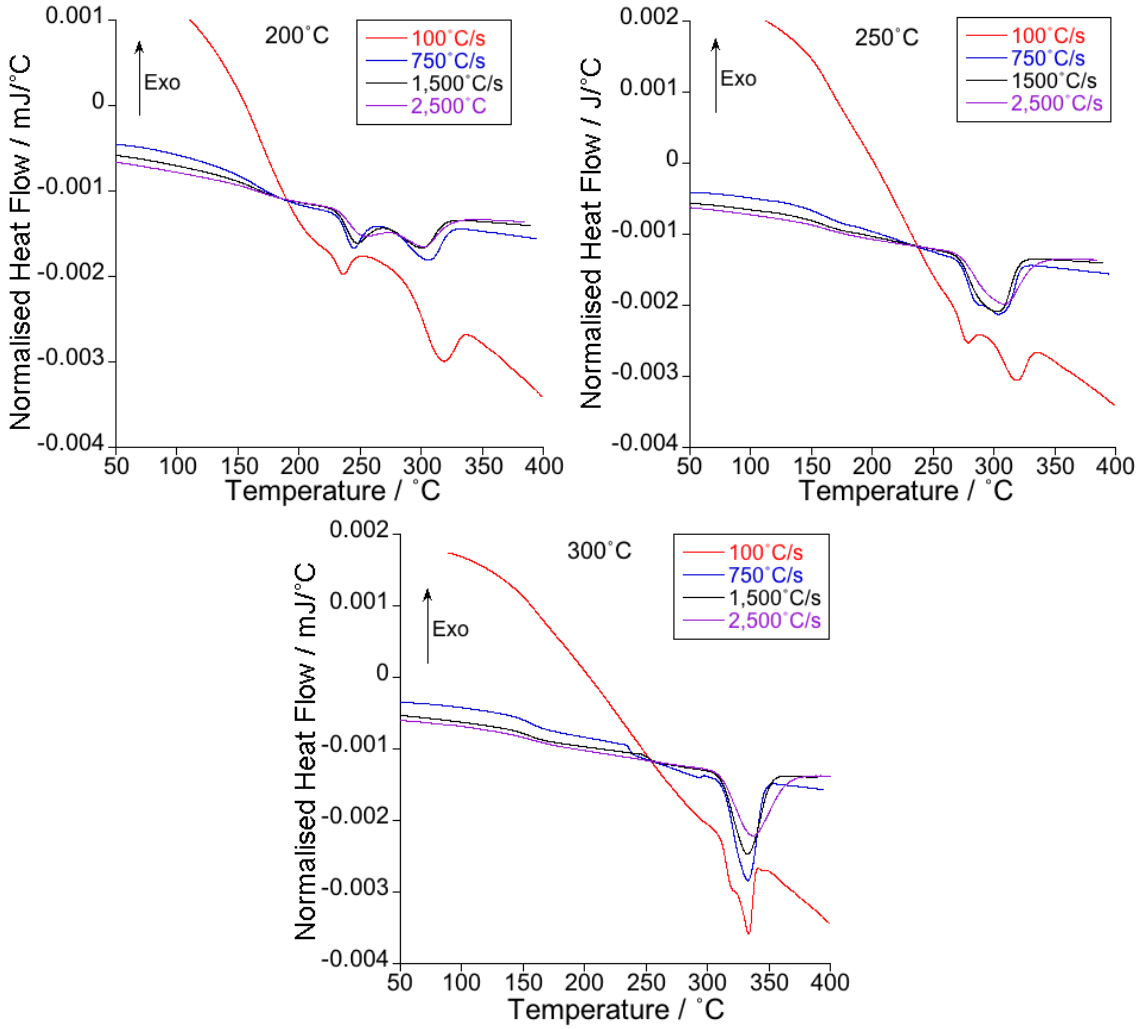

Figure 7-8 - Isothermal crystallisation of PEEK at (a) 200, (b) 250 and (c) 300. Method: Heating at 2,500˚C/s from 25˚C to 400˚C before cooling at 2,500˚C/s from 400˚C to T_c and held for one-hour. Cooling at 2,500˚C/s from T_c to 25˚C before final heating (traces shown) between 100 and 2,500˚C/s from 25 to 400˚C [11]

Isothermal crystallisation of PEEK at temperatures close to T_g results in the growth of small, thermally unstable crystals. Unstable crystals melt at low temperatures, providing stable nucleation points for recrystallisation and further melting. Crystallisation closer to T_m enables larger, more stable crystals to grow, reducing the thermodynamic driving force for recrystallisation. Thermally stable crystals result in a single melting endotherm if heating rate prevents recrystallisation. Heating fast, after isothermal crystallisation, reduces the time available for recrystallisation, resolving single endotherms at lower temperatures where recrystallisation is apparent on slow heating. FDSC enables complete vitrification of PEEK at any T_c followed by heating rates that do not induce crystallisation from an amorphous material. Heating rates up to 2,500˚C/s reduce the upper melting endotherm peak temperature of PEEK. These results support the idea that the double melting phenomenon is caused by melting-recrystallisation-melting and not a dual population of crystals.

7.5 Determining the Equilibrium Melting Temperature

A single peak can be resolved on heating after isothermal crystallisation, at temperatures above 260˚C for one-hour, at a rate of 1,500˚C/s and above where crystal stability is high, reducing the thermal drive for recrystallisation. The presence of a single endotherm provides sufficient data for further analysis of the equilibrium melting temperature (T_m^0). The elimination of double melting in PEEK provides a larger temperature range than has previously been possible for T_m^0 analysis on other calorimetry techniques. According to Wood and Bekkedahl (1946) and Hoffman and Weeks (1961), the inability to prevent recrystallisation, and thus double melting, can result in an inaccurate analysis of T_m^0. Analysis of T_m^0 by a number of authors using

CDSC has resulted in a T_m^0 range of 359-398˚C (Blundell and Osborn, 1983, Ko and Woo, 1996, Yang *et al.*, 2006, Lee and Porter, 1987).

Figure 7-9 shows a Hoffman-Weeks plot of the lower and upper endotherm peak T_m with T_c after a one-minute isothermal crystallisation dwell time. An upper endotherm temperature plateau is observed at a T_c below 250˚C. A reduction in the endotherm temperature is visible with increased heating rates due to a reduced time per unit temperature, reducing recrystallisation. The lower endotherm temperature shows a linear relationship between T_c and T_m. An increase in the upper T_m is apparent at all heating rates at elevated T_c.

At a heating rate of 100˚C/s a double endotherm is visible at all crystallisation temperatures but as heating rate and T_c increase, a single endotherm becomes apparent at high crystallisation temperatures. A single, high temperature endotherm is shown using CDSC after short isothermal crystallisation and is expected to occur from the growth of crystals on heating from nuclei formed after the short isothermal hold time. Data collection on CDSC was limited to a high T_c, due to the inability to prevent non-isothermal crystallisation during cooling at a rate of 100˚C/min.

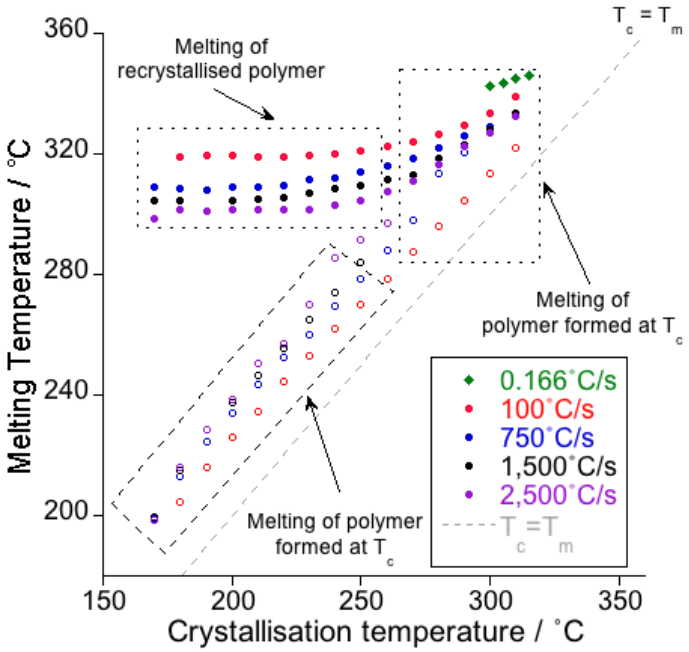

Figure 7-9 - A Hoffman-Weeks plot displaying peak T_m after one-minute isothermal crystallisation recorded on heating at 0.166˚C/s (10˚C/min) on CDSC and between 100˚C/s and 2,500˚C/s on FDSC. (Filled and open circles represent the upper and lower melting peaks respectively, the green data points were collected using CDSC)[11,12]

Figure 7-10 shows the upper endotherm T_m following isothermal crystallisation at 270˚C and above. The linear fit of T_m against T_c shows a lower gradient with slow heating, consequently, the intersection with T_c=T_m results in a T_m^0 value, 358.2˚C ± 4.0˚C shown in Figure 7-10. Hoffman-Weeks β values were calculated using Equation 7-1 and shown in Table 7-2.

$$T_m = T_m^0\left(1 - \frac{1}{2}\beta\right) + \frac{T_c}{2\beta}$$

Equation 7-1

The β values are calculated from the gradient of the linear fit to the data and describe the thickening factor of the polymer chain folds. Hoffman-Weeks express that β should

[12] All raw data is presented in the Appendix

be equal to one if recrystallisation does not occur on heating. The heating rate should be varied to determine the correct value of β. The mean step height of the folded polymer chain that melts out is β times as large as the mean step height of a primary nucleus (Hoffman and Weeks, 1961).

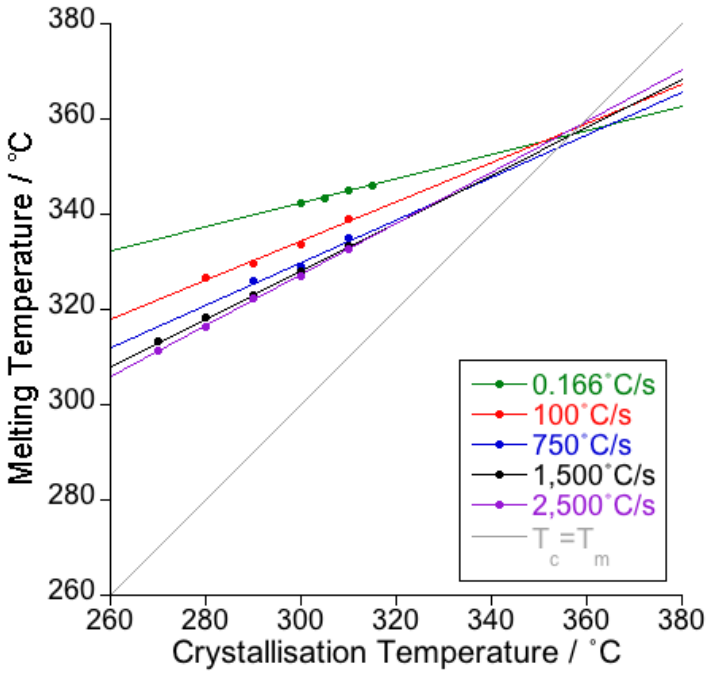

Figure 7-10 - Hoffman-Weeks data from the previous figure shows the upper melting endotherm peak temperature recorded on heating after isothermal crystallisation for one-minute at a heating rate of 0.166°C/s (10°C/min) on CDSC and between 100°C/s and 2,500°C/s on FDSC. [13]

Figure 7-11 shows a Hoffman-Weeks plot of the lower and upper endotherm peak T_m with T_c after a one-hour isothermal crystallisation dwell time. An upper endotherm temperature plateau at T_c below 250°C is observed. A reduction in the endotherm temperature is visible with increased heating rate due to a reduction in recrystallisation

[13] Thermal lag adjustment has been made to all data according to Equation 5-9.

as seen in Figure 7-9. The lower endotherm temperature shows a linear relationship of T_c and T_m. Similarly, a lower T_m is observed on heating at ≥750˚C/s revealing very good accuracy of the thermal lag correction and prevention of non-isothermal crystallisation. A double endotherm is visible after an isothermal crystallisation dwell time of one-hour of PEEK using CDSC. Larger sample size and high temperature isothermal crystallisation allows significant crystallisation to develop in comparison to data shown in Figure 7-9.

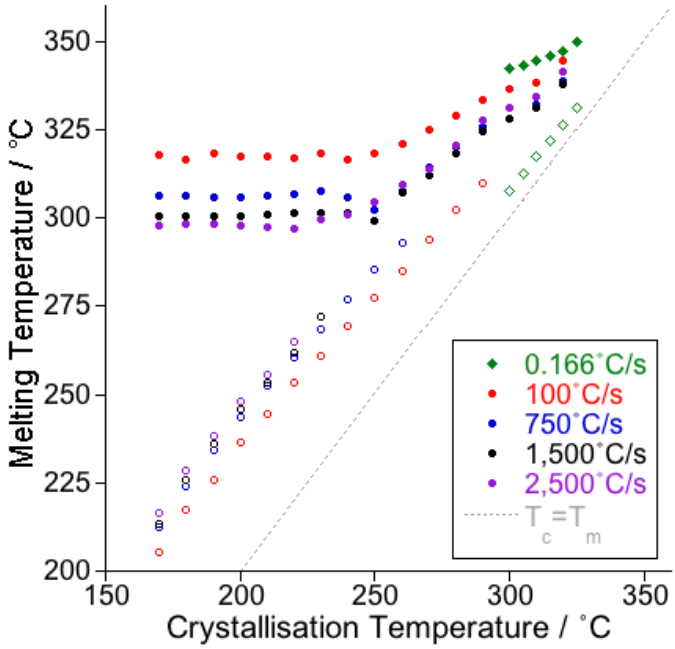

Figure 7-11 - A Hoffman-Weeks plot displaying peak T_m after one-hour isothermal crystallisation recorded on heating at 0.166˚C/s (10˚C/min) on CDSC and between 100˚C/s and 2,500˚C/s on FDSC. (Filled and open circles represent the upper and lower melting peaks respectively, the green data points were collected using CDSC) [12,13]

Similar upper T_m values were obtained at heating rates ≥750˚C/s, where non-isothermal crystallisation is prevented. The thermal lag adjustment shows good acceptance to the data where similar T_m values are expected. Higher T_m at lower heating rates is a direct result of increased time for recrystallisation and further non-isothermal crystallisation

to allow the formation of a more stable crystal with an elevated T_m. It is therefore hypothesised that heating rates in excess of 2,500˚C/s, corrected using the thermal lag correction shown in Equation 5-9, would result in the same upper T_m and β values as shown in Figure 7-12 and at heating rates between 750 and 2,500˚C/s.

Figure 7-12 shows the upper endotherm T_m following isothermal crystallisation at 260˚C and above. The linear fit of T_m against T_c shows a reduced gradient with slower heating, consequently, the intersection with $T_c=T_m$ results in a T_m^0 value, 362.4˚C ± 4.2˚C shown in Table 7-2. Hoffman-Weeks β values are shown in Table 7-2.

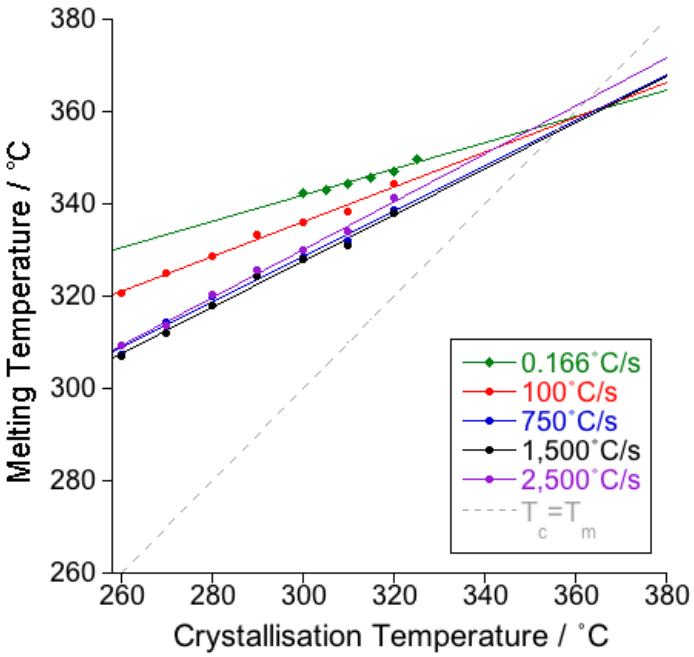

Figure 7-12 - Hoffman-Weeks plot from the previous figure shows the upper melting endotherm peak temperature recorded on heating after isothermal crystallisation for one-hour at a heating rate of 0.166˚C/s (10˚C/min) on CDSC and between 100˚C/s and 2,500˚C/s on FDSC [13]

Employing FDSC to eliminate the double melting endotherm phenomenon, a lower T_m^0 across both isothermal dwell times (one-minute and one-hour) suggests that T_m^0 is not

as high as previously thought. The rapid cooling achievable on FDSC prevents nucleation of PEEK before the isothermal T_c is reached. The application of a fast cooling rate, preventing unintentional nucleation reveals a lower T_m^0, agreeing with recent work (Yang *et al.*, 2006). In contrast to the work detailed by Hoffman and Weeks (1961), the presence of the double melting endotherm shows no impact upon the T_m^0, where T_c results in a shift in the upper endotherm T_m. The upper endotherm is influenced by the lower endotherm at high temperatures presenting dependence of the isothermally grown crystals in comparison to recrystallised material.

Table 7-2 - T_m^0 and β values with varied heating rate and isothermal hold time

	Isothermal Time			
Heating Rate /˚C/s	**One-Minute**		**One-Hour**	
	β	**T_m^0 / ˚C**	**β**	**T_m^0 / ˚C**
0.166	**1.50**	**356.7**	**1.43**	**358.6**
100	**1.30**	**362.1**	**1.24**	**358.1**
750	**1.11**	**354.2**	**0.98**	**359.9**
1,500	**1.00**	**356.7**	**0.98**	**357.2**
2,500	**0.93**	**359.0**	**0.93**	**366.6**

Hoffman-Weeks β values were calculated from the gradient of the slope of the upper endotherm T_m at high T_c using Equation 7-1. The β values are greater following a one-minute isothermal crystallisation time in comparison to the one-hour isothermal crystallisation time. The limited secondary crystallisation, after a one-minute isothermal, allows for more recrystallisation and thickening to occur on heating

compared to a one-hour isothermal crystallisation time where primary crystallisation is completed. A heating rate of 1,500˚C/s results in a β value of 1.00 and 0.98 for one-minute and one hour respectively. Heating at 1,500˚C/s is shown to be fast enough to prevent recrystallisation on heating, resulting in a β value of 1. Varied heating rates are beneficial to the calculation of β below and above 1 to allow an accurate calculation of T_m^0. Thickening effects described by Hoffman and Weeks (1961) permit a increased β value at slower heating rates due to increased mobility of the chains to allow recrystallisation to occur.

An accurate T_m^0 can therefore be calculated where the removal of recrystallisation on heating at 1,500˚C/s with a thickening factor, β =0.99 ± 0.01. The extrapolated method to the line $T_m=T_c$ specifies a T_m^0 equal to 156.95 ± 0.25˚C after an isothermal crystallisation time of one minute and one hour. No other work has been carried out, utilising the heating rate capacity on FDSC, where a significant change in heating rate allows an observation of the change in β to obtain the most accurate rate required as described by Hoffman and Weeks (1961). The lowest value of T_m^0 shown in previous literature by Yang *et al.* (2006) shows close agreement to this work. It can be seen that a faster cooling rate of 200˚C/min results in a lower T_m^0. (Lee and Porter, 1987) employed an identical cooling rate (200˚C/min) with a reported T_m^0 equal to 398 ± 4˚C, however, it was not explicitly stated if thermal lag effects were accounted for during heating at 320˚C/min, which may result in elevated T_m and thus T_m^0.

Table 7-3 - Previous literature values of equilibrium melting temperature of PEEK measured on CDSC

Authors	T_m^0 / ˚C	Heating Rate / ˚C/min	Cooling Rate / ˚C/min
Blundell and Osborn (1983)	398	20	20
Lee and Porter (1987)	398 ± 4	320	200
Ko and Woo (1996)[14]	390	10	<320
Chen and Porter (1993)[15]	384	20	200
Yang *et al.* (2006)	359.6	10	200

[14] A very limited data set for the estimation of T_m^0 was employed. The cooling rate was specified as the fastest rate applied, thus suggesting an inconsistent experiment methodology

[15] Twelve hour isothermal experiments up to 320°C

7.6 Conclusions

- Crystallisation in amorphous PEEK was prevented on heating between T_g and T_m during heating at rates >250˚C/s. Vitrification of PEEK from the melt was recorded cooling rates >75˚C/s
- The origin of the double melting endotehrm was evaluated as recrystallisation through a melting-recrystallisation-melting process. The elevation of heating rate reduced the time available for recrystallisation reducting the upper endotherm peak $T_{m,}$ a common observation of an endotherm formed from recrystallised material during heating
- A variety of heating rates employed after isothermal crystallisation, for one-minute and one-hour, provided a range of gradients (β values) from a Hoffman-Weeks plot. An optimum heating rate of 1,500˚C/s was selected, where β was calculated to be one in both-one minute and one-hour isothermal conditions. An equilibrium temperature, lower than previously suggested in the literature, was recorded as 356.95±0.25˚C

CHAPTER 8 LOW TEMPERATURE CRYSTALLISATION KINETIC COMPARISON OF POLY(LACTIC ACID) USING CONVENTIONAL DSC AND FLASH DSC

8.1 Introduction

This chapter aims to compare isothermal crystallisation kinetics of poly(lactic acid) (PLA) using conventional DSC (CDSC) and Flash DSC (FDSC) in low temperature isothermal conditions. These results will be used to complete a kinetic analysis of the data using Avrami and Hoffman-Lauritzen equations. A comparison of the kinetic data from both calorimetry techniques will be used to determine the applicability of data collection from heat of fusion.

8.2 Preventing Crystallisation on Cooling using Conventional and Flash DSC

Figure 8-1 shows heating traces at 10˚C/min following cooling from the melt between 1 and 80˚C/min using CDSC and between 10 and 1,000˚C/s using FDSC. In contrast to PCL and PEEK (Chapter 6 and 7 respectively), non-isothermal crystallisation of PLA can be significantly supressed (<1% crystallinity remaining) using CDSC. The results show a double melting endotherm after cooling at 1˚C/min, caused by non-isothermal crystallisation at low temperatures, forming unstable crystals, resulting in a melting-recrystallisation-melting process (Mustapa *et al.*, 2013). Cooling slower than 1˚C/min would permit crystal formation at a higher temperature, where the crystals are more thermally stable.

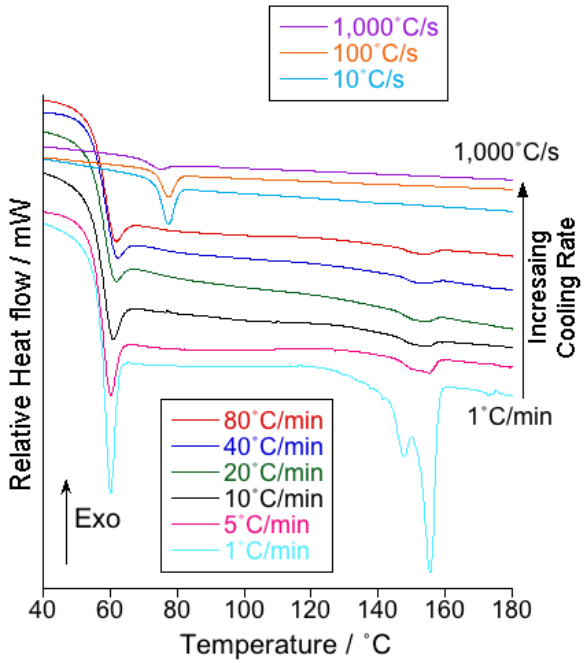

Figure 8-1 - The heating traces recorded at 10˚C/min after cooling at 1 to 80˚C/min on CDSC and 100 and 1,000˚C/s on FDSC[16]. Method: CDSC, heat at 10˚C/min from 25 to 200˚C before cooling at rates between 1 and 80˚C/min to 25˚C followed by a final heat (traces shown) at 10˚C/min; FDSC, heat at 100˚C/min from 25 to 200˚C before cooling between 10 and 1,000˚C/s from 200 to 25˚C followed by a final heat (traces shown) at 100˚C/s from 25 to 180˚C

Cooling between 5 and 80˚C/min shows a single, small endotherm with a peak melting temperature (T_m) of 156˚C. According to the results shown in Section 6.3.1.2, a faster cooling rates shows a depression in T_m. In PLA, cooling rates ≥5˚C/min do not impact T_m; thus, crystal growth was prevented on cooling and subsequent growth, from remaining nucleation sites that exist after cooling <80˚C/min, occurs on heating. A reduction in the area of the endotherm agrees with the drop in nucleation density with cooling rate in PLA as described by Salmerón Sánchez *et al.* (2007).

[16] No mass normalisation has been applied and thus the ΔC_p for CDSC and FDSC appear different.

Cooling rates employed on FDSC, at 10, 100 and 1,000˚C/s, only show a glass transition temperature (T_g). This is because the crystallisation process has been completely prevented where no melting can be observed. An equivalent heating rate was applied with respect to each calorimeter (10˚C/min in CDSC and 100˚C/s in FDSC) and thus thermal lag can be assumed minimal. The elevated T_g exhibited on FDSC traces is due to the fast cooling rates used (three orders of magnitude larger than CDSC) inhibiting molecular motion (vibration and rotation) at higher temperatures (Logan, 1982).

8.3 Isothermal crystallisation of Poly(Lactic Acid)

8.3.1 Low Temperature Isothermal Crystallisation of PLA using Conventional DSC

The results in Figure 8-2 show double melting of PLA on heating after isothermal crystallisation between 85 and 105˚C. On heating, after crystallisation at 85˚C for 240 and 360 minutes, an exothermic peak between the two endotherms can be observed. Double melting in PLA occurs through melting-recrystallisation-melting (Androsch *et al.*, 2014a) but the sequence of endotherm-exotherm-endotherm has not previously been observed using FDSC. An enlarged temperature separation (~20˚C) between the endotherms allows observation of an exotherm. The endotherm separation is reduced at a higher T_c, thus preventing the visible detection of an exothermic peak. It has been reported that isothermal crystallisation of PLA at 120˚C and above results in the formation of stable α crystals and below 120˚C, the formation of unstable α' crystal (Kawai *et al.*, 2007). Figure 8-2 (a)-(e) show no change in the upper endotherm peak T_m (156˚C). The increased molecular mobility of the chains at higher temperatures results in recrystallisation on heating and a more thermally stable α crystal with a corresponding elevated T_m.

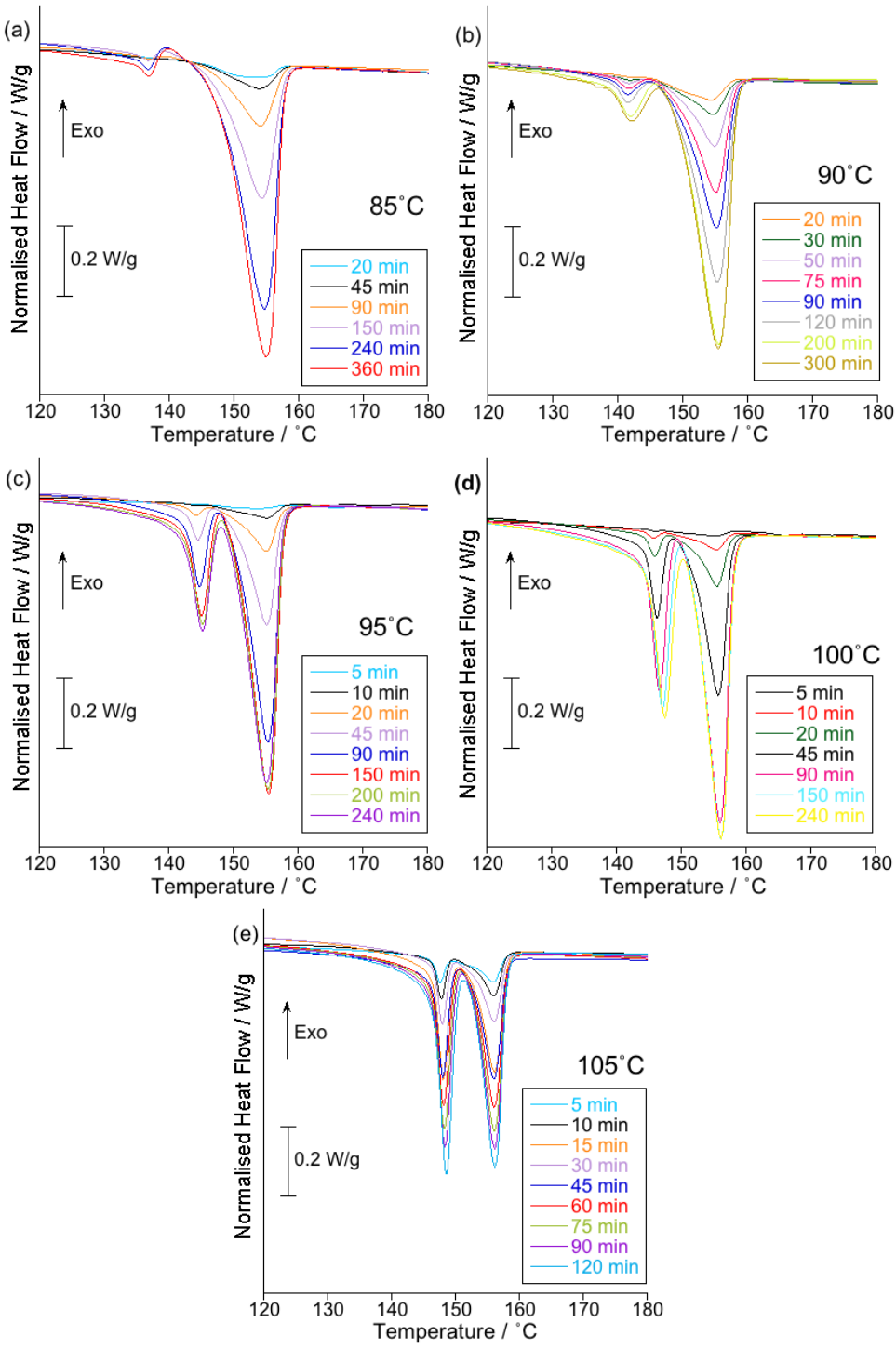

Figure 8-2 - CDSC heating traces after isothermal crystallisation at (a) 85˚C (b) 90˚C (c) 95˚C (d) 100˚C (e) 105˚C for varied time periods. Method: Heating at 10˚C/min from 25 to 200˚C before cooling at 80˚C/min from 200 to T_c and holding at T_c for times between 5 to 360 min. A final heat (traces shown) is made at 10˚C/min from T_c to 200˚C

At a low crystallisation temperature (T_c) (85 and 90˚C) the low temperature endotherm area is small where the rate of crystallisation is slow. At temperatures closer to T_g (59˚C), the rate of crystallisation is slow due to reduced chain mobility limiting crystal growth (Pan *et al.*, 2007). The upper endotherm area, corresponding to the recrystallised material, dominates the total enthalpy change measured (Figure 8-2 (a) and (b)). Crystallisation at 105˚C reveals a smaller upper endotherm area, equal in size to the lower endotherm. As the stability of the as-grown crystals increases, the thicker lamellae become thermally stable, reducing the amount of re-crystallisable material (Figure 8-2 (e)).

8.3.2 Low Temperature Isothermal Crystallisation of PLA using Flash DSC

Figure 8-3 (a)-(e) shows a single melting endotherm on heating at 100˚C/s after isothermal crystallisation between 85 and 105˚C. The low isothermal crystallisation temperatures shown demonstrate an increase in T_m with T_c. This rise in T_m is characteristic of an increase in crystal stability due to lamella thickness, l, according to the Gibbs-Thompson equation (Equation 8-2), where T_m^0 is the equilibrium T_m, σ_e is the surface free energy, ΔH_f is the heat of fusion and l is the lamella thickness.

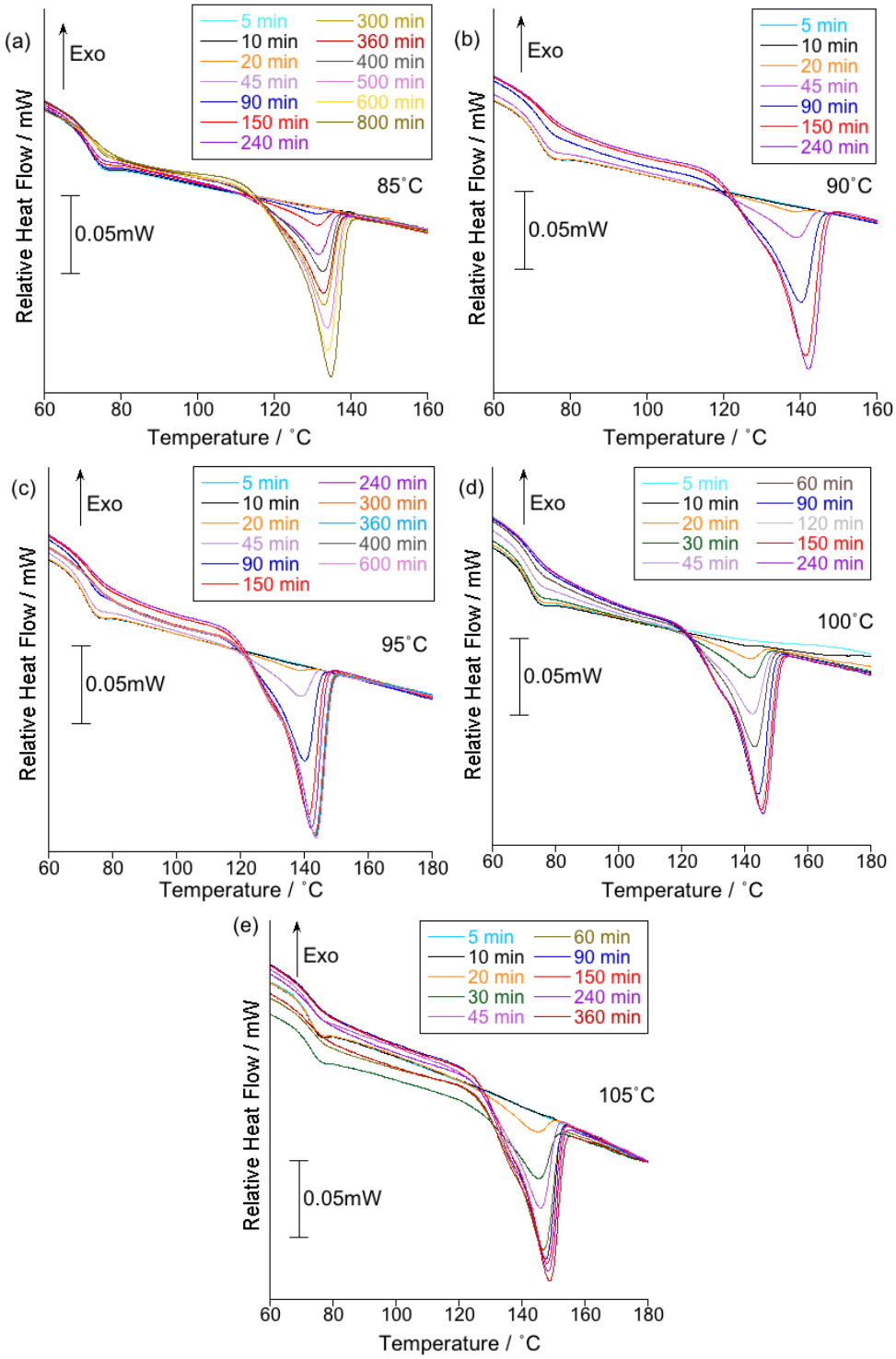

Figure 8-3 - FDSC heating traces at 100˚C/s following isothermal crystallisation (a) 85˚C (b) 90˚C (c) 95˚C (d) 100˚C (e) 105˚C at various time intervals. Method: Heat at 100˚C/s from 25 to 200˚C before cooling at 1,000˚C/min from 200 to T_c and holding at T_c for times between 5 to 800 min. A quench cool at 1,000˚C from T_c to 25˚C followed by a final heat (traces shown) at 100˚C/s from 25 to 200˚C

A comparable low temperature range has been previously tested with pre-crystallisation at 70˚C before further cold-crystallisation, where a single endotherm was observed on heating, representing the as-grown crystals (Androsch and Di Lorenzo, 2013b). In this thesis, applying a slow heating rate (100˚C/s), in relation to the FDSC, results in a negligible effect of thermal lag on the thermal transitions, providing a direct comparison of raw data collected from CDSC and FDSC (shown in Figure 8-4).

$$T_m = T_m^0\left(1 - \frac{2\sigma_e}{\Delta H_f l}\right)$$

Equation 8-1

$$l = \frac{2\sigma_e}{\Delta H_f\left(1 - \frac{T_m}{T_m^0}\right)}$$

Equation 8-2

8.3.3 Isothermal Crystallisation Comparison Between CDSC and FDSC

Figure 8-4 (a)-(e) displays CDSC and FDSC results after isothermal crystallisation between 85 and 105˚C. A comparison of the techniques shows an equivalent T_m between the lower endotherm of the unstable α'crystals in CDSC traces and the single endotherm in FDSC traces. The prevention of double melting using FDSC provides direct analysis of the unstable α' crystals from the melting endotherm. The data in Figure 8-4 provide comparable results without data reconfiguration through a thermal lag correction.

Recording ΔH_f on heating, by integration of the melting endotherm, can be a useful technique where the observation of the exothermic behaviour is not visible. Preventing recrystallisation on heating, using a fast heating rate on FDSC, provides new data for further kinetic analysis.

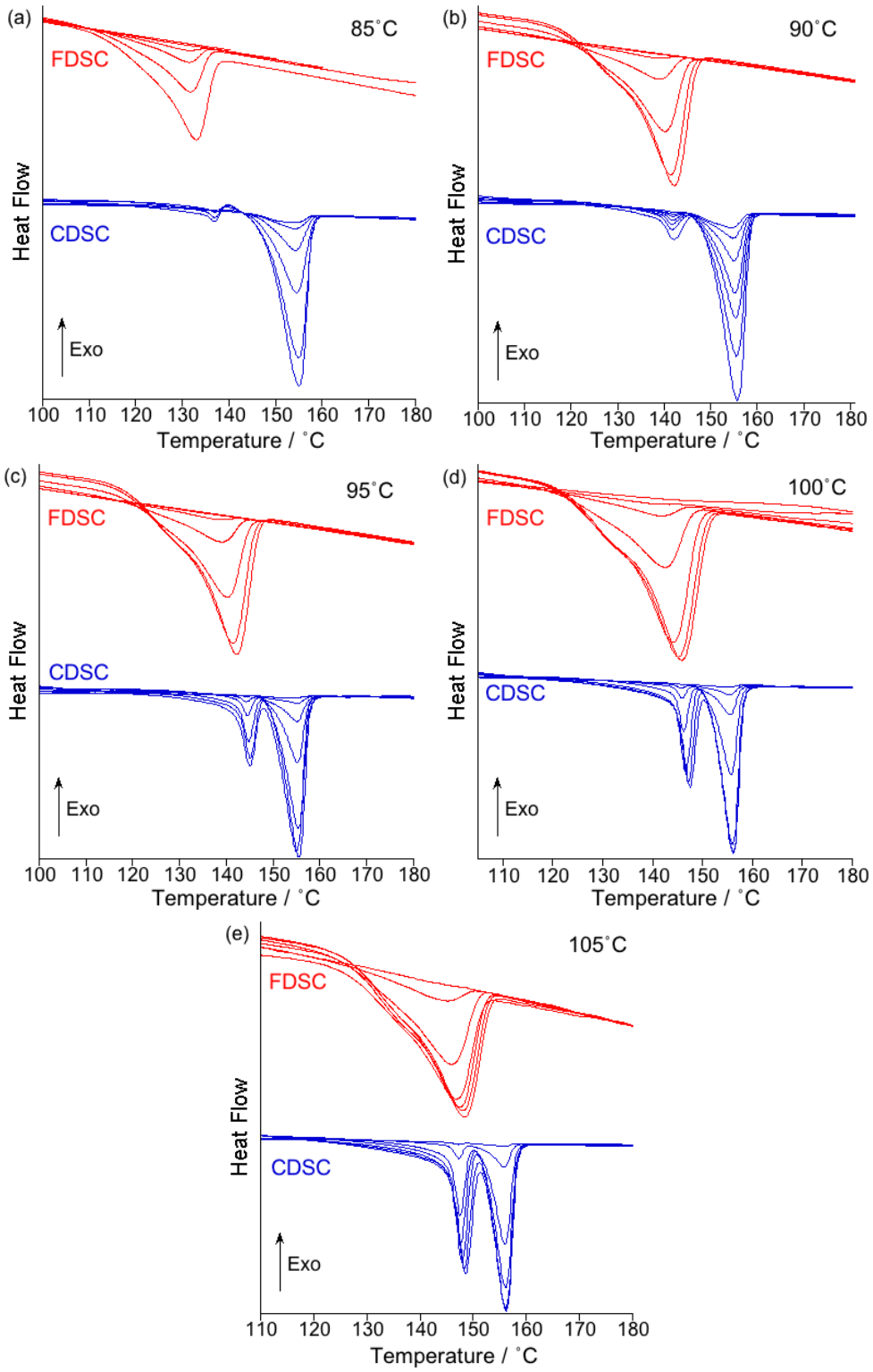

Figure 8-4 - Comparison of CDSC and FDSC traces after isothermal crystallisation at (a) 85˚C (b) 90˚C (c) 95˚C (d) 100˚C (e) 105˚C at various time intervals between 5 and 800 minutes

8.3.3.1 Avrami Analysis

The heat of fusion (shown in Figure 8-5) was recorded from the endothermic meting peaks shown in Figure 8-4. The sigmoidal primary crystallisation process was decoupled from the secondary crystallisation stage where appropriate (as shown in section 6.3) to resolve a relative crystallinity from 0 to 1 for Avrami analysis, where 1 represents the end of the primary crystallisation process.

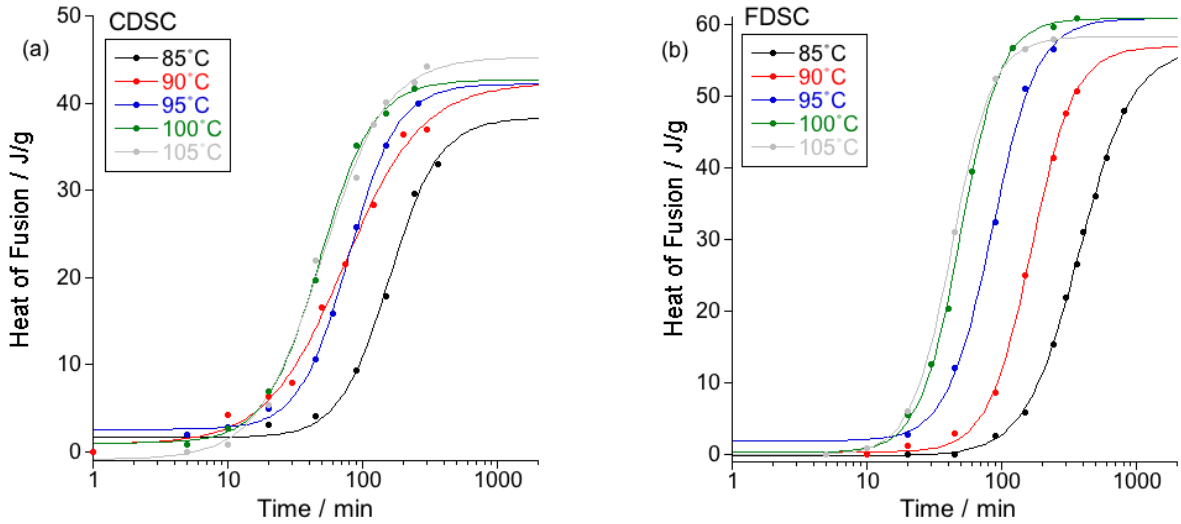

Figure 8-5 - Development of heat of fusion with log time in PLA during isothermal crystallisation between 85 and 105˚C using (a) CDSC (b) FDSC

Figure 8-6 shows the relative crystallinity of PLA in the T_c range 85 to 105˚C using CDSC and FDSC, (a) and (b) respectively. The relative crystallinity was calculated in the calorimetry techniques from the combined heat of fusion from all endotherms where applicable.

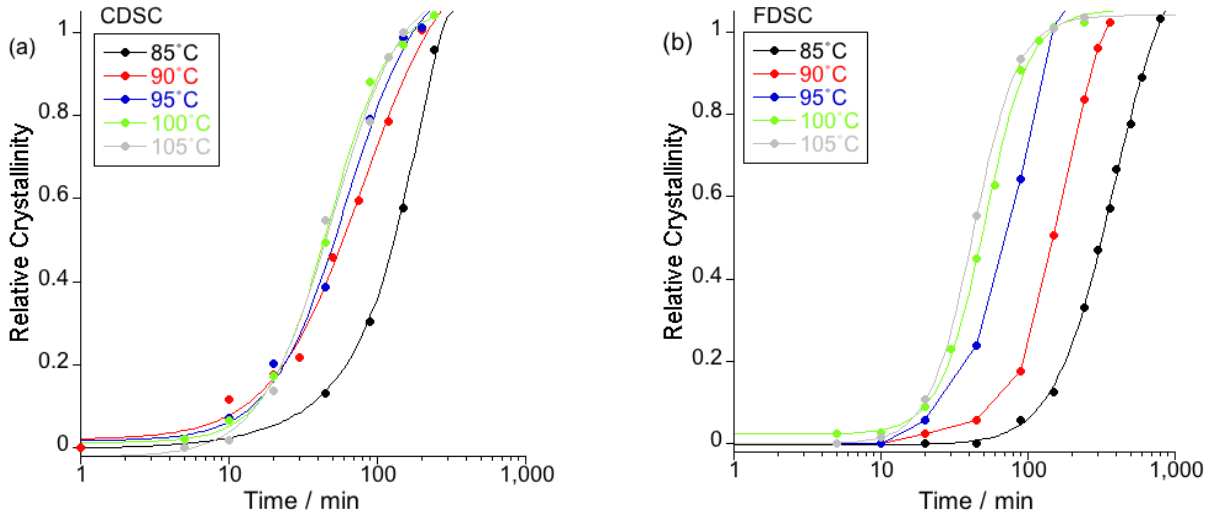

Figure 8-6 - Development of relative crystallinity with log time in PLA during isothermal crystallisation between 85 and 105˚C using (a) CDSC and (b) FDSC

Figure 8-7 (a) and (b) shows Avrami double log plots using CDSC and FDSC, respectively. Literature values taken from Zhang et al. (2015) provides data according to the exothermic heat flow recorded during isothermal crystallisation on CDSC with the same grade of PLA (2002D). Figure 8-7 (b) shows a series of straight, nearly parallel lines from data collected using FDSC. The CDSC data, shown in Figure 8-7 (a), displays irregular, closely packed lines. This non-conforming data, according to the Avrami relationship, is expected to occur from the endothermic area calculation integrating both endotherms on heating. This method of data collection from both endotherms does not provide results representative of the as-grown crystal at each isothermal T_c due to the recrystallisation behaviour seen in PLA. An accurate separation of ΔH_f from each endotherm was not possible. The gradient of the lines in the Avrami double log plots are equal to the Avrami exponent, n, and the intercept at log t is log K, where K is the Avrami rate constant (Equation 1-9). CDSC and FDSC values of n and log k are listed in Table 8-1

and illustrated in Figure 8-8. The Avrami exponent, n, according to Avrami, should be an integer value.

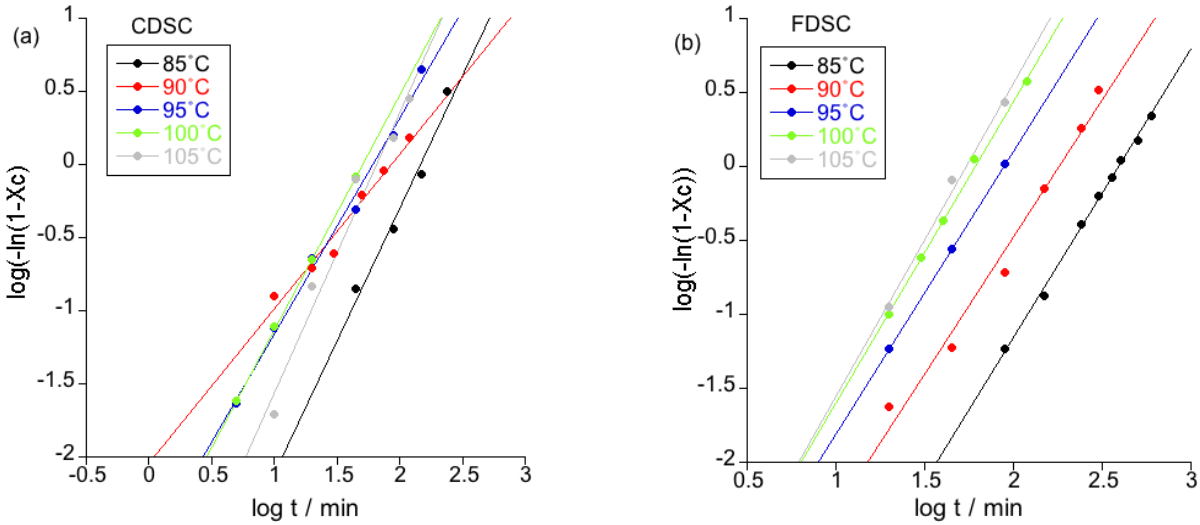

Figure 8-7 - An Avrami analysis of primary crystallisation of PLA using (a) CDSC (b) FDSC

A consistent value of 2.0±0.1 was obtained for all isothermal crystallisation temperatures using FDSC. The similarity between this data and the literature was very good, with comparable 'n' values close to 2 in the current work, using FDSC, and the literature, measuring the integral of the crystallisation exotherm (Zhang *et al.*, 2015). An Avrami value on 2 predicts the growth of disc-like crystal structures that grow in a two-dimensional plane.

Table 8-1 - Avrami 'n' and k values for CDSC and FDSC (literature values Zhang *et al.* (2015))

	Avrami exponent 'n'			Log Rate constant / min^{-n}		
Crystallisation Temperature / ˚C	CDSC	FDSC	Zhang *et al.* (2015)	CDSC	FDSC	Zhang *et al.* (2015)
85	1.8	1.9	-----	-3.91	-5.05	-----
90	1.1	2.1	1.99	-2.05	-4.18	-4.64
95	1.5	1.9	1.99	-2.64	-3.71	-4.04
100	1.6	2.0	2.03	-2.72	-3.62	-3.48
105	1.9	2.1	1.99	-3.46	-3.67	-3.67

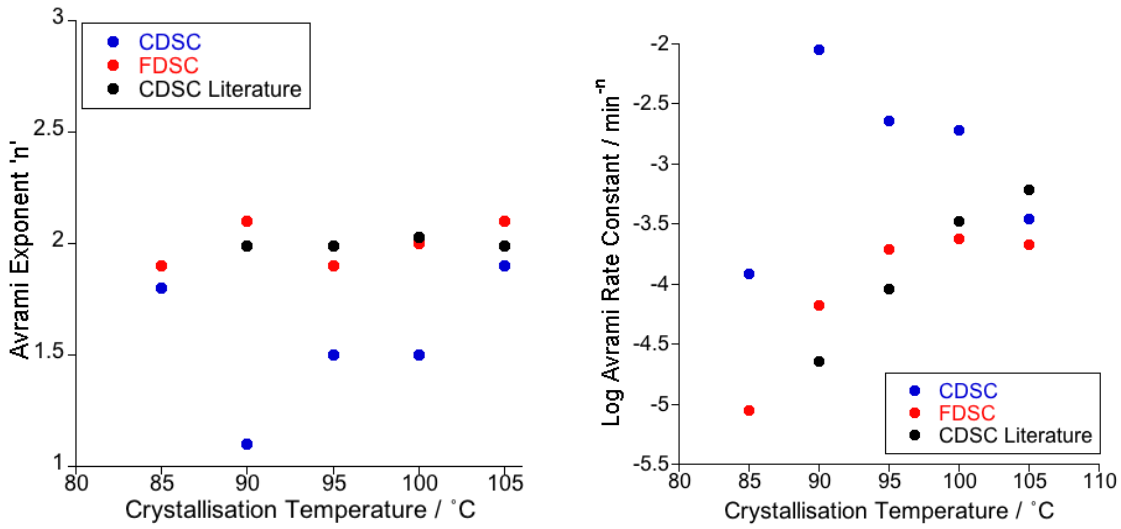

Figure 8-8 - A comparison of the Avrami analysis of 'n' and log k obtained using CDSC and FDSC (Literature values - Zhang et al. (2015))

8.3.3.2 Half-Life Analysis

Figure 8-9 shows a comparison of the crystallisation half-life using CDSC, FDSC and CDSC literature. The half-life was determined from the Avrami parameters n and log k shown in Table 8-1 using Equation 6-3. The results show a maximum crystallisation rate at 105˚C in FDSC; however, without further experimental data an accurate maximum crystallisation rate cannot be determined. This maximum is observed with a reduction in the crystallisation half-life with increased T_c. The continual reduction in the half-life using FDSC shows good agreement to the literature with an additional temperature extension to 85˚C revealing an increase in half-life as chain mobility decreases with temperature. A longer half-life at low temperature is shown using FDSC and the literature in comparison to CDSC. The combination of the enthalpy extracted from both endotherms in CDSC and the inability to prevent crystallisation during cooling (shown in Figure 8-1) increases the apparent crystallisation rate, resulting in a shorter half-life. Therefore the ΔH_f obtained from the double endotherm does not represent the true crystallisation half-life of the as-grown crystals at T_c.

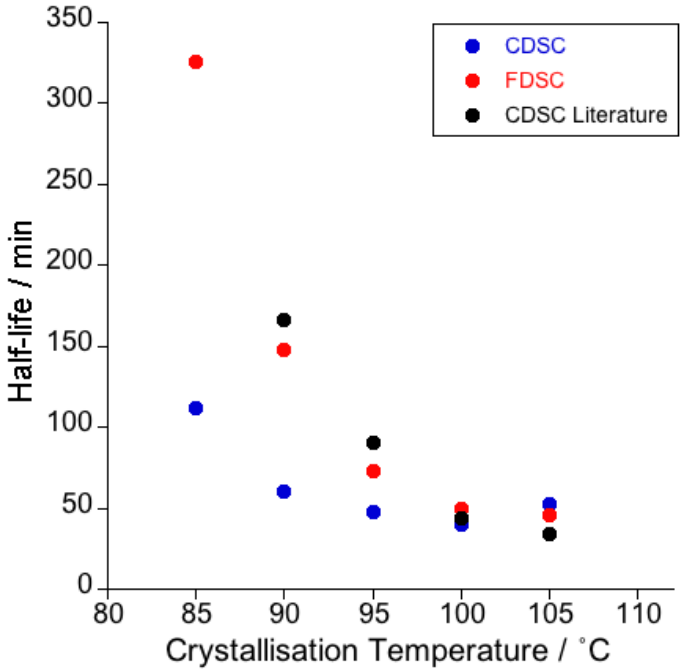

Figure 8-9 - A comparison of PLA crystallisation half-life measured using both CDSC and FDSC (Literature values - Zhang et al. (2015))

PLA half-life after crystallisation at low temperatures has been previously carried out on FDSC using a pre-nucleation methodology (Androsch and Di Lorenzo, 2013a, Androsch and Di Lorenzo, 2013b). A maximum crystallisation rate was determined at 105°C showing good agreement to the data recorded in this study. The half-life values are not explicitly defined in the study but can be seen to record a shorter half-life due an annealing stage above T_g before isothermal crystallisation introducing nuclei, influencing the crystallisation rate.

8.3.4 Temperature Dependence of Crystallisation Growth Rates

Modifying the Hoffman-Lauritzen equation (Equation 1-8) by replacing the growth rate with the reciprocal of the half-life of crystallisation permits the nucleation constant (K_g) to be determined from the gradient of the linear plot: $(In(1/t½)+(U^*/R(T_c - T_\infty))$ against $1/(T_c\Delta Tf)$ shown in Figure 8-10.

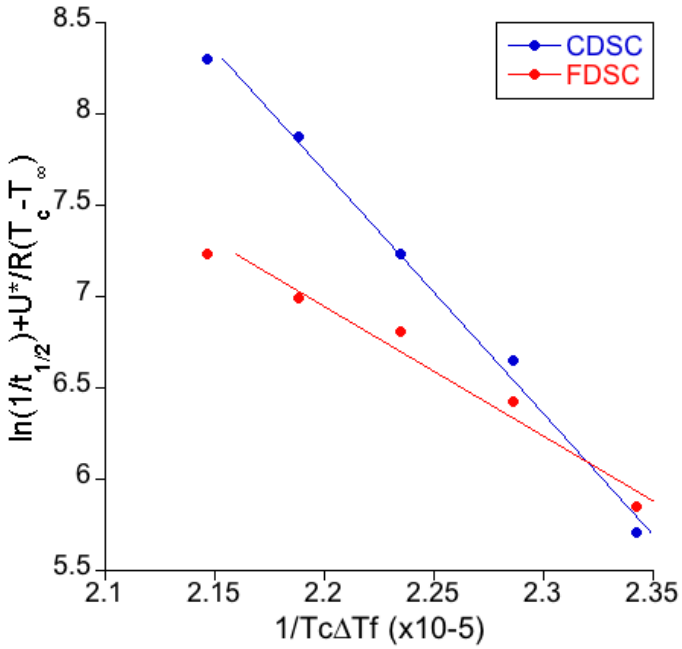

Figure 8-10 - A Hoffman-Lauritzen plot for PLA using CDSC and FDSC

The results in Figure 8-10 show different gradients in the data obtained using CDSC and FDSC. A more negative gradient is seen in the CDSC data and occurs as a consequence of the previously mentioned shorter half-life calculated from the Avrami plot in Figure 8-7. The nucleation constant and equilibrium half-life $(t½)_0$ are shown in Table 8-2. FDSC data ($6.87x10^{-5}$) does not agree with the CDSC value in this study ($13.17x10^{-5}$); however, it shows good agreement to the literature ($6.02x10^{-5}$). In this temperature range, according to previous literature on PLA, a K_g value ~$6x10^{-5}$ represents the nucleation regime III (Tsuji *et al.*, 2005, Kawai *et al.*, 2007). In Regime III the nucleation rate is much greater than the growth rate (Hoffman and Miller, 1997). A change in the nucleation regime from regime III to regime II, as K_g decreases, has been shown to occur at crystallisation temperature >120˚C, where more stable α crystals form (Abe *et al.*, 2001, Kawai *et al.*, 2007).

Table 8-2 - PLA Hoffman-Lauritzen primary crystallisation growth data

Instrument	K_g ($x10^{-5}$)	$(t_{½})_0$
CDSC	**13.17**	**$8.0x10^9$**
FDSC	**6.87**	**$3.8x10^9$**

Irregular crystallisation data obtained from ΔH_f in CDSC from the double endotherm does not agree with previous literature; however, the agreement of the Avarmi and Hoffman-Lauritzen literature values to FDSC, where the ΔH_f was recorded from melting from the single endotherm, provides accurate crystallisation data of as-grown crystals at T_c. Further comparative analysis of the crystallisation kinetics of PLA is presented in Chapter 9.

8.4 Conclusions

- A reduction in nucleation density of PLA is possible through cooling rates available on CDSC. A cooling rate between 5 and 80˚C/min is fast enough to prevent crystal growth but not nucleation. The increased rates available on FDSC show complete suppression of the crystallisation process after cooling at 100˚C/s.
- Low temperature isothermal crystallisation of PLA produces unstable as-grown crystals. Heating slowly using CDSC promotes a melting-recrystallisation-melting behaviour, resulting in double melting. The faster heating of FDSC (100˚C/s) prevents the recrystallisation of the unstable as-grown crystals resulting in a single endotherm for further kinetic analysis.
- Crystallisation kinetic analysis of PLA using the Avrami equation shows dissimilar results for the two calorimetry techniques. The collection of ΔH_f from the single endotherm shown on FDSC shows comparable results to previous literature on PLA. The combined ΔH_f from both endotherms on CDSC results in a variation of the Avrami exponent and a shortened half-life in comparison to the literature and FDSC.
- The Avrami analysis on FDSC shows good agreement to previous literature on PLA 2002D with an Avrami exponent of 2.0±0.1 and a comparable half-life with crystallisation temperature. The Hoffman-Lauritzen relationship on FDSC shows a nucleation constant comparable to previous literature, related to regime III.
- The heating rates available on FDSC provide an uninterrupted analysis of the as-grown crystals on heating through the removal of double melting and thus an independent analysis of the as-grown unstable α' crystals.

CHAPTER 9 LASER FLASH ANALYSIS OF POLY(LACTIC ACID)

9.1 Introduction

This chapter aims to measure changes in thermal diffusivity in PLA using laser flash apparatus (LFA). The beginning of the chapter investigates the change in thermal diffusivity of PLA at the glass transition temperature, between 45 and 70˚C. The later part of the chapter explores low temperature isothermal crystallisation kinetics through a change in thermal diffusivity with time. The resulting crystallisation data obtained from 'real' time measurements of thermal diffusivity with time will be compared to previous Flash DSC and conventional DSC kinetic analysis.

9.2 Instrument Modifications and Technical Procedures

Laser flash apparatus (LFA) has a temperature range from 25 to 1,600˚C and is most commonly used for ceramics and metals where diffusivity is measured at large temperature intervals, 50-200˚C. The temperature region that will be required for this work with PLA is between 25 and 105˚C. Isothermal crystallisation experiments will be carried out at 5˚C intervals from, 85-105˚C, where small errors in the sample temperature may result in large errors in the recorded data i.e. crystallisation half-life. Therefore, it is important that the temperature of the sample is accurate.

The accuracy of the LFA sample thermocouple located on the apparatus tube (Figure 4-9) was compared to a calibrated external thermocouple. The external thermocouple was attached to the apparatus tube next to the LFA sample thermocouple to measure as accurately as possible any temperature deviation. To ensure the temperature of the

furnace was equalised, average thermocouple temperatures were measured over a 10-minute period (Figure 9-2). The average temperatures of the external thermocouple, at five isothermal temperatures, are shown in Table 9-1. The temperature of the external thermocouple was >3˚C higher than the LFA sample thermocouple at all isothermal temperatures. The thermocouple within the LFA does not provide an accurate representation of the temperature between 85 and 105˚C; therefore, the temperature recorded using the external thermocouple will be taken as the corrected value.

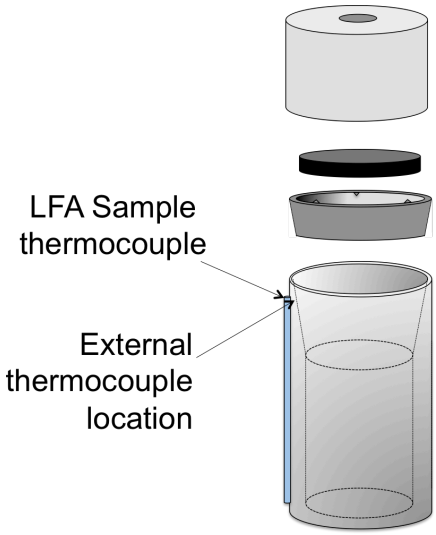

Figure 9-1 - Sample holder apparatus showing the location of the external sample thermocouple and LFA sample thermocouple. The external thermocouple location for temperature calibration was next to the LFA sample thermocouple to determine errors in the thermocouple readings

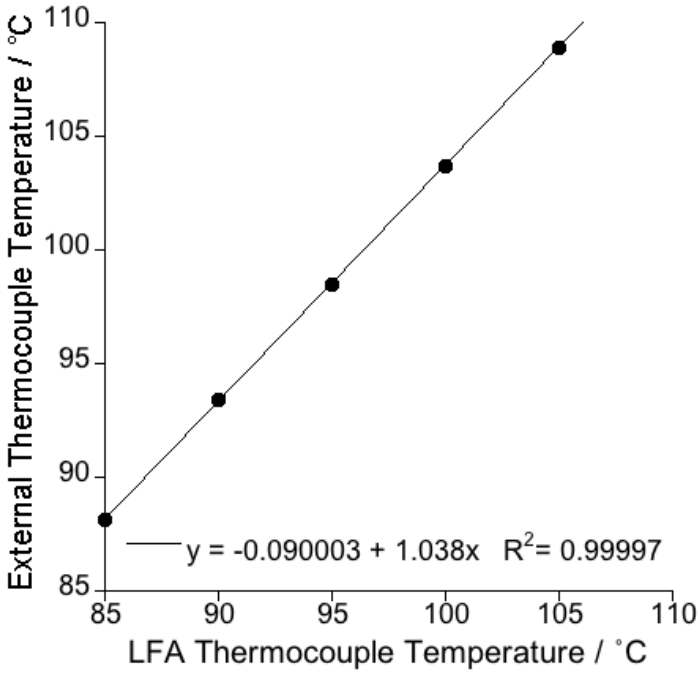

Figure 9-2 - The difference between the LFA sample thermocouple and the external thermocouple temperature

Table 9-1 - The temperature difference between LFA sample thermocouple and external thermocouple temperature

LFA Sample Thermocouple Temperature / ˚C	External Thermocouple Temperature / ˚C
85	**88.1**
90	**93.4**
95	**98.5**
100	**103.7**
105	**108.9**

9.3 Sample Temperature Calibration

The external thermocouple temperature location was changed from the initial furnace temperature measurement and placed on the top surface of the sample, providing a direct temperature profile of the sample surface (Figure 9-3).

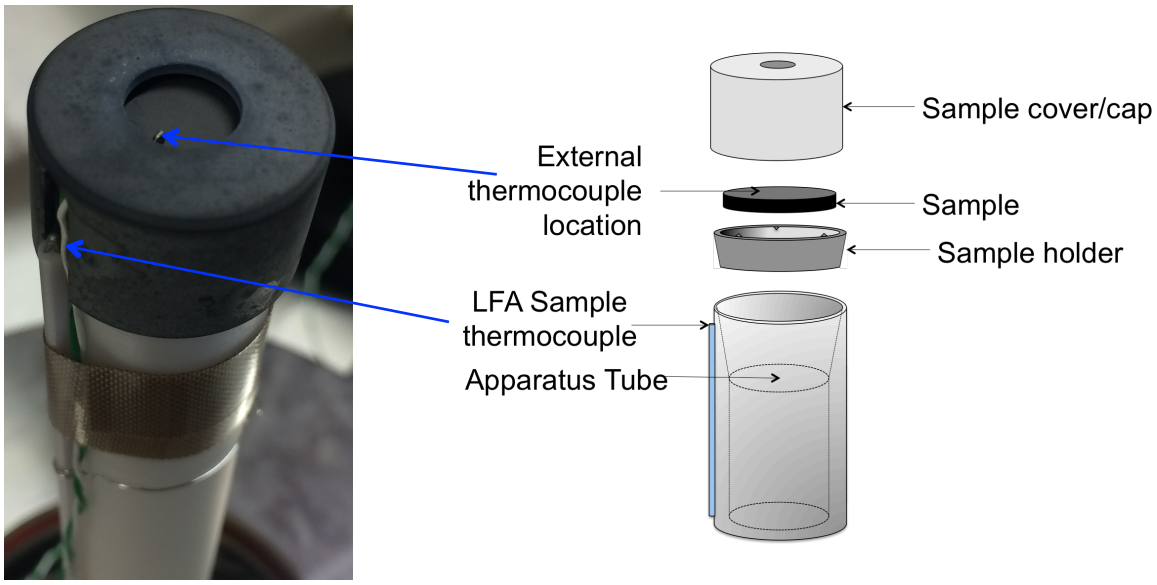

Figure 9-3 - The location of the LFA sample and external thermocouple

Figure 9-4 (a) shows a 1.4˚C increase over 5 seconds as the heat pulse from the laser passes through the sample. This temperature change is an unavoidable consequence of the technique. In the application of an isothermal experiment this technique would not provide a continual isothermal condition due to this sample temperature fluctuation. However, it has been shown in previous literature that isothermal conditions are never possible due to temperature change of the sample during thermal transitions. Guan and Phillips (2005) found a stabilisation in the temperature of the crystal growth face during cooling as crystallisation required a constant temperature at the growth face, preventing a reduction in the programmed temperature. The change in crystal growth rate with time corresponds to the temperature stabilisation causing deviation in the sample

temperature by up to 30˚C from the expected temperature profile. Therefore, a temperature rise of 1.4˚C, caused by the laser pulse over a 5 second period of crystallisation in slow crystallising poly(lactic acid) (PLA), can be assumed to have a minimal affect on the overall crystallisation rate.

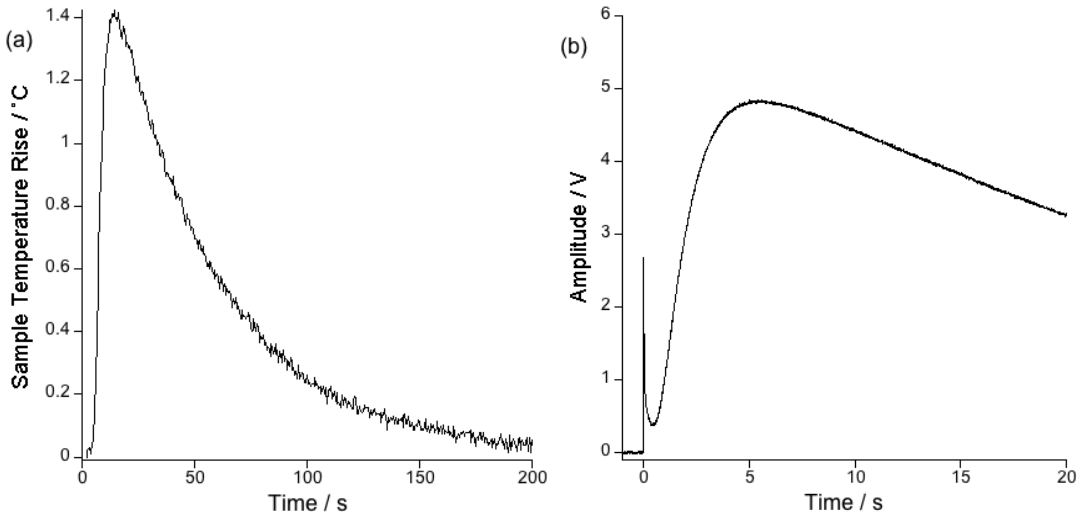

Figure 9-4 - (a) Temperature profile of a PLA sample from the time of the laser shot recorded from the external thermocouple temperature and (b) the IR detector voltage change with time

According to the parameters available in the proprietary software, laser shots can be fired at the sample every minute. The impact of multiple laser shots in a short time period on a polymer sample may increase the sample temperature over time. The time required for the sample temperature to return to the furnace temperature was found to be in the region of 200 seconds (Figure 9-4). Therefore, a minimum shot time interval of three minutes (180 seconds) is considered sufficient in a multiple laser shot method to ensure sample temperature returns to the furnace temperature.

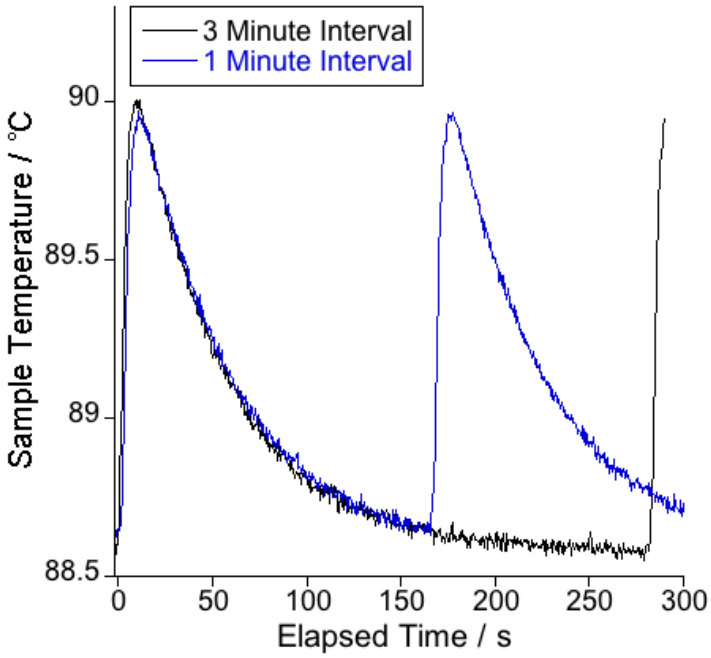

Figure 9-5 - A comparison of the interval between the programmed and experimentally timed laser shot

To ensure the heat from the laser pulse was dissipated from the sample prior to the next shot, a multiple shot method was used with a programmed shot interval times of one and three minutes. Figure 9-5 shows the time recorded between laser shots was 165 and 280 seconds for a programmed one- and three-minute intervals respectively. This anomaly occurs as a consequence of the proprietary software ensuring that temperature and baseline IR voltage are acceptable before each laser shot is fired.

The time interval between successive one-minute shots was too close to the time required for the sample to return to the furnace temperature; therefore, a multiple one-minute shot method was used to observe the maximum temperature of the sample over a one-hour period. Figure 9-6 shows a continual maximum temperature of the sample throughout the programmed one-minute shot interval. The complete recovery of sample temperature is not required for the calculation of thermal diffusivity and therefore, a

cool down period of 165 seconds is sufficient in maintaining a constant sample temperature.

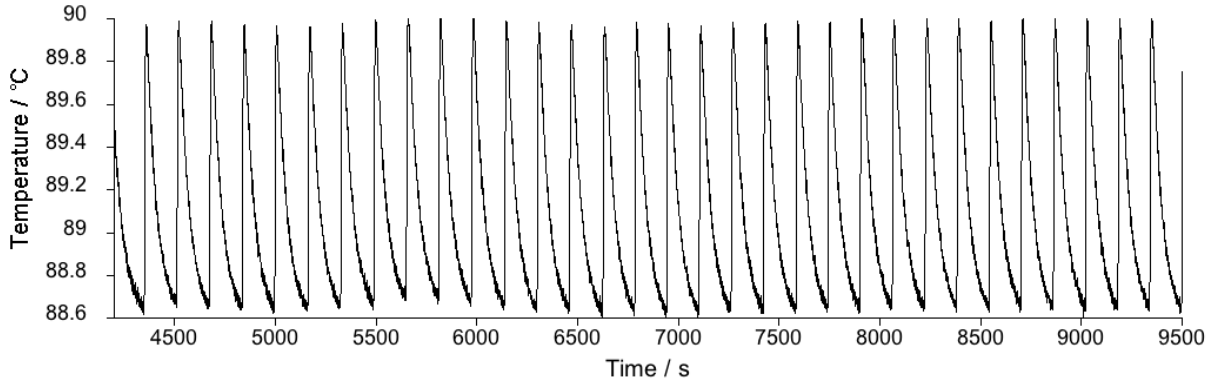

Figure 9-6 - Sample temperature with time as multiple laser shots are applied at a programmed interval of one minute

9.4 Results and Discussion

9.4.1 Glass Transition Temperature Analysis

A thermal diffusivity reduction of 0.046 mm^2/s is shown in amorphous PLA (blue data) in Figure 9-7 as temperature increases from 40 to 70˚C. In contrast, in semi-crystalline PLA (red data), crystallised at 130˚C for 64 hours, a smaller reduction in diffusivity is observed, 0.022 mm^2/min, approximately half that of the amorphous sample (Figure 9-7). A second semi-crystalline sample of PLA (black) was isothermally crystallised at 70˚C for 4 hours and a smaller drop in thermal diffusivity was apparent (0.034 mm^2/s) in contrast to the amorphous sample, but a larger drop compared to the other semi-crystalline sample, 130˚C.

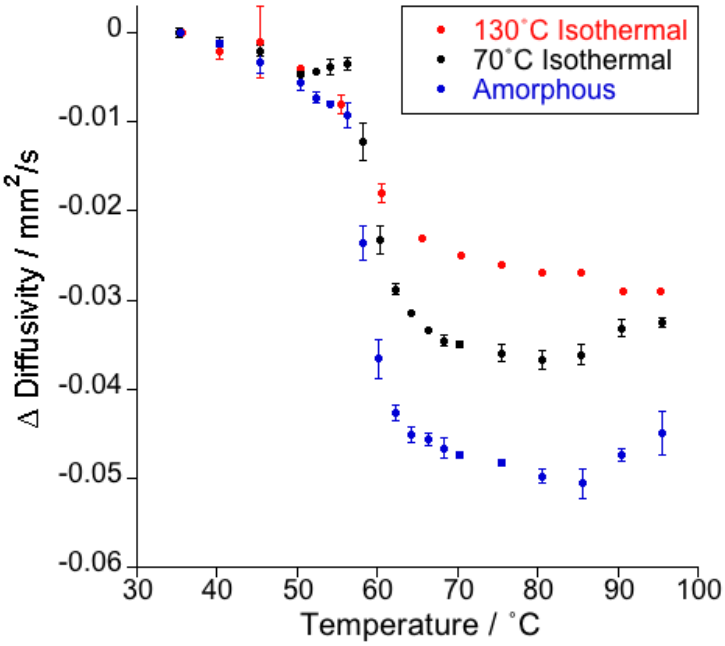

Figure 9-7 - The change in diffusivity with temperature in samples with differing thermal treatment; quench cool – amorphous, isothermal crystallisation for 64 hours at 70˚C and 130˚C

The repeatability of thermal diffusivity measurements presented sample-to-sample errors in the thermal diffusivity at equivalent temperatures. These errors could result from a number of reasons: inclusions in the sample, thickness of carbon spray or the diffusivity measurement limit of the LFA. The conductive carbon spray was applied to individual samples and therefore may have resulted in different thicknesses influencing thermal diffusivity, but the influence of the carbon spray thickness (3.5±0.5μm) would be minimal. The diffusivity measurement of polymers is limited by the error on the LFA (a minimum accuracy of 0.01mm^2/s); however, the thermal diffusivity change from below T_g to above T_g was maintained irrespective of the starting thermal diffusivity value at 35˚C. Therefore, it can be stated that although samples were visually both solid and absent of bubbles, the variation in the sample to sample diffusivity values at 35˚C

results in the assumption that inclusions may be present in the samples in the form of air or impurities.

Although the repeatability of a direct thermal diffusivity values can be varied, the change in the sample diffusivity was consistent across samples. Therefore, the change in diffusivity was used to show a more accurate comparison between samples with differing morphologies.

A similar difference in semi-crystalline and amorphous samples can be shown through the change in the specific heat (ΔC_p) at T_g in CDSC. A larger ΔC_p is shown in Figure 9-8 for an amorphous sample compared to a semi-crystalline sample. The ΔC_p values for all samples are shown in Table 9-2 where a larger ΔC_p is shown for the semi-crystalline sample held at 70˚C compared to the sample isothermally crystallised at 130˚C.

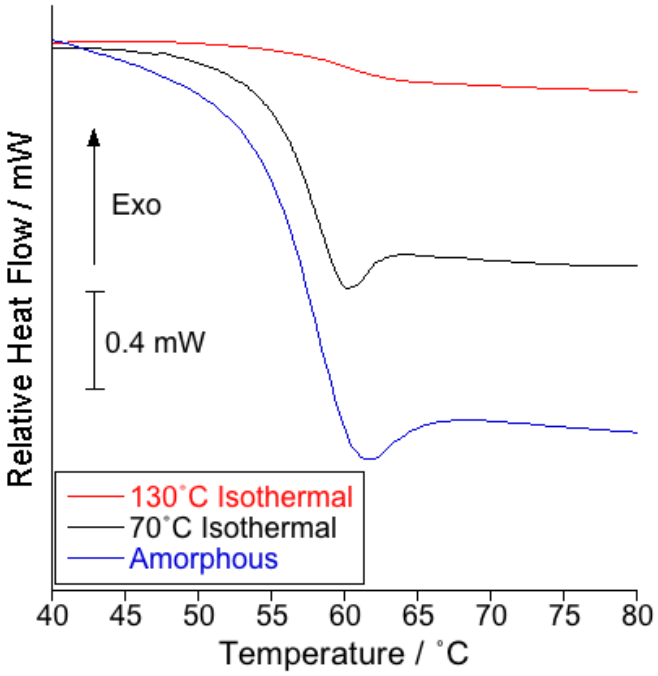

Figure 9-8 - Relative heat flow using CDSC from 40 to 80˚C in amorphous PLA, and semi-crystalline PLA isothermally crystallised at 70˚C and 130˚C

Table 9-2 - A comparison of the change in specific heat and change in diffusivity in the glass transition temperature region (between 40 and 70˚C)

	Crystallinity (%)	ΔC_p (J/g˚C)	Δ Diffusivity (mm^2/s) ±0.002	ΔC_p / ΔDiffusivity
Amorphous	**<1***	**0.53**	**0.046**	**11.5**
70˚C	**28 ±5**	**0.38**	**0.034**	**11.7**
130˚C	**55 ±5**	**0.24**	**0.022**	**10.9**

*Less than 1% crystallinity can be shown after cooling at 80˚C/min in Figure 8-1, air-cooling is faster than 80˚C/min and thus can be assumed <1%.

The ΔC_p measured using CDSC occurs as the amorphous regions within PLA gain enough thermal energy to allow molecular motion. In the case of amorphous PLA, this is 100% of the sample. The semi-crystalline sample isothermally held at 130˚C for 4 hours

reveals a single high temperature endotherm on heating (Figure 9-9); which, by integrating the melting endotherm, ΔH_f was calculated to measure the degree of crystallinity, 0.51. According to ΔC_p, the crystalline fraction in semi-crystalline PLA, held at 130˚C, can be estimated as 0.55, from the ratio of ΔC_p of semi-crystalline and amorphous PLA using Equation 9-1 showing good agreement to ΔH_f.

$$Crystalline\ Fraction = 1 - \frac{\Delta C_p(c)}{\Delta C_p(a)}$$

Equation 9-1

The semi-crystalline sample isothermally held at 70˚C grows unstable crystals with a low melting temperature (T_m) undetectable on CDSC (Figure 9-9). The recrystallisation behaviour shown in Chapter 8, after low temperature isothermal crystallisation, prevents the measure of as-grown crystals. Therefore, to predict the degree of crystallinity, the crystalline fraction of semi-crystalline PLA, held at 70˚C, was calculated as 0.28 using (Equation 9-1). The presence of crystals was also shown using hot stage microscopy to verify crystallisation at 70˚C, shown in Figure 9-10.

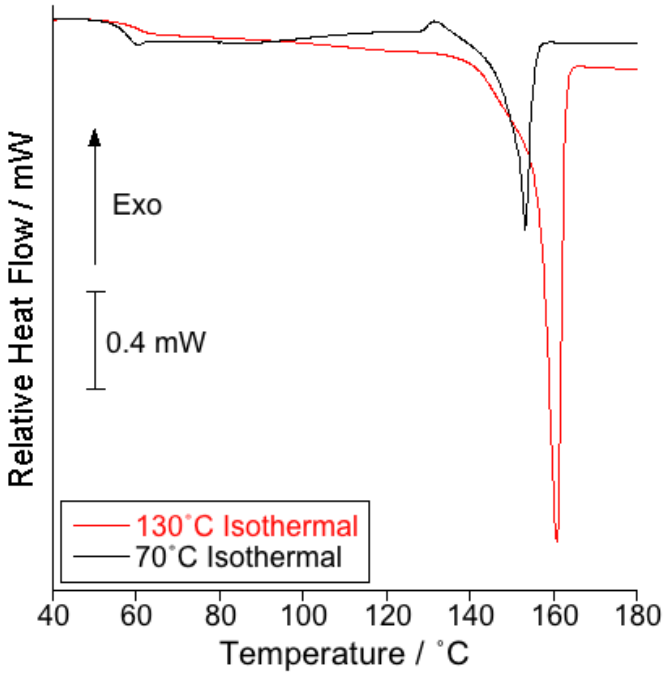

Figure 9-9 - Semi-crystalline PLA isothermally crystallised at 70 and 130˚C

A comparable ratio of the change in specific heat and change in diffusivity is shown in Table 9-2. A good relationship between the change in diffusivity and ΔC_p can conclude that the reduction in the diffusivity at T_g is a consequence of a change in the amorphous region in PLA, decreasing the phonon mean free path. The amorphous chains undergo two changes at T_g that promote scattering of phonons: increases in molecular motion and free volume.

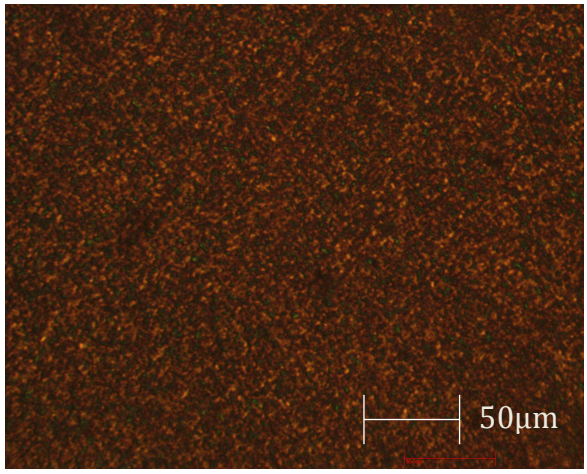

Figure 9-10 - A hot stage microscopy image through a polarisation filter of PLA spherulites grown at 70˚C from a thin film

9.4.2 Isothermal Crystallisation on Laser Flash Analysis

A rise in thermal diffusivity with temperature indicates an increased phonon free path and a reduction in phonon scattering associated to growth of crystal structures. PLA, as shown in Chapter 8, has along half-life of crystallisation in comparison to PCL and PEEK (Chapter 6 and 7 respectively). PLA provides an opportunity to observe thermal diffusivity change with temperature under isothermal conditions. A control experiment was carried out ~10˚C below T_g, at 45˚C to ensure no change in thermal diffusivity was recorded with time. A linear regression provides evidence that a change in diffusivity is not a consequence of error within the LFA measurements[17].

Five isothermal crystallisation temperatures were chosen between 88.1 and 108.9˚C (temperature calibration from 85-105˚C). There are two district regions that exhibit a near linear variation of diffusivity with time. These regions correspond to primary and secondary crystallisation processes that resemble data shown on PET using FTIR (Chen

[17] Diffusivity data at 45˚C is shown in the Appendix

et al., 2013, Chen *et al.*, 2016). Primary crystallisation is shown by a steep increase in thermal diffusivity as the polymer chains develop long-range order within the system, increasing the phonon mean free path. The increase in crystallinity decreases the defect scattering and free volume in the randomly orientated amorphous region. This initial increase in thermal diffusivity can be compared to isothermal experiments on CDSC and FDSC (Chapter 8), where an increase in the change of heat of fusion is observed with time (Xiao *et al.*, 2010, Cai *et al.*, 2011, Zhang *et al.*, 2015).

The second region corresponds to secondary crystallisation, a one-dimensional diffusion controlled process after primary crystallisation and crystal impingement has occurred (Schultz, 1969, Cai *et al.*, 2011). The increase in the lamella thickness during secondary crystallisation increases the mean free path of the phonons, increasing thermal diffusivity of PLA.

To enable comparison of the data and further kinetic analysis, the change in diffusivity with time was extracted from the raw data in Figure 9-11 and converted to a relative diffusivity from 0 to 1. Figure 9-12 shows the intersection between the tangent of the primary and secondary regions (representing the relative diffusivity value 1) enabling the secondary crystallisation data to be decoupled from the primary data (shown in Chapter 6). The separation of primary and secondary processes enables an Avrami analysis to be conducted. The relative crystallinity data against log time for all crystallisation temperatures is shown in Figure 9-13. A clear increase in the rate of crystallisation can be observed with an increase in T_c.

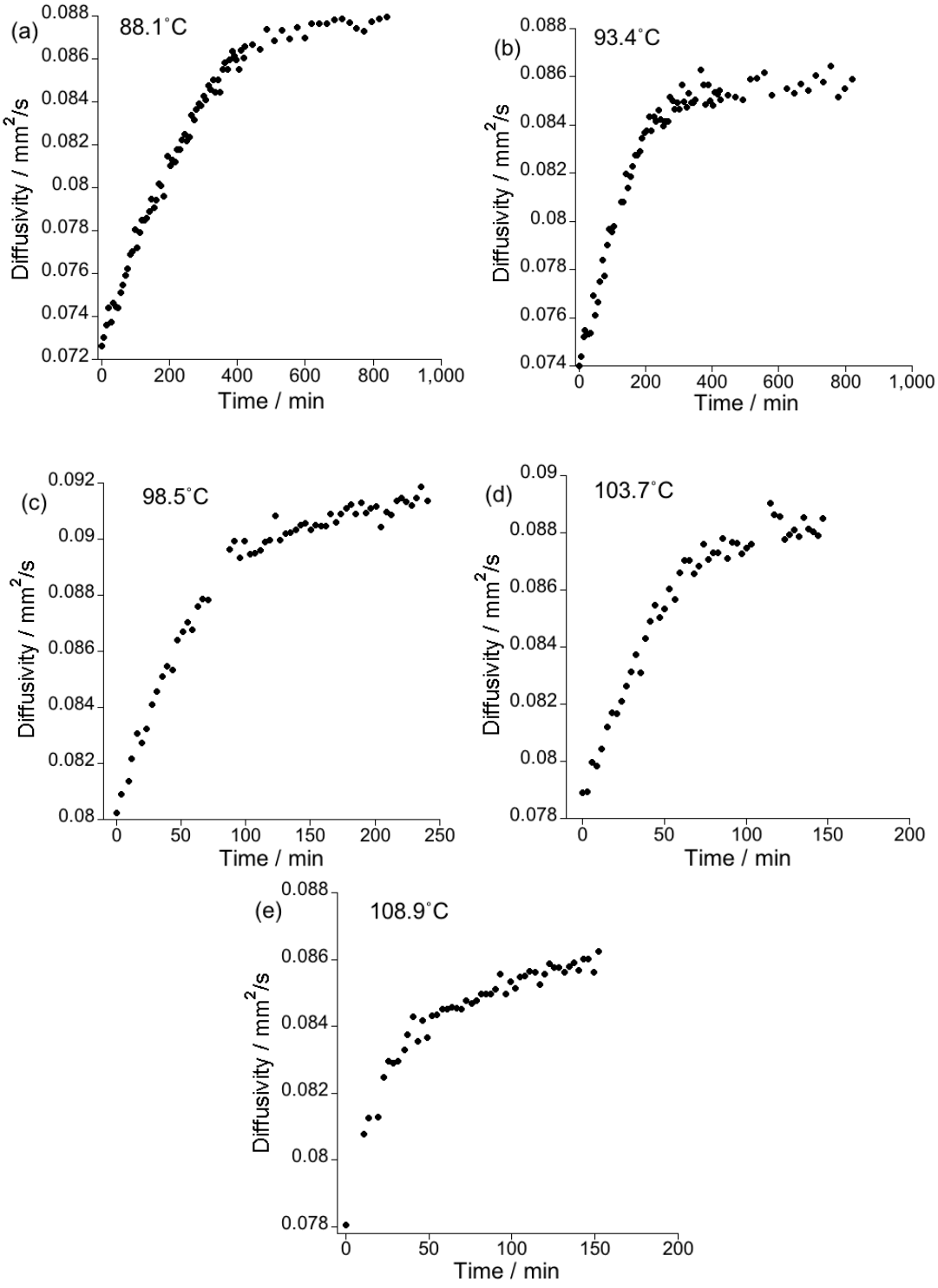

Figure 9-11 - Thermal diffusivity of PLA with time at (a) 88.1˚C, (b) 93.4˚C (c) 98.5˚C, (d) 103.7˚C, (e) 108.9˚C. Each data point defines one laser shot measurement

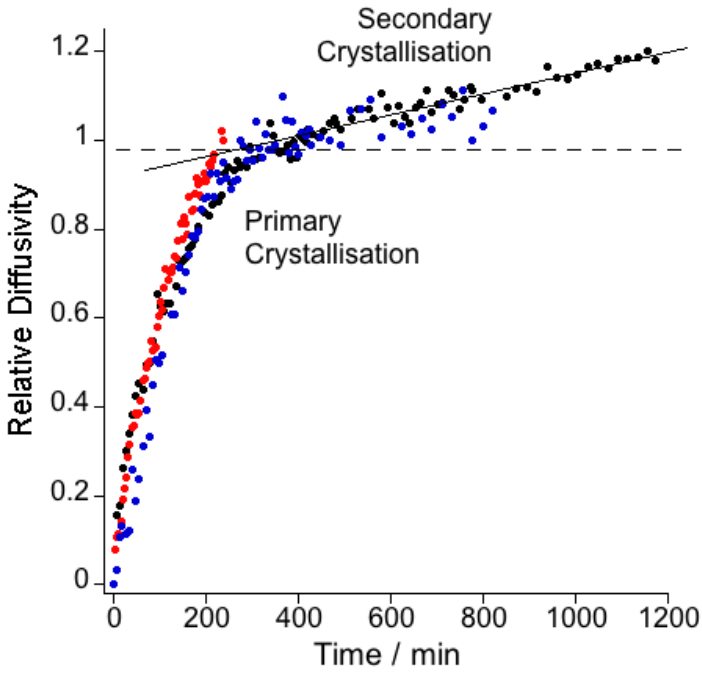

Figure 9-12 - The intersection of the linear primary and secondary crystallisation regions shows end of primary crystallisation and is equal to a relative crystallinity of 1. Isothermal crystallisation diffusivity measurements at 93.4˚C

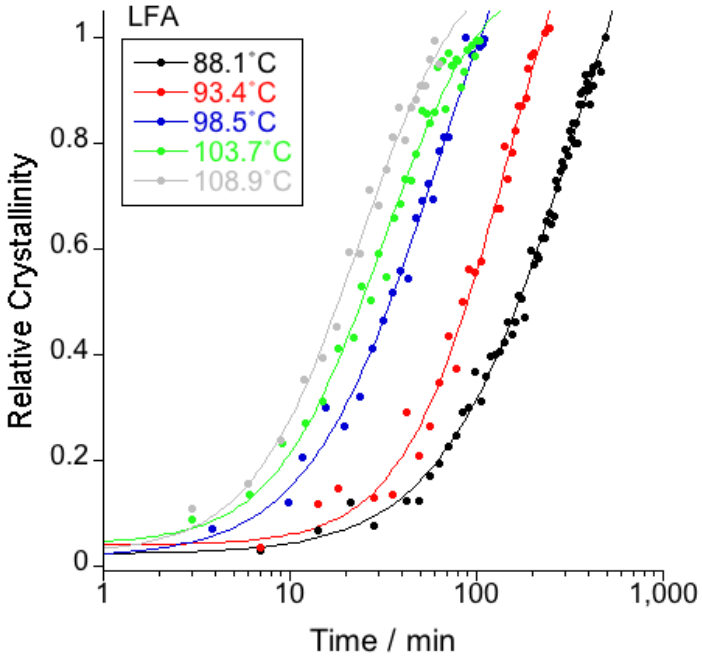

Figure 9-13 - The development of crystallinity with time in PLA during cold-crystallisation measured using LFA

Figure 9-14 shows an Avrami double log plot of all crystallisation data recorded at different isothermal crystallisation temperatures. A series of straight, nearly parallel lines were obtained from the Avrami plot. The gradient of the lines in the Avrami double log plot are equal to the Avrami exponent, n, and the intercept at log t is the log of the rate constant, K (Equation 1-9). The Avrami exponent 'n' values are listed in Table 9-3 and show a constant value of 2.0±0.1. The 'n' value of 2 predicts the growth of disc-like crystal structures in a two-dimensional plane. The Avrami parameters were required to calculate the crystallisation half-life using Equation 1-12 and are also shown in Table 9-3. The 'n' values show good agreement to results obtained by Zhang *et al.* (2015) on the same grade of PLA calculated from the exotherm on CDSC (CDSC literature).

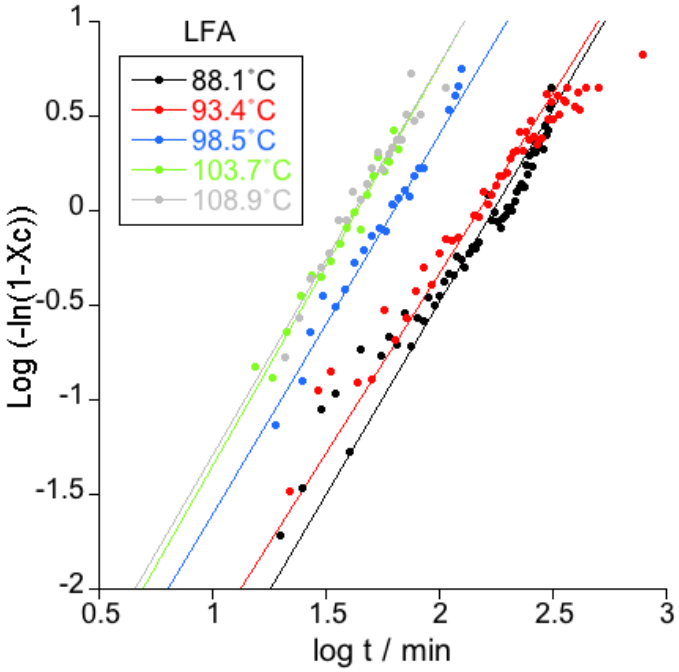

Figure 9-14 - Avrami double log plot for primary crystallisation of PLA between 88.1 and 108.9°C using LFA

Table 9-3 - Crystallisation half-life, Avrami rate constant and exponent recorded from isothermal crystallisation temperatures between 88.1 and 108.9˚C using LFA

Crystallisation Temperature / ˚C	Half-Life / min	Rate constant 'log k' / min^{-n}	Avrami exponent 'n' ±0.1
88.1	158.28	-4.6038	2.0
93.4	123.01	-4.1193	1.9
98.5	52.08	-3.6000	2.0
103.7	36.60	-3.4705	2.1
108.9	35.34	-3.3480	2.1

Figure 9-15 shows a comparison of the crystallisation half-life calculated from the Avrami parameters n and log k using Equation 6-3. The results show a reduction in the crystallisation half-life with increased T_c and a good comparison to the CDSC literature data.

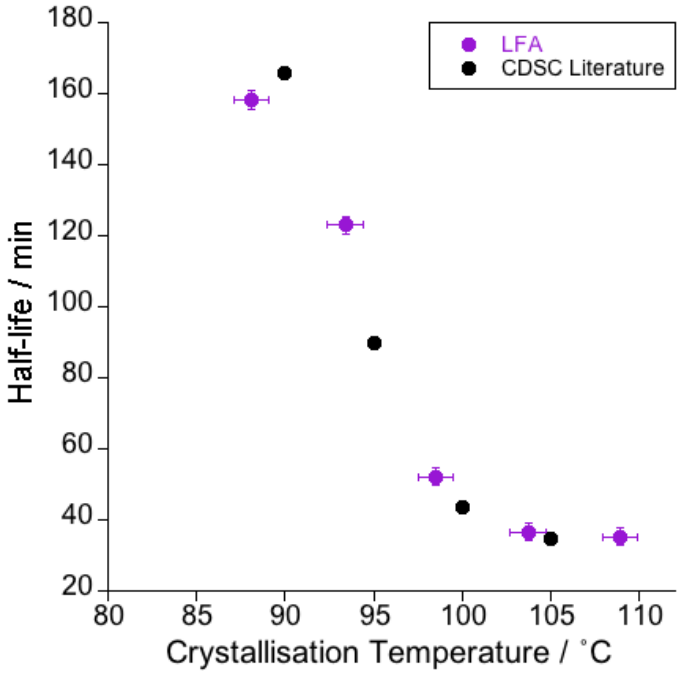

Figure 9-15 - The crystallisation half-life of PLA as a function of crystallisation temperature[18]

The primary crystallisation reciprocal of half-life can be used to substitute growth rate in the Hoffman-Lauritzen relationship (Equation 1-9). Figure 9-16 shows a $(In(1/t_{½})+(U^*/R(T_c - T_\infty))$ against $1/(T_c\Delta Tf)$ plot of the crystallisation data recorded on LFA. A linear relationship shows a single nucleation regime at low crystallisation temperatures. The growth of unstable α' crystals at low temperature occurs through regime III according to comparative literature data ($6.02x10^{-5}$) (Kawai *et al.*, 2007). The nucleation constant (K_g) was $6.58x10^{-5}$, determined from the gradient ($-K_g$) of the linear plot $(In(1/t_{½})+(U^*/R(T_c - T_\infty))$ against $1/(T_c\Delta Tf)$, and the equilibrium half-life $(t_{½})_0$ was $2.0x10^{9}$.

[18] The error on the x-axis is an average of the change in temperature of the sample due to the laser shot and the y-axis error shows the standard deviation

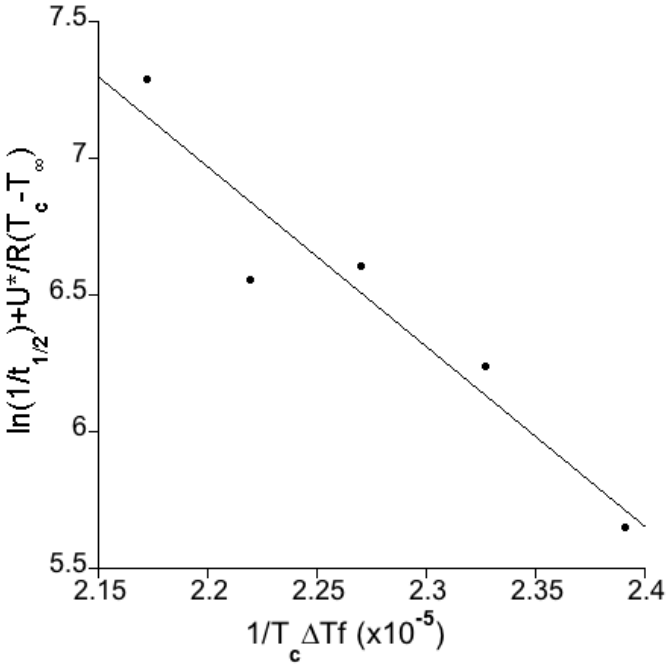

Figure 9-16 - A Hoffman-Lauritzen plot for PLA using LFA

Table 9-4 - Hoffman-Lauritzen primary crystallisation growth data

Instrument	K_g (x10^{-5})	$(t_{½})_0$
LFA	6.58	2.0x10^9

9.5 Comparison of LFA crystallisation kinetics with FDSC

The results obtained from FDSC (Chapter 8) and LFA provide an uninterrupted set of data, representing as-grown crystals grown at low temperature. The data presented using CDSC (Chapter 8) shows the change in enthalpy on heating delivering data from both as-grown and recrystallisation endotherms, accurate separation of the data was not possible and thus the total enthalpy change was considered. A comparison of the LFA and FDSC shows a novel insight into the collection of crystallisation kinetic data by preventing double melting during heating and real time collection of diffusivity data with crystallisation time (Figure 9-17).

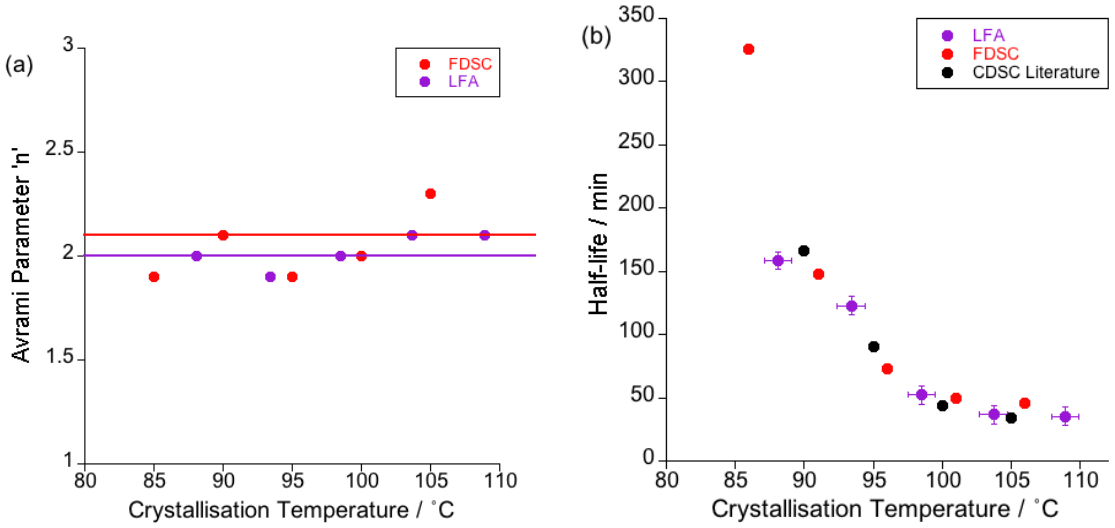

Figure 9-17 - A comparison of kinetics data collected using LFA and FDSC (a) Avrami exponent 'n' and (b) crystallisation half-life data

The Avrami exponent 'n' shows a continuous value of 2.0±0 for both LFA and FDSC. The similarity between the two techniques shows a good representation of the as-grown crystal growth mechanism recorded using the change in the enthalpy and the change in diffusivity for FDSC and LFA respectively. The elimination of the recrystallisation peak in the analysis of both techniques provides comparable results and to literature values on CDSC, n=2.0±0.1 (Zhang *et al.*, 2015). The half life-values show an excellent comparison across both techniques. The variability in the half-life with sample size in PLA expressed in Chapter 4 can be ignored from this data due to the FDSC sample size showing accuracy and comparison to the LFA and the reported CDSC literature values.

Finally, a comparison of the Hoffman-Lauritzen relationship provides further evidence for the kinetic analysis of PLA obtained through LFA and FDSC (Figure 9-18). The results show nearly parallel lines in the analysis with similar nucleation constants that are comparable to literature data (6.02×10^{-5}) (Kawai *et al.*, 2007). The nucleation constant (K_g) and $(t½)_0$ values are shown in Table 9-5.

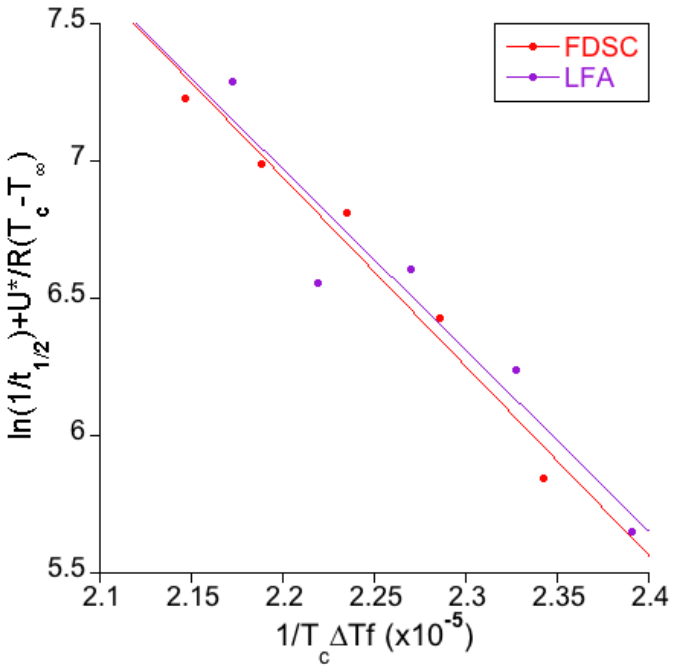

Figure 9-18 - A comparison of K_g from data obtained through LFA and FDSC

Table 9-5 - Hoffman-Lauritzen primary crystallisation growth data

Instrument	K_g (x10^{-5})	$(t_{½})_0$
FDSC	6.87	3.8x10^9
LFA	6.58	2.0x10^9

9.6 Conclusion

- The calibration of the LFA furnace temperature presented >3˚C deviation in all isothermal temperatures. The calibration of the LFA temperature also resulted in the discovery of a sample temperature rise of 1.4˚C as a consequence of the laser shot, where an elevated sample temperature was maintained for ~200 seconds
- The increase in molecular motion of the polymer chains induced through thermal energy at the glass transition temperature reduces the thermal diffusivity of the sample as chain motions induce scattering of phonons. Small spherulites grown close to T_g have a larger impact on the scattering of phonons representing a larger drop in diffusivity at T_g in comparison to larger spherulites grown close to T_m
- Crystallisation of PLA chains under isothermal conditions was recorded with a change in diffusivity of the sample with time. The increase in diffusivity was comparable to calorimetry and FTIR experiments where crystallinity is measured with time
- The change in diffusivity was converted to a relative diffusivity and applied to an Avrami analysis and Hoffman-Lauritzen relationship. The growth of two-dimensional disc-like crystals and a nucleation constant comparable to regime III showed good agreement to previous literature
- A final comparison of the LFA and FDSC shows a novel insight into the collection of crystallisation kinetic data through the prevention of double melting on heating and the real time collection of diffusivity data with crystallisation time

CHAPTER 10 CONCLUSIONS AND FURTHER WORK

10.1 Conclusions

Flash DSC, a relatively new chip calorimeter, has been used to produce a number of novel findings across a range of thermoplastics: poly(ε-caprolactone) (PCL), poly(ether-ether-ketone) (PEEK) and poly(lactic acid) (PLA). PCL crystallisation half-life was faster on Flash DSC (FDSC) than shown in the literature on conventional DSC (CDSC). Nuclei formed rapidly, growing in rod or disc-like crystal structures, consistent with Avrami exponent 1, at temperatures between 5 and 30˚C and ~2 at 40˚C. Samples of approximately 50 ng have a surface area to volume ratio 100 times greater than a 5 mg CDSC sample. It was suggested that small samples (~50 ng) generate a large number of heterogeneous nuclei on the sample surface, initiating faster crystallisation.

The temperature dependence upon crystallisation growth rate was completed for the first time on PCL using FDSC. This study presented a change in nucleation regime between 15 and 20˚C from regime II to regime I.

FDSC enabled analysis of double melting in PEEK, showing a reduction in peak melting temperature (T_m) and size with elevated heating rates. The reduction and removal of the upper endotherm enabled a new insight into the equilibrium melting temperature (T_m^0), independently analysing the crystals grown at the crystallisation temperature (T_c). The optimum heating rate for a Hoffman-Weeks analysis of PEEK was found to be 1,500˚C/s, producing a thickening factor equal to one and a T_m^0 equal to 156.95˚C ± 0.25˚C. Rapid

cooling to T_c prevented non-isothermal crystallisation and in addition to applying a range of heating rates as specified by Hoffman and Weeks, T_m^0 was calculated lower than previously reported in the literature.

FDSC prevented recrystallisation in PLA resulting in a T_m equal to the lower of the two temperature endotherms exhibited using CDSC. FDSC was subsequently used to perform an Avrami analysis of PLA at low crystallisation temperatures between 85 and 105˚C. An Avrami exponent value of 2 suggested disc-like growth of crystals showing good agreement to results obtained in the literature using exothermic data on CDSC. The temperature dependence upon crystallisation growth rate was completed for the first time on PLA using FDSC, demonstrating nucleation of crystal growth through regime III. Heat of fusion data recorded from double melting using CDSC illustrated the inaccuracy of this method from recrystallisation enthalpy.

Finally, laser flash apparatus (LFA) was used to measure changes in thermal diffusivity in thermally treated PLA between 45 and 70˚C. Larger crystal size and greater crystallinity percentage resulted in a smaller reduction in thermal diffusivity between glassy and rubbery states. The difference in thermal diffusivity was comparable to the change in specific heat measured using CDSC.

For the first time, crystallisation kinetics were measured using LFA, showing a change in thermal diffusivity with time during isothermal crystallisation of PLA. During low temperature isothermal crystallisation of PLA, a significant increase in thermal diffusivity was observed, revealing ‘real time’ crystallisation data. These results

produced crystallisation kinetics comparable to those obtained from FDSC. Both FDSC and LFA have been shown in this study to be alternative methods in measuring crystallisation kinetics in PLA, preventing recrystallisation, unavoidable when using CDSC.

10.2 Further Work

FDSC has been advantageous in studying crystallisation kinetics of PCL, PEEK and PLA in detail that has not previously been reported using calorimetry techniques. However, a disadvantage of FDSC is the method of sample preparation due to the intricate and time-consuming nature of the process, making repeatability of sample geometry and mass challenging. A new method of material application to the sensor would be beneficial in reproducing sample masses and geometry, enhancing accuracy of data. Thin film application, polymer solvent solution and ink jet printing are methods that may develop further this procedure.

Currently, the accepted method for thermal lag adjustment uses a reference material, such as indium. The thermal diffusivity of metallic and polymeric materials can significantly differ; thus, with large thermal lag occurring at fast scanning rates, a more detailed adjustment would increase the accuracy of data analysis. The use of LFA and FDSC in parallel could be exploited to measure accurate thermal lag in polymer samples. Phonon transport was shown to change with crystallinity and temperature and thus multiple thermal lag adjustments may be needed to provide the most accurate data correction.

Fast heating rates have been extremely useful in the prevention of recrystallisation at high crystallisation temperatures. The analysis of low temperature isothermal crystallisation is limited due to the occurrence of rapid recrystallisation of unstable crystals in PCL and PEEK. It would be advantageous to extend this knowledge using the high sensitivity and scanning rate capabilities of FDSC, where the observed transitions obstruct or reduce the magnitude of other transitions due to simultaneous processes. Simulation modelling would help to model the location and magnitude of transitions where simultaneous transitions occur.

LFA analysis on PLA at the glass transition temperature provided new, interesting data regarding crystal sizes in PLA. Analysis over a broader range of crystal sizes and crystallinity in PLA would provide additional data to determine the importance of crystal size. An extended temperature range of thermal diffusivity data above T_g would provide further data on the recrystallisation of both unstable and melting of crystals. Further work in this area including the use of a liquid sample holder may also help develop the modelling of thermal transitions in PLA.

LFA and FDSC both show identical crystallisation kinetic data and would benefit from another, more conventional technique in order to provide comparable crystallisation kinetics analysis. Fourier transform infrared spectroscopy (FTIR) can be used to resolve crystallisation and would provide further results to support the kinetic data recorded in this study.

References

ABE, H., KIKKAWA, Y., INOUE, Y. & DOI, Y. 2001. Morphological and Kinetic Analyses of Regime Transition for Poly[(S)-lactide] Crystal Growth. *Biomacromolecules,* 2**,** 1007-1014.

ACIERNO, S., DI MAIO, E., IANNACE, S. & GRIZZUTI, N. 2006. Structure development during crystallization of polycaprolactone. *Rheologica Acta,* 45**,** 387-392.

ADAM, G. & GIBBS, J. H. 1965. On the Temperature Dependence of Cooperative Relaxation Properties in Glass‐Forming Liquids. *The Journal of Chemical Physics,* 43**,** 139-146.

ADAMOVSKY, S. A., MINAKOV, A. A. & SCHICK, C. 2003. Scanning microcalorimetry at high cooling rate. *Thermochimica Acta,* 403**,** 55-63.

AGARWAL, S. & SPEYERER, C. 2010. Degradable blends of semi-crystalline and amorphous branched poly(caprolactone): Effect of microstructure on blend properties. *Polymer,* 51**,** 1024-1032.

AHMED, J., ZHANG, J.-X., SONG, Z. AND VARSHNET, S.K. 2009. Thermal Properties of Polylactides: Effect of molecular mass and nature of lactide isomer. *Journal of Thermal Analysis and Calorimetry,* 95**,** 957-964.

AL LAFI, A. G. & HAY, J. N. 2017. The isothermal crystallization of poly(ether ether ketone) by two-dimensional differential scanning calorimetry correlation mapping. *Journal of Applied Polymer Science,* 134**,** n/a-n/a.

ANDROSCH, R. & DI LORENZO, M. L. 2013a. Crystal Nucleation in Glassy Poly(l-lactic acid). *Macromolecules,* 46**,** 6048-6056.

ANDROSCH, R. & DI LORENZO, M. L. 2013b. Kinetics of crystal nucleation of poly(L-lactic acid). *Polymer,* 54**,** 6882-6885.

ANDROSCH, R., SCHICK, C. & LORENZO, M. L. D. 2014a. Melting of Conformationally Disordered Crystals (α' -Phase) of Poly(L-lactic acid). *Macromolecular Chemistry and Physics,* 215**,** 1134-1139.

ANDROSCH, R., ZHURAVLEV, E. & SCHICK, C. 2014b. Solid-state reorganization, melting and melt-recrystallization of conformationally disordered crystals (α' -phase) of poly (l-lactic acid). *Polymer,* 55**,** 4932-4941.

ARAS, L. & RICHARDSON, M. J. 1989. The glass transition behaviour and thermodynamic properties of amorphous polystyrene. *Polymer,* 30**,** 2246-2252.

AVRAMI, M. 1940. Kinetics of Phase Change. II Transformation‐Time Relations for Random Distribution of Nuclei. *The Journal of Chemical Physics,* 8**,** 212-224.

BAHAR, I., ERMAN, B. & MONNERIE, L. 1992. Kinematics of Polymer Chains with Freely Rotating Bonds in a Restrictive Environment. 2. Conformational and Orientational Correlations. *Macromolecules,* 25**,** 6315-6321.

BARNES, H. T. 1906. Ice Formation. *Wiley***,** 266.

BASSETT, D. C. & CARDER, D. R. 1973. Lamellar thickening and chain-extended growth of polyethylene. *Polymer,* 14**,** 387-389.

BASSETT, D. C., OLLEY, R. H. & AL RAHEIL, I. A. M. 1988. On crystallization phenomena in PEEK. *Polymer,* 29**,** 1745-1754.

BASSETT, D. C. & PATEL, D. 1994. Isothermal lamellar thickening and the distribution of thermal stability in spherulitic isotactic poly(4-methylpentene-1). *Polymer,* 35**,** 1855-1862.

BERKELEY, E. 1912. Solubility and Supersolubility from the Osmotic Standpoint. *Philosophical Magazine,* 254-268**,** 2.

BLUNDELL, D. J. & OSBORN, B. N. 1983. The morphology of poly(aryl-ether-ether-ketone). *Polymer,* 24**,** 953-958.

BOSQ, N., GUIGO, N., ZHURAVLEV, E. & SBIRRAZZUOLI, N. 2013. Nonisothermal Crystallization of Polytetrafluoroethylene in a Wide Range of Cooling Rates. *The Journal of Physical Chemistry B,* 117**,** 3407-3415.

BRÉDAS, J. L. & SILBEY, R. 2012. *Conjugated Polymers: The Novel Science and Technology of Highly Conducting and Nonlinear Optically Active Materials*, Springer Netherlands.

CAI, J., LIU, M., WANG, L., YAO, K., LI, S. & XIONG, H. 2011. Isothermal crystallization kinetics of thermoplastic starch/poly(lactic acid) composites. *Carbohydrate Polymers,* 86**,** 941-947.

CAPE, J. A. & LEHMAN, G. W. 1963. Temperature and Finite Pulse‐Time Effects in the Flash Method for Measuring Thermal Diffusivity. *Journal of Applied Physics,* 34**,** 1909-1913.

CEBE, P. & HONG, S.-D. 1986. Crystallization behaviour of poly(ether-ether-ketone). *Polymer,* 27**,** 1183-1192.

CHAO, S.-C., CHEN, M. & CHUNG, C.-T. 1998. Isothermal Crystallization and Melting Behavior of Short Carbon Fibre Reinforced Poly(ether ether ketone) Composites. *Journal of Polymer Research,* 5**,** 221-226.

CHEN, F. C., POON, Y. M. & CHOY, C. L. 1977. Thermal diffusivity of polymers by the flash method. *Polymer,* 18**,** 129-136.

CHEN, H.-L. & PORTER, R. S. 1993. Melting behavior of poly(ether ether ketone) in its blends with poly(ether imide). *Journal of Polymer Science Part B: Polymer Physics,* 31**,** 1845-1850.

CHEN, Y.-F. & WOO, E. M. 2008. Growth regimes and spherulites in thin-film poly(ε-caprolactone) with amorphous polymers. *Colloid and Polymer Science,* 286**,** 917-926.

CHEN, Z., HAY, J. N. & JENKINS, M. J. 2013. The kinetics of crystallization of poly(ethylene terephthalate) measured by FTIR spectroscopy. *European Polymer Journal,* 49**,** 1722-1730.

CHEN, Z., HAY, J. N. & JENKINS, M. J. 2016. The effect of secondary crystallization on crystallization kinetics – Polyethylene terephthalate revisited. *European Polymer Journal,* 81**,** 216-223.

CHOY, C. L. 1977. Thermal conductivity of polymers. *Polymer,* 18**,** 984-1004.

CHOY, C. L., CHEN, F. C. & LUK, W. H. 1980. Thermal conductivity of oriented crystalline polymers. *Journal of Polymer Science: Polymer Physics Edition,* 18**,** 1187-1207.

CHUN, Y. S., LEE, H. S., JUNG, H. C. & KIM, W. N. 1999. Thermal properties of melt-blended poly(ether ether ketone) and poly(ether imide). *Journal of Applied Polymer Science,* 72**,** 733-739.

COWIE, J. M. G. 1991. *Polymers: Chemistry and Physics of Modern Materials,* London, Chapman and Hall.

COWIE, J. M. G. & FERGUSON, R. 1993. Physical ageing of poly(methyl methacrylate) from enthalpy relaxation measurements. *Polymer,* 34**,** 2135-2141.

DANDY, L. O. 2015. *Supercritical Fluids and Their Application to the Recycling of High-Performance Carbon Fibre Reinforced Composite Materials.* PhD, University of Birmingham.

DOS SANTOS, W. N., DE SOUSA, J. A. & GREGORIO JR, R. 2013. Thermal conductivity behaviour of polymers around glass transition and crystalline melting temperatures. *Polymer Testing,* 32**,** 987-994.

DOS SANTOS, W. N., IGUCHI, C. Y. & GREGORIO JR, R. 2008. Thermal properties of poly(vinilidene fluoride) in the temperature range from 25 to 210 °C. *Polymer Testing,* 27**,** 204-208.

DOS SANTOS, W. N., MUMMERY, P. & WALLWORK, A. 2005. Thermal diffusivity of polymers by the laser flash technique. *Polymer Testing,* 24**,** 628-634.

ELZEIN, T., NASSER-EDDINE, M., DELAITE, C., BISTAC, S. & DUMAS, P. 2004. FTIR study of polycaprolactone chain organization at interfaces. *Journal of Colloid and Interface Science,* 273**,** 381-387.

EVANS, U. R. 1945. The laws of expanding circles and spheres in relation to the lateral growth of surface films and the grain-size of metals. *Transactions of the Faraday Society,* 41**,** 365-374.

FAKIROV, S. & AVRAMOVA, N. 1982. Applicability of the Gibbs–Thomson equation to nylon-6. *Journal of Polymer Science: Polymer Letters Edition,* 20**,** 635-641.

FURUSHIMA, Y., TODA, A., ROUSSEAUX, V., BAILLY, C., ZHURAVLEV, E. & SCHICK, C. 2016. Quantitative understanding of two distinct melting kinetics of an isothermally crystallized poly(ether ether ketone). *Polymer,* 99**,** 97-104.

GUAN, B. X. & PHILLIPS, P. J. 2005. Does isothermal crystallization ever occur? *Polymer,* 46**,** 8763-8773.

HATTORI, M. 1962. Thermal conductivity of polytetrafluoroethylene and polytrifluorochloroethylene. *Kolloid-Zeitschrift und Zeitschrift für Polymere,* 185**,** 27-31.

HOFFMAN, J. D. & LAURITZEN, J. I. 1961. Crystallization of Bulk Polymers With Chain Folding: Theory of Growth of Lamellar Spherulites. *Journal of Research of the National Bureau of Standards - A. Physics and Chemistry,* 65A.

HOFFMAN, J. D., LAURITZEN, J. I., JR., PASSAGLIA, E., ROSS, G. S., FROLEN, L. J. & WEEKS, J. J. 1969. Kinetics of polymer crystallization from solution and the melt. *Kolloid-Zeitschrift und Zeitschrift für Polymere,* 231**,** 564-592.

HOFFMAN, J. D. & MILLER, R. L. 1997. Kinetic of crystallization from the melt and chain folding in polyethylene fractions revisited: theory and experiment. *Polymer,* 38**,** 3151-3212.

HOFFMAN, J. D. & WEEKS, J. J. 1961. Melting Process and the Equilibrium Melting Temperature of Polychlorotrifluoroethylene. *Journal of Research of the National Bureau of Standards - A. Physics and Chemistry,* 66A**,** 13-128.

HSIAO, B. S., SAUER, B. B., VERMA, R. K., ZACHMANN, H. G., SEIFERT, S., CHU, B. & HARNEY, P. 1995. New Insight of Isothermal Melt Crystallization in Poly(aryl ether ether ketone) via Time-Resolved Simultaneous Small-Angle X-ray Scattering/Wide-Angle X-ray Diffraction Measurements. *Macromolecules,* 28**,** 6931-6936.

HUANG, Y.-P., XU, X., LUO, X.-L. & MA, D.-Z. 2002. Molecular Weight Dependence of the Melting Behaviour of Poly(caprolactone). *Chinese Journal of Polymer Science,* 20**,** 45-51.

IERVOLINO, E., VAN HERWAARDEN, A. W., VAN HERWAARDEN, F. G., VAN DE KERKHOF, E., VAN GRINSVEN, P. P. W., LEENAERS, A. C. H. I., MATHOT, V. B. F. & SARRO, P. M. 2011. Temperature calibration and electrical characterization of the differential scanning calorimeter chip UFS1 for the Mettler-Toledo Flash DSC 1. *Thermochimica Acta,* 522**,** 53-59.

JENKINS, M. J. 2001. Crystallisation in miscible blends of PEEK and PEI. *Polymer,* 42**,** 1981-1986.

JENKINS, M. J. & HARRISON, K. L. 2006. The effect of molecular weight on the crystallization kinetics of polycaprolactone. *Polym. Adv. Technol.,* 17**,** 474–478.

JIN, L., BALL, J., BREMNER, T. & SUE, H.-J. 2014. Crystallization behavior and morphological characterization of poly(ether ether ketone). *Polymer,* 55**,** 5255-5265.

JOHNS, A. I., RASHID, S., WATSON, J. T. R. & CLIFFORD, A. A. 1986. Thermal Conductivity of Argon, Nitrogen and Carbon Dioxide at Elevated Temperatures and Pressures. *Journal of the Chemical Society,* 1**,** 2235-2246.

KAWAI, T., RAHMAN, N., MATSUBA, G., NISHIDA, K., KANAYA, T., NAKANO, M., OKAMOTO, H., KAWADA, J., USUKI, A., HONMA, N., NAKAJIMA, K. & MATSUDA, M. 2007. Crystallization and Melting Behavior of Poly (l-lactic Acid). *Macromolecules,* 40**,** 9463-9469.

KO, T. Y. & WOO, E. M. 1996. Changes and distribution of lamellae in the spherulites of poly(ether ether ketone) upon stepwise crystallization. *Polymer,* 37**,** 1167-1175.

KOLESOV, I., MILEVA, D., ANDROSCH, R. & SCHICK, C. 2011. Structure formation of polyamide 6 from the glassy state by fast scanning chip calorimetry. *Polymer,* 52**,** 5156-5165.

KOLSTAD, J. J., VINK, E. T. H., DE WILDE, B. & DEBEER, L. 2012. Assessment of anaerobic degradation of Ingeo™ polylactides under accelerated landfill conditions. *Polymer Degradation and Stability,* 97**,** 1131-1141.

LATTIMER, M. P., HOBBS, J. K., HILL, M. J. & BARHAM, P. J. 1992. On the origin of the multiple endotherms in PEEK. *Polymer,* 33**,** 3971-3973.

LAURITZEN, J. I. & HOFFMAN, J. D. 1973. Extension of theory of growth of chain‐folded polymer crystals to large undercoolings. *Journal of Applied Physics,* 44**,** 4340-4352.

LEE, Y. & PORTER, R. S. 1987. Double-melting behavior of poly(ether ether ketone). *Macromolecules,* 20**,** 1336-1341.

LEE, Y., PORTER, R. S. & LIN, J. S. 1989. On the double-melting behavior of poly(ether ether ketone). *Macromolecules,* 22**,** 1756-1760.

LOGAN, S. R. 1982. The origin and status of the Arrhenius equation. *Journal of Chemical Education,* 59**,** 279.

LOHSE, D. J. & GAYLORD, R. J. 1978. The Amorphous Contribution to the Modulus of a Semi-Crystalline Polymer. *Polymer Engineering & Science,* 18**,** 512-517.

LONG, Y., SHANKS, R. A. & STACHURSKI, Z. H. 1995. Kinetics of polymer crystallisation. *Progress in Polymer Science,* 20**,** 651-701.

LÓPEZ-RODRÍGUEZ, N., LÓPEZ-ARRAIZA, A., MEAURIO, E. & SARASUA, J. R. 2006. Crystallization, morphology, and mechanical behavior of polylactide/poly(ε-caprolactone) blends. *Polymer Engineering & Science,* 46**,** 1299-1308.

MACDONALD, R. T., MCCARTHY, S.P., & GROSS, R.A. 1996. Enzymatic Degradability of Poly(lactide): Effects of Chain Stereochemistry and Material Crystallinity. *Macromolecules***,** 7356-7361.

MATHOT, V., PYDA, M., PIJPERS, T., VANDEN POEL, G., VAN DE KERKHOF, E., VAN HERWAARDEN, S., VAN HERWAARDEN, F. & LEENAERS, A. 2011. The Flash DSC 1, a power compensation twin-type, chip-based fast scanning calorimeter (FSC): First findings on polymers. *Thermochimica Acta,* 522**,** 36-45.

MDLETSHE, T. S., MISHRA, S. B. & MISHRA, A. K. 2015. Studies on the effect of silicon carbide nanoparticles on the thermal, mechanical, and biodegradation properties of poly(caprolactone). *Journal of Applied Polymer Science,* 132**,** n/a-n/a.

MIHAI, M., HUNEAULT, M. A. & FAVIS, B. D. 2009. Crystallinity development in cellular poly(lactic acid) in the presence of supercritical carbon dioxide. *Journal of Applied Polymer Science,* 113**,** 2920-2932.

MOLDOVER, M. R., TRUSLER, J. P. M., EDWARDS, T. J., MEHL, J. B. & DAVIS, R. S. 1988. Measurement of the Universal Gas Constant <math><mi>R</mi></math> Using a Spherical Acoustic Resonator. *Physical Review Letters,* 60**,** 249-252.

MORIKAWA, J., TAN, J. & HASHIMOTO, T. 1995. Study of change in thermal diffusivity of amorphous polymers during glass transition. *Polymer,* 36**,** 4439-4443.

MUCHA, M., TYLMAN, M. & MUCHA, J. 2015. Crystallization kinetics of polycaprolactone in nanocomposites. *Polimary,* 60**,** 686-692.

MUSTAPA, I. R., SHANK, R. A. & KONG, I. 2013. Melting Behaviour and Dynamic Mechanical Properties of Poly(lactic acid)-Hemp-Nanosilica

Composites. *Asian Transactions on Basic and Applied Sciences,* 3**,** 29-37.

MUTHUKUMAR, M. 2004. Nucleation in Polymer Crystallization. *Advances in Chemical Physics.* John Wiley & Sons, Inc.

O'NEILL, M. J. & WATSON, E. S. 1966. Differential microcalorimeter. Google Patents.

PAN, P., KAI, W., ZHU, B., DONG, T. & INOUE, Y. 2007. Polymorphous Crystallization and Multiple Melting Behavior of Poly(l-lactide): Molecular Weight Dependence. *Macromolecules,* 40**,** 6898-6905.

PAPKOV, V. S., GERASIMOV, M. V. & DUBOVIK, I. I. 1997. Disordering of crystalline PEEK upon mechanical treatment. *Polymer Engineering & Science,* 37**,** 1280-1285.

PARKER, W. J., JENKINS, R. J., BUTLER, C. P. & ABBOTT, G. L. 1961. Flash Method of Determining Thermal Diffusivity, Heat Capacity, and Thermal Conductivity. *Journal of Applied Physics,* 32**,** 1679-1684.

PHILLIPSON, K., JENKINS, M. J. & HAY, J. N. 2016. The effect of a secondary process on crystallization kinetics – Poly (ϵ-caprolactone) revisited. *European Polymer Journal,* 84**,** 708-714.

PIJPERS, T. F. J., MATHOT, V. B. F., GODERIS, B., SCHERRENBERG, R. L. & VAN DER VEGTE, E. W. 2002. High-Speed Calorimetry for the Study of the Kinetics of (De)vitrification, Crystallization, and Melting of Macromolecules†. *Macromolecules,* 35**,** 3601-3613.

POEL, G., ISTRATE, D., MAGON, A. & MATHOT, V. 2012. Performance and calibration of the Flash DSC 1, a new, MEMS-based fast scanning calorimeter. *Journal of Thermal Analysis and Calorimetry,* 110**,** 1533-1546.

R. AURAS, L.T. LIM, SELKE, S. E. M. & H.TSUJI 2010. *Poly (lactic acid) Synthesis, Structures, Properties, Processing and Applications,* New Jersey.

RATHI, S., CHEN, X., COUGHLIN, E. B., HSU, S. L., GOLUB, C. S. & TZIVANIS, M. J. 2011. Toughening semicrystalline poly(lactic acid) by morphology alteration. *Polymer,* 52**,** 4184-4188.

SALMERÓN SÁNCHEZ, M., MATHOT, V. B. F., VANDEN POEL, G. & GÓMEZ RIBELLES, J. L. 2007. Effect of the Cooling Rate on the Nucleation Kinetics of Poly(l-Lactic Acid) and Its Influence on Morphology. *Macromolecules,* 40**,** 7989-7997.

SCHEIRS, J. 2000. *Compositional and Failure Analysis of Polymers: A Practical Approach,* Australia, John Wiley & Sons.

SCHULTZ, J. M. 1969. Transient effects in the crystallization of polyethylene. *Journal of Polymer Science Part A-2: Polymer Physics,* 7**,** 821-827.

SCHULTZ, J. M. 2001. *Polymer Crystallization: The Development of Crystalline Order in Thermoplastic Polymers*, American Chemical Society.

SHARPLES, A. 1966. *Introduction to Polymer Crystallization,* London, Edward Arnold.

SHEN, C., WANG, Y., LI, M. & HU, D. 2011. Crystal modifications and multiple melting behavior of poly(L-lactic acid-co-D-lactic acid). *Journal of Polymer Science Part B: Polymer Physics,* 49**,** 409-413.

SHUKLA, D., NEGI, Y. S., UPPADHYAYA, J. S. & KUMAR, V. 2012. Synthesis and Modification of Poly(ether ether ketone) and their Properties: A Review. *Polymer Reviews,* 52**,** 189-228.

SÖDERGÅRD, A. & STOLT, M. 2002. Properties of lactic acid based polymers and their correlation with composition. *Progress in Polymer Science,* 27**,** 1123-1163.

SRIVASTAVA, G. P. 1990. *Physics of Polymers,* New York.

TAMMANN, G. 1898. Number of nuclei in supercooled liquids. *Z Phys Chem,* 25**,** 441-479.

TARDIF, X., PIGNON, B., BOYARD, N., SCHMELZER, J. W. P., SOBOTKA, V., DELAUNAY, D. & SCHICK, C. 2014. Experimental study of crystallization of PolyEtherEtherKetone (PEEK) over a large temperature range using a nano-calorimeter. *Polymer Testing,* 36**,** 10-19.

TOFT, M. 2011. *The Effect of Crystalline Morphology on the Glass Transition and Enthalpic Relaxation in Poly(Ether-Ether-Ketone).* Masters of Research, The University of Birmingham.

TRUJILLO, M., ARNAL, M. L., MÜLLER, A. J., MUJICA, M. A., URBINA DE NAVARRO, C., RUELLE, B. & DUBOIS, P. 2012. Supernucleation and crystallization regime change provoked by MWNT addition to poly(ε-caprolactone). *Polymer,* 53**,** 832-841.

TSUJI, H., TEZUKA, Y., SAHA, S. K., SUZUKI, M. & ITSUNO, S. 2005. Spherulite growth of l-lactide copolymers: Effects of tacticity and comonomers. *Polymer,* 46**,** 4917-4927.

TSUTSUMI, N., TAKIZAWA, T. & KIYOTSUKURI, T. 1990. Thermal diffusivity of polymers by flash radiometry: correlation between thermal diffusivity and fine structure of poly(ethylene terephthalate). *Polymer,* 31**,** 1925-1931.

TURNBULL, D. & FISHER, J. C. 1949. Rate of Nucleation in Condensed Systems. *The Journal of Chemical Physics,* 17**,** 71-73.

VAN HERWAARDEN, S., IERVOLINO, E., VAN HERWAARDEN, F., WIJFFELS, T., LEENAERS, A. & MATHOT, V. 2011. Design, performance and analysis of thermal lag of the UFS1 twin-calorimeter chip for fast scanning calorimetry using the Mettler-Toledo Flash DSC 1. *Thermochimica Acta,* 522**,** 46-52.

VANDEN POEL, G. & MATHOT, V. B. F. 2006. High-speed/high performance differential scanning calorimetry (HPer DSC): Temperature calibration in the heating and cooling mode and minimization of thermal lag. *Thermochimica Acta,* 446**,** 41-54.

WANG, J., LI, Z., PÉREZ, R. A., MÜLLER, A. J., ZHANG, B., GRAYSON, S. M. & HU, W. 2015. Comparing crystallization rates between linear and cyclic poly(epsilon-caprolactones) via fast-scan chip-calorimeter measurements. *Polymer,* 63**,** 34-40.

WOOD, L. A. & BEKKEDAHL, N. 1946. Crystallization of unvulcanized rubber at different temperatures. *Journal of Research of the National Bureau of Standards - A. Physics and Chemistry,* 36.

WUNDERLICH, B. 1976. *Macromolecular physics Vol. 2 Vol. 2,* New York [u.a., Academic Press.

WURM, A., ZHURAVLEV, E., ECKSTEIN, K., JEHNICHEN, D., POSPIECH, D., ANDROSCH, R., WUNDERLICH, B. & SCHICK, C. 2012. Crystallization and Homogeneous Nucleation Kinetics of Poly(ε-caprolactone) (PCL) with Different Molar Masses. *Macromolecules,* 45**,** 3816-3828.

XIAO, H. W., LI, P., REN, X., JIANG, T. & YEH, J.-T. 2010. Isothermal crystallization kinetics and crystal structure of poly(lactic acid): Effect of triphenyl phosphate and talc. *Journal of Applied Polymer Science,* 118**,** 3558-3569.

YANG, Y., DAI, X. & ZHANG, L. 2006. Crystallisation Kinetics of Compatibilized Blends of Liquid Crystalline Polymer With PEEK. *Polymer Composites,* 27**,** 642-650.

YOUNG, R. J. & LOVELL, P. A. 1991. *Introduction to Polymers,* USA, CRC Press.

YOUNG, S. W. 1911. Mechanical Stimulus To Crystallisation in Super-Cooled Liquids.1. *Journal of the American Chemical Society,* 33**,** 148-162.

YOUNG, S. W. & VAN SICKLEN, W. J. 1913. The mechanical stimulus to crystallization. *American Chemical Society,* 37**,** 1067-1078.

ZHANG, C., ZHAI, T., TURNG, L.-S. & DAN, Y. 2015. Morphological, Mechanical, and Crystallization Behavior of Polylactide/Polycaprolactone Blends Compatibilized by l-Lactide/Caprolactone Copolymer. *Industrial & Engineering Chemistry Research,* 54**,** 9505-9511.

ZHURAVLEV, E. & SCHICK, C. 2010. Fast scanning power compensated differential scanning nano-calorimeter: 1. The device. *Thermochimica Acta,* 505**,** 1-13.

ZHURAVLEV, E., SCHMELZER, J. W. P., ABYZOV, A. S., FOKIN, V. M., ANDROSCH, R. & SCHICK, C. 2015. Experimental Test of Tammann's Nuclei Development Approach in Crystallization of Macromolecules. *Crystal Growth & Design,* 15**,** 786-798.

ZHURAVLEV, E., SCHMELZER, J. W. P., WUNDERLICH, B. & SCHICK, C. 2011. Kinetics of nucleation and crystallization in poly(ε-caprolactone) (PCL). *Polymer,* 52**,** 1983-1997.

ZHURAVLEV, E., WURM, A., PÖTSCHKE, P., ANDROSCH, R., SCHMELZER, J. W. P. & SCHICK, C. 2014. Kinetics of nucleation and crystallization of poly(ε-caprolactone) – Multiwalled carbon nanotube composites. *European Polymer Journal,* 52**,** 1-11.

Appendix 1 - SUPPORTING FIGURES AND DATA

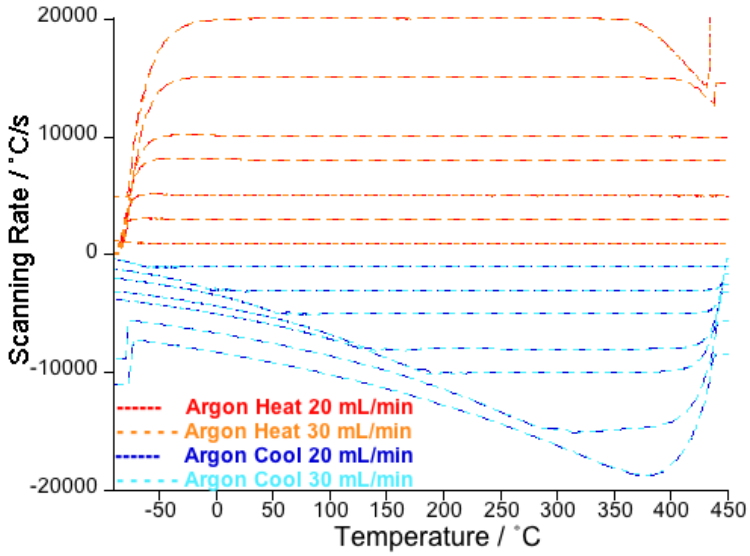

Figure A1-1– The performance of he FDSC chip using argon as a purge gas at a flow rate of 20 and 30 mL/min between -90 and 450˚C

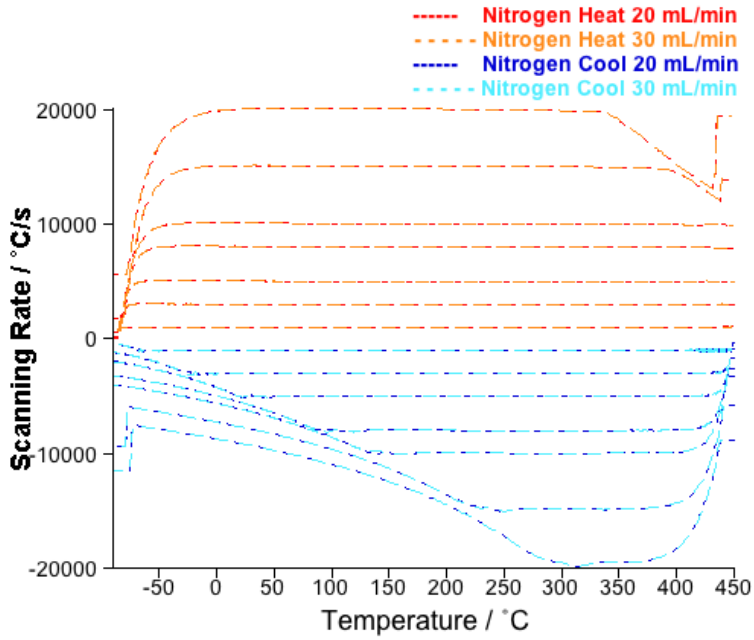

Figure A1-2– The performance of he FDSC chip using nitrogen as a purge gas at a flow rate of 20 and 30 mL/min between -90 and 450˚C

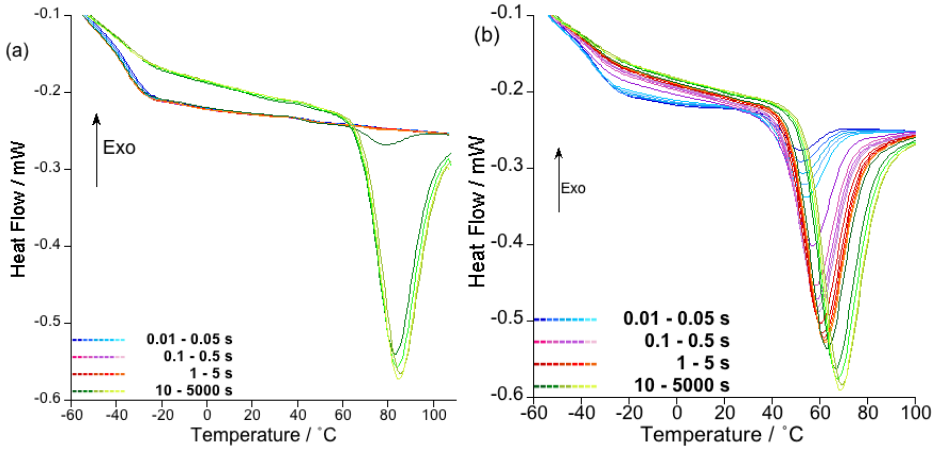

Figure A1-3 – Isothermal crystallisation of PCL with time (a) 40˚C (b) 20˚C

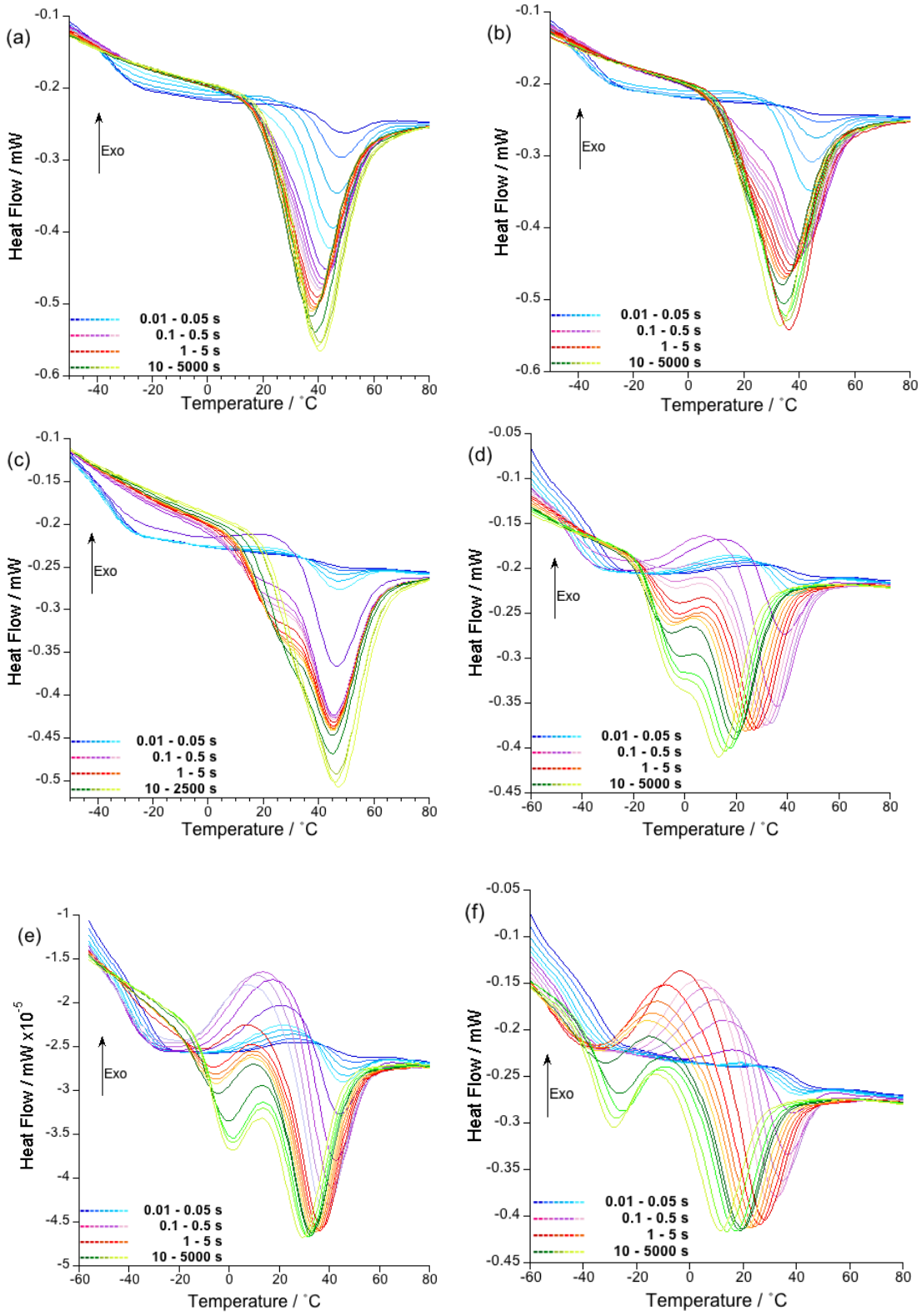

Figure A1-4 - Isothermal crystallisation of PCL with time (a) 0˚C (b) -10˚C (c) -20˚C (d) -30˚C (e) -40˚C (f) -50˚C

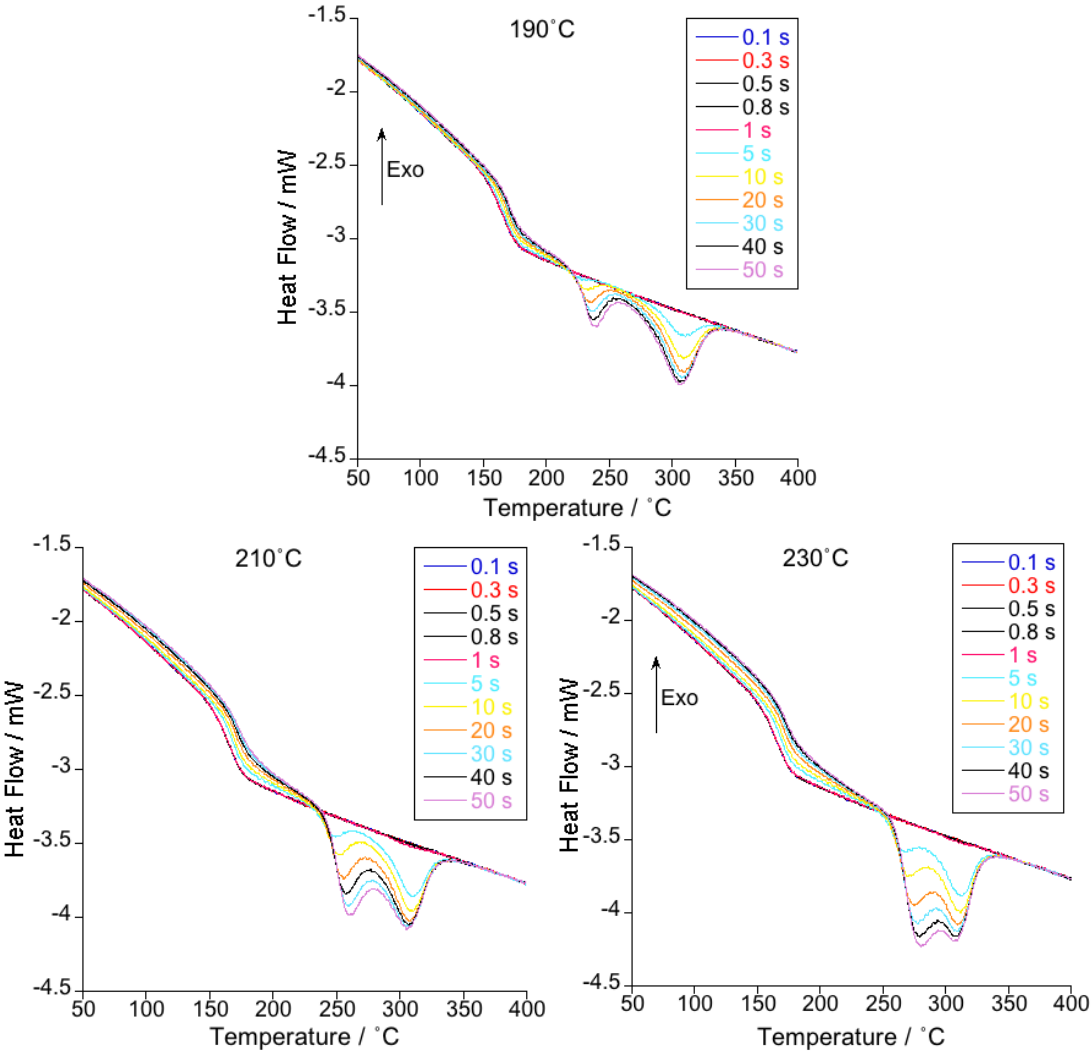

Figure A1 5 - Heating following isothermal crystallisation of PEEK for 0.1-50 s time intervals, heating and cooling at 2,500˚C/s: 190, 210 and 230˚C

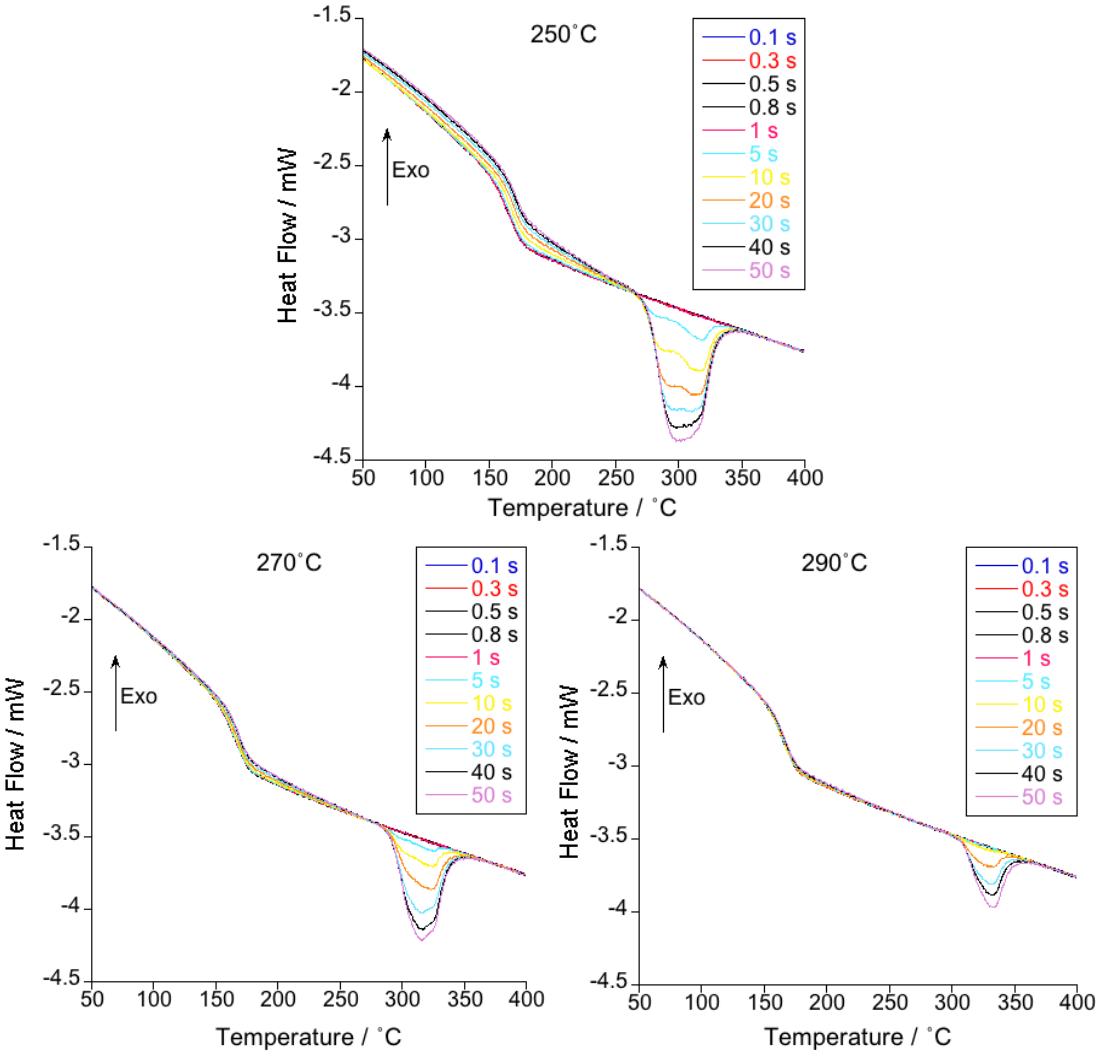

Figure A1-6 - Heating following isothermal crystallisation of PEEK for 0.1-50 s time intervals, heating and cooling at 2,500˚C/s: 250, 270 and 290˚C

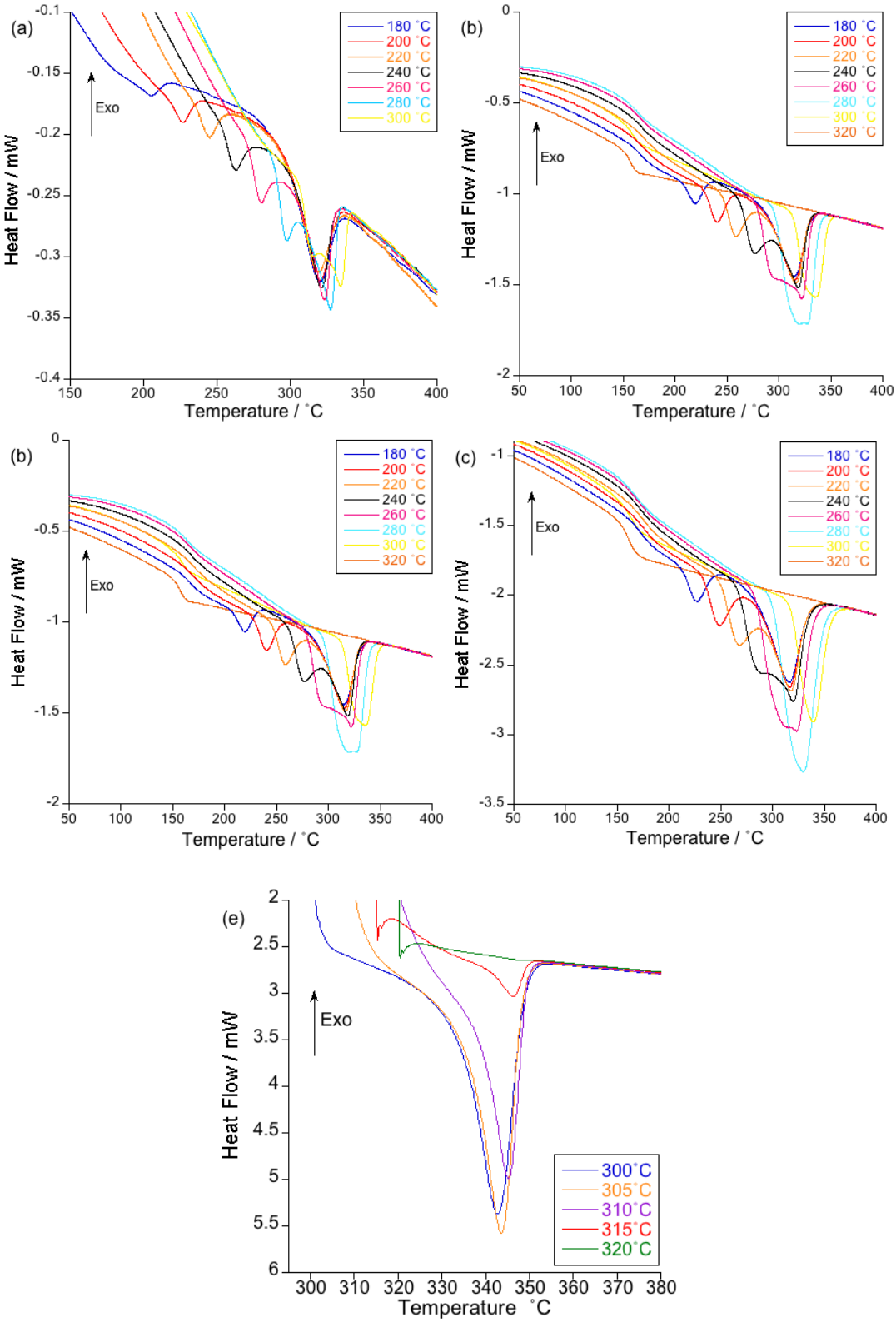

Figure A1- 7- Raw data for one minute isothermal crystallisation of PEEK at varied heating rates (a) 100˚C/s (b) 750˚C/s (c) 1,500˚C/s (d) 2,500˚C/s (e) 0.1667˚C/s

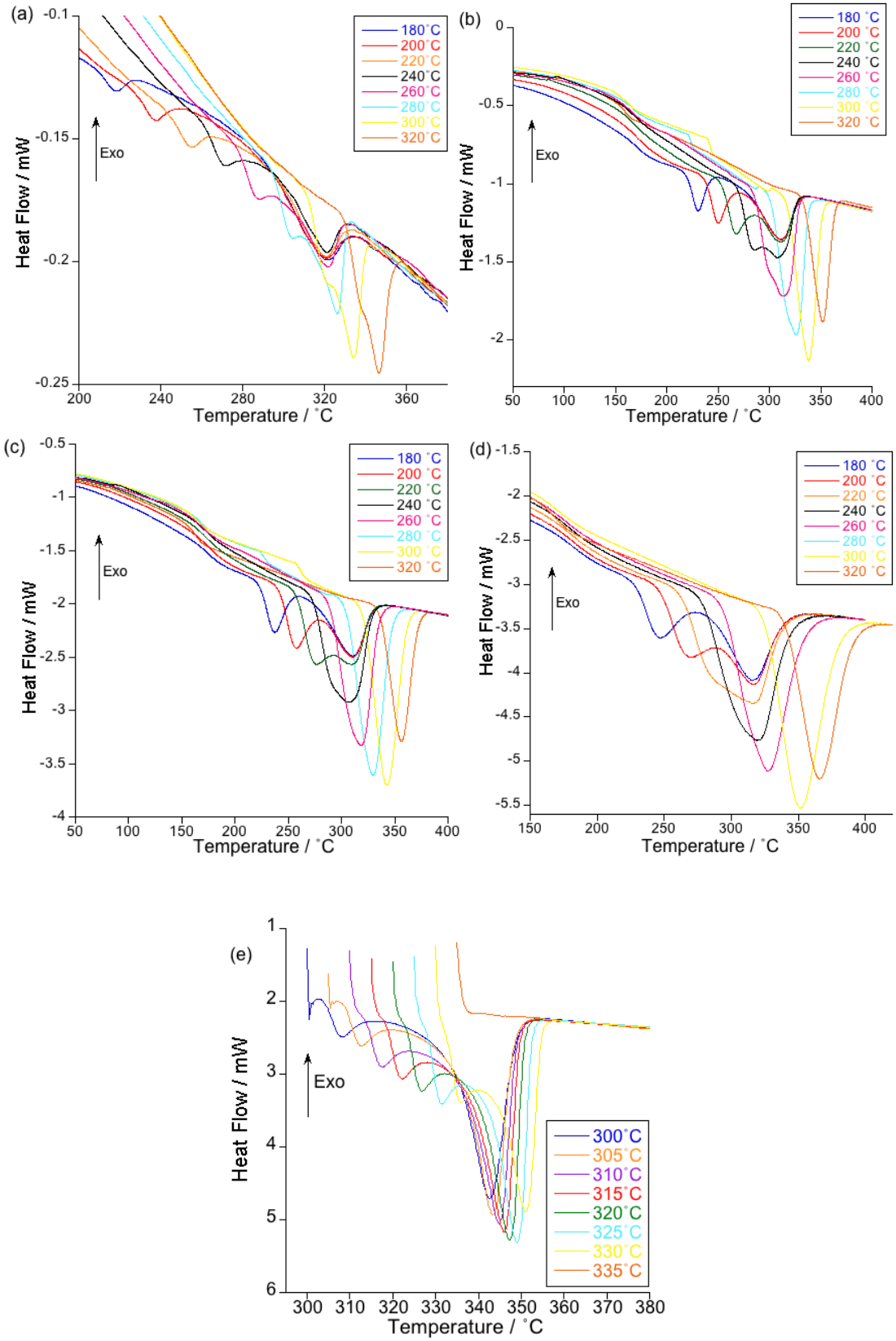

Figure A1 8 - Raw data for one minute isothermal crystallisation of PEEK at varied heating rates (a) 100˚C/s (b) 750˚C/s (c) 1,500˚C/s (d) 2,500˚C/s (e) 0.1667˚C/s

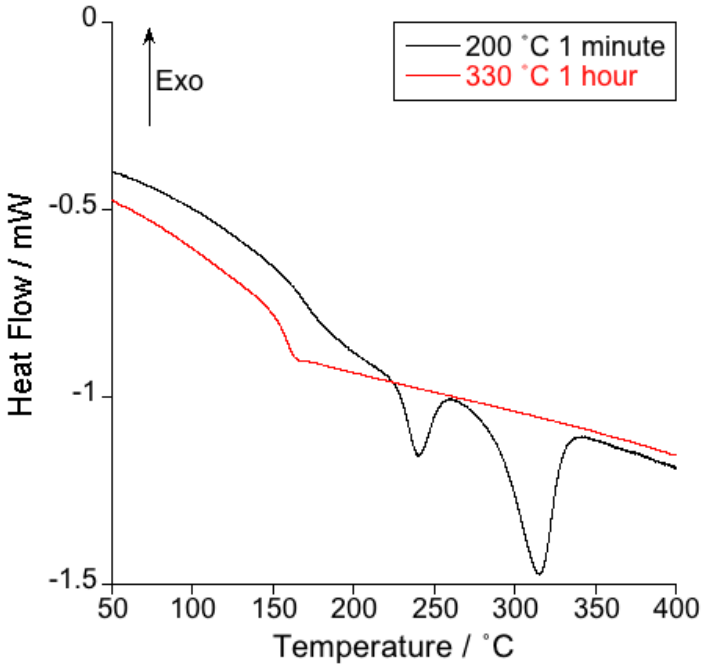

Figure A1-9 - FDSC heating traces after crystallisation at 200 and 330°C for one minute and one hour respectively.

The results in Figure A1-9 show double melting after a short, one-minute, low temperature isothermal hold at 200°C (black curve) and after a long, one-hour, isothermal hold at high temperature at 330°C, no melting was observed on heating (red curve). (Note, the inability to observe a crystallisation exotherm during isothermal crystallisation on FDSC results in the analysis of the heat of fusion from during heating.) Isothermal crystallisation was achieved through fast cooling from the melt for both crystallisation times followed by a rapid cool below T_g, providing a larger temperature curve (both methodologies are shown in Figure A1-10.

The formation of double melting, after crystallisation at 200°C, is expressed to represent melting-recrystallisation-melting. The upper endotherm, representing crystals grown non-isothermally on heating, shows a melting endset

temperature of 330˚C. High temperature crystallisation is very slow due to the high mobility of the polymer chains resulting in slow, difficult nucleation. The absence of melting represents the failure for crystallisation after one hour at 330˚C after. In previous literature, the highest T_c on PEEK was 328.6˚C, showing double melting after 34 hours (Lee and Porter, 1987).

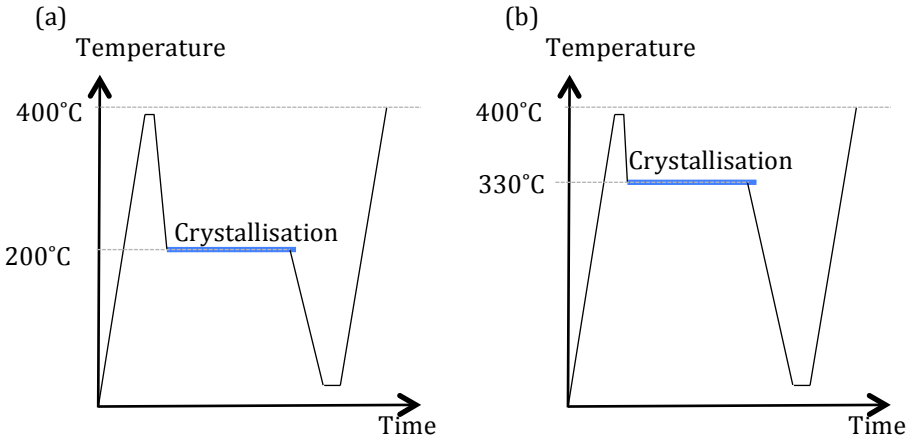

Figure A1-10 - Isothermal crystallisation at (a) 200˚C for one minute and (b) 330˚C for one hour with heating and cooling rates 750˚C/ and 2,500˚C respectively.

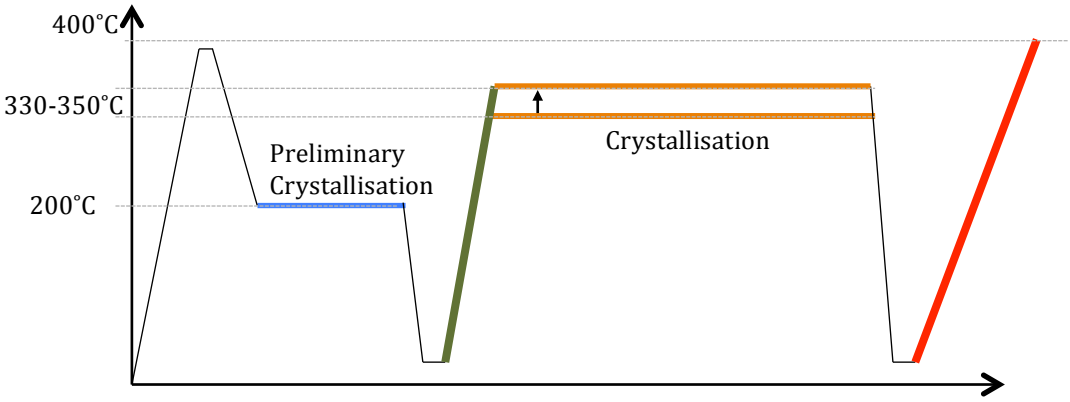

Figure A1-11 – Methodology for high temperature crystallisation between 330 and 350˚C, following preliminary crystallisation at 200˚C. (Heating and cooling at 750 and 2,500˚C/s respectively)

The methodology in Figure A1-11 shows a combination of the two methodologies shown in Figure A1-10. Preliminary crystallisation was carried out at 200˚C for one minute to introduce crystallinity into the sample. Subsequent heating melts the isothermally grown and recrystallised crystals (green line). At 330˚C a five minute isothermal hold was carried out before a rapid cool and final heat to 400˚C (red line). No crystallinity was apparent at a T_c of 330˚C after one hour (Figure A1-9); however, after preliminary crystallisation at 200˚C and further crystallisation at 330˚C, a single, high temperature endotherm was observed at 355˚C (Figure A1-12) (light blue trace). The visible high temperature endotherm is predicted to represent crystal growth at 330˚C after only 5 minutes.

The growth of crystals at 330˚C after preliminary crystallisation suggests the presence of nucleation regions. Theses regions are hypothesised to be thick sections of lamella, that remain stable at high temperature. The thick lamellae originate from the crystals grown on heating following preliminary crystallisation. These regions act as nuclei for growth to occur in 5 minutes.

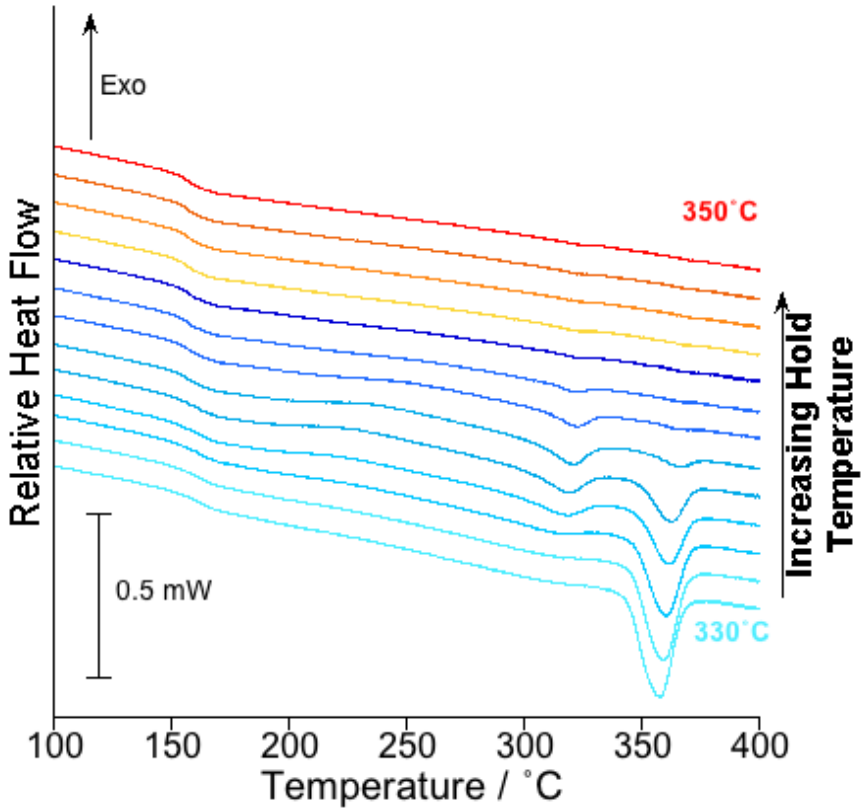

Figure A1-12 – Heating curves following high temperature crystallisation between 330 and 350˚C, following preliminary crystallisation at 200˚C.

Increasing the T_c from 330 to 350˚C, while maintaining a constant preliminary T_c, 200˚C, provides information on the thermal stability of the nucleation regions. The results show a number of interesting changes (Figure A1-12). The first change demonstrates an increase in the single (upper) endotherm peak temperature. This provides evidence (according to Thomson and Gibbs) that the upper melting endotherm is linked to the growth of lamella at 330 to 350˚C as previously predicted.

The second change shows that as T_c rises, an exotherm at 225˚C and a lower temperature endotherm, at 314˚C, develop. The size of the exotherm and endotherm increase with T_c up to 336˚C before a further rise in T_c shows a

reduction in the peak areas. The presence of an exotherm, followed by an endotherm represents a non-isothermal crystallisation process on heating (Blundell and Osborn, 1983). The double melting in PEEK at 200˚C has been previously discussed to occur as a result of a melting-recrystallisation-melting process. The upper endotherm in Figure A1-13 (black curve) represents the recrystallisation on heating after preliminary crystallisation at 200˚C. An identical T_m is exhibited by the lower endotherm (blue trace), of which is independent of T_c (Figure A1-13). This lower temperature endotherm is observed on heating after preliminary and high temperature crystallisation between 336 and 344˚C. The visible exotherm and the identical T_m provide further support to the undetectable melting-recrystallisation-melting process debated by authors to represent the cause double melting (Blundell, 1987, Jonas et al., 1995, Tardif et al., 2014).

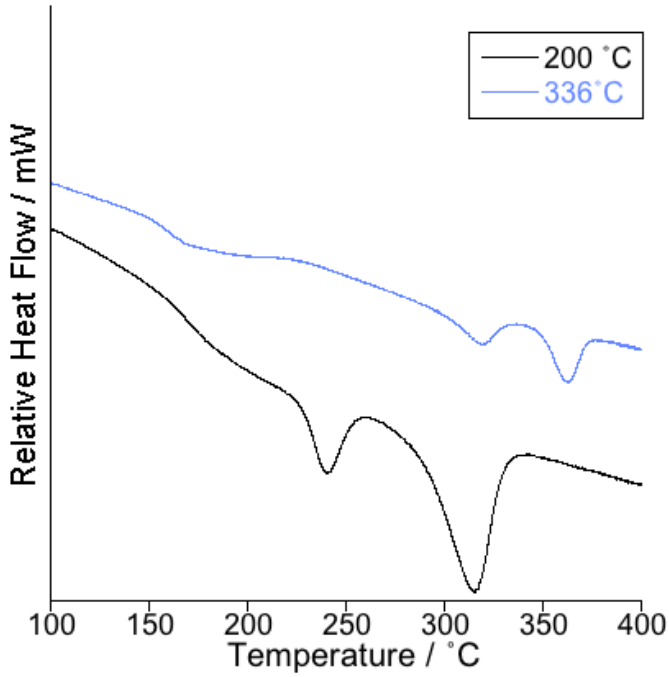

Figure A1-13 - A comparison of heating traces after a 200˚C isothermal only and the subsequent heating following crystallisation at 336˚C.

If it is assumed that the growth of a single, high temperature, endotherm occurs as a result of growth on all thermally stable nucleation regions; the growth of a low temperature endotherm will only occur if a nucleus exists on heating. The results in Figure A1-14 show as T_c increases, the upper endotherm area falls and the lower endotherm area increases. However, above a T_c of 336˚C, a reduction in both endotherms occurs with an increase in T_c. It can therefore be assumed that as T_c increases, fewer thermally stable nuclei are utilised for growth. Thus as T_c rises, growth of the lamella structure at high temperature becomes more difficult; and at T_c <336˚C the nucleation regions become thermally unstable, disordering into an amorphous liquid as the lower endotherm areas falls. At a T_c of 345˚C, all nucleation regions are thermally unstable and no melting endotherms are visible after isothermal crystallisation or on heating.

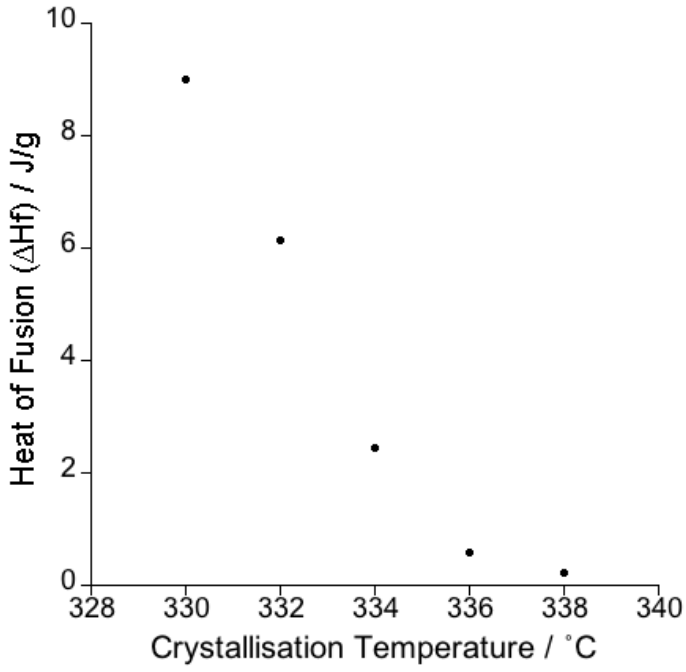

Figure A1-14 – The reduction in heat of fusion of the upper endotherm with crystallisation temperature

These results show high temperature growth after short isothermal hold times. The visible recrystallisation during heating in the presence of nucleation regions provides further evidence to the unobservable recrystallisation seen during double melting after low temperature isothermal crystallisation. The thermal stability of the recrystallised lamella is greater than the endset temperature and as T_c rises, the possibility for growth to develop on all existing nuclei decreases in conjunction with crystal growth rate.

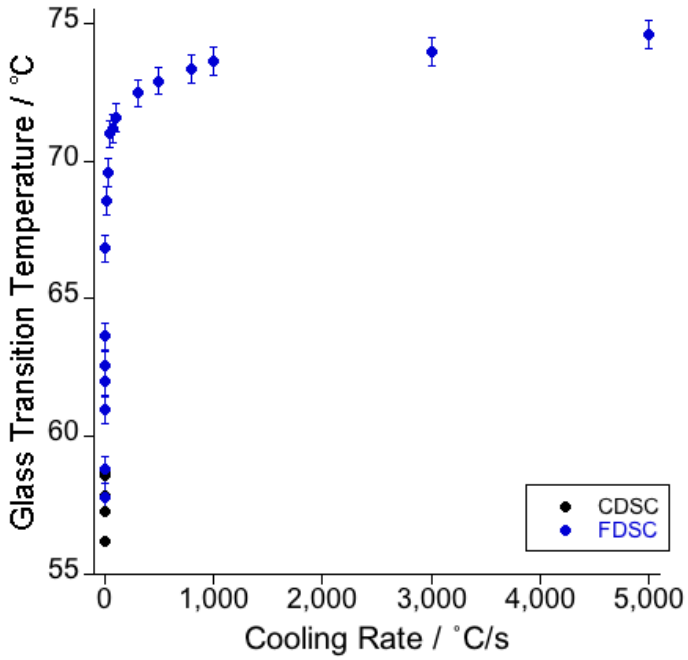

Figure A1-15 - The change in glass transition temperature with cooling rate ,

Figure A1-15 shows an increase in T_g with cooling rate recorded using both CDSC and FDSC. The overlap between the two techniques shows exceptional reliability. The fast scanning rates available on FDSC provide an extension to data previously unattainable. An exceptionally large range of cooling rates (eight orders of magnitude) were permitted through the overlap of the two techniques: 0.01˚C/min to 80˚C/min using CDSC and 10˚C/min to 5,000˚C/s using FDSC. A

maximum cooling rate of 5,000˚C/s was employed, ensuring an accurate cooling rate was applied from the operating window determined in Chapter 4.

Elevated cooling rate inhibits molecular motion (vibration and rotation) at higher temperatures, resulting in an elevated T_g (Figure 1-2). PLA shows a large endothermic physical aging peak on T_g after all cooling rates (shown in Figure A1-17). The Richardson method (explained in Figure 3-6) was therefore employed for all traces. A non-linear relationship of T_g with cooling rate suggests an upper limit of T_g may be achievable through rapid cooling.

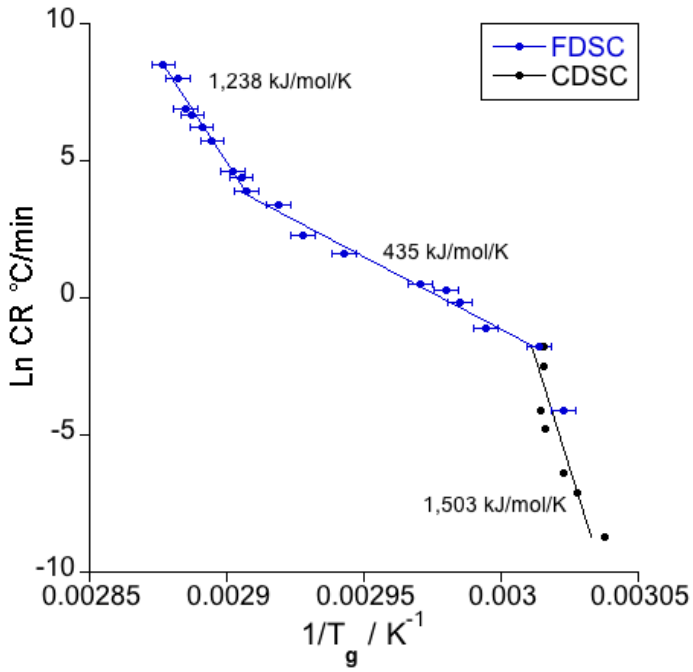

Figure A1-16 - Arrhenius plot of ln cooling rate against the reciprocal Tg of PLA measured by CDSC and FDSC

Figure A1-16 shows an Arrhenius plot of PLA combining data from CDSC and FDSC. The activation energy (E_a) calculated from the CDSC data was 1,503 kJ/mol/K, using Equation 1-1. This value shows good agreement with a number

of other papers (1,500 kJ/mol/K) (Vasanthakumari and Pennings, 1983, Iannace and Nicolais, 1997, Kawai et al., 2007).

The FDSC data shows a non-Arrhenius evolution, producing a curved data set with two values of E_a with respect to the applied cooling rate. The E_a calculated following cooling between 0.0166 to 50˚C/s was 435kJ/mol/K. This result indicates that by reducing or preventing the crystallinity of PLA, the glass transition has greater molecular mobility and a lower activation energy. A confounding calculation of the E_a was seen between 50-5,000˚C/s resulted in 1,238 kJ/mol/K. Dhotel et al. (2015) recorded a decrease in the E_a of Poly(ethylene terephthalate) (PET) and Polystyrene (PS) with cooling rate on FDSC. An increase in the E_a of the Arrhenius plot in Figure A1-16 shows an agreement with the results found by Dhotel et al. (2015) on PS where the increase can be observed at high cooling rates; however, the author does not acknowledge this change. The cooling rate at which the increase is observed in PS is 1,500˚C/s, a faster cooling rate compared to the rate observed in PLA, 50˚C/s.

The clear non-linear relationship of T_g with cooling rate is observed in excess of 50˚C/s in Figure A1-16 The change in the E_a due to the non-linear relationship between T_g and cooling rate cannot be used for the Arrhenius analysis; therefore, the increase in the E_a after cooling >50˚C/s is inapplicable.

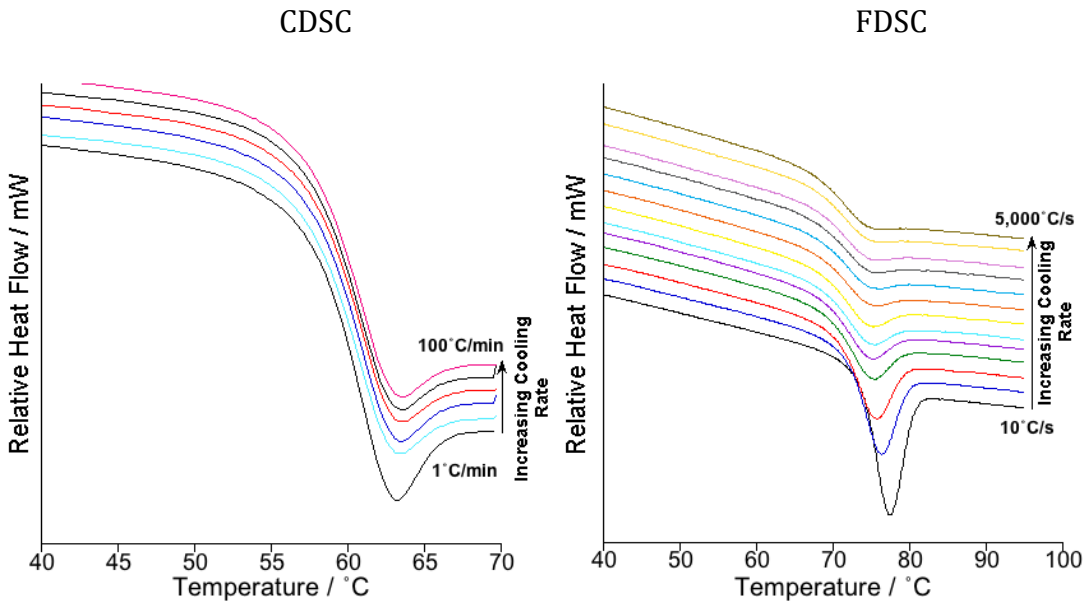

Figure A1-17 - Raw data using CDSC and FDSC with change in cooling rate

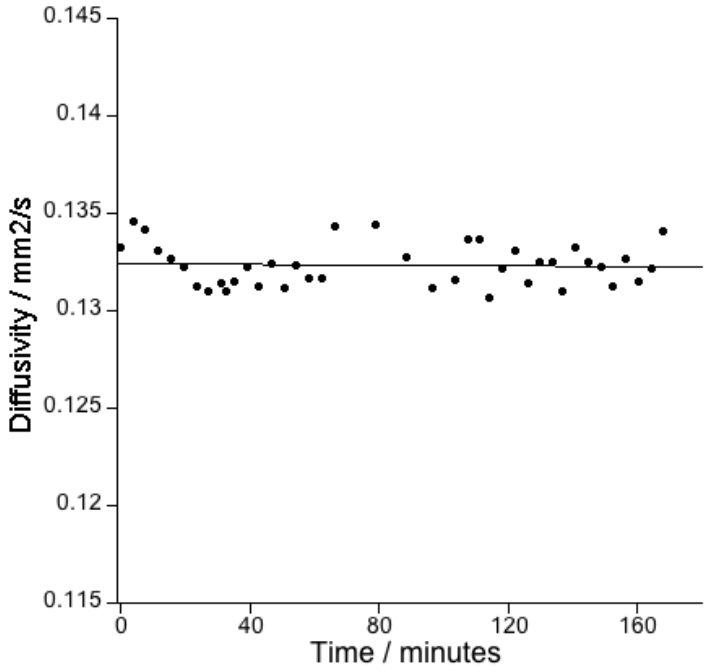

Figure A1-18 - Diffusivity with time at 45˚C

APPENDIX 2 - CO2 ASSISTED BLENDING OF POLY(LACTIC ACID) AND POLY(E-CAPROLACTONE)

ACCEPTED FOR PUBLICATION IN THE EUROPEAN POLYMER JOURNAL ON 12TH DECEMBER 2016

CO_2 ASSISTED BLENDING OF POLY(LACTIC ACID) AND POLY(Ε-CAPROLACTONE)

S.H. Murphy[1] J.J. Marsh[1], C.A. Kelly[1] , G.A. Leeke[2] and M.J. Jenkins[1*]

*[1] School of Metallurgy and Materials, University of Birmingham, Birmingham, B15 2TT – m.j.jenkins@bham.ac.uk**

*[2] School of Chemical Engineering, University of Birmingham, Birmingham, B15 2TT g.a.leeke@bham.ac.uk**

Abstract

Poly(lactic acid) (PLA) is gaining increasing interest from the packaging industry as a biodegradable alternative to oil based polymers such as polypropylene (PP) and polyethylene terephthalate (PET). However, its' inherent brittle nature prevents widescale commercial use. Blending in order to improve the Young's modulus, yield stress and elongation to break, provides a possible alternative although many polymers have been found to be immiscible with PLA. In this study, high pressure carbon dioxide (CO_2) was utilised during blending to encourage miscibility between two normally immiscible polymers: poly(ε-caprolactone) (PCL) and poly(lactic acid) (PLA). Blends were prepared by melt blending in the presence of carbon dioxide (CO_2) and compared to solvent casting and melt blending with a single-screw extruder. CO_2 assisted blends demonstrated a significant reduction in the size and number of PCL domains in a PLA matrix, and consequently improved the adhesion between phases at the microscale. The optimum melt blend composition for Young's modulus, yield stress and elongation to break was found to be 75% PLA and 25% PCL. Mechanical properties of PLA 2002D blends were further improved when prepared by CO_2 assisted melt blending.

Keywords: Poly(lactic acid), Poly(ε-caprolactone), blends, carbon dioxide, extrusion.

1. Introduction

The use of biodegradable polymers is becoming increasingly widespread as their applications broaden into both the biomedical [1] and food packaging industries [2]. Persistent rapid growth in the consumption of biodegradable plastics is forecast for the foreseeable future [3]. Among biopolymers, poly(lactic acid) (PLA) is the most prevalent in the market place, due to availability and relatively low cost of production compared to other biopolymers [4]. It is extensively used in various medical applications, such as drug delivery [5] and scaffolds in tissue engineering [6]. Additionally, there is a growing interest in the use of PLA as food packaging because PLA can be derived from natural sustainable resources and can biodegrade if correctly composted. PLA is produced from lactic acid which can be obtained from renewable (sustainable) resources such as corn and sugarcane [7, 8]. It has therefore attracted attention as an alternative to synthetic non-biodegradable polymers. However, it has been reported that PLA is relatively brittle [9] and this has limited its range of applications. Blending with other biodegradable polymers offers a possible solution to this problem. If two polymers are miscible, their mechanical, thermal and physical properties combine to generate intermediate properties, relative to their composition. Therefore, by selecting a miscible biopolymer with greater ductility, the brittle characteristics of PLA can be improved. There have been a number of attempts to improve the mechanical properties of PLA in this way by inclusion of a soft elastomeric heteropolymer into PLA. This has been identified as a method to improve the Young's modulus of the polymer blend [10, 11].

Poly(ε-caprolactone) (PCL) is a partially crystalline, biodegradable, aliphatic polyester with a low glass transition temperature in the region of -60 °C. PCL has a relatively low tensile Young's modulus and yield stress and is ductile at room temperature. PCL can exhibit elongation-to-break values in the region of 800%. Despite immiscibility being previously reported for PLA and PCL, the ductility of PCL makes it a desirable blend component for PLA [12].

PLA/PCL blends, produced through solvent casting from chloroform [10, 13] and methylene chloride [14], were found to be immiscible using DSC, DMA and SEM. Choi *et al.* [13] studied the effect of compatibilsers; P(LLA-*co*-εCL) and P(LLA-*b*-εCL), on the morphology of PLA/PCL blends. Miscibility was not obtained, however there was a reduction in size of the dispersed PCL domains.

Broz *et al.* [14] found poor adhesion at the phase boundary interface and confirmed immiscibility and phase separation through NMR. It was hypothesised that to improve the mechanical properties of the blend, the samples should be annealed in the single-phase region of the LCST phase-diagram to enhance interfacial adhesion. It was concluded that interfacial adhesion may occur when the majority phase is PCL [10].

PLLA/PCL blends have also been produced through a conventional melt-mixer followed by reprocessing into plaques [9, 15]. Improvements were seen in the mechanical properties and the fracture toughness of PLA with the addition of just 5% PCL. The improvement is a result of multiple craze formation, nucleated by debonding of spherulite interfaces. SEM and DSC confirmed phase separation using this production method, although some adhesion was seen between phases.

In other polymer blend systems, high pressure and supercritical carbon dioxide (CO_2) assisted blending has been exploited in the production of PCL/PHB [16], PE/PS [17, 18] and PLA/PEG blends [19]. However, it has yet to be explored in the blending of PCL and PLA. The introduction of CO_2 into the melt has been seen to promote miscibility in polymer systems [16-18]. CO_2 is able to diffuse into the free volume of the system allowing Lewis acid-base reactions to occur, reducing the chain entanglements by inhibiting the secondary interactions between the chains [20]. This expands the chain separations and facilitates chain motions. Blends of PE/PS prepared in the presence of CO_2 demonstrated a reduction in the size of the dispersed phase from a few microns to submicrons [17].

It can be seen from previous research that the blending of PCL and PLA has been found to be immiscible when prepared through solution and melt blending. Blending PLA and PCL in the presence of CO_2 has not been reported. Therefore, the aim of this work is to compare the domain size and mechanical and thermal properties of PLA/PCL blends formed by solution, melt and CO_2 assisted blending. More specifically, to determine whether CO_2 can induce miscibility in polymer blend systems that has been shown otherwise to be immiscible.

2. Materials and Methods

2.1 Materials

Poly-DL-(lactic acid) (PLA) grades; semi-crystalline 2002D and amorphous 4060D in the form of pellets were supplied by NatureWorks LLC (Nebraska, USA). Poly(ε-caprolactone) (PCL) grade CAPA 6800 (M_w 212,000 g mol^{-1}) was supplied as pellets by Perstorp UK Ltd (Warrington, UK). The properties of all three polymers can be found in Table 1. CO_2 (purity 99.9 %v/v) was obtained from BOC (Birmingham, UK) and used as received.

Table 1: Properties of the polymers used within this paper (*[21] **[22])

Polymer	T_g (˚C)	T_m (˚C)	D-lactide Content (%)	M_w (g mol^{-1})
PLA 2002D	55	154	4*	194,000
PLA 4060D	52	-----	11-13**	181,000
PCL CAPA 6800	-60	60	-----	212,000

2.2 Blend Preparation

Blends were prepared by solution casting, melt extrusion and CO_2 assisted melt extrusion. The following PLA/PCL compositions were produced for each preparation method; 0/100, 25/75, 50/50, 75/25 and 100/0 by weight.

2.2.1 Solution Blending

Dichloromethane was chosen as a common solvent to dissolve both PLA and PCL. The required masses of each polymer (totalling 4 g) were dissolved in dichloromethane (40 ml) to give a 10% w/v solution. The solutions were then

covered and stirred for 2 hours to ensure complete dissolution of both polymers. Films were cast into petri dishes, 9 cm in diameter, covered with glass lids and left to slowly evaporate for 2-3 days. Slow evaporation prevented the development of voids in the blend samples.

2.2.2 Production of Melt Blends by Extrusion

Prior to extrusion, the PLA grades were dried to remove any residual moisture. Drying temperatures and times were selected in accordance with the processing data sheets provided by Natureworks. Consequently, PLA 4060D was subjected to 4 hours at 45 °C and 2002D for 2 hours at 90 °C. The dried polymer was subsequently stored in desiccators with silica gel (previously dried).

The melt blends were produced using a Rondol (Staffordshire, UK) bench top linear 25 mm rotating single-screw extruder with a L/D (length/diameter) ratio of 25:1. The screw possesses a general purpose profile of 3:1 compression ratio. It was made of high strength carbon steel, heat-treated, polished and removable to enable cleaning. The screw speed was infinitely variable between 0 and 120 rpm. The barrel was also composed of heat-treated high strength carbon steel, fitted with a pressure relief valve for over pressure protection. The temperature was controlled through a series of heaters, one in each of the three zones. The barrel and die temperatures were controlled between 0-300 ˚C and cooled using a tangential water cooling system. A stainless steel two roll take-off unit (with cooling / polishing rolls) placed after the die, cooled the extrudate before passing onto a conveyor belt.

Blends of pellets, pre-mixed by mass, were added to the hopper of the extruder in 200 g batches. Barrel and die temperatures were set to 160 °C and 170 °C, respectively. The pressure in the screw was monitored using an external pressure transducer. Samples were extruded through a 1 mm slit die and passed through the cooled rollers onto a conveyor belt. Screw speeds of 20 and 30 rpm were selected.

2.2.3 Production of Carbon Dioxide Assisted Blends

Blends were also produced in the presence of CO_2 using the same extruder as discussed above, however the extruder was modified to allow the injection of CO_2 into the polymer melt.

CO_2 was injected via a custom made design of 4 injection ports, 2 on either side of the barrel, into zones 2 and 3 (see figure 1 for extruder set-up). A Jasco pump (Model PU-2086 Plus) fitted with a chiller head enabled CO_2 to be pumped in liquid form. A pressure relief valve was installed to prevent over pressurisation in the extruder. The pressure in the extruder was monitored using a pressure transducer to within 0.1 bar using a Druck PTX (Leicester, UK) transducer.

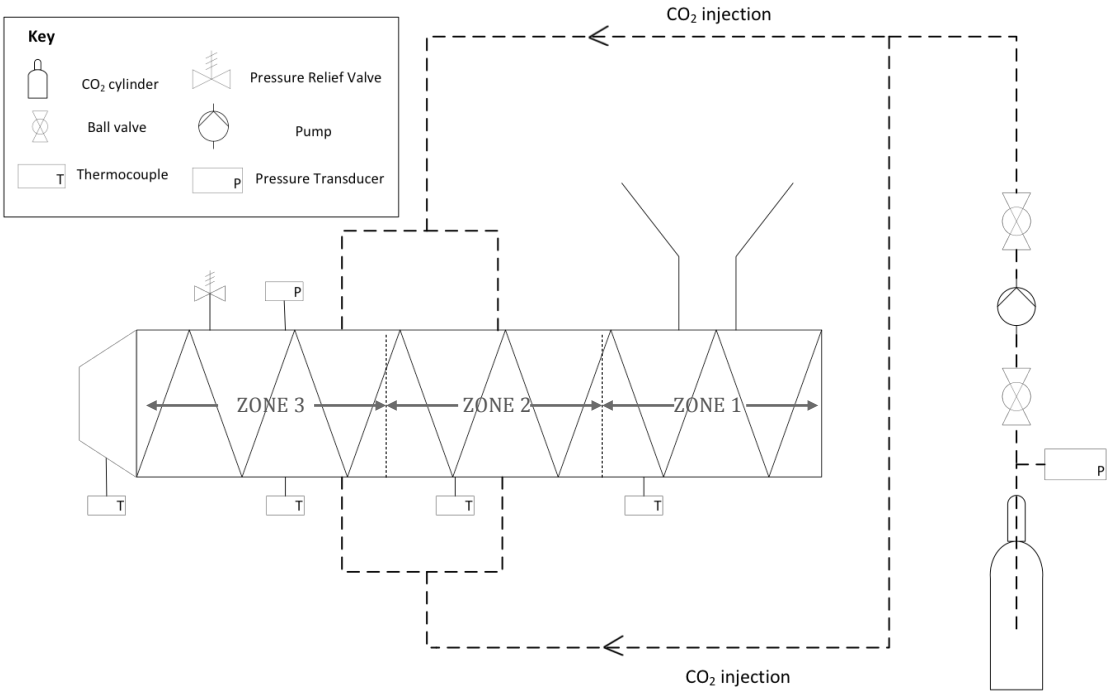

Figure 1. Schematic of the extruder set-up illustrating the injection of CO_2.

CO_2 was added at a specific concentration in relation to the polymer flow rather than at a set pressure to maintain consistency throughout the polymer. This resulted in an average combined CO_2/polymer pressure of 67 bar in the extruder. In order to calculate the CO_2 concentration for addition into the extruder, each polymer was extruded at both 20 and 30 rpm and the average of three extruded masses per

minute was calculated for each screw speed. The CO_2 flow rate (g/min) was then calculated as a wt% of the measured polymer mass extruded per minute using equation 1. This enabled the input of a given concentration of CO_2, in relation to the polymer, into the extruder. This calculated value was converted into ml/min as CO_2 was injected as liquid. Equation 2 shows this conversion. The density of CO_2 was calculated by NIST web-book [23] as 0.91898 g/ml based on the CO_2 pressure (4.8 MPa) and temperature (4 ˚C) in the pump.

$$\boldsymbol{Flow\ rate_{CO2}\ (g/min)} = \frac{\boldsymbol{CO_2\ Concentration\ (wt\%)}}{\mathbf{100}} \times \boldsymbol{Flow\ rate_{polymer}\ (g/\mathrm{min}\ )}$$

[Eq. 1]

$$\boldsymbol{Flow\ rate_{CO2}\ (ml/\mathrm{min})} = \frac{\boldsymbol{Flow\ rate_{CO2}\ (g/\mathrm{min})}}{\boldsymbol{Density_{CO2}\ (g/ml)}}$$

[Eq. 2]

CO_2 is known to depress the melting point of semi-crystalline polymers, it was found that blends of PLA and PCL could be readily extruded at reduced barrel and die temperatures of 150 °C and 160 °C, respectively. As the Gibbs free energy equation states that blending is proportional to temperature, the reduced processing conditions will not enhance miscibility and therefore any effects observed will be due to the presence of CO_2 alone.

2.3 Microstructural, Mechanical and Thermal Analysis

Fracture surfaces were produced by a flexural loading of the blend samples following immersion in liquid nitrogen. The fracture surfaces were mounted on an aluminium stub using conductive carbon adhesive discs and coated in gold using a Polaron SC7640 sputter coater. Coating the samples for 3 minutes deposited approximately 10 to 12 nm of gold, which provided sufficient conductivity to minimize charging of the sample surface. Samples were imaged using a Phillips (XL30 ESEM) scanning electron microscope. An accelerating voltage of 10 kV was selected.

Tensile tests were carried out using a mechanical test instrument (Instron 5566) interfaced to a PC. The instrument was controlled using proprietary Instron Merlin software. Samples were cut into a standard 25 mm (L_o) 'dog-bone' shape. The width of the narrow central section was 4 mm and the thickness was recorded from a three-point average. Stress-strain curves were recorded at 25 ˚C and at a strain rate of 10 mm/min. Young's modulus, elongation to break and yield stress were determined from the resulting stress-strain curves. A minimum of 5 repeats were performed for each blend system.

Thermal analysis of the blends was performed using a Mettler Toledo DSC1 (Greifensee, Switzerland) purged with nitrogen at a gas flow rate of 100 cm^3/min. The instrument was interfaced to a personal computer and controlled using proprietary STARe software (version 11). The thermal response of the instrument was calibrated from the enthalpy of fusion of a known mass of indium (99.999% pure). The temperature of the calorimeter was calibrated using the melting point of tin. Samples of around 5-7 mg were contained in aluminium pans with an empty pan used as a reference. The glass transition temperature (T_g), melting point (T_m) and enthalpy of fusion (ΔH_f) of the blends were measured from the initial heating run at 10 ˚C/min.

3. Results and Discussion

3.1 Microstructural Characterisation

The blends created by solvent casting from dichloromethane showed clear evidence of gross phase separation for each of the blend systems. Relatively large domains (up to 10 μm) were observed by SEM (Figure 2a, 2b and supplementary information). This observation is in accordance with other studies in which clear phase separation is reported, although it should be noted that these observations were made in blends produced from different grades of PLA and PCL [24]. No difference was observed between the two grades of PLA.

a) b)

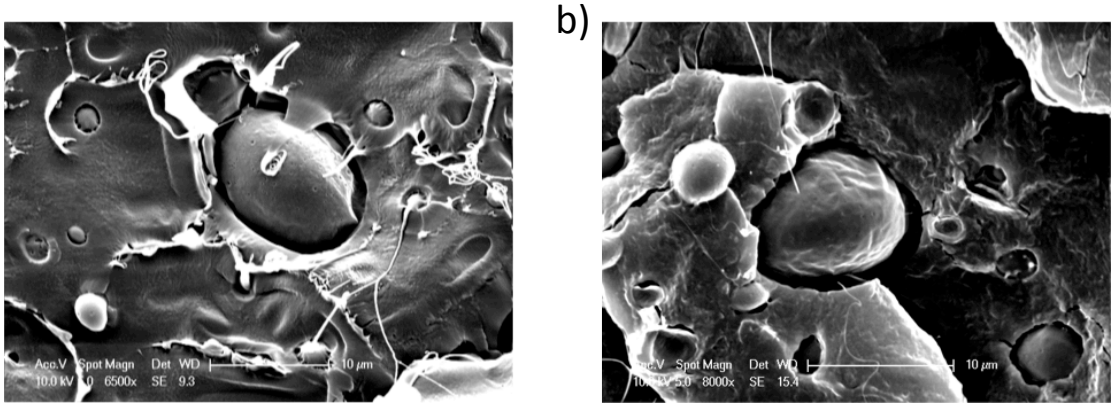

Figure 2a and b. SEM images of solvent cast **(2a):** 75/25 PLA 4060D/PCL and **(2b):** 75/25 PLA 2002D/PCL.

Solution casting from dichloromethane dissolves both polymers allowing constituent polar groups to interact. However, slow evaporation of the solvent (which was required in order to reduce the formation of voids) provides time for the polymers to phase separate and encourages crystallinity to develop causing further phase separation. The observation of phase separation in previous PLA/PCL solvent-cast blends was attributed to crystallisation of PCL and expulsion of PLA in these crystalline regions through spherulitic growth [25]. It was noted that phase separation may also be induced by the presence of a third component, the solvent. Solvent-casting these blends promotes phase separation and may not reflect the true morphology of the two component systems.

The polymer blend solution was initially transparent and no interfacial boundary layers were observed as a result of any solution density differences. Therefore, molecular level mixing was assumed to have taken place. Subsequently, no boundary layers were observed to develop on evaporation of the solvent, yet the final blend was grossly phase separated. Clearly, the phase separation observed in this preparation method was induced by crystallisation of the homopolymers from solution.

As seen above for solvent cast blends, at a composition of 75/25 PLA/PCL, the immiscibility results in the formation of PCL spheres within the PLA 4060D and

2002D matrices. On fracturing the material prior to SEM analysis, PCL spheres can drop out of the fracture surface resulting in the formation of concave holes. The number and dispersion of these concave holes and PCL spheres can be used to assess the miscibility.

Melt blending with a single screw extruder was also found to yield a phase separated system at all compositions, screw speeds and PLA grades investigated. However, a clear improvement in dispersion and domain size (reduced from 10 μm by solvent casting to around 1 μm by melt blending) was observed in the 75/25 PLA/PCL composition (Figures 3a, 3b and supplementary information).

a) b)

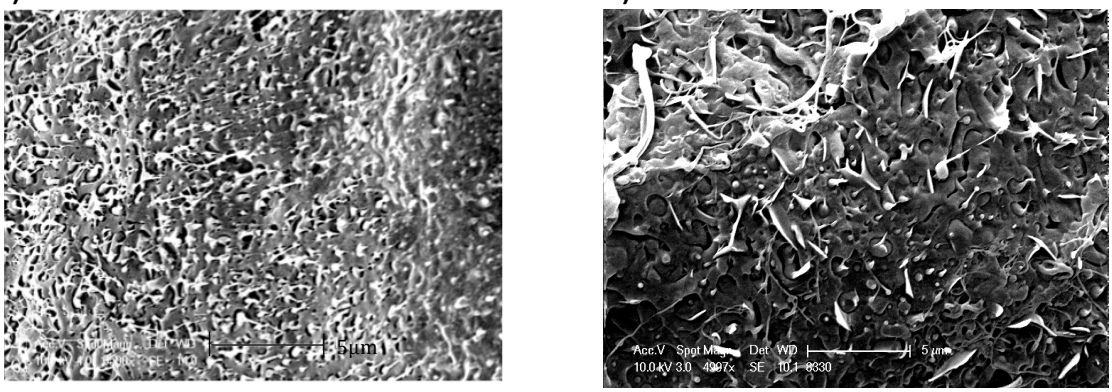

Figure 3a and b. SEM images of melt blends produced with a single screw extruder at 160 ˚C. **(3a):** 75/25 PLA 4060D/PCL at 20 rpm. **(3b):** 75/25 PLA 2002D/PCL at 30 rpm.

The application of heat (160 °C which is above the melting points of both polymers) combined with the shear forces of mechanical mixing during melt blending, initially creates a higher level of dispersion allowing the blends to transform from the two phase into the one phase region of the LCST curve [12]. Previous work has also shown that the low interfacial tension and similar viscosities of the two polymers contribute to both size and homogeneity of the dispersed phase and final sample morphology [26].

The morphology of the blend system is stabilised on cooling after exiting from the die at the end of the barrel. If there is vitrification of the PLA component prior to the

crystallisation-induced phase separation of PCL from the blend, a miscible system will be retained. However, in this case, the cooling rate was insufficient to limit the phase separation of PCL, although an enhanced dispersion was still evident.

A further improvement in the dispersion, as indicated by a reduction in the size and quantity of the PCL domains, was observed when the blends were prepared in the presence of CO_2 (Figures 4a, 4b and supplementary information). Similar to the melt blends, the blend composition that showed the greatest reduction in size and dispersion of domains was 75/25 PLA/PCL for both PLA grades. Domain sizes in these blends were around 0.2 μm in diameter. However, all blends produced in the presence of CO_2 showed a high degree of porosity (around 100 nm in diameter) due to the effect of depressurisation of the blend system on exit from the extruder. These are easily distinguishable from the concave holes formed by loss of PCL domains as small cylindrical voids. Similar images were obtained for PLA 4060D and PLA 2002D.

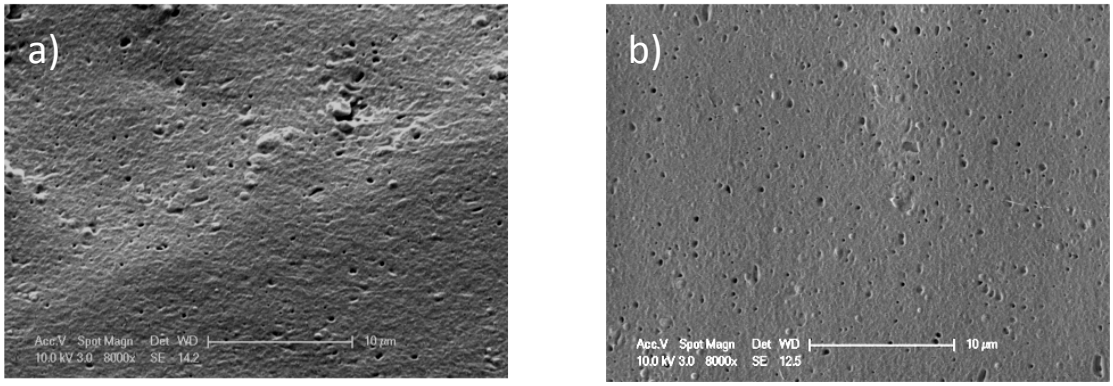

Figure 4a and b. SEM images of blends produced in the presence of 10% carbon dioxide at 150 ˚C. **(4a):** 75/25 PLA 4060D/PCL at 20 rpm. **(4b):** 75/25 PLA 2002D/PCL at 30 rpm.

Similar enhanced miscibility in the presence of CO_2 has been previously reported [16-19]. The gaseous properties of CO_2 enables its diffusion into the free volume of polymers, between the individual chains. Once inside, CO_2 forms Lewis acid-base interactions with the carbonyl groups (present in both PLA and PCL). This disrupts the inter/intra molecular interactions, decreasing the number of chain entanglements within the polymers and consequently reduces their melting point

and viscosity [20]. The creation of additional free volume and increased chain mobility enables better interaction and mixing between the two polymers, enhancing the potential for miscibility in this system. Blend morphology has been investigated in other polymer systems: PE/PS blends and PS/PMMA using carbon dioxide [17, 18, 27]. These blends showed a significant decrease in the size of the dispersed phase from a few microns to submicron by injecting CO_2. This enhanced miscibility means more intimate mixing of PLA and PCL resulting in consistency throughout the material.

A completely miscible blend system will display only one phase in an SEM image. Large spherical domains of the minor phase dispersed within the major phase were found by SEM following solvent blending, indicating poor miscibility. Melt extrusion was found to reduce the size of these domains and CO_2 assisted melt extrusion reducing them further, indicating the highest miscibility of the two polymers.

3.2 Mechanical characterisation

Figure 5 shows a representative example of the engineering stress-strain curves for all PLA 4060D/PCL blends produced by melt blending. The curve for 100% PLA is shown as an inset due to the dramatic change in elongation-to-break. It is clear that with increasing PCL content in the blend, the tensile behaviour of the blend system changed dramatically: the reduction in yield stress was compensated by a significant increase in elongation at break. The same trend was also apparent in the PLA 2002D/PCL system.

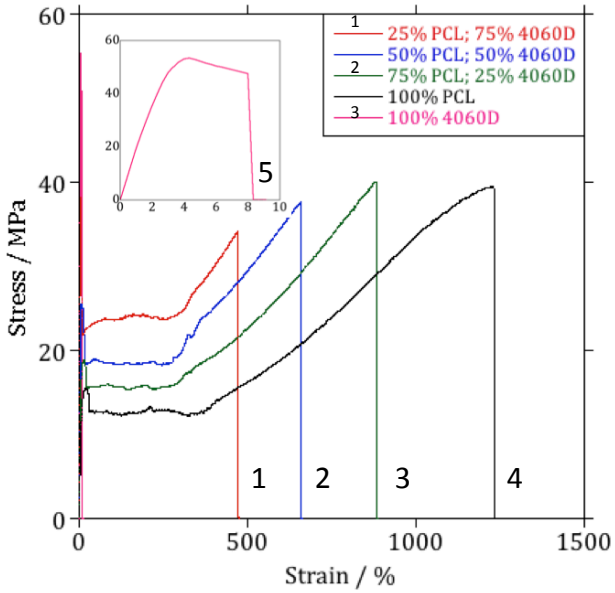

Figure 5. An example of the engineering stress-strain curves for the mechanically blended PLA 4060D/PCL blend system. Inset top left is the result for 100% PLA.

Figures 6, 7 and 8 illustrate the variation of mechanical properties with composition for both blend systems and all three preparation methods. The mechanical properties of the blends produced by melt and CO_2 assisted extrusion generally change linearly with composition, suggesting that they are obeying the rule of mixtures.

Pure PCL has a much higher elongation to break than both PLA 4060D and 2002D. The results (Figure 6) show a reduction in the elongation to break as the content of both grades of PLA is increased, indicative of blending. This coincides with the SEM for both melt and CO_2 assisted blending. No significant difference was observed between the two methods. The porosity generated on venting the CO_2 from the polymer following extrusion introduces stress concentration sites into the structure, resulting in premature breakage. Further evidence is the reduction in elongation to break values for pure PCL produced in the presence of CO_2 compared to melt blending.

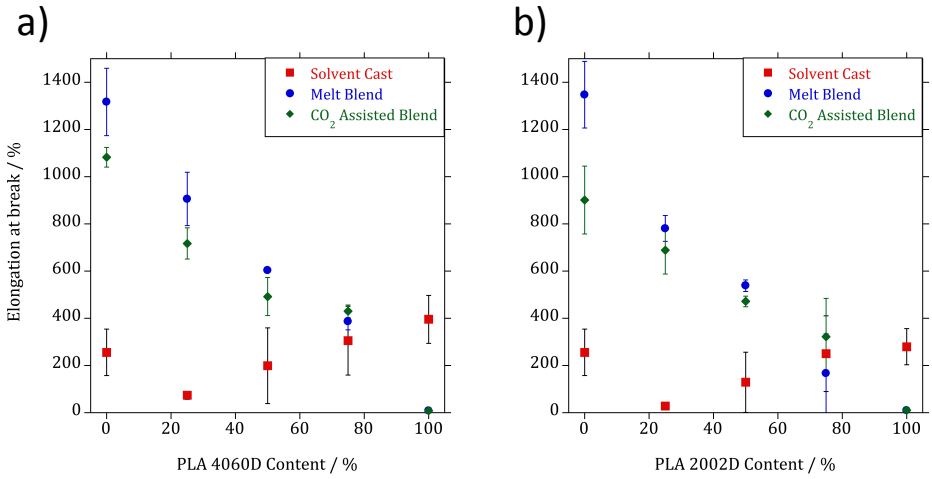

Figure 6a and 6b. A comparison of elongation at break for solvent cast, melt and CO_2 assisted blends of **(6a):** PLA 4060D and **(6b):** PLA 2002D/PCL at various compositions. The standard uncertainty is denoted by error bars, which represents the standard deviation averaged over multiple experiments.

In contrast to these results, the blends formed through solvent casting are markedly different. An initial reduction in the elongation is observed on the addition of both PLA 4060D and 2002D, which increases again as the proportion of PLA rises. The much lower values obtained compared to the other processing techniques are attributed to gross phase separation of the two components. Residual solvent is also known to act as a plasticiser in solvent cast polymers and blends which accounts for the increase in elongation to break for pure PLA 4060D and 2002D compared to the other blending methods. In contrast, the elongation to break of PCL is reduced to below the value of PLA following solvent casting. This leads to an increase in elongation to break as the PLA content is increased within the blend.

Figure 7 shows an increase in Young's modulus as PLA 4060D and 2002D content increases for melt blending with and without the presence of CO_2. There are little differences in the values between the two blending methods, with exception of 75% PLA 2002D, where there is a marked increase in the Young's modulus when blended in the presence of CO_2, suggesting enhanced miscibility for this blend.

The solvent blending produced samples with a much lower modulus as a result of phase separation between the individual components.

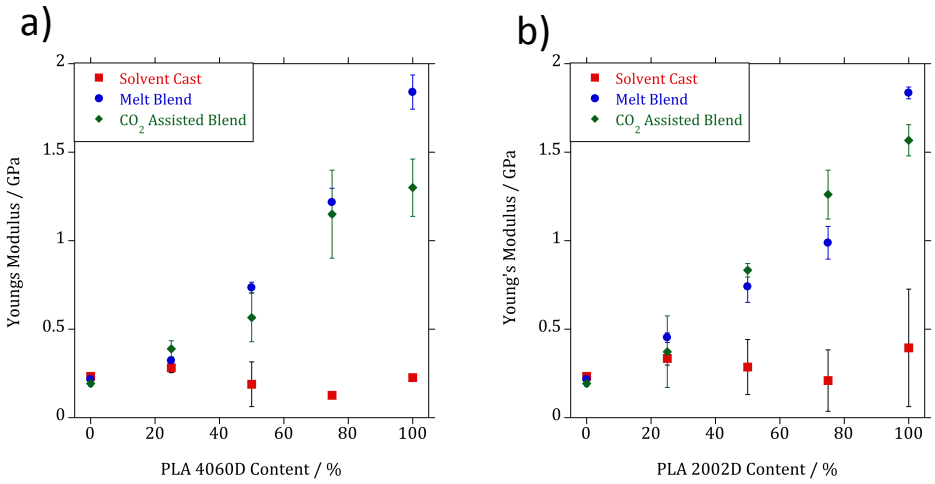

Figure 7a and 7b. A comparison of Young's Modulus for solvent cast, melt and CO_2 assisted blends of **(7a):** PLA 4060D and **(7b):** PLA 2002D/PCL at various compositions. The standard uncertainty is denoted by error bars, which represents the standard deviation averaged over multiple experiments.

There is little difference in the yield stress between the two melt blending techniques for PLA 4060D and PCL blends (Figure 8a and b). Interestingly, an improvement in the yield stress was observed in the PLA 2002D/PCL blends when blended in the presence of CO_2, becoming more significant as the PLA content increased. This is likely to be a result of enhanced mixing when processed with CO_2, creating smaller PCL domains in the material and therefore smaller inclusions that cause the material to fracture. Solvent blended samples displayed a significantly lower yield stress compared to melt blended methods. Solvent casting was found to have no effect on yield stress of pure PCL, however, the strength of pure PLA was significantly reduced due to plasticisation by solvent residue. This coupled with poor miscibility resulted in the low yield stress values obtained.

The melt blend results differ from those published previously where complete phase separation resulted in a negative deviation from linearity in all mechanical properties [10]. A likely explanation is that the method mentioned in the paper included an

additional thermal processing step using a hot-press, to produce suitable samples for mechanical testing. As this involves heating in a static environment it will promote phase separation.

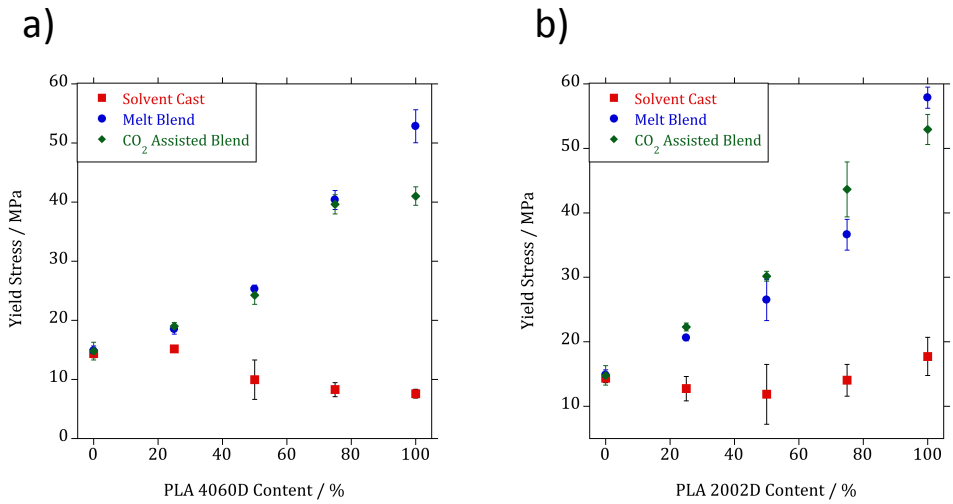

Figure 8a and 8b. A comparison of yield stress for solvent cast, melt and CO_2 assisted blends of **(8a):** PLA 4060D and **(8b):** PLA 2002D/PCL at various compositions. The standard uncertainty is denoted by error bars, which represents the standard deviation averaged over multiple experiments.

A suitable packaging material must have a sufficiently high Young's modulus and yield stress to prevent weakening under load in addition to a high elongation to break, preventing brittle fractures of the product. In light of this, the most suitable melt blend was found to be 75% PLA (both 4060D and 2002D) with 25% PCL. However, the properties of the 2002D blend were enhanced further through melt blending in the presence of CO_2, denoted by a higher Young's modulus and yield stress with no change in elongation to break. This concurs with the above SEM results, which show a smaller PCL domain size and quantity when processed in the presence of CO_2, indicating increased miscibility.

Although not fully evident from mechanical testing analysis, due to porosity created during CO_2 venting, a clear improvement in the miscibility of PLA and PCL when melt blended in the presence of CO_2, is observed by SEM. This indicates that CO_2 has influenced the interfacial tension between both polymers enabling better mixing and dispersion of phases. The finer dispersion of PCL domains results in lower number of

stress concentration points throughout the sample. This result is consistent with Todo *et al.* [9] who found that larger PCL domains within PCL/PLA blends hasten the initiation of fracture by inducing more severe stress concentrations than smaller phases within the blends.

3.3 Thermal Analysis

DSC was used to explore changes to the thermal transition temperatures in 75/25 PLA/PCL blends, where the best mechanical properties and smallest domain sizes were obserevd. Figures 9a and 9b show the DSC traces of 75/25 PLA/PCL and respective homopolymers for the PLA 4060D/PCL and PLA 2002D/PCL blends produced with and without the presence of CO_2. As a result of the completely amorphous nature of PLA 4060D, only one melting endotherm corresponding to PCL was observed by DSC in the subsequent blends (Figure 9a). The temperature of this transition was found to decrease following blending, indicative of miscibility, by the larger reduction of the CO_2 assisted blend's melting point. The observation of two melting peaks in figure 9b confirms that phase separation has taken place in blends made by both techniques, and that any interactions in the melt were not significant enough to develop / retain complete miscibility on cooling. However, the melting point of PCL was again found to decrease following melt and CO_2 assisted blending, illustrating partial miscibility.

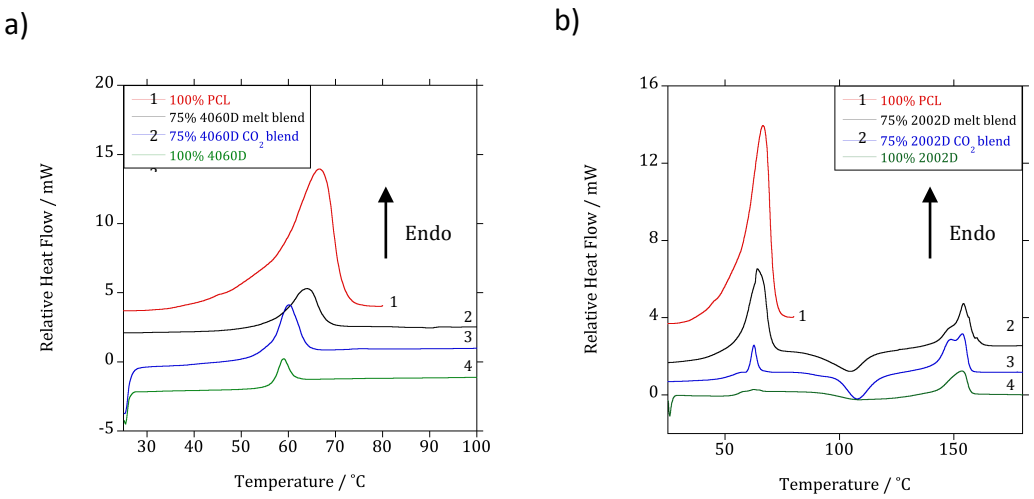

Figure 9a and 9b. A comparison of DSC traces **of (9a):** 75/25 PLA 4060D/PCL and **(9b):** 75/25 PLA 2002D/PCL produced by melt and CO_2 assisted blending with their homopolymers.

The pure PCL samples exhibit much larger melting endotherms for the PCL component (figure 9a and 9b) than those observed for the blended systems. In the PLA 2002D blend, this peak is further reduced when blended in the presence of CO_2, exhibiting corresponding ΔH_f PCL values of 62.66 J/g for 100% PCL, 46.6 J/g for the melt blend and 17.14 J/g for the blend produced in the presence of carbon dioxide. Division of these enthalpies of fusion by the value for 100 % crystalline PCL, 139 J/g [28], gives the crystallinity of the PCL component within the blend. From this it can be seen that there is a surprisingly low degree of crystallinity in the CO_2 assisted blend with PLA 2002D (12.3% compared with 33.5 % for melt blended). The reduction in crystallinity may be associated with fractionated crystallisation of the PCL component, influenced by a decreased number of nuclei per domain as the size decreases[29]. Similar results have been observed in PCL/PHB blends, where fractionated crystallisation also occurs in the PCL component [30]. This result was attributed to the dispersion of PCL into isolated domains, greater in number than the available active heterogeneities usually present in the bulk homopolymer [30]. A reduction in PCL crystallinity corresponding with decreased domain size has also been reported in PLLA/PCL blends [13].

The glass transition of PLA 4060D in each of the blends (Figure 9a) and PLA 2002D in the melt blend (Figure 9b) cannot be determined as a result of the overlapping transition with the melting endotherm of PCL. However, the glass transition of PLA 2002D (Figure 9b) can be partially seen immediately prior to the PCL melting endotherm in the PLA 2002D blend produced in the presence of carbon dioxide. The midpoint of this transition was found to be 52 ˚C compared to 56 ˚C exhibited by the homopolymer. This slight reduction in the T_g of PLA 2002D suggests the development of partial miscibility.

Cold crystallisation is observed between the melting peak of PCL and PLA 2002D (figure 9b) suggesting that PCL may be acting as a nucleating agent for PLA. The finer distribution of PCL domains (acting as more nucleating points) within the CO_2 assisted blend may allow additional crystallisation to occur upon heating. It has been

commonly reported [31, 32] that PLA exhibits relatively slow crystallisation kinetics and it has been found that within the time-scales of a conventional DSC experiment run at 10 ˚C/min, PLA will not undergo crystallisation (on cooling) from the melt. Therefore, it is unusual to observe a melting endotherm post processing. The double melting peak on the PLA component for the CO_2 assisted blend indicates the formation of different lamellae sizes, often explained by the melt-recrystallisation model [8, 9]. The appearance of multiple melting peaks is reported in numerous partially crystalline polymers [33] such as poly(ether-ether-ketone) (PEEK) [34, 35], poly(ethylene terephthalate) (PET) [36], poly(butylene napthalate) (PBN) [37], nylon-6 [38] and biodegradable polymers such as poly($_L$-lactide-*co*-glycolide) (PLGA) [39], and poly (lactic acid) (PLA) [40]. Many explain the double melting behaviour using the melt-recrystallisation model [41]. According to this model, the low temperature and high temperature endothermic peaks in the DSC melting trace are attributed to melting of original crystals (formed upon previous cooling) and to the melting of crystals formed within the heating scan of the experiment.

The reduced size of the PCL melting endotherm in the CO_2 assisted 75/25 PLA 2002D/PCL blend is an indication of increased miscibility over the PLA 4060D polymer and may explain the enhanced Young's modulus and yield stress results observed previously. The smaller endotherm is indicative of lower crystallinity, arising due to a greater dispersion of PCL within the PLA 2002D domain. This greater dispersion will also result in fewer weak points within the structure and a strength comparative to PLA 2002D as observed in the mechanical testing results.

4. Conclusions

Blends produced by solvent casting display immiscibility across all compositions. A significant improvement in mechanical properties and polymer domain size was observed through melt blending using a single screw extruder. The 75/25 PLA (4060D and 2002D)/PCL blend was identified as having the optimum mechanical properties with the highest Young's modulus and yield stress with a high elongation to break. Although the mechanical properties of the CO_2 assisted blends showed

little improvement on samples made by melt blending, the SEM images clearly indicate an improvement at the microscale with smaller and fewer PCL domains observed. However, porous structures have been observed which may explain the lack of a significant improvement in mechanical properties. Regardless of the porosity, an improvement in mechanical properties was found for the 75/25 PLA 2002D/ PCL blend following CO_2 assisted extrusion, corresponding to an increase in both the Young's modulus and yield stress compared to the other blending techniques.

Data sets from the above work may be requested from the authors by email (M.J.Jenkins@bham.ac.uk).

5. References

[1] Z. Zhang, O. Ortiz, R. Goyal, and J. Kohn, "Biodegradable Polymers," in *Handbook of Polymer Applications in Medicine and Medical Devices*, K. Modjarrad and S. Ebnesajjad, Eds., ed Oxford: William Andrew Publishing, 2014, pp. 303-335.

[2] M. Bhattacharya, R. L. Reis, V. Correlo, and L. Boesel, "Material properties of biodegradable polymers," in *Biodegradable polymers for industrial applications*, R. Smith, Ed., ed Cambridge: Woodhead Publishing Limited, 2005.

[3] IHS. (2012). *Biodegradable Polymers*. Available: http://www.ihs.com/products/chemical/planning/ceh/biodegradable-polymers.aspx

[4] W. Groot, J. V. Krieken, O. Sliekersl, and S. De Vos, "Production and Purification of Lactic Acid and Lactide," in *Poly(lactic acid) Synthesis, Structures, Properties, Processing, and Applications*, R. Auras, L.-T. Lim, S. E. M. Selke, and H. Tsuji, Eds., ed New Jersey: Wiley, 2010.

[5] K. S. Soppimath, T. M. Aminabhavi, A. R. Kulkarni, and W. E. Rudzinski, "Biodegradable polymeric nanoparticles as drug delivery devices," *Journal of Controlled Release,* vol. 70, pp. 1-20, 1/29/ 2001.

[6] V. Guarino, F. Causa, P. Taddei, M. di Foggia, G. Ciapetti, D. Martini*, et al.*, "Polylactic acid fibre-reinforced polycaprolactone scaffolds for bone tissue engineering," *Biomaterials,* vol. 29, pp. 3662-3670, 9// 2008.

[7] D. Garlotta, "A Literature Review of Poly(Lactic Acid)," *Journal of Polymers and the Environment,* vol. 9, pp. 63-84, 2001.

[8] NatureWorksLLC. (2013). *How Ingeo Is Made*. Available: http://www.natureworksllc.com/The-Ingeo-Journey/Eco-Profile-and-LCA/How-Ingeo-is-Made

[9] M. Todo, S. D. Park, T. Takayama, and K. Arakawa, "Fracture micromechanisms of bioabsorbable PLLA/PCL polymer blends," *Engineering Fracture Mechanics,* vol. 74, pp. 1872-1883, 2007.

[10] N. López-Rodríguez, A. López-Arraiza, E. Meaurio, and J. R. Sarasua, "Crystallization, morphology, and mechanical behavior of polylactide/poly(ε-caprolactone) blends," *Polymer Engineering & Science,* vol. 46, pp. 1299-1308, 2006.

[11] J. Zhao, X. Yuan, Y. Cui, Q. Ge, and K. Yao, "Preparation and characterization of poly(L-lactide)/ poly(ϵ-caprolactone) fibrous scaffolds for cartilage tissue engineering," *Journal of Applied Polymer Science,* vol. 91, pp. 1676-1684, 2004.

[12] J. C. Meredith and E. J. Amis, "LCST phase separation in biodegradable polymer blends: poly(D,L-lactide) and poly(ϵ-caprolactone)," *Macromolecular Chemistry and Physics,* vol. 201, pp. 733-739, 2000.

[13] N.-S. Choi, C.-H. Kim, K. Y. Cho, and J.-K. Park, "Morphology and hydrolysis of PCL/PLLA blends compatibilized with P(LLA-co-ϵCL) or P(LLA-b-ϵCL)," *Journal of Applied Polymer Science,* vol. 86, pp. 1892-1898, 2002.

[14] M. E. Broz, D. L. VanderHart, and N. R. Washburn, "Structure and mechanical properties of poly(,-lactic acid)/poly([var epsilon]-caprolactone) blends," *Biomaterials,* vol. 24, pp. 4181-4190, 2003.

[15] C. L. Simões, J. C. Viana, and A. M. Cunha, "Mechanical properties of poly(ε-caprolactone) and poly(lactic acid) blends," *Journal of Applied Polymer Science,* vol. 112, pp. 345-352, 2009.

[16] M. J. Jenkins, Y. Cao, L. Howell, and G. A. Leeke, "Miscibility in blends of poly(3-hydroxybutyrate-co-3-hydroxyvalerate) and poly(ε-caprolactone) induced by melt blending in the presence of supercritical CO2," *Polymer,* vol. 48, pp. 6304-6310, 2007.

[17] M. Lee, C. Tzoganakis, and C. B. Park, "Extrusion of PE/PS blends with supercritical carbon dioxide," *Polymer Engineering & Science,* vol. 38, pp. 1112-1120, 1998.

[18] M. Lee, C. Tzoganakis, and C. B. Park, "Effects of supercritical CO2 on the viscosity and morphology of polymer blends," *Advances in Polymer Technology,* vol. 19, pp. 300-311, 2000.

[19] C. A. Kelly, A. Naylor, L. Illum, K. M. Shakesheff, and S. M. Howdle, "Supercritical CO2: A Clean and Low Temperature Approach to Blending PDLLA and PEG," *Advanced Functional Materials,* vol. 22, pp. 1684-1691, 2012.

[20] Z. Shen, M. A. McHugh, J. Xu, J. Belardi, S. Kilic, A. Mesiano*, et al.*, "CO2-solubility of oligomers and polymers that contain the carbonyl group," *Polymer,* vol. 44, pp. 1491-1498, 2003.

[21] M. Mihai, M. A. Huneault, and B. D. Favis, "Crystallinity development in cellular poly(lactic acid) in the presence of supercritical carbon dioxide," *Journal of Applied Polymer Science,* vol. 113, pp. 2920-2932, 2009.

[22] P. Krishnamachari, J. Zhang, J. Lou, J. Yan, and L. Uitenham, "Biodegradable Poly(Lactic Acid)/Clay Nanocomposites by Melt Intercalation: A Study of Morphological, Thermal, and Mechanical Properties," *International Journal of Polymer Analysis and Characterization,* vol. 14, pp. 336-350, 2009/05/19 2009.

[23] NIST. (2011). *NIST Chemistry WebBook*. Available: http://webbook.nist.gov/chemistry/fluid/

[24] J. López, C. Ramírez, M. J. Abad, L. Barral, J. Cano, and F. Díez, "Dynamic mechanical analysis of an epoxy/thermoplastic blend: polymerization-induced phase separation," *Polymer International,* vol. 51, pp. 1100-1106, 2002.

[25] H. Tsuji and Y. Ikada, "Blends of aliphatic polyesters. I. Physical properties and morphologies of solution-cast blends from poly(DL-lactide) and poly(ε-caprolactone)," *Journal of Applied Polymer Science,* vol. 60, pp. 2367-2375, 1996.

[26] L. P. B. M. Janssen and S. Nalawade, P., "Polymer Extrusion with Supercritical Carbon Dioxide," in *Supercritical Carbon Dioxide: in Polymer Reaction Engineering*, M. F. Kemmere and T. Meyer, Eds., ed Germany: WILEY-VCH, 2005.

[27] M. D. Elkovitch, D. L. Tomasko, and L. J. Lee, "Supercritical carbon dioxide assisted blending of polystyrene and poly(methyl methyacrylate)," *Polymer Engineering & Science,* vol. 39, pp. 2075-2084, 1999.

[28] N. Lopez-Rodriquez, A. Lopez-Arraiza and E. Meaurio and J.R. Sarasua, "Crystallisation, morphology and mechanical behaviour of polylactide/poly(ε-caprolactone) blends" *Polymer Engineering and Science*, vol. 46(9), pp.1299-1308, 2006.

[29] L. A. Utracki, *Polymer Blends* vol. 11: Rapra Technology, 2000.

[30] D. Lovera, L. Márquez, V. Balsamo, A. Taddei, C. Castelli, and A. J. Müller, "Crystallization, Morphology, and Enzymatic Degradation of Polyhydroxybutyrate/Polycaprolactone (PHB/PCL) Blends," *Macromolecular Chemistry and Physics,* vol. 208, pp. 924-937, 2007.

[31] M. Salmerón Sánchez, V. B. F. Mathot, G. Vanden Poel, and J. L. Gómez Ribelles, "Effect of the Cooling Rate on the Nucleation Kinetics of Poly(l-Lactic Acid) and Its Influence on Morphology," *Macromolecules,* vol. 40, pp. 7989-7997, 2007/10/01 2007.

[32] W. T. Zhai, Y. Ko, W. L. Zhu, A. S. Wong, and C. B. Park, "A Study of the Crystallization, Melting, and Foaming Behaviors of Polylactic Acid in Compressed CO2," *International Journal of Molecular Sciences,* vol. 10, pp. 5381-5397, Dec 2009.

[33] S. Z. D. Cheng and B. Wunderlich, "Thermal analysis of thermoplastic polymers," *Thermochimica Acta,* vol. 134, pp. 161-166, 10// 1988.

[34] S. Z. Cheng, M. Cao, and B. Wunderlich, "Glass transition and melting behavior of poly (oxy-1, 4-phenyleneoxy-1, 4-phenylenecarbonyl-1, 4-phenylene)(PEEK)," *Macromolecules,* vol. 19, pp. 1868-1876, 1986.

[35] B. B. Sauer, W. G. Kampert, E. Neal Blanchard, S. A. Threefoot, and B. S. Hsiao, "Temperature modulated DSC studies of melting and recrystallization in polymers exhibiting multiple endotherms," *Polymer,* vol. 41, pp. 1099-1108, 2// 2000.

[36] P. J. Holdsworth and A. Turner-Jones, "The melting behaviour of heat crystallized poly(ethylene terephthalate)," *Polymer,* vol. 12, pp. 195-208, 3// 1971.

[37] M. Yasuniwa, S. Tsubakihara, and T. Fujioka, "X-ray and DSC studies on the melt-recrystallization process of poly(butylene naphthalate)," *Thermochimica Acta,* vol. 396, pp. 75-78, 2003.

[38] M. Todoki and T. Kawaguchi, "Origin of double melting peaks in drawn nylon 6 yarns," *Journal of Polymer Science: Polymer Physics Edition,* vol. 15, pp. 1067-1075, 1977.

[39] Y. Wang and J. F. Mano, "Multiple melting behaviour of poly(l-lactide-co-glycolide) investigated by DSC," *Polymer Testing,* vol. 28, pp. 452-455, 2009.

[40] M. Yasuniwa, S. Tsubakihara, Y. Sugimoto, and C. Nakafuku, "Thermal analysis of the double-melting behavior of poly(L-lactic acid)," *Journal of Polymer Science Part B: Polymer Physics,* vol. 42, pp. 25-32, 2004.

[41] B. Wunderlich, *Macromolecular Physics* vol. 3. London: Academic Press, 1980.

APPENDIX 3 - LFA ALTERNATIVE SAMPLE PREPARATION METHODS

The laser parameters show substantial impact upon the sample preparation and usability. Initial sample preparation was carried out under laser conditions of 400V with a pulse time of 0.8 ms. Increased pulse time provides a reduction in noise and thus is desirable. However, the application of a long pulse time on the surface of a polymer with graphite causes the removal of the graphite. A series of different layers were applied to the sample surface to increase wettability of the graphite. Increased wettability is expected to increase the interaction of the graphite and the sample.

The use of a thin metallic layer (e.g. gold or platinum) has been expressed by dos Santos et al. (2005) and dos Santos et al. (2008). The addition of the metallic layer eliminates the transparency of a transparent polymer. The addition of the gold is not recorded in the diffusivity measurements.

Three different sample preparations were used to determine the most acceptable layer applied to the sample prior to the graphite spray. The three preparation methods used were: graphite only, gold, and high temperature grease. The high temperature grease was applied to two samples in a thick and thin layer. Figure A3-1 shows the repeatability of three shots with different layer preparation methods.

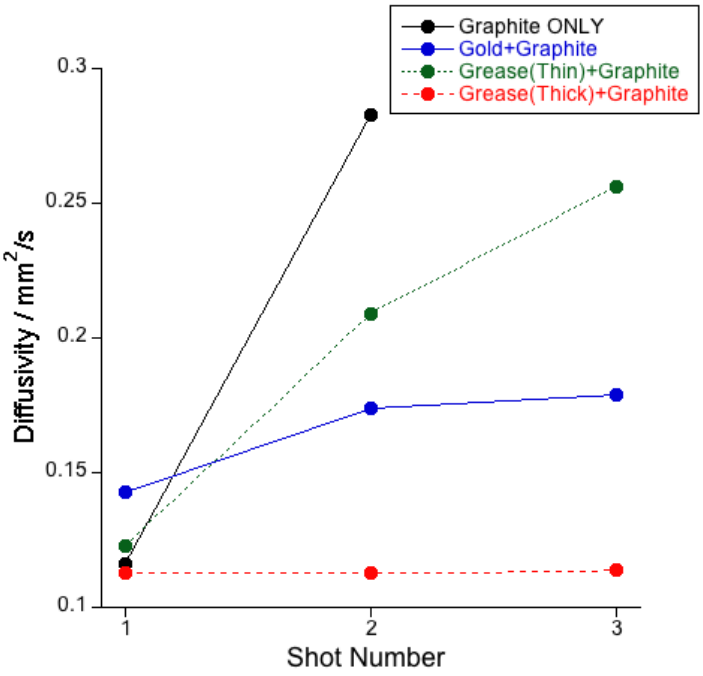

Figure A3 -1 - Repeatability of diffusivity with different layer preparation method

'Graphite only' prevents the ability to record multiple shot data, the graphite is removed through the power of the laser. The addition of a layer of gold was suggested by dos Santos et al. (2008) but did show a removal of the graphite layer (Figure A3-2). The diffusivity increase was not as high as the graphite only as the gold layer prevented the laser from penetrating the transparent sample. Reflective metal however can cause reflection of the laser. The addition of grease to help increase the wetting of the graphite to the surface provided greater results in comparison to the gold and graphite for the purpose of repeatability. The layer must not be too thin, to prevent the graphite from falling off the sample surface. The thick layer enabled three shots to be made with no change in diffusivity. The presence of the grease does not show a change in diffusivity, using the first shot of graphite only as a comparison.

Preparation Method	Pre laser shot	Post 3 laser shots
None	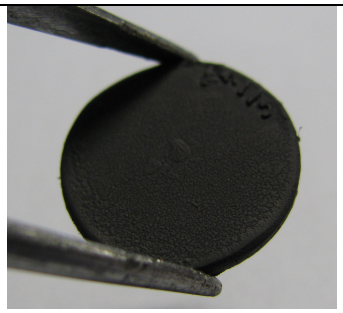	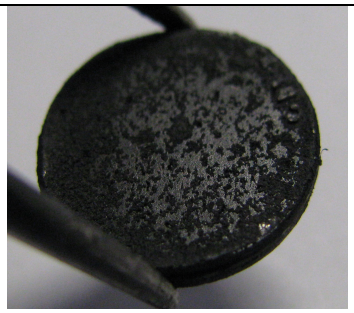
Grease Thin Layer	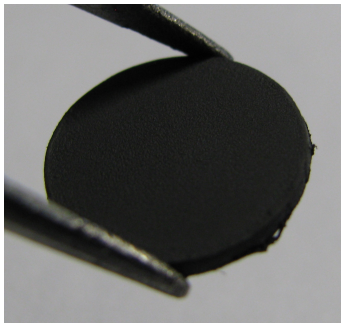	
Gold	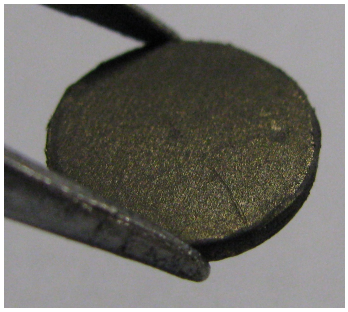	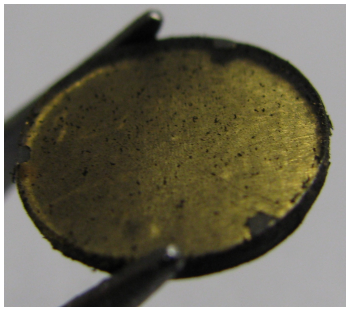
Grease Thick Layer	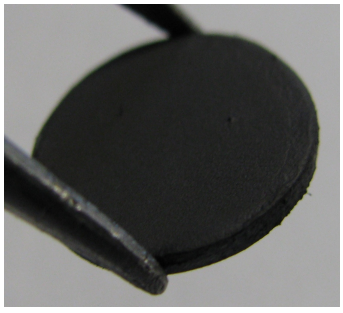	

Figure A3 - 2 - Photos of LFA samples before and after 3 laser shots with different preparation methods

The thickness of the grease layer was subsequently explored to determine the repeatability of the diffusivity measurement with thickness of grease on the

sample surface. The grease thickness was shown to be an important factor in Figure A3-1. The mass of the grease was calculated using laboratory scales and using Equation A3-1 the thickness of the grease was calculated. The grease mass applied to the sample and a layer of graphite was applied to the sample onto the grease. Five laser shots were applied to the sample to determine a change in diffusivity with shot number and diffusivity of the initial laser shot (Figure A3-3).

$$\frac{{}^{m}/_{\rho}}{2\pi\left(\frac{d}{2}\right)^{2} + \pi d t_{sample}} = \frac{v_{grease}}{SA_{sample}} = t_{grease}$$

Equation A3 – 1

m is the mass of the grease, ρ is the density of the grease, d is the diameter of the sample, t_{sample} and t_{grease} are the thickness of the sample and grease respectively, v_{grease} is the volume of the grease and SA_{sample} is the surface area of the sample.

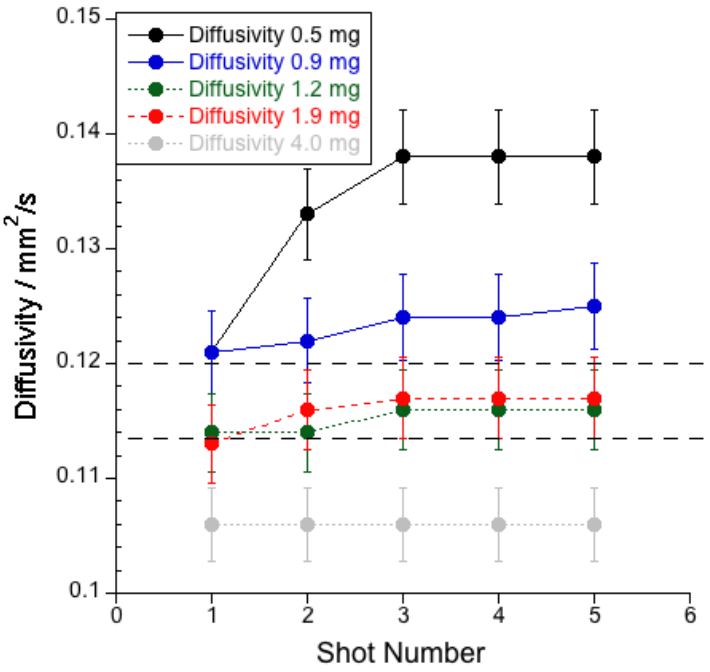

Figure A3 -3 - Diffusivity change with shot number for LFA sample with varied grease mass at 40.5 ± 0.5˚C.

Thicker grease layers resulted in greater repeatability, but as expected, a thicker sample produced a lower diffusivity reading (grease thickness was not taken into account for diffusivity calculations, only PLA sample thickness as a maximum thickness increase was calculated at 1.3%). The dotted lines in Figure 3 show the diffusivity value obtained in Figure A3-1 with graphite only applied to the sample on shot 1. A standard error of 3% was applied to the value. The repeatability of sample with a grease thickness of 1.2 and 1.0 mg show a repeatable value in the centre of the acceptable region. The initial diffusivity is lower for shots 1 and 2, but repeatability for shots 3-5 show a standard error of zero. This repeatability and accuracy of diffusivity enables grease to be applied with no detrimental effect on the diffusivity of the sample with repeatability for multiple lase shot runs. The high temperature grease provides constant properties up to 200˚C, a temperature in excess of the melting point of PLA.

APPENDIX 4 – BIOPAC PACKAGING REPORT

Biopac Packaging Project

Biodegradable laminated films

Joseph Marsh

PROJECT AIM

To create a laminated film of two biodegradable polymers with no explicit adhesive will allow for the most environmentally friendly structure to be created.

Aims

Project Aims

To create a laminated film of two biodegradable polymers with no explicit adhesive will allow for the most environmentally friendly structure to be created. The main aim of the project is to look into the adhesion of these two polymers through the use of heat and pressure to determine the adhesion properties of the two materials.

Research Aims

Create a laminate of two biodegradable polymer films (cellulose and polylactic acid). Study the processing parameters that will lead to the greatest adhesion using a systematic approach and results from mechanical and thermal analysis in conjunction with scanning electron microscopy.

Literature Review

Cellulose

Cellulose is one of the most important natural and synthetic polymeric materials substances. It is the world's most abundant natural, biodegradable and renewable polymer (Nada et al., 2009).

Cellulose is a homopolysaccharide, long chain of β-D-glucopyranose units that are linked together by (1-4)-glycosidic bonds. Plant cell walls are formed from cellulose and in its native state is crystalline but can also be amorphous under certain conditions. Cellulose is relatively inert as it forms numerous inter- and intramolecular hydrogen bonds.

The chemical formula of cellulose is $C_6H_{10}O_5$, and the chemical structure is shown in Figure 1 (Smith, 1937).

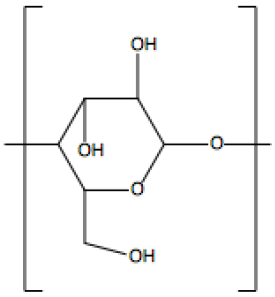

Figure 1 - Chemical Structure of cellulose

The stability of cellulose has been explored using thermogravimetry thermograms and has been seen to reveal a number of weight loss regions (Roig et al., 2011). The first stage of weight loss shows a 10% between 50 and 200 ˚C suspected to be the loss of weight from absorbed or bound water within the sample. The second stage of degradation ranged from 200-350 ˚C with the fastest decomposition rate resulting in a 50% weight loss is a result of degradation of cellulose. A slower weight loss occurs between 350 and 700 ˚C due to pyrolysis and decomposition of cellulose to form condensation cross-linking ring structure (Roig et al., 2011).

The resultant gases were collected and determined through the TGA process. Between 250 and 350 ˚C carbon monoxide was given off and between 250 and 350 ˚C carbon dioxide given off. Using differential scanning calorimetry a glass transition of dehydrate cellulose was found to be 84 ± 1 ˚C (Roig et al., 2011) (Wunderlich, 2005) (Shen et al., 2014). The heat for crystallisation for cellulose is reported to be 123 Jg^{-1} (Schroeter and Felix, 2005).

Polylactic acid (PLA)

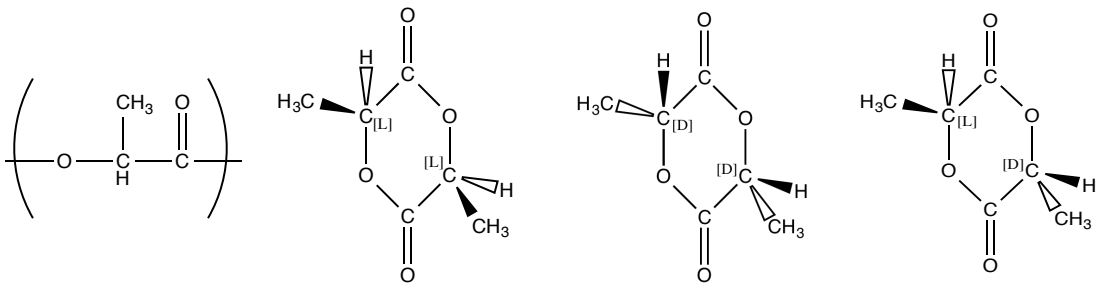

Figure 2 - PLA repeat unit and stereoisomer chemical structures

Polylactic acid (PLA) is a riged linear polyester that is produced using corn starch. It is an eco-freindsly biomaterial that has be found to have excellent

properties for the use in the commercial word. PLA however is brittle and hydrophobic (Lin et al., 2009).The presence of asymmetrical carbon atoms leads to different stereoisomers (MacDonald, 1996). PLA's stereoisomerism varies dependent on the carbonyl and the methyl groups (Södergård and Stolt, 2002) (Figure 2). These variations produces D and L lactides. In their purest form, when they have their highest optical purity, they are able to crystallise. The most common form is L-lactic acid (2-hydroxy propionic acid) and is natural, however through microorganisms D(+) –lactic acid can also be produced. Consequently, the addition of D and L within a the polymer can prevent crystallisation, resulting in an amorphous polymer (Auras et al., 2010).

PLA has a glass transition temperature of 60 ˚C, and dependent upon the degree of D and L lactide content, a melting temperature of around 163 ˚C (Lin et al., 2009). The equilibrium melting point of PLA films has been observed to be at 211-212 ˚C (Tsuji and Ikada, 1995).

The two isomers, D and L-lactide can allow three distinct materials to be formed that vary in crystallinity, thermal, mechanical and degredation properties and (Lin et al., 2009). The different isomer formations allow Poly(D-lactic acid) (PDLA), Poly(L-lactic acid) PLLA, and meso-PLA to form Figure 2.

PLA degradation is seen to have a reduced effect as a result of the drying of the pellets before processing. It was found by Le Marec et al. (2014) to have a 20% reduction in number average molar mass for undried pellets compared to a drop of just 3% for dried pellets held at 170 ˚C for 30 minutes. The degradation rate

constant was reduced by a factor of two when PLA has been dried prior to processing.

PLA blends

PLA has been a focus of blending in recent years as a result of its biodegradable and bio-renewable properties. It has been reported to blend with PEG(Sheth et al., 1997), PVA(Gajria et al., 1996) and PMMA(Zhang et al., 2003). The blending of PLA with cellulose to create a fully biodegradable blend has been explored using a solvent mix of Chloroform and acetone in acid condition. The mixing of solvents improved the mechanical properties and compatibility of the blend films (Witthayaprapakorn et al., 2013). It has been seen that the blending of PLA and cellulose acetate films are partially compatible when solvent cast blended (Girdthep et al., 2011).

Project proposal from literature review

The use of the hot press allows both materials to be heated above their melting temperature and into the melt giving the materials greater energy for mobility in the chains. This increased mobility provides a greater opportunity for adhesion between the two materials. To achieve full miscibility between the two materials the free energy must be negative according to the thermodynamic equation of Gibbs free energy

Equation 1 where the solubility parameters of the materials are too far apart, the free energy of mixing is positive and other means are needed to reduce the interfacial tension to allow adhesion/ partial miscibility (Strehmel and Strehmel,

2000). It is also possible to allow adhesion between the surfaces of two materials. Immiscible materials can be useful within the industrial workplace. ABS is a commercially available immiscible polymer where droplets of Butadiene are distributed throughout a more brittle matrix to prevent crack propagation.

$$\Delta G^* = \Delta H_m - T\Delta S$$

Equation 1 - Gibbs free energy

Testing

Differential Scanning Calorimetry (DSC)

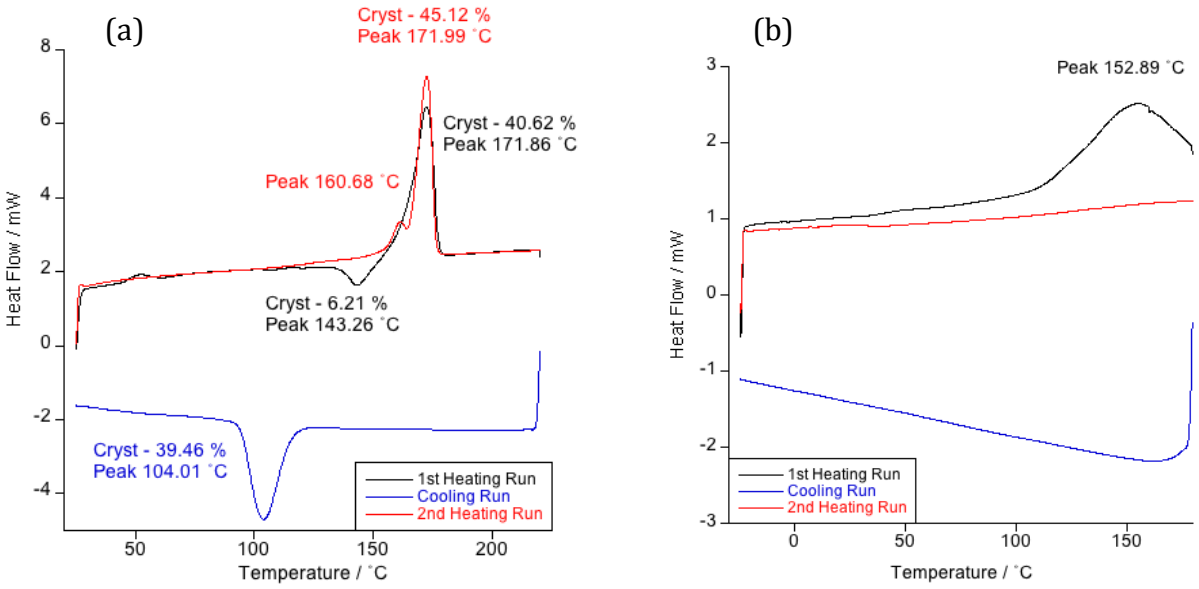

Figure 3 - DSC traces for (a) PLA and (b) cellulose run at 10 ˚C/min to reveal the thermal transitions of the polymers

Experimental and Methodology

Differential canning calorimetry (DSC) was carried out using a Mettler Toledo DSC1 interfaced with a Pc and connected to a Hubble cooler. This was used to determine the thermal transition off the polymers and this is important for the parameters that are included in the further experimentation. All scanning rate were recorded at 10 ˚Cmin^{-1}.

Results and Discussion

The DSC trace in Figure 3 reveals a double melting peak on the PLA that may be a result of the addition of nanofillers, causing two different crystal structure to form, or a variety in the lamella thickness (Yang, 2010). These act as nucleating agents and result in a melting peak of 171.99 ˚C with a significant degree of crystallinity developing on the cooling cycle. Cellulose shown in Figure 3 does not show any crystallinity on the cooling cycle but on the first heat reveals an endothermic behaviour. This was later shown not to be the meting point of cellulose.

PLA film manufacturing

Experimental and Methodology

A Moore hot press with variable temperature and pressure was integrated with a water irrigation cooling system in the press plates. The press was used at pressures less than 10 tons and at temperature up to 200 ˚C.

The endset melting point of PLA was shown to be 176.1 ˚C, the point at which all the crystals have melted. The PLA films were created using a temperature of 180 ˚C to ensure that the PLA was in the melt during processing.

Samples of PLA film were created using PLA pellets placed into the press within a mold of thickness ~ 200 μm. The pellets were heated for 3 minutes with no pressure at 180 ˚C, pressure was subsequently applied for 2 minutes at 180 ˚C

before water cooled through a water irrigation system through the hot plates for 20 minutes at a pressure of 10 tons.

A series of temperatures and pressures were selected as a result of the thermal analysis testing to allow the materials to be in the melt (above the T_m) and have the greatest possible chance for adhesion.

The sample temperature testing range varied from 150-200 ˚C
The sample pressure testing range varied from ~0.5 -10 tons.
The sample time testing range varied from 5-25 minutes.

These conditions allowed us to determine the temperatures and pressures that were of an optimum combination to allow the samples to adhere to one another. Once a number of optimum combinations were tested, the time restrain was tested to allow the process to replicate the industrial manufacture of the produce as close as possible.

The details of all the samples that were made are shown in Table 1 with corresponding temperature / pressure and time periods.

Table 1 - Detail of all the processing parameters used to create all the bi- and tri-layer film laminates

Sample Number (Biopac #)	Temperature / ˚C	Pressure / Tons	Time / minutes (Heat+pressure+cool)
4	160	10 ± 1	3+2+20
5	160	10 ± 1	3+2+20
6	160	10 ± 1	3+2+20
7	170	10 ± 1	3+2+20
8	170	10 ± 1	3+2+20
9	170	10 ± 1	3+2+20
10	170	10 ± 1	3+2+20
11	200	10 ± 1	3+2+20
12	170	10 ± 1	3+2+20
13	170	10 ± 1	3+2+20
14a	170	10 ± 1	3+2+20
14b	170	10 ± 1	3+2+20
14c	170	10 ± 1	3+2+20
15a	170	5 ± 1	3+2+20
15b	170	5 ± 1	3+2+20
15c	170	5 ± 1	3+2+20
16a	170	5 ± 1	3+2+20
16b	170	5 ± 1	3+2+20
16c	170	5 ± 1	3+2+20

16d	**170**	**5 ± 1**	**3+2+20**
17	**170**	**10 ± 1**	**3+2 (5)**
18	**170**	**5 ± 1**	**3+2 (5)**
19	**170**		
20	**170**	**0**	**(10)**
21	**170**	**3 ± 1**	**3+2 (5)**
22	**170**	**1 ± 1**	**3+2 (5)**
23	**165**	**3 ± 1**	**3+2 (5)**
24	**170**	**3 ± 1**	**3+2 (5)**
25	**165**	**3 ± 1**	**3+2 (5)**
26	**160**	**3 ± 1**	**3+2 (5)**
27	**155**	**3 ± 1**	**3+2 (5)**
28	**150**	**3 ± 1**	**3+2 (5)**
29	**180**	**3 ± 1**	**3+2 (5)**
30	**180**	**0 - 1**	**5 (5)**
31	**170**	**0 - 1**	**5 (5)**
32	**175**	**0 - 1**	**5 (5)**
33	**175**	**0 - 1**	**2 (5)**
34	**175**	**0 - 1**	**3 (1)**
35	**175**	**0 - 1**	**3 (3)**
36	**175**	**0 - 1**	**5 (5)**

Mechanical Testing Samples	Temperature / ˚C	Pressure / Tons	Time / minutes (Heat+pressure+cool)
I1	175	0-1	5 (5)
I2	175	0-1	5 (5)
I3	175	10	3+2+20
I4	175	0 - 1	3+2+20
I5	175	0 - 1	5 (5)
I6	175	0 - 1	5 (5)

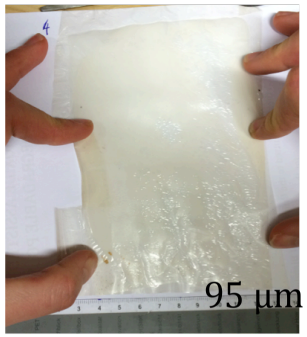

Sample 4: Some light adhesion but curled as a result of the processing of the PLA orientation

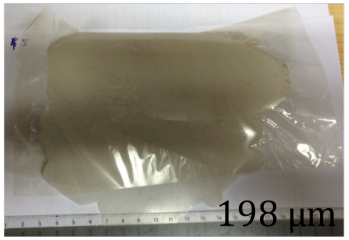

Sample 5 Where the cellulose does not overlap, the is good adhesion on the edge.

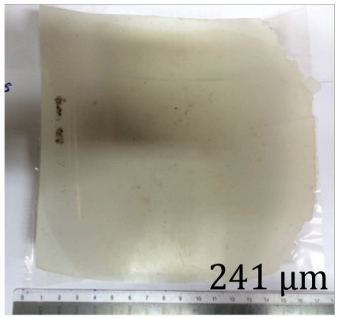

Sample 6: PLA & UNDRIED cellulose BI-layer
Adhesion compare to sample 5 is not as good as the ability to peak and contact and edge is easier with this sample.

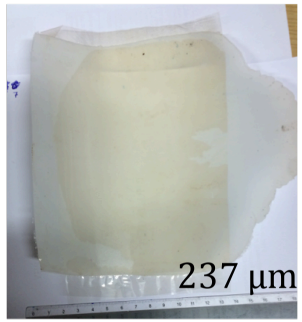

Sample 7 PLA & cellulose BI-layer
The dried PLA shows less adhesion than the PLA to the undried cellulose.

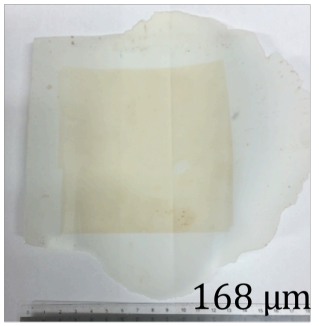

Sample 8: PLA & DRIED cellulose BI-layer
No edges to allow the cellulose to be pulled away from the PLA as the cellulose has been able to press into the PLA during the melt of PLA.

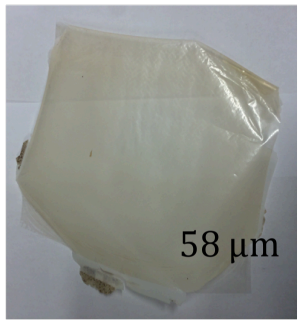

Sample 9: PLA & UNDRIED cellulose BI-layer
Smaller PLA square spread due to pressure to the size of the cellulose. Resulted in a thinner film. Adhesion in the center where layer were thin appeared good

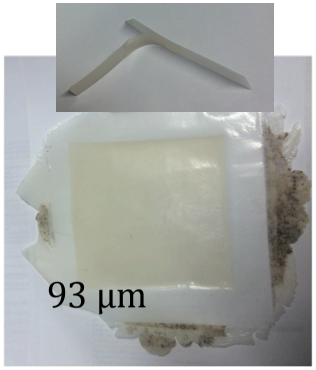

Sample 10: PLA & UNDRIED cellulose BI-layer
Good adhesion on the sample no visible difference on the layer on the cellulose where it meets the PLA.
Once a sample was cut from the sample and a bending moment applied, the fracture of the brittle PLA revealed the two layers.

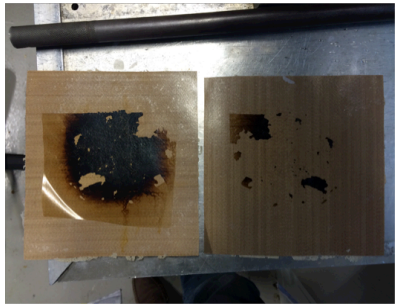

Sample 11:
PLA & UNDRIED cellulose BI-layer
Burnt PLA, cellulose has discoloration but sample time and temperate caused failure of film. PLA has degraded.

Sample 12: PLA & UNDRIED cellulose BI-layer
Cellulose stuck severely to the Al sheet but left an indent into the PLA where the pressure had caused it to move into the surface during the PLA melt.

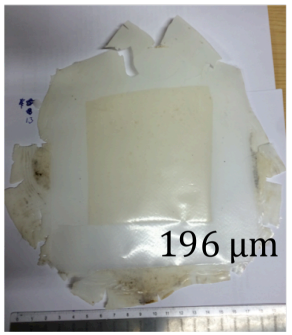

Sample 13: PLA & UNDRIED cellulose BI-layer
PTFE used instead of the Al, cellulose pushed into the PLA resulting in the appearance of good adhesion. No splitting from the PLA.

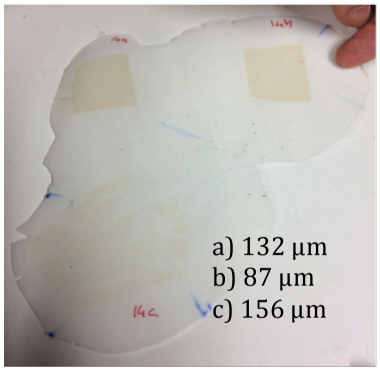

Sample 14: : PLA & UNDRIED cellulose BI-layer (a,b) TRI-layer (c)
Determine if the set up of the cellulose PLA on top or bottom. No change in the curling. Tri layer show pressure causes the fracturing of the cellulose layer.

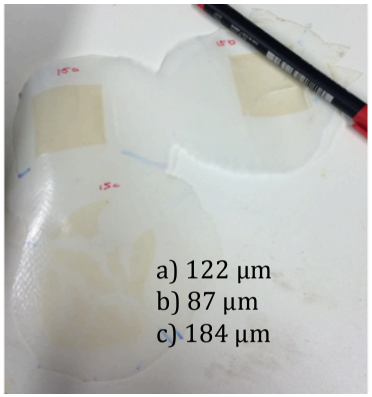

Sample 15: PLA & UNDRIED cellulose BI-layer (a,b) TRI-layer (c)
The lower pressure still resulted in the fracture of the cellulose in the tri-layer. Larger sections of cellulose are visible between the PLA. Reveals there is some adhesion between the PLA and cellulose inside.

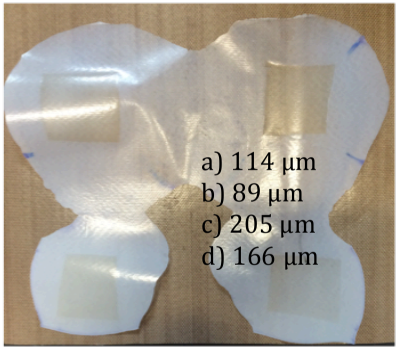

Sample 16: : DRIED (a,b) & UNDRIED (c,d) PLA & UNDRIED cellulose BI-layer
The dried PLA appeared to spread more but this is a result of the hot press plate orientation. PLA dried appears more brittle. Undried PLA was used to prevent the brittle nature.

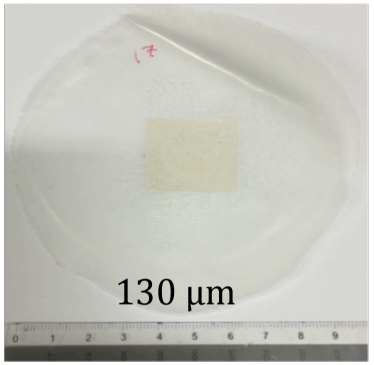

Sample 17: PLA & UNDRIED cellulose BI-layer
Sample was heated for 3 minutes, pressure applied for 2 minutes and the sample was removed from the press, after 5 minutes the sample was taken off the PTFE sheets. Pulling off instantly resulted in the PLA still above Tm and bubbled.

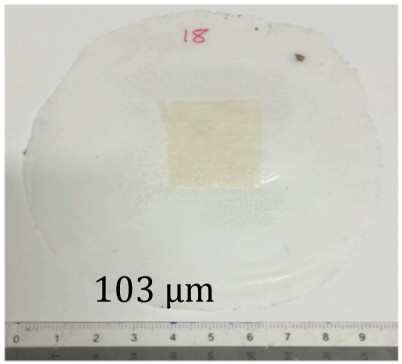

Sample 18: PLA & UNDRIED cellulose BI-layer
Unusual effect on the surface, maybe a result of fast cooling out of the plates or due to the sample removal from the sheets as he PLA is still in liquid state/bubbles forming

Sample 20: PLA & UNDRIED cellulose BI-layer
No adhesion at all with no pressure or heat from above.

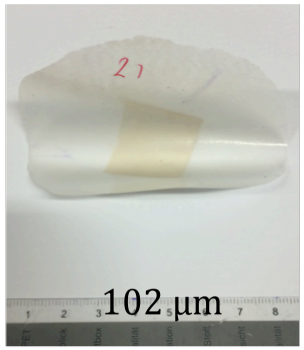

Sample 21: PLA & UNDRIED cellulose BI-layer
No unusual effect on the surface but no difference in the removal of the sample.

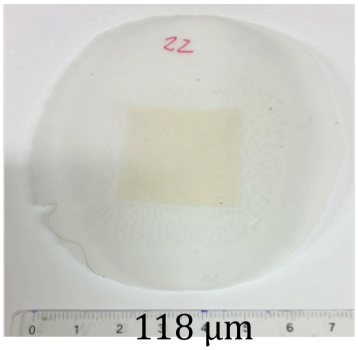

Sample 22: PLA & UNDRIED cellulose BI-layer Unusual surface effect but adhesion is still good between PLA and cellulose.

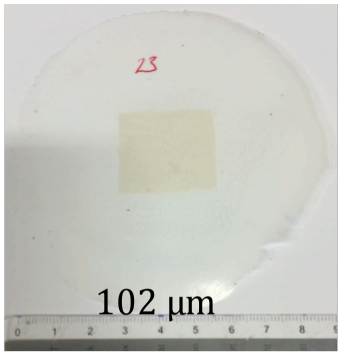

Sample 23: PLA & UNDRIED cellulose BI-layer
Good adhesion and same surface effect, due to the PLA bubbling.

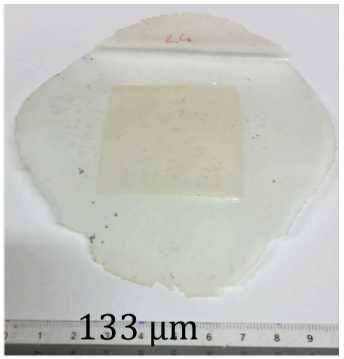

Sample 24: PLA & UNDRIED cellulose BI-layer
Good adhesion again with low pressure. PLA slightly bubbles again. Bubbles only present in samples removed from the press at temperature. So evaluated to be a result of fast cooling.

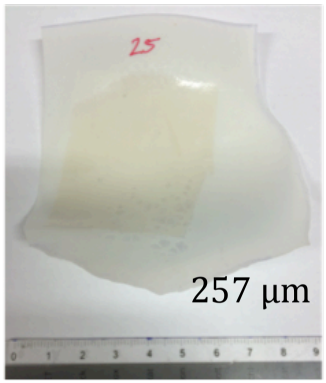

Sample 25: PLA & UNDRIED cellulose BI-layer
Lower temperature starts to reduce the adhesion of the cellulose on the edges as the PLA crystal are no all fully melted.

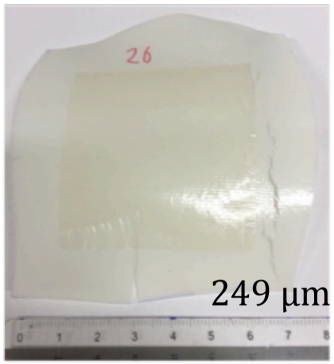

Sample 26: PLA & UNDRIED cellulose BI-layer
PLA cracked due to lower temperature and pressure caused the fracture of the PLA. Cellulose has a ruffled effect on the surface.

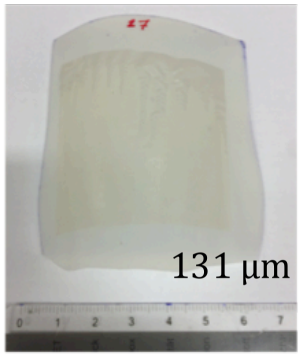

Sample 27: PLA & UNDRIED cellulose BI-layer
No cracking of the PLA as the temperature too low to allow any movement in the PLA. Poor adhesion on the edges of the cellulose as a result of the low processing temperature.

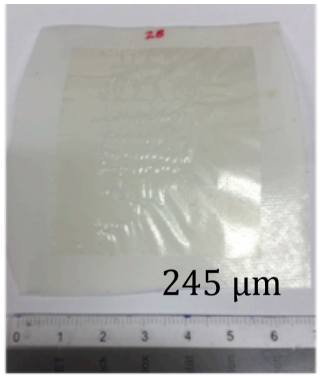

Sample 28: PLA & UNDRIED cellulose BI-layer
Very ruffled cellulose surface very little adhesion on the surface due to low processing temperature.

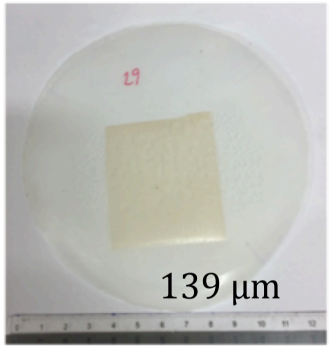

Sample 29: PLA & UNDRIED

cellulose BI-layer

PLA spread and a clear gap is seen between the cellulose and PLA where shrinkage has occurred on crystallisation.

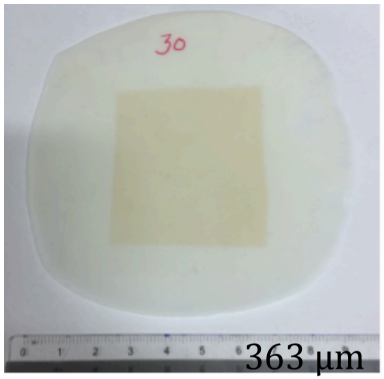

Sample 30: PLA & UNDRIED cellulose TRI-layer
PLA reaches liquid phase and traps the cellulose in the center due to adhesion of the PLA sheets. No fracturing is seen.when force is applied.

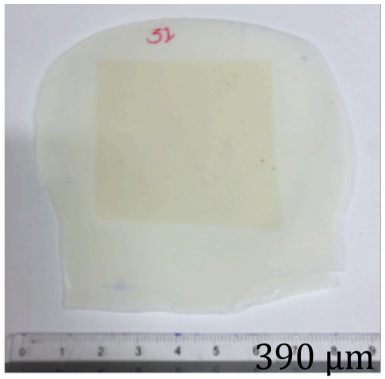

Sample 31: PLA & UNDRIED cellulose TRI-layer
Visible lap between the top and bottom PLA layers. The temperature of 170 ˚C slightly too low for that period of time to allow full melting and reputation between the two PLA layers form a single layer.

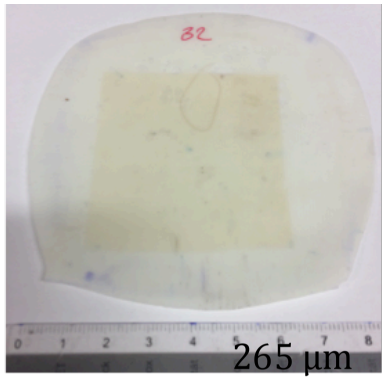

Sample 32: PLA & UNDRIED cellulose TRI-layer
Better adhesion finish than sample 31. Very similar to sample 30, but 5 ˚C lower processing temperature to reduced industrial manufacturing costs for future development.

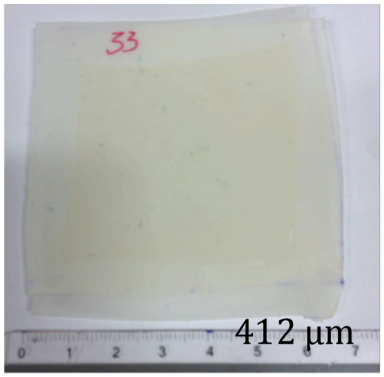

Sample 33: PLA & UNDRIED cellulose TRI-layer
Good adhesion but the melt was not maintained for long enough to produce a smooth sample with no evidence of a dingle film. The PLA layers are still visibly two layers

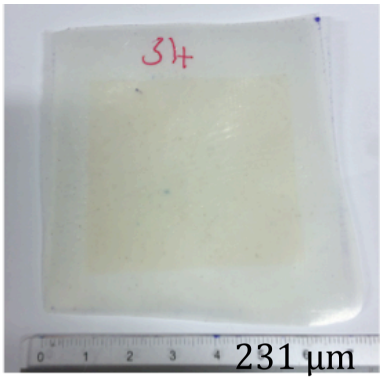

Sample 34: PLA & UNDRIED cellulose TRI-layer
A rough sample surface with a number of bubbles potentially as a result of removing the sample quickly after processing as a result of a number of different samples with bubbled surfaces.

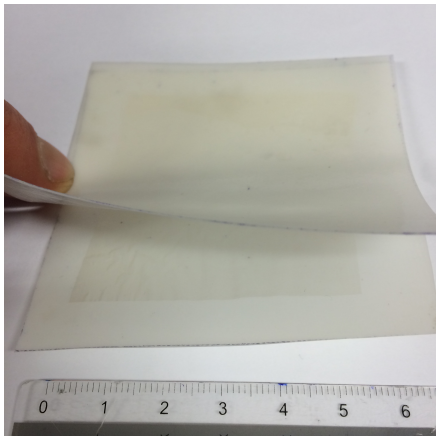

Sample 35: PLA & UNDRIED cellulose TRI-layer
Had very little pressure (0 tons) resulting in the layers being able to be pulled apart after the processing. Pressure is needed to force the PLA sheets together.

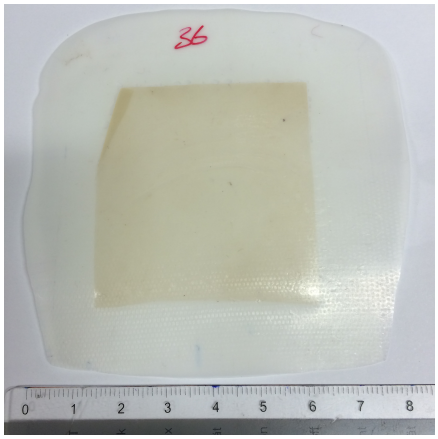

Sample 36: PLA & UNDRIED cellulose TRI-layer
The sample shows good initial evidence of adhesion and compare to sample 24 where the pressure is greater and temperature is lower adhesion is still as good.

Results of hot press samples

The samples showed a good level of adhesion throughout with the tri-layer structures encapsulating the cellulose preventing the removal of the cellulose. A number of the samples that showed the best adhesion results were used to created bi/tri-layers for mechanical testing.

The samples that showed the best adhesion were:

Sample 10 – Bi-layer at 180 ˚C, 10 tons, with a 20 minute cool using water irrigation

Sample 32 - Tri-layer at 175 ˚C with 0-1 tons; 5 minute cool out of the hot press

Variations of the basic parameter used in samples 10 and 32 were made and tested mechanically. This enabled the adhesion of the layers to be assed in greater detail compare to peeling of the layers by hand.

Variations of Sample 32:

I1 - a tri layer structure (5 minutes at pressure and 5 minutes out of the press to cool)

I2 - a tri layer structure with cellulose abrasion (5 minutes at pressure and 5 minutes out of the press to cool) (not completed due to time restraints)

Variations of Sample 10:

I3 - a bi-layer at 10 tons (3 minutes to heat, 2 minutes at pressure and 20 minutes at pressure cooled by water irrigation)

I4 - a bi-layer at 10 tons (3 minutes to heat, 2 minutes at pressure and 5 minutes out of the press to cool)

I5 - a bi-layer at 0-1 ton (5 minutes at pressure and 5 minutes out of the press to cool)

I6 - a bi-layer at 0-1 ton with cellulose abrasion (5 minutes at pressure and 5 minutes out of the press to cool)

Scanning electron microscopy (SEM)

Experimental and methodology

Cryogenic fracture with liquid nitrogen was not possible as a result of the ductility of the cellulose sample. The sample was cut using a scalpel to achieve a sharp edge with the lowest possibility of the delamination on the observed area. Samples were glued to an aluminium stub and coated with platinum using a Polaron SC7640 sputter coater creating a layer of 10-12 nm to allow for sufficient conductivity, The samples were photographed using a Phillips XL30 (ESEM) with an acceleration voltage of 10 kV and a magnification of 200 – 8000x.

Results and Discussion

The SEM was used to look into the joint of the PLA and cellulose to see if adhesion was present. It was seen in two samples that there were very small areas of fibrils that connected the PLA and the cellulose. All samples due to the prevention of the cryogenic fracture showed splitting of the PLA and cellulose layers. In samples 24 and 26 (Figure 4) there are areas of fibrils although the size of the fibrils was very small. It is possible that there is presence of fibrils in other samples that was not visible due to the splitting of PLA and cellulose resulting in

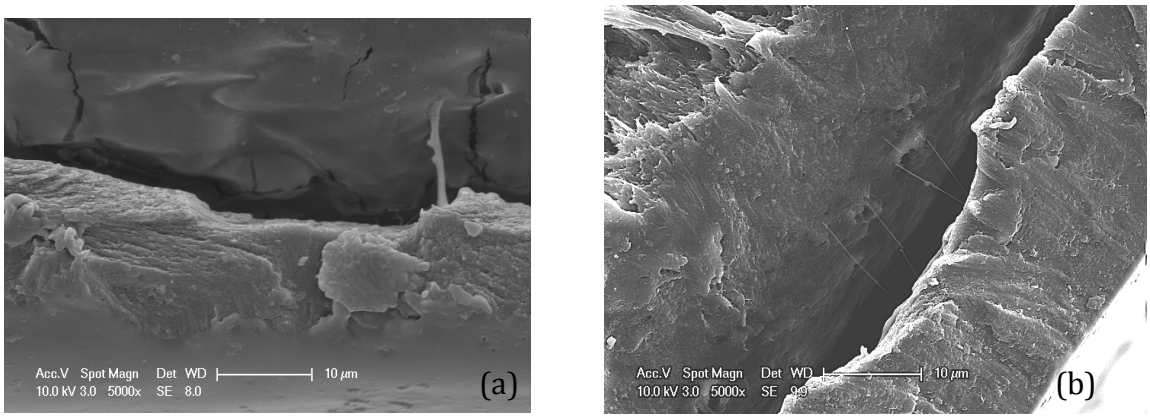

Figure 4 - Sample 24 (a) and 26 (b) showing fibrils connecting the two polymer layers.

fracture of the fibrils. Due to time constraints only a small number of the samples were observed and analysed using SEM.

Mechanical testing

Experimentation and Methodology

The samples were mechanically tested on an Instron 5566 with a 100 KN load cell, interfaced to a PC. The instrument was controlled using Bluehill software. Standard dog-bone samples of width 4 mm and length 26 mm were used and the thickness was determined using a three-point average. A crosshead speed of 0.5 mm/min was used due to the brittle nature of PLA.

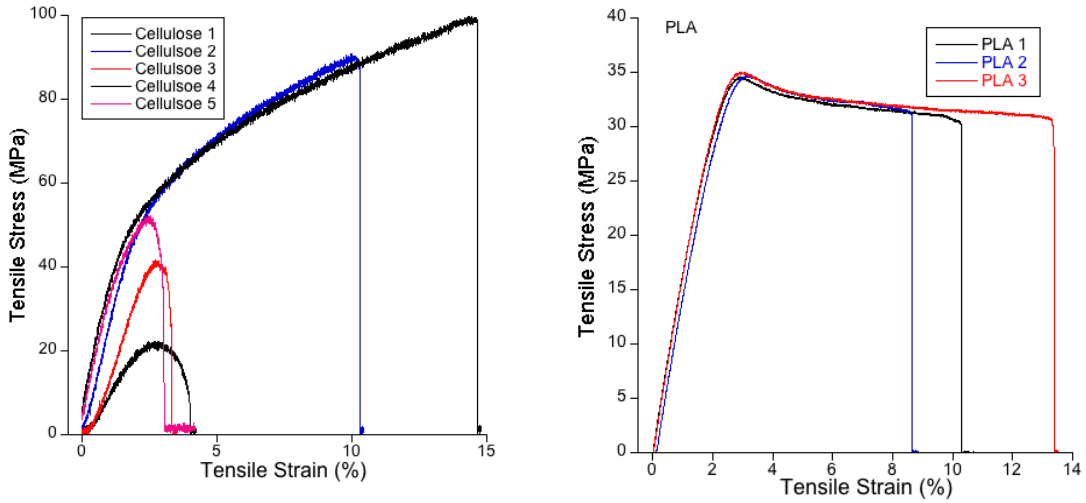

Figure 5 - Homopolymer PLA and cellulose tested together with no prior processing

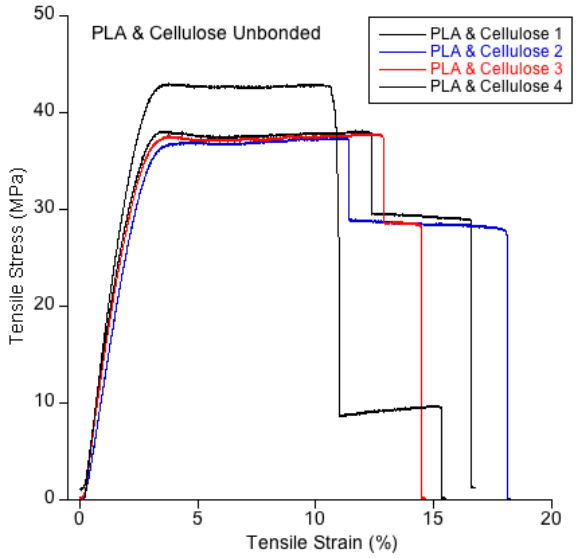

Figure 1 - Mechanical testing of the homopolymers cellulose

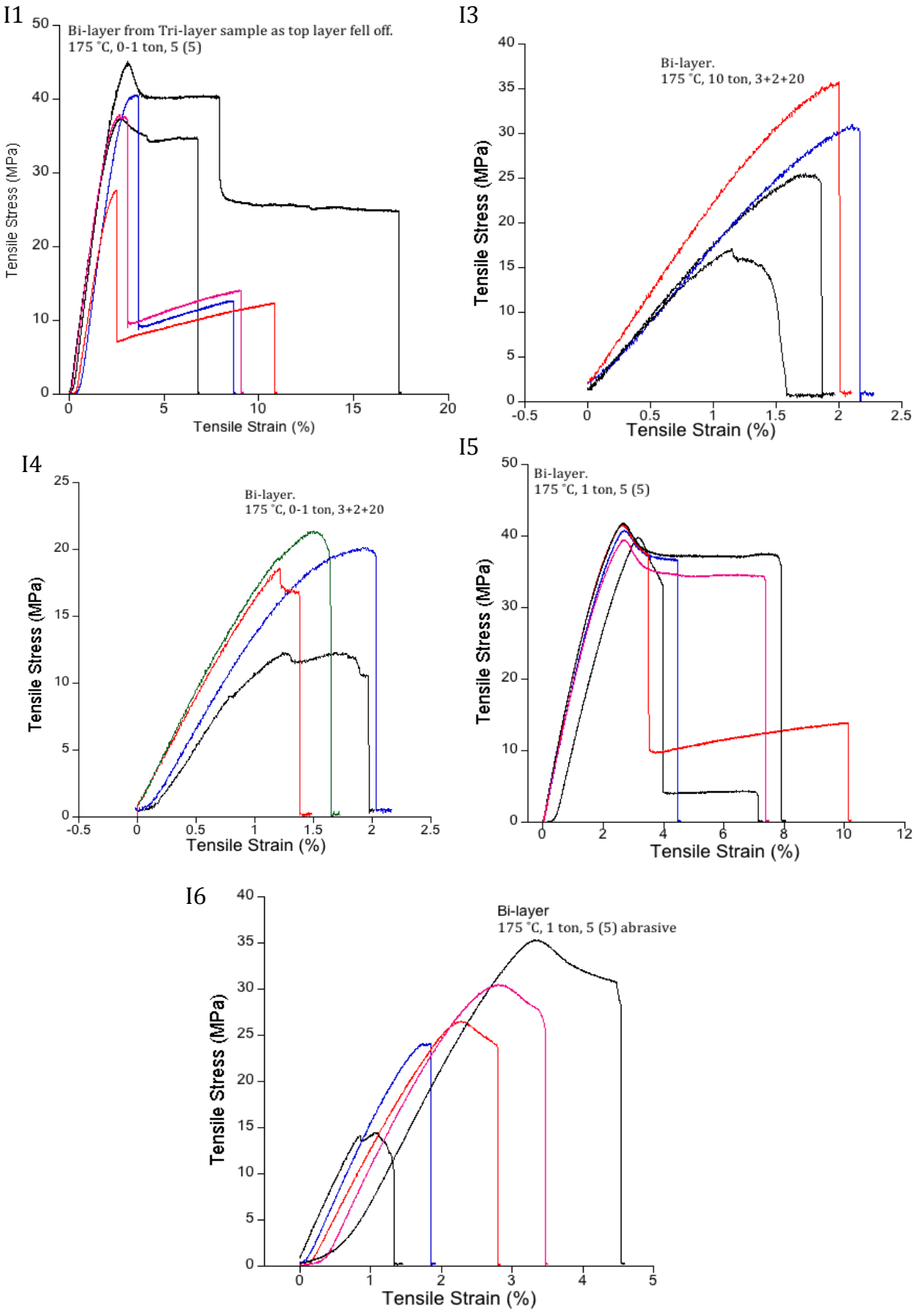

Figure - 7 - Mechanical testing graphs for samples I1 and I3 - I6

Results and discussion

The mechanical testing results enable one to look at the level of adhesion between the two polymer films. Crack propagation at fracture on laminated materials that have good adhesion act as one and causes single fracture of the laminate. If low adhesion levels are present, two fracture points are seen and thus the laminate acts as separate materials during the test. This was shown in **Fig** where both materials were tested without any prior processing. All samples showed a clear fracture of the PLA before the cellulose fracture at a greater tensile strain.

Table 2 - Mechanical data from mechanical testing

Sample	Tensile Strength / MPa	Tensile Strain / %
PLA	34.7	11.05
I3	35.2	2.05
I4	18.16	1.92
I5	40.7	8.26
I6	26.18	3.59

The long cooling period in samples I3 and I4 showed that the pressure of the press did not have a big affect on the sample adhesion (I3 was pressed at 10 tons and I4 was pressed at 0-1 tons). The slow cool of these samples allows for a great amount of crystallinity to develop. When the sample is cooled quickly in all the other samples. Nucleation is reduced, resulting in reduced crystallinity percentage in the sample. This allows for greater elongation of the sample as a result of the increase in amorphous regions within the sample.

Samples I3, I4, and I6 in Figure 7 show single fracture on all samples tested. The tensile strain was very low for all these samples and it is presumed that there has been a level of degradation and oxidation that has occurred as a result of the processing. In sample I5 out of the five repeats, three show a single fracture point with a good degree of elongation and a high tensile strain (Figure 7 and Table 2). This shows that the level of adhesion was good enough to allow for crack propagation to develop through the entire sample after development of a uniform neck as a result of a more amorphous sample. The results shown by I6 in Figure 7 reveal a lower elongation to break and tensile stress compare to sample I5 that has the same processing parameters. Both samples show yield points and thus act in a similar manor where the development of a uniform neck is present and drawing occurs. The reduced strain in sample I6 is a result of the mechanical abrasion applied to the sample causing an increase in surface area but also and increases in the number of stress concentration sites.

Conclusion

The combination of mechanical testing and hot press results showed that the pressure did not have a significant affect upon the adhesion achieved from the bi-layer. The time that the laminate was in the press and the cooling time did show a difference. Allowing the sample to cool slowly allowed good adhesion to occur in the absence of mechanical abrasion. A brittle structure was found on the fast cooled samples compare to the slow cooled due to the amount of amorphous polymer in the samples. Mechanical abrasion allowed for a fast cool and a shorter process to reveal good adhesion properties.

The SEM images revealed that there is a small amount of adhesion and attraction between the layers that allows them to create a single laminated sheet. The tri-layer construction yields a better finish in appearance and physical malleability, however the reduction of heat on the cellulose inner layer as a result of the PLA acting as a barrier reduces the adhesion between the PLA and cellulose.

Overall little adhesion was seen between the cellulose and the PLA. Applying heat and pressure to samples can enhance the adhesion but not to a sufficient degree where the sample are not able to the delaminated upon fracture. The properties can be changes and a laminated structure created, but minimal interaction is seen between the two laminated layers.

References

BHATTACHARYA, M., REIS, R. L., CORRELO, V. & BOESEL, L. 2005. Material properties of biodegradable polymers. *In:* SMITH, R. (ed.) *Biodegradable polymers for industrial applications.* Cambridge: Woodhead Publishing Limited.

BLUNDELL, D. J. 1987. On the interpretation of multiple melting peaks in poly(ether ether ketone). *Polymer,* 28**,** 2248-2251.

BLUNDELL, D. J. & OSBORN, B. N. 1983. The morphology of poly(aryl-ether-ether-ketone). *Polymer,* 24**,** 953-958.

BROZ, M. E., VANDERHART, D. L. & WASHBURN, N. R. 2003. Structure and mechanical properties of poly(,-lactic acid)/poly([var epsilon]-caprolactone) blends. *Biomaterials,* 24**,** 4181-4190.

CHENG, S. Z., CAO, M. & WUNDERLICH, B. 1986. Glass transition and melting behavior of poly (oxy-1, 4-phenyleneoxy-1, 4-phenylenecarbonyl-1, 4-phenylene)(PEEK). *Macromolecules,* 19**,** 1868-1876.

CHENG, S. Z. D. & WUNDERLICH, B. 1988. Thermal analysis of thermoplastic polymers. *Thermochimica Acta,* 134**,** 161-166.

CHOI, N.-S., KIM, C.-H., CHO, K. Y. & PARK, J.-K. 2002. Morphology and hydrolysis of PCL/PLLA blends compatibilized with P(LLA-co-ϵCL) or P(LLA-b-ϵCL). *Journal of Applied Polymer Science,* 86**,** 1892-1898.

DHOTEL, A., RIJAL, B., DELBREILH, L., DARGENT, E. & SAITER, A. 2015. Combining Flash DSC, DSC and broadband dielectric spectroscopy to determine fragility. *Journal of Thermal Analysis and Calorimetry,* 121**,** 453-461.

DOS SANTOS, W. N., IGUCHI, C. Y. & GREGORIO JR, R. 2008. Thermal properties of poly(vinilidene fluoride) in the temperature range from 25 to 210 °C. *Polymer Testing,* 27**,** 204-208.

DOS SANTOS, W. N., MUMMERY, P. & WALLWORK, A. 2005. Thermal diffusivity of polymers by the laser flash technique. *Polymer Testing,* 24**,** 628-634.

ELKOVITCH, M. D., TOMASKO, D. L. & LEE, L. J. 1999. Supercritical carbon dioxide assisted blending of polystyrene and poly(methyl methyacrylate). *Polymer Engineering & Science,* 39**,** 2075-2084.

GARLOTTA, D. 2001. A Literature Review of Poly(Lactic Acid). *Journal of Polymers and the Environment,* 9**,** 63-84.

GROOT, W., KRIEKEN, J. V., SLIEKERSL, O. & DE VOS, S. 2010. Production and Purification of Lactic Acid and Lactide. *In:* AURAS, R., LIM, L.-T., SELKE, S. E. M. & TSUJI, H. (eds.) *Poly(lactic acid) Synthesis, Structures, Properties, Processing, and Applications.* New Jersey: Wiley.

GUARINO, V., CAUSA, F., TADDEI, P., DI FOGGIA, M., CIAPETTI, G., MARTINI, D., FAGNANO, C., BALDINI, N. & AMBROSIO, L. 2008. Polylactic acid fibre-reinforced polycaprolactone scaffolds for bone tissue engineering. *Biomaterials,* 29**,** 3662-3670.

HOLDSWORTH, P. J. & TURNER-JONES, A. 1971. The melting behaviour of heat crystallized poly(ethylene terephthalate). *Polymer,* 12**,** 195-208.

IANNACE, S. & NICOLAIS, L. 1997. Isothermal crystallization and chain mobility of poly(L-lactide). *Journal of Applied Polymer Science,* 64**,** 911-919.

IHS. 2012. *Biodegradable Polymers* [Online]. Available: http://www.ihs.com/products/chemical/planning/ceh/biodegradable-polymers.aspx.

JANSSEN, L. P. B. M. & NALAWADE, S., P. 2005. Polymer Extrusion with Supercritical Carbon Dioxide. *In:* KEMMERE, M. F. & MEYER, T. (eds.) *Supercritical Carbon Dioxide: in Polymer Reaction Engineering.* Germany: WILEY-VCH.

JENKINS, M. J., CAO, Y., HOWELL, L. & LEEKE, G. A. 2007. Miscibility in blends of poly(3-hydroxybutyrate-co-3-hydroxyvalerate) and poly(ε-caprolactone) induced by melt blending in the presence of supercritical CO2. *Polymer,* 48**,** 6304-6310.

JONAS, A. M., RUSSELL, T. P. & YOON, D. Y. 1995. Synchrotron X-ray Scattering Studies of Crystallization of Poly(ether-ether-ketone) from the Glass and Structural Changes during Subsequent Heating-Cooling Processes. *Macromolecules,* 28**,** 8491-8503.

KAWAI, T., RAHMAN, N., MATSUBA, G., NISHIDA, K., KANAYA, T., NAKANO, M., OKAMOTO, H., KAWADA, J., USUKI, A., HONMA, N., NAKAJIMA, K. & MATSUDA, M. 2007. Crystallization and Melting Behavior of Poly (l-lactic Acid). *Macromolecules,* 40**,** 9463-9469.

KELLY, C. A., NAYLOR, A., ILLUM, L., SHAKESHEFF, K. M. & HOWDLE, S. M. 2012. Supercritical CO2: A Clean and Low Temperature Approach to Blending PDLLA and PEG. *Advanced Functional Materials,* 22**,** 1684-1691.

KRISHNAMACHARI, P., ZHANG, J., LOU, J., YAN, J. & UITENHAM, L. 2009. Biodegradable Poly(Lactic Acid)/Clay Nanocomposites by Melt Intercalation: A Study of Morphological, Thermal, and Mechanical Properties. *International Journal of Polymer Analysis and Characterization,* 14**,** 336-350.

LE MAREC, P. E., FERRY, L., QUANTIN, J.-C., BÉNÉZET, J.-C., BONFILS, F., GUILBERT, S. & BERGERET, A. 2014. Influence of melt processing conditions on poly(lactic acid) degradation: Molar mass distribution and crystallization. *Polymer Degradation and Stability,* 110**,** 353-363.

LEE, M., TZOGANAKIS, C. & PARK, C. B. 1998. Extrusion of PE/PS blends with supercritical carbon dioxide. *Polymer Engineering & Science,* 38**,** 1112-1120.

LEE, M., TZOGANAKIS, C. & PARK, C. B. 2000. Effects of supercritical CO2 on the viscosity and morphology of polymer blends. *Advances in Polymer Technology,* 19**,** 300-311.

LEE, Y. & PORTER, R. S. 1987. Double-melting behavior of poly(ether ether ketone). *Macromolecules,* 20**,** 1336-1341.

LIN, Y.-C., CHO, J., TOMPSETT, G. A., WESTMORELAND, P. R. & HUBER, G. W. 2009. Kinetics and Mechanism of Cellulose Pyrolysis. *The Journal of Physical Chemistry C,* 113**,** 20097-20107.

LÓPEZ, J., RAMÍREZ, C., ABAD, M. J., BARRAL, L., CANO, J. & DÍEZ, F. 2002. Dynamic mechanical analysis of an epoxy/thermoplastic blend: polymerization-induced phase separation. *Polymer International,* 51**,** 1100-1106.

LÓPEZ-RODRÍGUEZ, N., LÓPEZ-ARRAIZA, A., MEAURIO, E. & SARASUA, J. R. 2006. Crystallization, morphology, and mechanical behavior of

polylactide/poly(ε-caprolactone) blends. *Polymer Engineering & Science,* 46**,** 1299-1308.
LOVERA, D., MÁRQUEZ, L., BALSAMO, V., TADDEI, A., CASTELLI, C. & MÜLLER, A. J. 2007. Crystallization, Morphology, and Enzymatic Degradation of Polyhydroxybutyrate/Polycaprolactone (PHB/PCL) Blends. *Macromolecular Chemistry and Physics,* 208**,** 924-937.
MACDONALD, R. T., MCCARTHY, S.P., & GROSS, R.A. 1996. Enzymatic Degradability of Poly(lactide): Effects of Chain Stereochemistry and Material Crystallinity. *Macromolecules***,** 7356-7361.
MEREDITH, J. C. & J. AMIS, E. 2000. LCST phase separation in biodegradable polymer blends: poly(D,L-lactide) and poly(ϵ-caprolactone). *Macromolecular Chemistry and Physics,* 201**,** 733-739.
MIHAI, M., HUNEAULT, M. A. & FAVIS, B. D. 2009. Crystallinity development in cellular poly(lactic acid) in the presence of supercritical carbon dioxide. *Journal of Applied Polymer Science,* 113**,** 2920-2932.
NADA, A.-A. M. A., EL-KADY, M. Y., EL-SAYED, E. S. A. & AMINE, F. M. 2009. Preparation and Charactorization of Microcrystalline Cellulose (MCC). *BioResources,* 4.
NATUREWORKSLLC. 2013. *How Ingeo Is Made* [Online]. Available: http://www.natureworksllc.com/The-Ingeo-Journey/Eco-Profile-and-LCA/How-Ingeo-is-Made.
NIST. 2011. *NIST Chemistry WebBook* [Online]. Available: http://webbook.nist.gov/chemistry/fluid/.
ROIG, F. D. R., DANTRAS, E., DANDURAND, J. & LACABANNE, C. 2011. Influence of hydrogen bonds on glass transition and dielectric relaxations of cellulose. *Journal of Physics D: Applied Physics,* 44.
SALMERÓN SÁNCHEZ, M., MATHOT, V. B. F., VANDEN POEL, G. & GÓMEZ RIBELLES, J. L. 2007. Effect of the Cooling Rate on the Nucleation Kinetics of Poly(l-Lactic Acid) and Its Influence on Morphology. *Macromolecules,* 40**,** 7989-7997.
SAUER, B. B., KAMPERT, W. G., NEAL BLANCHARD, E., THREEFOOT, S. A. & HSIAO, B. S. 2000. Temperature modulated DSC studies of melting and recrystallization in polymers exhibiting multiple endotherms. *Polymer,* 41**,** 1099-1108.
SCHROETER, J. & FELIX, F. 2005. Melting cellulose. *Cellulose,* 12**,** 159-165.
SHEN, W., HU, T. & FAN, W. 2014. Cellulose generated-microporous carbon nanosheets with nitrogen doping. *RSC Advances,* 4**,** 9126-9132.
SHEN, Z., MCHUGH, M. A., XU, J., BELARDI, J., KILIC, S., MESIANO, A., BANE, S., KARNIKAS, C., BECKMAN, E. & ENICK, R. 2003. CO2-solubility of oligomers and polymers that contain the carbonyl group. *Polymer,* 44**,** 1491-1498.
SIMÕES, C. L., VIANA, J. C. & CUNHA, A. M. 2009. Mechanical properties of poly(ε-caprolactone) and poly(lactic acid) blends. *Journal of Applied Polymer Science,* 112**,** 345-352.
SMITH, H. D. 1937. Structure of Cellulose. *Industrial & Engineering Chemistry,* 29**,** 1081-1084.
SÖDERGÅRD, A. & STOLT, M. 2002. Properties of lactic acid based polymers and their correlation with composition. *Progress in Polymer Science,* 27**,** 1123-1163.

SOPPIMATH, K. S., AMINABHAVI, T. M., KULKARNI, A. R. & RUDZINSKI, W. E. 2001. Biodegradable polymeric nanoparticles as drug delivery devices. *Journal of Controlled Release,* 70**,** 1-20.

STREHMEL, V. & STREHMEL, B. 2000. *Polymer Modification: Principles, Techniques, and Applications,* Basel, Switzerland, Marcel Dekker, Inc.

TARDIF, X., PIGNON, B., BOYARD, N., SCHMELZER, J. W. P., SOBOTKA, V., DELAUNAY, D. & SCHICK, C. 2014. Experimental study of crystallization of PolyEtherEtherKetone (PEEK) over a large temperature range using a nano-calorimeter. *Polymer Testing,* 36**,** 10-19.

TODO, M., PARK, S. D., TAKAYAMA, T. & ARAKAWA, K. 2007. Fracture micromechanisms of bioabsorbable PLLA/PCL polymer blends. *Engineering Fracture Mechanics,* 74**,** 1872-1883.

TODOKI, M. & KAWAGUCHI, T. 1977. Origin of double melting peaks in drawn nylon 6 yarns. *Journal of Polymer Science: Polymer Physics Edition,* 15**,** 1067-1075.

TSUJI, H. & IKADA, Y. 1995. Properties and morphologies of poly(l-lactide): 1. Annealing condition effects on properties and morphologies of poly(l-lactide). *Polymer,* 36**,** 2709-2716.

TSUJI, H. & IKADA, Y. 1996. Blends of aliphatic polyesters. I. Physical properties and morphologies of solution-cast blends from poly(DL-lactide) and poly(ε-caprolactone). *Journal of Applied Polymer Science,* 60**,** 2367-2375.

UTRACKI, L. A. 2000. *Polymer Blends*, Rapra Technology.

VASANTHAKUMARI, R. & PENNINGS, A. J. 1983. Crystallization kinetics of poly(l-lactic acid). *Polymer,* 24**,** 175-178.

WANG, Y. & MANO, J. F. 2009. Multiple melting behaviour of poly(l-lactide-co-glycolide) investigated by DSC. *Polymer Testing,* 28**,** 452-455.

WUNDERLICH, B. 1980. *Macromolecular Physics,* London, Academic Press.

WUNDERLICH, B. 2005. Basics of Thermal Analysis. *Thermal Analysis of Polymeric Materials.* Springer Berlin Heidelberg.

YANG, J. 2010. Origin of double melting peaks of α-form isotactic polypropylene: Recrystallization and lamellar thickness hierarchy. *Journal of Applied Polymer Science,* 118**,** 1520-1526.

YASUNIWA, M., TSUBAKIHARA, S. & FUJIOKA, T. 2003. X-ray and DSC studies on the melt-recrystallization process of poly(butylene naphthalate). *Thermochimica Acta,* 396**,** 75-78.

YASUNIWA, M., TSUBAKIHARA, S., SUGIMOTO, Y. & NAKAFUKU, C. 2004. Thermal analysis of the double-melting behavior of poly(L-lactic acid). *Journal of Polymer Science Part B: Polymer Physics,* 42**,** 25-32.

ZHAI, W. T., KO, Y., ZHU, W. L., WONG, A. S. & PARK, C. B. 2009. A Study of the Crystallization, Melting, and Foaming Behaviors of Polylactic Acid in Compressed CO2. *International Journal of Molecular Sciences,* 10**,** 5381-5397.

ZHANG, Z., ORTIZ, O., GOYAL, R. & KOHN, J. 2014. Biodegradable Polymers. *In:* MODJARRAD, K. & EBNESAJJAD, S. (eds.) *Handbook of Polymer Applications in Medicine and Medical Devices.* Oxford: William Andrew Publishing.

ZHAO, J., YUAN, X., CUI, Y., GE, Q. & YAO, K. 2004. Preparation and characterization of poly(L-lactide)/ poly(ϵ-caprolactone) fibrous scaffolds

for cartilage tissue engineering. *Journal of Applied Polymer Science,* 91**,** 1676-1684.

APPENDIX 5 – POSTER PRESENTED AT FLASH DSC CONFERENCE IN SWITZERLAND

Thermal Analysis of PHB-co-HV Using Flash DSC

Joseph J. Marsh[1], Shona H. Murphy[1], Catherine A. Kelly[1], Gary A. Leeke[2], and Mike J. Jenkins[1]
[1]School of Metallurgy and Materials and [2]School of Chemical Engineering, University of Birmingham, Birmingham, UK.
jxm097@bham.ac.uk

Introduction

- Current packaging systems are generally made from a mixture of polymers making them hard to recycle, which leads to the majority being land filled following use
- One alternative is to use biodegradable polymers obtained from sustainable sources; such as polyhydroxybutyrate (PHB) copolymers
- Poly(3-hydroxybutyrate) (PHB) is biodegradable aliphatic polyester, produced using a wide range of microorganisms
- Incorporating other monomeric units into HB polymer chains can lead to copolymers with improved properties

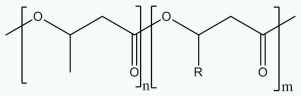

Figure 1: PHB copolymer

- The syntheses of PHB with co-polymers such as Poly-(3-hydroxyvalerate) (HV) reduces the glass and melting temperatures to improve processing conditions. The sample analysed in these experiments has a 3% HV content
- PHB-co-HV degrades close to the melting temperature and thus results in instability in the melting stage

Aim

- Characterise thermal transitions in PHB-co-HV at elevated heating and cooling rates

Experimental

- PHB-co-HV pellets were microtomed and cut using a scalpel into a sample mass of 116 ng
- Using a hair the sample was transferred onto a UFS1 calorimeter twin chip which was inserted into a Mettler Toledo Flash DSC1.
- Argon purged gas was used, flow rate of 30 mLmin^{-1}

Results

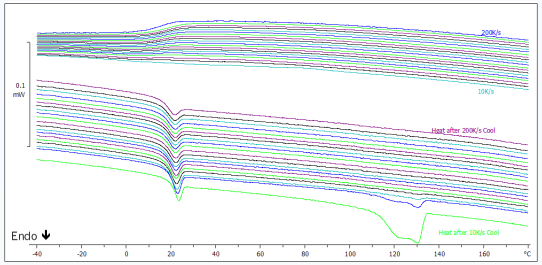

Figure 2: Cooling at rates between 10 and 200 Ks^{-1} with a constant heat at 200 Ks^{-1} to preventing crystallisation.

- The crystallisation of PHB-co-HV can be prevented through cooling at rates greater than 60 Ks^{-1}. This can be visually observed via elimination of the melting peak on the reheat
- A glass transition temperature (T_g) was observed for all the heating traces. An aging peak can be seen to be more pronounced at the lower cooling rates. This may be a result of additional time spent below the T_g

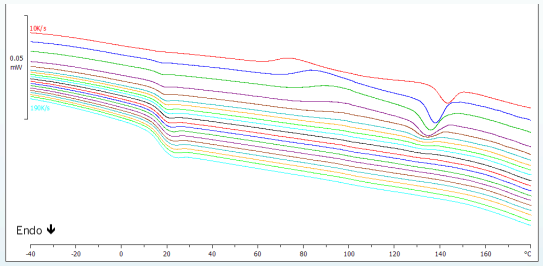

Figure 3 Apparent heat capacity of 1µg PHBV from Flash on heating between 10 and 190Ks^{-1} heating rates after cooling at 1,000 Ks^{-1}.

- Cold crystallisation can be prevented through heating at rates greater than 120 Ks^{-1} thereby retaining an amorphous polymer
- Slower heating rates from the glassy amorphous phase at -80 ˚C allows observation of cold crystallisation
- The aging peak on T_g is less prominent in Fig 3 due to the faster cooling rate adopted in this experiment

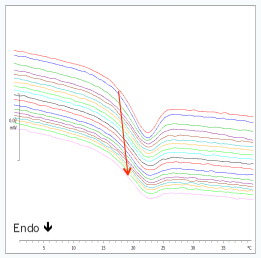

Figure 4a: The variation in T_g with cooling rate as measured on the reheat at 200 Ks^{-1}.

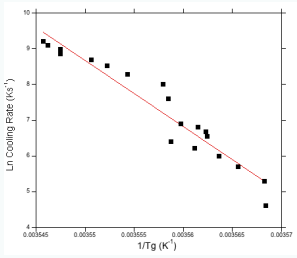

Figure 4b: Arrhenius plot yielding an activation energy of 1653 kJmol^{-1}. R^2 = 0.926

- The T_g increases from 17.24 ˚C to 19.03 ˚C with a cooling rate variation from 100 to 10,000 Ks^{-1}
- Activation energy of 1653 kJmol^{-1} was calculated by the Arrhenius equation. Harris (1995) found activation energy of 166 kJmol^{-1}

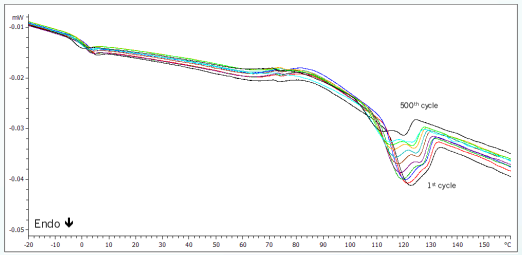

Figure 6: PHB-co-HV subjected to 500 heat cool cycles and held at 185 ˚C for 0.1 s every cycle.

- After the sample is subjected to 500 cycles a clear reduction can be seen in the melting point and the crystallinity suggesting that degradation is occurring

Conclusions

- Hot and cold crystallisation of PHB-co-HV can be prevented at 60 and 120 Ks^{-1}, respectively. An activation energy of 1653 kJmol^{-1} was calculated using the T_g.

Acknowledgements

Funding for this study was obtained from the European Union; FP7, project number 289521

References: [1] Harris, A. (1995) Aging of Poly(3-hydroxybutyrate) and its copolymers. PhD thesis, University of Birmingham

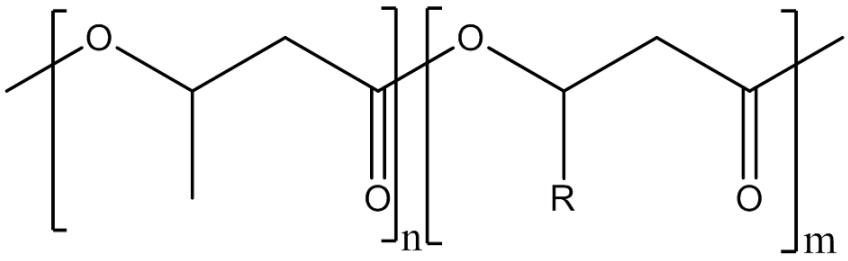

Figure 1 – PHB copolymer

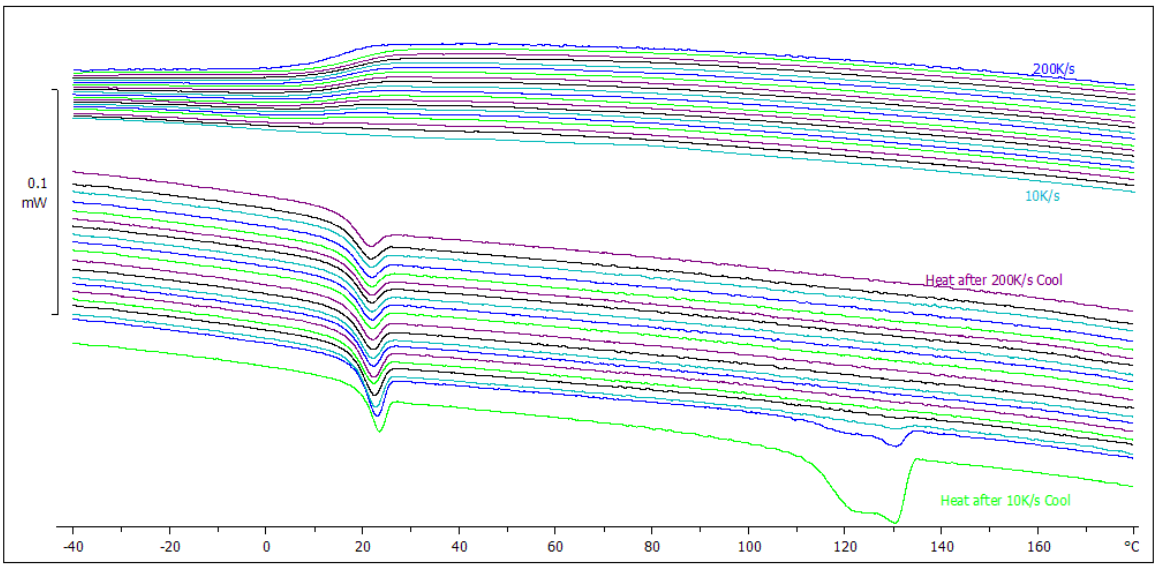

Figure 2 - Cooling at rates between 10 and 200˚C/s with a constant heat at 200˚C/s to preventing crystallisation

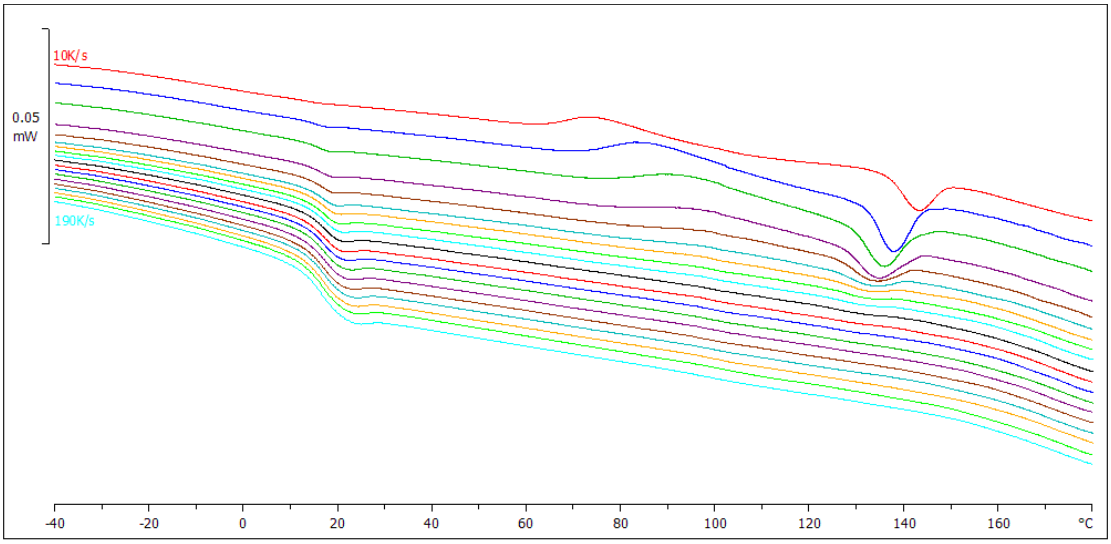

Figure 3 - Apparent heat capacity of 1µg PHBV from Flash on heating between 10 and 190˚C/s heating rates after cooling at 1,000˚C/s

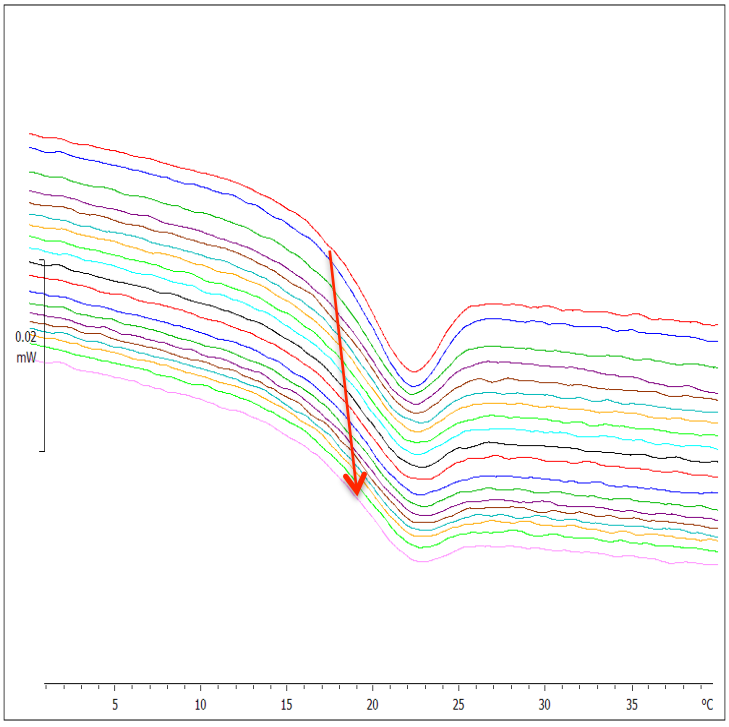

Figure 4a - The variation in T_g with cooling rate as measured on the reheat at 200˚C/s

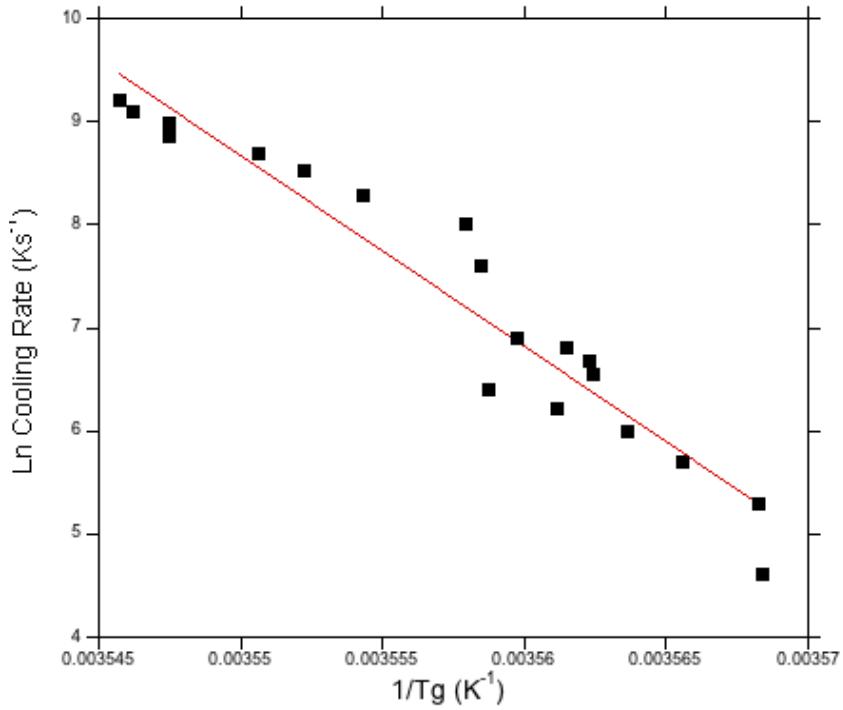

Figure 4b - Arrhenius plot yielding an activation energy of 1653 kJmol^{-1}. R^2 = 0.926

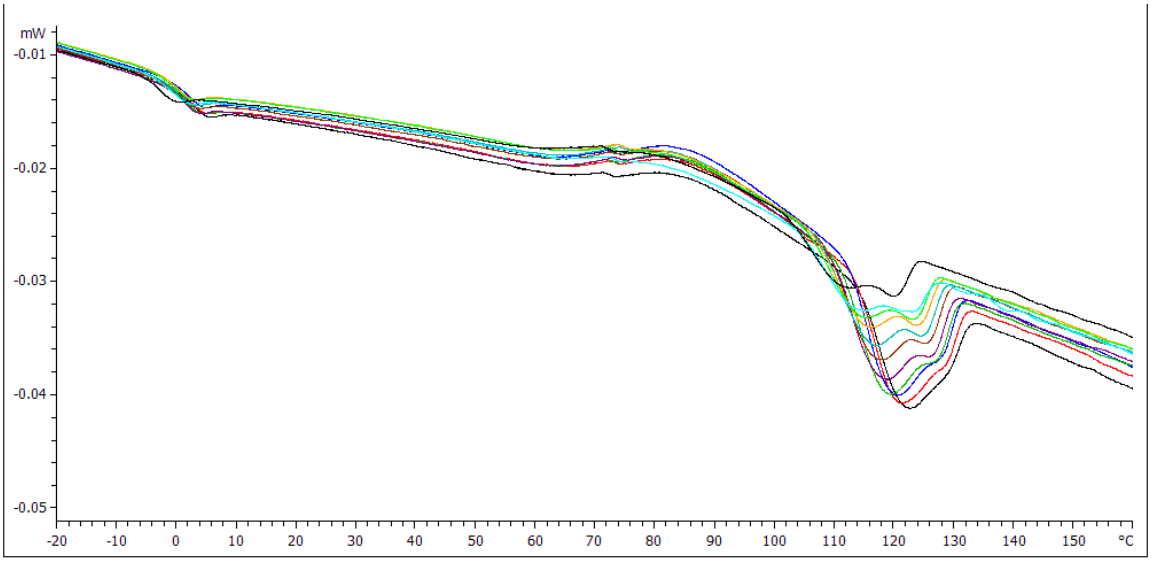

Figure 5 - PHB-co-HV subjected to 500 heat cool cycles and held at 185 ˚C for 0.1 s every cycle.